Functionalization strategies for the development of innovative biochips

Ricardo Alvarado- Meza

Communauté
UNIVERSITÉ Grenoble Alpes

THÈSE

Pour obtenir le grade de

DOCTEUR DE LA COMMUNAUTE UNIVERSITE GRENOBLE ALPES

Spécialité : **Chimie - Biologie**

Arrêté ministériel : 25 mai 2016

Présentée par

Ricardo ALVARADO-MEZA

Thèse dirigée par **Yoann ROUPIOZ, DR, CNRS**
et codirigée par **Loïc LEROY, MCF, UGA**

préparée au sein du **CEA Grenoble**
Institut Nanosciences et Cryogénie (INAC)
Service : Systèmes Moléculaires et NanoMatériaux pour l'Énergie et la Santé (SYMMES)
Groupe : Chimie pour la Reconnaissance et l'Etude des Assemblages Biologiques (CREAB)
dans **l'École Doctorale de Chimie et Sciences du Vivant**

Stratégies de fonctionnalisation pour le développement de biopuces innovantes

Thèse soutenue publiquement le **6 de Novembre 2018**,
devant le jury composé de :

M. Éric PEYRIN
Professeur à l'Université Grenoble Alpes (Grenoble), Président du jury
M. Jean Pierre CLOAREC
Professeur à l'École Centrale (Lyon), Rapporteur
Mme. Anne Chantal GOUGET
Directrice adjointe du LPMC, Ecole Polytechnique (Paris), Rapporteur
Mme. Emmanuelle TREVISIOL
Chargée de recherche LAAS (Toulouse), Examinatrice
M. Yoann ROUPIOZ
Directeur de Recherche au CEA (Grenoble), Directeur de thèse
M. Loïc LEROY
Maître de conférences à l'Université Grenoble Alpes (Grenoble), Co-encadrant de thèse

Abstract

Functionalization strategies for the development of innovative biochips

A plethora of biologically relevant processes depends directly on the effective secretion of biomolecules, from regulatory molecules to structural components. Thus, the analysis of complex biological processes requires the development of novel biosensing tools. Therefore, the aim of this thesis is to provide versatile strategies for the generation of innovative biosensors and biochips based on Surface Plasmon Resonance (SPR). As a result from this research, an indirect photofunctionalization method was developed. This procedure allowed the generation of protein microarrays in fully aqueous conditions while preserving the functionality of the grafted proteins. Furthermore, we created and evaluated a novel microstructured SPR biochip for real-time monitoring of cellular secretions. This microstructured biochip presents two different optical phenomena which could be used for cell detection and the monitoring of their secretions. Finally, multiple functionalization strategies were evaluated for the conception of a nanostructured fiber-bundle SPR biochip. Among the approaches, the generation of photoreactive self-assembled monolayers was the most adapted to this system and are currently being optimized. Once achieved, this nanostructured biochip could pave the way for further development of promising *in vivo* biosensing systems.

Keywords: Surface Plasmon Resonance; surface chemistry; microarray; biosensing.

Résumé

Stratégies de fonctionnalisation pour le développement de biopuces innovantes

Une pléthore de processus biologiquement pertinents dépend directement de la sécrétion de biomolécules dans le milieu extracellulaire, aux fonctions régulatrices ou composants structurels. L'analyse de processus biologiques complexes nécessite ainsi la mise au point de nouveaux outils de biodétection. Par conséquent, le but de cette thèse est de fournir des stratégies polyvalentes pour la génération de biocapteurs et de biopuces innovants basés sur la Résonance des Plasmons de Surface (SPR). À l'issue de ces travaux, une méthode de photofonctionnalisation indirecte a été mise au point. Ce procédé a permis de générer des micro-réseaux de protéines dans des conditions entièrement aqueuses, et ainsi de préserver la fonctionnalité des protéines greffées. De plus, nous avons créé et évalué une nouvelle biopuce SPR microstructurée pour le suivi en temps réel des sécrétions cellulaires. Cette biopuce microstructurée présente deux phénomènes optiques différents qui peuvent être utilisés pour la détection cellulaire et le suivi de leurs sécrétions. Enfin, de multiples stratégies de fonctionnalisation ont été évaluées pour la conception d'une biopuce SPR nanostructurée à faisceau de fibres optiques. Parmi ces approches, la génération de monocouches photoréactives auto-assemblées a été la plus adaptée à ce système et est en cours d'optimisation. Une fois réalisée, cette biopuce nanostructurée pourrait ouvrir la voie à la poursuite du développement de systèmes prometteurs de biodétection *in vivo*.

Mots clés: Résonance Plasmons de Surface; chimie de surface; biopuce; biodétection.

Acknowledgments

There is an extensive list of people to whom I feel grateful since, in one way or the other, they have helped me during my stay in Grenoble as well as for the development of this thesis. Yet, to avoid boring the reader (some people actually read the "acknowledgments") I will try to keep this section relatively short.

First of all, I want to express my gratitude to my family and close friends whose constant support gave me strength, laughs and tons of love in the moments that I needed them the most. Then, I want to thank all the CREAB team for being absolutely awesome! Specially my supervisors, Yoann Roupioz and Loïc Leroy. They have not only taught me far more than I could ever thank them for, but they also have been extremely nice and have had (a lot!) of patience during this whole process.

This thesis would not have been possible without the collaboration with numerous amazing scientists which provided their expertise in different fields, access to specialized equipment and constructive feedback. Among them (without a particular order), I would like to thank Olivier Dellea (CEA - Liten), Cyril Herrier (SyMMES), Brigitte Pepin (SyMMES), Christian Lombard (SyMMES), Patrice Marche (IAB), Elodie Bidal (SyMMES), Karim Vindas (SyMMES) and Cloé Desmet (SyMMES).

Also, special thanks to Robert Baptist, Alain Ibanez, Sara Aldabe, LANOTEC and all the NanoAndes network to which I will always be in debt. Thanks to them, I was able to arrive to Grenoble for a short internship in the lab that would eventually receive me as a doctoral student. Also, I want to thank the EDCSV for providing my funding during these three years and to Marlen Murillo (thanks a lot Mar!) who trusted me and offered her help in a moment of need.

Well, to lighten up the mood I would not dare to finish this short section without a very special mention: dark chocolate, whose delightful taste brightens up my days.

Finally, although I am not much of a fan of Edison, during several moments of my project I could perfectly relate to one of his quotes and so, I decided to share it with you:

"I Have Not Failed. I Have Just Found
10000 Things That Do Not Work."
Thomas Alba Edison

Without further ado, let me present you my work.

Pura vida!

Contents

List of Figures

1 General introduction

Contents

1.1 Biosensors and biochips

Evolution has doted living organisms with a multitude of sensing strategies which allows them to perceive, interact and adapt to their surroundings. Among such organisms, humans have successfully used their highly developed cognitive capabilities to expand their natural senses. By using artificial tools to overcome our limitations, we have been able to observe previously unknown phenomena, leading to a better understanding of the structure and inner workings of the universe and even ourselves. Specifically, when used for detecting biomolecule interactions (biosensing), these sensing technologies have become of paramount relevance in biomedicine (*e.g.* drug discovery, disease diagnosis and monitoring), food safety and environmental monitoring, just to cite a few examples. On the other hand, the ever increasing complexity of the systems to be studied drives a constant development of innovative biosensing devices. Considering this need, the aim of this doctoral thesis consists in providing different platforms for the creation of novel biosensing systems. However, before expanding on this subject, a proper description regarding what are these biosensing systems and how they can be produced is required.

1.1.1 Definitions

To start, we can define a biosensor as a device that employs biological components for sensing a specie of interest (either biological or not)[1]. This device consists of a biological recognition system (called bioreceptor) that interacts with the analyte and a transducer which converts this biochemical interaction into a quantifiable and processable signal[2,3] (Figure 1.1).

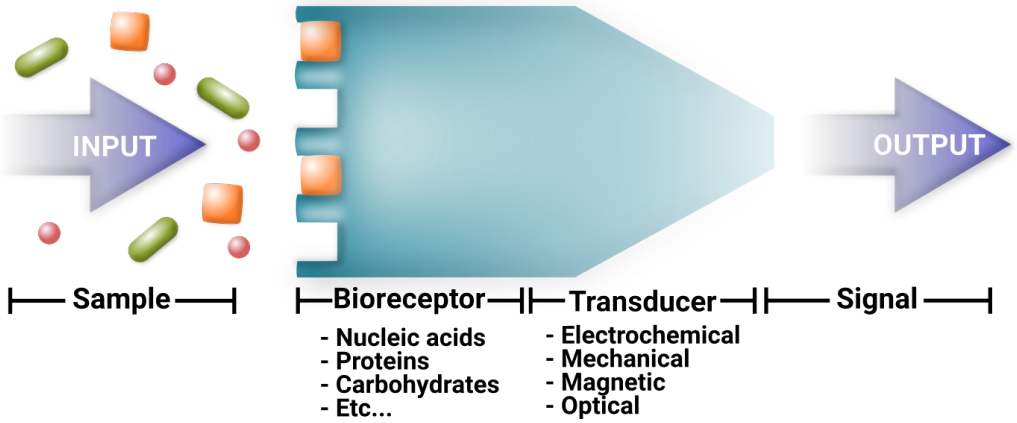

Figure 1.1 – Schematic representation of the elements of a biosensor. Inspired from Vidotti et al.[4] and Chambers et al.[5].

The first biosensor was created by Leland Clark as a natural progression from his work on electrodes for sensing oxygen[6]. By immobilizing an enzyme, a glucose oxidase, on platinum electrodes, Clark and Lyons[7] created the first prototype of a electrochemical

glucose sensor. Thanks to this simple yet revolutionary device, Clark is acknowledged as the "father of biosensors"[6] paving the way for an explosive growth in the field[2].

The widespread use of biosensors has had a profound impact in our society, spanning over as diverse array of fields such as drug discovery, disease diagnosis, food safety, environmental monitoring, forensics and military applications[8]. Nevertheless, this also created new needs such as the simultaneous monitoring of multiple analytes. As a solution for this necessity, more complex sensing systems, namely biochips, have been developed. These systems consist of arrays of individual biosensors (with varying specificity) that can be monitored individually, generally, using the same transducer[2].

1.1.2 Overview of biosensing methods

An ever increasing variety of biosensing strategies is constantly being developed. A simple way to classify biosensors consists in separating them into two general groups, namely label-based and label-free methods[9]. Label-based approaches require the coupling of the analyte with a label that induces a unique response on the transducer, whereas in label-free technologies the signal is directly generated via *in situ* interaction of the analyte with the transducer[9].

Although they are usually more sensitive, label-based assays present major drawbacks such as: (a) They do not provide information related to binding kinetics as the measurements are endpoint read-outs and (b) they require numerous washing stages which are time consuming, may lead to human errors, reduce effective throughput, complicates sample preparation and increases the costs[10]. Therefore, there has been an enormous drive to develop label-free methods as they offer an important reduction in cost, experimental artifacts and complexity of the assays while providing quantitative real-time information[9,10].

So far, most label-free sensing devices are developed using either electrochemical[11] or optical[9,12–14] transduction methods, which we can briefly describe as follows:

1.1.2.a Electrochemical-based transduction

These systems use electrodes as a transduction element providing quantitative or semi-quantitative information regarding analyte detection[15]. When biomolecular interactions occur in the sensing regions, measurable fluctuations in the electric properties between a series of electrodes are observed[16] (Figure 1.2). Based on which type of property is measured, we can subgroup electrochemical systems into: amperometric/voltammetric, potentiometric, conductometric, Field-Effect Transistor (FET) and impedance systems[11].

In the case of amperometric/voltammetric systems, they are based on measuring current fluctuations caused by oxidation/reduction of electroactive species[15]. Such redox processes occur due to a biochemical reaction that can be related to the concentration of the analyte in the solution[15]. Potentiometric biosensors measure charge accumulation or electric potential between electrodes at near zero current during the biorecognition pro-

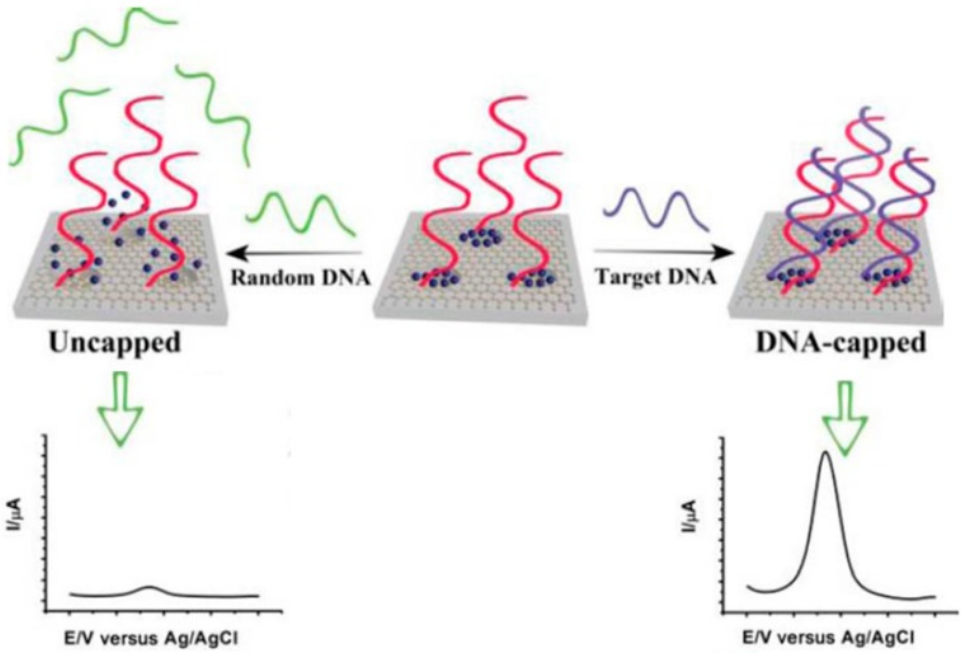

Figure 1.2 – Schematic display of a voltammetric nucleic acid-based biosensor. Hybridization with target DNA causes a conformation change which alters the amount of redox-active molecules near the surface. Adapted by Campuzano et al.[17] from Wu et al.[18].

cess[3,11,19]. On the other hand, alterations in the conductive properties of the medium between electrodes are the foundation of conductometric biosensors[3]. Impedance systems are based, as its name implies, on impedance (electric resistance and reactance) alterations[3,11]. Finally, FET biosensors provide an electric current caused by potentiometric effects at a gate electrode[3,20].

Electrochemical systems are relatively simple to operate, able to measure optically turbid samples and they employ readily available equipment which allows the development of low cost instrumentation and further miniaturization[15]. Nevertheless, they also present some inconveniences such as being susceptible to external electromagnetic interference and are usually harder to multiplex[15].

1.1.2.b Optical-based transduction

This type of sensors offers the largest number of possible labeled and label-free strategies since optical biosensing can be performed by many different spectroscopic techniques (absorption, fluorescence, phosphorescence, chemiluminescence, Raman, refraction, dispersion spectrometry, among many others)[2]. Furthermore, by monitoring distinct properties of the light (such as amplitude, energy, polarization, wavelength, decay-time and/or phase) it is possible to develop a myriad of biosensing methods[2].

Some of the most widely used optical label-free biosensing methods are: ellipsometry, Surface-Enhanced Raman Scattering (SERS) and Surface Plasmon Resonance (SPR)[9].

Among them, SPR has become the most popular strategy[9], as the data generated are simple to analyze[21], does not require complicated surface nanofabrication processes[22], allows high levels of multiplexing[12], is compatible with real-time analysis of biointeractions as the sensing speed is not a limiting factor[23] and multiple SPR-based sensing devices have been already commercialized[21].

1.2 Surface plasmon resonance sensors

1.2.1 Principle of surface plasmon resonance

In this section, I will provide just an overview of the Surface Plasmon Resonance (SPR) phenomena. For a detailed physical description refer to Homola[24].

However, before talking about SPR, I will like to briefly introduce the formation of evanescent waves via total internal reflection in media of distinct Refractive Indexes (RI). When light travels from a dielectric with higher RI (Dielectric$_a$), to another of lower RI (Dielectric$_b$), it can undergo a phenomena called Total Internal Reflection (TIR) if the angle of incidence (θ_i) is larger than the critical angle (θ_c, defined as the angle whose refraction is 90°) as described by Snell's law in Equation 1.1.

$$\theta_i > \theta_c = arcsin\left(\frac{n_{cladding}}{n_{core}}\right) \tag{1.1}$$

Under TIR, the reflection process comes along with the generation of an evanescent field which corresponds to the penetration of the electromagnetic field of the incident light into dielectric$_b$[25]. The intensity of this evanescent field is present at its maximum at the interface between the media and decays exponentially as it penetrates the dielectric$_b$[26] (Figure 1.3a). Fluctuation in the RI inside the penetration range of the TIR evanescent field can induce in shifts in the intensity of the reflected light. However, those shifts usually are very weak and so amplification strategies such as SPR have been developed[27].

For SPR to occur, a thin metallic layer (commonly gold) is deposited on the surface of the dielectric$_a$. At the metal-dielectric interface (1), natural occurring charge-density oscillations (Surface Plasmon Polaritons, SPPs) are present[24,28]. Then, at a specific combination of wavelength and incidence angle (which varies based on the refractive indexes of the media, thickness and nature of the metal layer), the TIR evanescent field can excite the SPPs which in turn form an electric evanescent field, a SPP evanescent field, which couples with the TIR evanescent field enhancing it[26] (Figure 1.3b). Since this coupling phenomena is highly sensitive to RI fluctuations (inside the few hundred nanometers penetrated by the SPP evanescent field), monitoring of the metal surface can be performed with high sensitivity (in the range of 10^{-7} - 10^{-6} Refractive Index Units, RIU)[28–30].

(1). This occurs for both interfaces: Dielectric$_a$-metal and Dielectric$_b$-metal. However, we will focus on the boundary between Dielectric$_b$-metal.

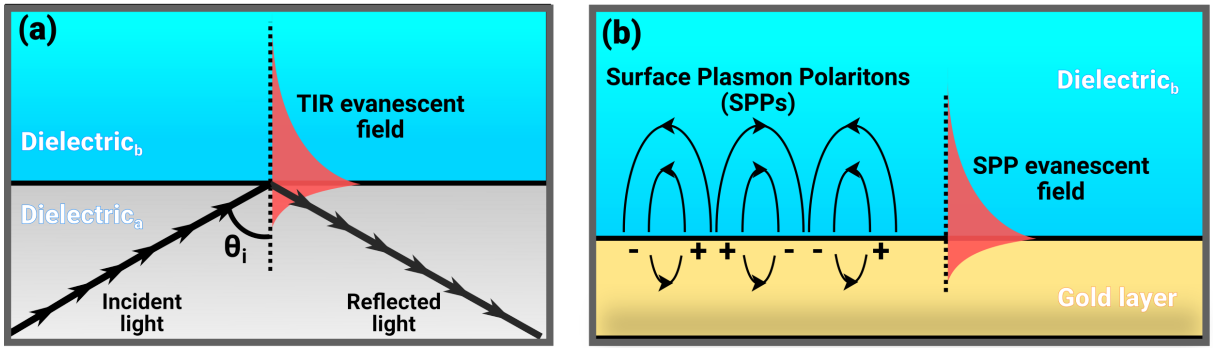

Figure 1.3 – Schematic representation of the SPR phenomena. (a) Formation of a TIR evanescent field and (b) Coupling of surface plasmons with the TIR evanescent wave.

1.2.2 Types of SPR sensors

Different types of configurations for exciting SPPs by incident light are possible. Based on how the SPR coupling conditions are performed, one can classify SPR sensors into: (a) prism-based; (b) diffraction grating and (c) based on optical waveguides[24] (Figure 1.4).

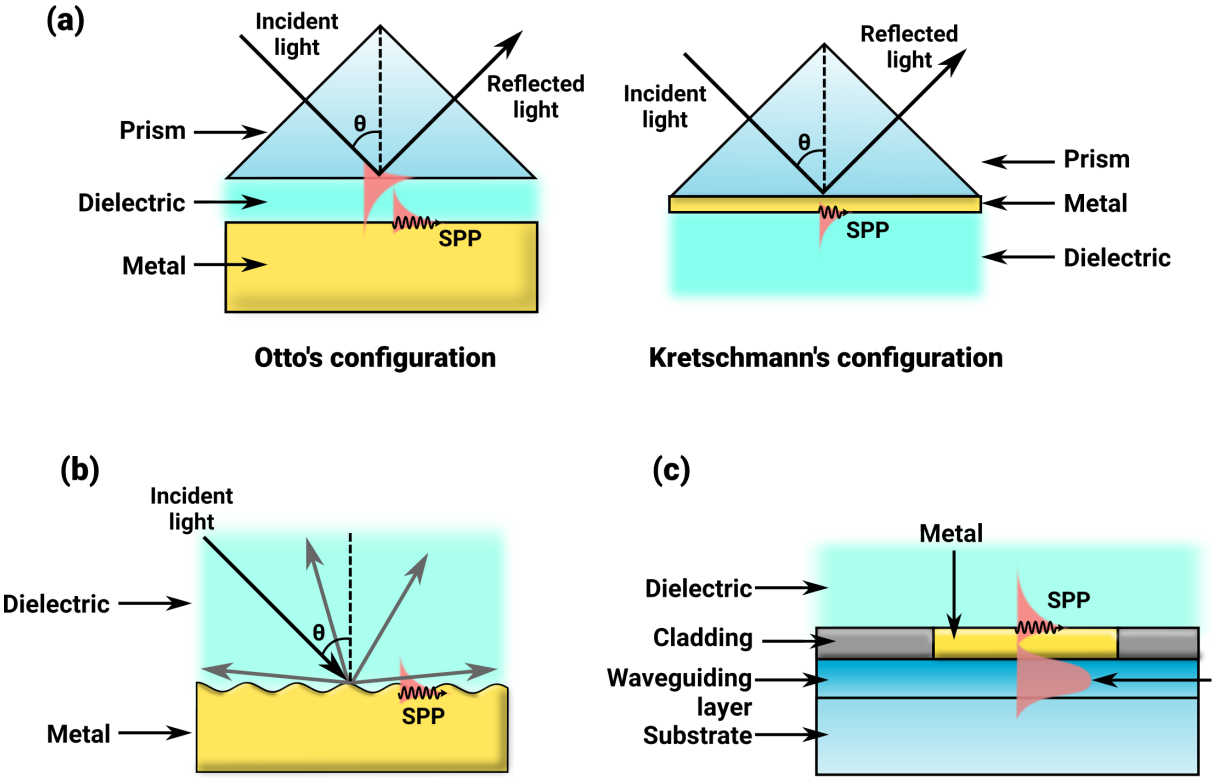

Figure 1.4 – Schematic representation of different SPR configurations based on the method used for excitation of the surface plasmons. (a) Prism coupling method (Otto's configuration to the left and Kretschmann's on the right); (b) Grating coupling and (c) Waveguide coupling. Images based on artwork by Homola[24].

1.2.2.a Prism coupling

The most popular system for exciting surface plasmons is the use of prisms[24]. In this case, a prism guides the light into the metallic layer at an angle at which the incident light experiences TIR and so, generates an evanescent wave (E_{TIR})[24,31]. Coupling of both evanescent waves (E_{TIR} produced via TIR and E_{SPP} generated by excitation of SPPs) occurs as previously described.

Two different configurations have been developed to exploit this process, namely Otto's[32] and Kretschmann's[33] geometries (Figure 1.4a).

In case of Otto's geometry, TIR occurs at the interface between the prism and the dielectric medium while the metallic layer is positioned a few micrometers away from the prism. As the gold layer is inside the penetration depth E_{TIR}, excitation of SPPs and coupling of the evanescent fields can occur[24,31].

In Kretschmann's configuration, the sensing system employs a high refractive index prism in direct contact with a thin metal film ($<$ 100 nm of thickness) which, in turn, is exposed to the dielectric medium (mostly aqueous solutions)[24]. The evanescent wave penetrates through the metal film and couples with the surface plasmons in the interface of the sensing medium and the metal[24,31]. This configuration has become the most popular one as it does not require precise control on the distance between the gold layer and the prisms.

1.2.2.b Grating coupling

In this method, incident light traverses the dielectric medium and interacts with a grated metal layer (with a defined pattern periodicity and depth), light gets diffracted from the pattern and then it can generate SPR phenomena over different zones of the grating when the coupling conditions are achieved[24] (Figure 1.4)b. One of the main drawbacks of this method is the fact that light traverses the dielectric medium, which can modify the signal independently of the RI at the surface[34]. Yet, this method is attractive as the grating replaces the need for expensive glass prisms. Furthermore, disposable gratings can easily be mass produced and, since the optical configuration required is similar than for ellipsometry instruments, this method is considered to be relatively affordable[34].

1.2.2.c Waveguide coupling

Another type of coupling system involves the use of single or multi-mode optical waveguides (such as optical fibers as it is further discussed in Chapter 4). Briefly, light propagates through a waveguide via TIR until it enters a region where a thin metallic layer has been deposited (Figure 1.4c). At such point, if the coupling conditions are achieved, SPR is generated allowing to monitor RI changes in the surroundings of the metal coating[35].

1.3 Surface functionalization approaches

Controlled grafting of the biorecognition molecules over the sensing layer is one of the most crucial parameters in biosensor development. As novel biosensing systems are developed, there is a constant drive towards the creation of compatible functionalization methods. Among the numerous strategies, one can clearly observe two main categories: direct and indirect immobilization methods.

Direct functionalization methods involve the immobilization of the biorecognition element directly on the transducer. Whereas, indirect approaches are based on a multi-step process at which a intermediate layer is formed on the transducer (usually a polymeric layer such as carboxymethyl dextran[36] or a Self-Assembled Monolayer, SAM, of a specific compound) and then the probes of interest are chemically attached to this layer.

Considering that the formation of SAMs is a fundamental part of the strategies developed in this thesis, I will mainly focus in introducing biofunctionalization strategies based on this method.

SAMs can be defined as assemblies of organic molecules whose spontaneous arrangement on a substrate, under specific conditions, leads to semi-crystalline and even crystalline 2D structures[37]. They can be created over numerous substrates but silane-based SAMs are possibly the most frequently used[38]. In the specific case of SPR sensors, gold is the most common substrate as this metal provides a convenient range of angles and wavelengths combinations for generating the SPR phenomena as well as being stable in most solutions used for biological assays[39].

Regarding SAM formation on gold surfaces, since its discovery by Nuzzo and Allara[40] in 1983, the use of sulfur-containing molecules have become the dominant method[41]. Gold acts as a soft electron-pair acceptor allowing the formation of dative bonds (2) with some soft electro-pair donors as is the case of sulfur containing molecules[42], phosphines[43] and primary[44] amines (both of which form weaker SAMs) and, recently, carbenes[41]. Then, the formation of SAMs can be described as a subtle energetic interplay between gold-sulfur (or other electro-pair donor) and inter-molecular lateral forces[45]. These later forces define the crystallinity of the SAM as the molecules try to maximize their lateral attractive interactions (van der Waals and hydrogen bonding for example)[45] (Figure 1.5).

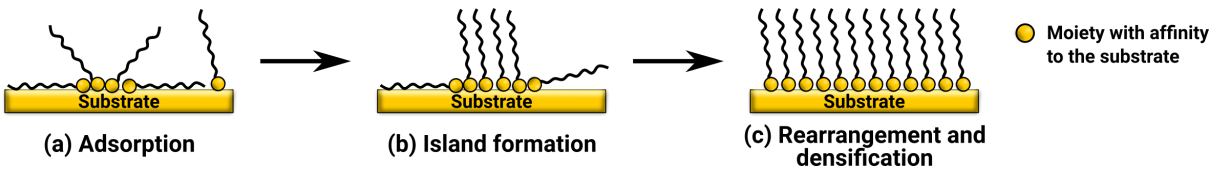

Figure 1.5 – Graphical representation of SAM formation stages: (a) Initial adsorption on surface, (b) reorientation and island formation and (c) rearrangement and densification.

(2). Also known as coordinate covalent bonds in which a single atom provides both electrons instead of each atom sharing one electron.

1.4 Direct functionalization for SPR biosensing

Among the direct functionalization approaches, we can mention adsorptive immobilization and electropolymerization.

1.4.1 Direct immobilization via adsorption

These are the simplest and most popular methods in solid-phase assays[42,46]. They usually rely on the spontaneous immobilization of biomolecules to low-energy surfaces (plastics for example) via hydrophobic effects (as in ELISA coatings)[42] but can also occur on metallic surfaces.

In terms of kinetics, the adsorbing molecule suffers three distinct phases[47]:

1. Displacement to the surface via convection and diffusion
2. Reversible and labile attachment at contact; and
3. Spreading and conformational rearrangement.

For physisorption, water molecules play an important role as they compete with the probe for potential attachment sites on the surface[42]. Conformational changes after protein adsorption are a product of an entropic phenomenon caused by the degree of organization of the water molecules[42]. The cohesion (high internal energy) of water promotes exclusion of low-energy sites (as are hydrophobic domains) which agglomerate via hydrophobic effects[42]. This phenomena does not only apply to proteins adsorbed via hydrophobic effects, but also to any protein attached to poorly hydrated surfaces[42]. Moreover, it may cause irreversible modifications that may affect their functionality and promote clustering of proteins (in case they have some degree of lateral mobility)[42,48,49]. An example of this was observed on antibodies adsorbed over polysterene surfaces, extensive denaturing was reported resulting in >90% of inactive binding sites[50].

In the case of chemisorption, chemical interaction of the surface affinity group with the metal occurs after the second phase. A common example of a chemisorption process are gold-thiol interactions as was previously introduced. This reaction is caused by the fact that gold can act as soft electron-pair acceptor (a weak Lewis acid) with strong affinity to soft electro-pair donnors (weak Lewis bases) such as thiols (R-SH), disulfides (RS-SR) and thioethers (R-S-R)[42]. Therefore, direct immobilization of the biomolecules can be performed via naturally/artificially present thiol/disulfide moieties[42].

As direct adsorption processes are prone to induce important conformational changes in proteins, this process is more suited to biomolecules whose activity does not depend on their tertiary structure, such as is the case of oligonucleotides[51,52] and peptides[53].

1.4.2 Electropolymerization of pyrrole

Another direct patterning method is the electropolymerization of polypyrrole. This polymer presents exceptional stability, conductivity and biocompatibility[54]. Furthermore, it

forms uniform films with easily tunable thickness for which this method has been extensively used by our research team for surface functionalization with biosensing applications[55–59]. By applying a potential difference, a solution of pyrrole monomers undergoes electropolymerization (Figure 1.6). Schweiger et al.[60] describes this process as an anodic oxidation on the working electrode where the first step is the formation of pyrrole radical cations leading to the formation of cationic dimers (which turn into neutral dimers by proton elimination). Rather than coupling with monomeric radical cations, the oxidized dimers couple with each other rapidly increasing the molecule size until forming an insoluble polypyrrole polymer on the gold surface[61].

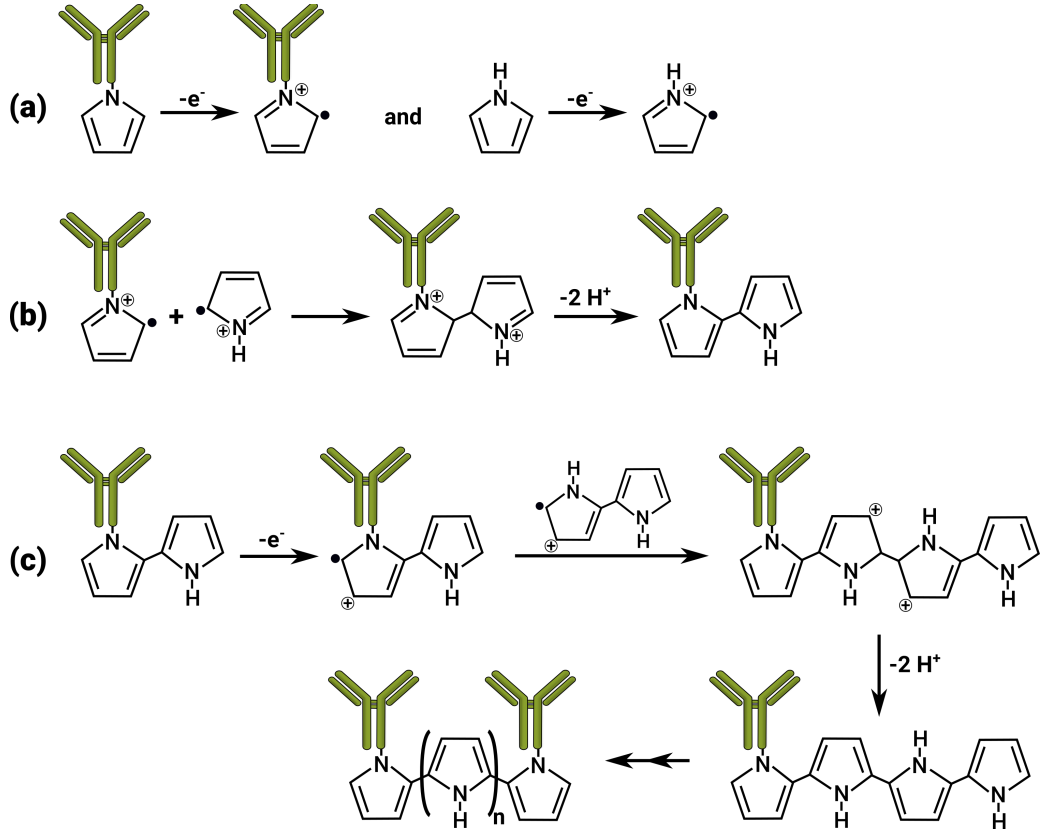

Figure 1.6 – Electropolymerization of pyrrole monomers. (a) Formation of pyrrole radical cations; (b) Formation of cationic dimers, and then, neutral pyrrole dimers and (c) Polymerization based on either dimer, tetramer or n-mer (where n represents an even number) interaction. Modified from Schweiger et al.[60].

1.5 Indirect functionalization for SPR biosensing

Indirect methods are multi-step procedures where the gold surface is first functionalized with one or multiple layers of a molecule. Then, the probes can be attached either via non-covalent methods (electrostatic interactions or hydrophobic effects), covalent linking or by bioaffinity-coupling[42,45].

1.5.1 Non-covalent immobilization

Non-covalent immobilization of biomolecules can be performed via hydrophobic effects or electrostatic interactions[45] (Figure 1.7). A typical example of protein immobilization on hydrophobic SAMs is the grafting of azurin over alkanethiols[62–64].

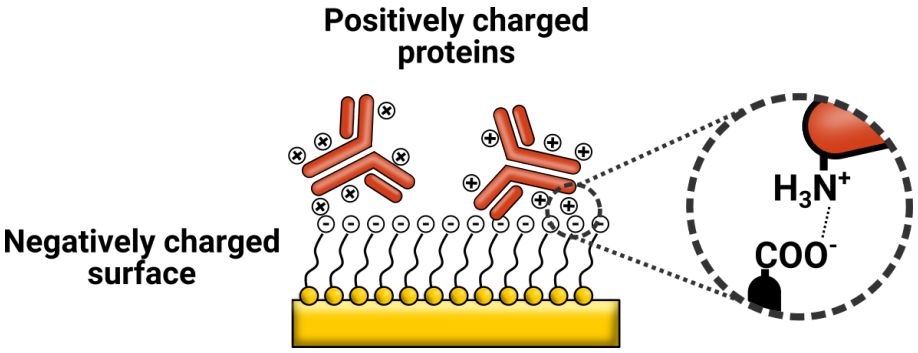

Figure 1.7 – Scheme of electrostatic immobilization of charged proteins.

Electrostatic immobilization can be performed on SAMs or hydrogels that present either positively charged amines ($R-NH_3^+$) or negatively charged carboxyl ($R-COO^-$) moieties exposed on the surface[45]. Grafting of the biomolecules is performed by adjusting the pH of the buffer based on the isoelectric point [(3)] of the biomolecule in order to assure that the probe is adequately charged[45]. However, if this process is not accompanied by an irreversible secondary attachment (such as hydrophobic effects or covalent linking), this adsorption is fully reversible with high ionic strength buffers as the counter-ions will mask the surface charges[42].

However, it is important to highlight that, even if there have been successful examples of non-covalent immobilization, this method could induce drastic conformational changes and protein denaturation on some sensitive samples, reducing their activity[65]. Moreover, these interactions lack intrinsic selectivity making them prone to non-specific adsorption[42].

1.5.2 Covalent immobilization

This is the most frequently used method as it forms stable covalent bonds between the probe and the sensor's coating. As an incredibly vast amount of strategies have been developed (and reviewed[42,45,66]), in this manuscript we will only comment on some of the most frequent approaches.

(3). The isoelectric point (pI) corresponds to the pH at which a molecule presents no net charge. It is calculated as the average of the acid dissociation constants (pK_a) of the acidic/basic moieties, amino and carboxyl functionalities, of the molecule

1.5.2.a Amine coupling via reactive esters

This has been the most frequent immobilization technique due to its versatility, simplicity and high coupling yields[42,66]. This method has been extensively studied and optimized allowing an effective coupling between primary amines and carboxylated surfaces[66,67].

During this reaction, exposed carboxyl moieties are activated by a carbodiimide, 1-Ethyl-3-(3-dimethylaminopropyl)carbodiimide (EDC) being the most common, forming an O-acylisourea[42] (Figure 1.8). The activated isourea is highly reactive to nucleophiles (*e.g.* primary and secondary amines, hydrazides, primary alcohols, etc) including water molecules[42,66]. Therefore, the O-acylisourea intermediate can suffer from hydrolysis in seconds unless it is converted into an active ester by addition of N-hydroxysuccinimide (NHS)[42,45]. While the half-life of the isourea intermediate was in the order of seconds, NHS-esters can last minutes at pH between 8-9 to hours at pH 4-5[42].

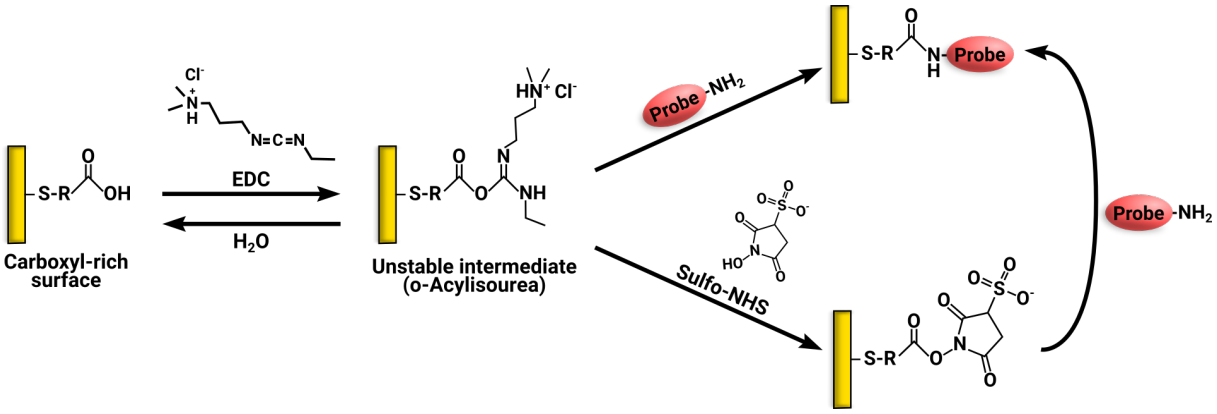

Figure 1.8 – Coupling of primary amines to carboxyl exposed moieties of a thiol-based SAM on a gold substrate. Image inspired from Hermanson[66].

1.5.2.b Amine coupling via reductive amination

Amines can readily interact with carbonyl moieties (*e.g.* aldehydes: RC(=O)H and ketones: RC(=O)R') forming labile Schiff bases which can be stabilized into secondary amines by a reducing agent[42,66] (Figure 1.9). Common reducing agents include sodium borohydride ($NaBH_4$) and sodium cyanoborohydride ($NaBH_3CN$)[68]. The main advantage of $NaBH_3CN$ lies in being a milder reducing agent compared to $NaBH_4$, this allows specific reduction of the Schiff bases while not affecting the free aldehyde moieties on the rest of the surface, allowing multi-step processes[42,66,68].

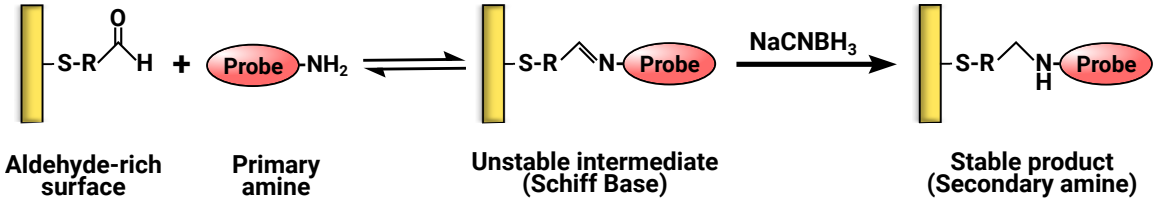

Figure 1.9 – Coupling of primary amines to aldehyde exposed moieties of a thiol-based SAM on a gold substrate. Image inspired from Hermanson [66].

1.5.2.c Thiol coupling via maleimides

Another way of grafting biomolecules is the coupling of sulfhydryl functionalities (R-SH, thiols) with maleimide moieties (Figure 1.10). Thiols irreversibly react with the double bond of the maleimides which undergo an alkylation reaction resulting into a thioether bond [42,66].

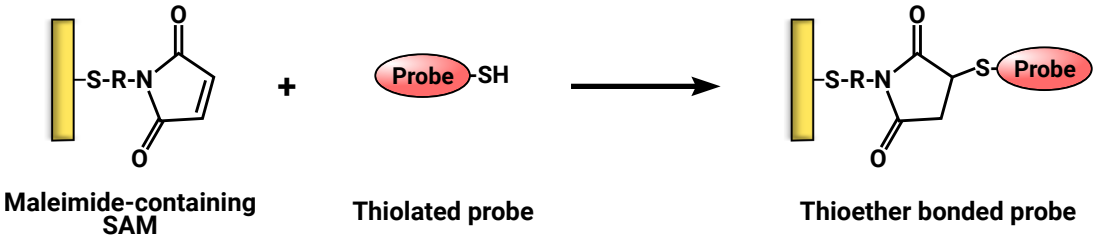

Figure 1.10 – Coupling of thiols by maleimide exposed moieties on a thiol-based SAM over a gold substrate. Image inspired from Hermanson [66].

When performed at a pH between 6.5 - 7.5, this reaction is specific for thiols (at pH 7.0 the reaction kinetics for thiols is 3 orders of magnitude faster than for amines) [42,66,69–72]. Other compounds can be used for thiol coupling via alkylation reactions such as haloacetyl compounds, acryloyl compounds, arylating agents (4) and aziridines [66]. However, these are not as popular as maleimide moieties due to low specificity, rapid hydrolysis or for presenting low solubility in aqueous buffers [66].

1.5.2.d Thiol coupling by disulfide exchange

Continuing with the use of thiols for biomolecule grafting, another coupling strategy involves disulfide exchange. For this, the most common approach involves the use of pyridyl dithiols [42,66].

As shown in Figure 1.11, this compound can undergo an exchange reaction with free thiols yielding only one disulfide product as the leaving group is transformed into a non-thiolated molecule (pyridine-2-thione) [42,66].

(4). These are aromatic compounds with an element on the ring that can undergo nucleophilic substitution

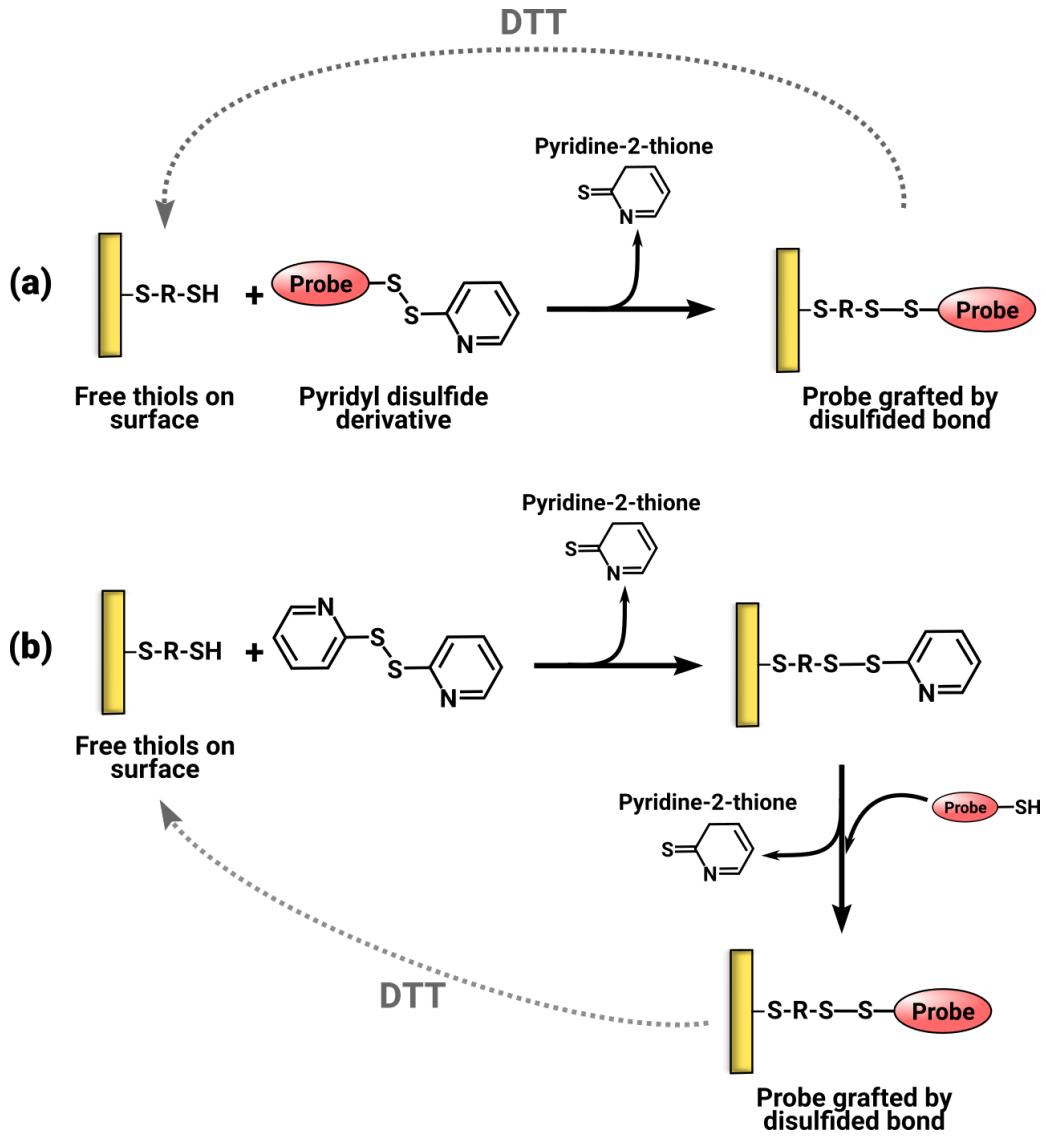

Figure 1.11 – Coupling of thiols via disulfide exchange on a thiol-based SAM over a gold substrate. DTT is used to restore initial state of the surface. Image inspired from Hermanson [66] and Gedig [42].

Aqueous solubility of pyridyl dithiols can be enhanced by using PEG and several of these PEGylated derivatives are commercially available [66]. In general, disulfide coupling reactions provide some interesting advantages as they can be performed in a broad range of pH and buffers (including those compatible with physiological conditions) and the surface can be fully regenerated by using reducing agents such as: dithiothreitol (DTT) or dithioerythritol (DTE), 2-mercaptoacetic acid, 2-mercaptoethanol or 2-mercaptoethylamine [42,66,73].

1.5.2.e Immobilization approaches based on click chemistry

Click chemistry is an abstract concept covering a whole set of reactions that allow the formation of carbon-heteroatom (mostly N, O, and S) bonds [74]. However, to be considered

as a "click reaction", they have to fit a stringent set of criteria which involves: a modular nature of the reaction (process based on building blocks), high yields, inoffensive byproducts (and easily removed by non-chromatographic methods), must be highly specific for one product, ideally insensitive to oxygen and water, relatively simple product isolation and, finally, the solvent used (if any) must be water-based or easily removable[74–76].

Based on their chemical mechanism, it is possible to classify click chemistry reactions into four main groups[74,75]:

— Cycloadditions of unsaturated compounds,

— Nucleophilic substitution, most of which are based on ring-opening reactions of epoxides, aziridines, aziridinium ions, and episulfonium ions;

— Non-aldol carbonylation which forms ureas, thioureas, aromatic heterocycles, oxime ethers, hydrazones and amides; and

— Additions to carbon-carbon multiple bonds.

However, another approach consists of classifying them based on their biocompatibility. The coupling of biomolecules via click reactions requires even stricter criteria involving processes performed under physiological conditions (neutral pH, in aqueous solutions and at a very limited temperature range), with low reactant concentrations, extremely high selectivity and performed in acceptable time scales (in the range of minutes) while also preserving the biological function of the species[76,77].

Among the numerous "click reactions" described so far, we can highlight three methods that have been widely studied and present readily commercial reagents[77] for its use in biomolecule coupling and surface functionalization (as seen in Figure 1.12):

— **Copper (I) catalyzed Azide - Alkyne Click Chemistry reaction (CuAAC):** The typical example of click chemistry based on the reaction of azides with alkynes via the formation of a triazole moiety[75]. This reaction depends on the presence of a metal catalyst (such as cooper) since terminal alkynes are normally unreactive to azides[78,79]. Moreover, these reactions can be further accelerated by the use of microwaves or ultrasound[80].

— **Strain-promoted Azide - Alkyne Click Chemistry reaction (SPAAC):** This is a copper-free method using strained-alkynes, which have a much lower activation energy compared to terminal alkynes and thus, do not require a metal catalyst[76,81]. By removing the metal catalyst, which presents certain levels of toxicity as well as can affect the structural conformation of some proteins, SPAAC can be used for a variety of applications including the conjugation of biomolecules on living organisms (cultured cells)[82,83]. Numerous cyclooctyne-derivatives have been developed and employed in this method such as difluorinated cyclooctynes[84,85] (DIFO), dimethoxy-azacyclooctyne[86] (DIMAC), dibenzocyclooctyne[87] (DIBO), bicyclononyne[88] (BCN), dibenzo - aza- cyclooctyne[89] (DIBAC, also called ADIBO[90] or aza-DBCO[91]), among several others[92].

— **Tetrazine - Alkene Ligation:** Tetrazine is a water soluble molecule able to react irreversibly with the alkenes forming stable dihydropyrazine products and molecu-

lar nitrogen[93]. This reaction is highly selective[94], occurs several hundred-fold faster in aqueous media than in organic solvents[95] and can be performed with isolated biomolecules or even *in vivo*[93]. Beside its selectivity and high yields, tetrazine reactions present very fast kinetics compared to the alternatives mentioned so far[94,96]. Specifically, when interacting with trans-cyclooctene (TCO) it presents the fastest reaction rate of all click reactions (in the order of 2.8×10^6 $M^{-1}.s^{-1}$)[97].

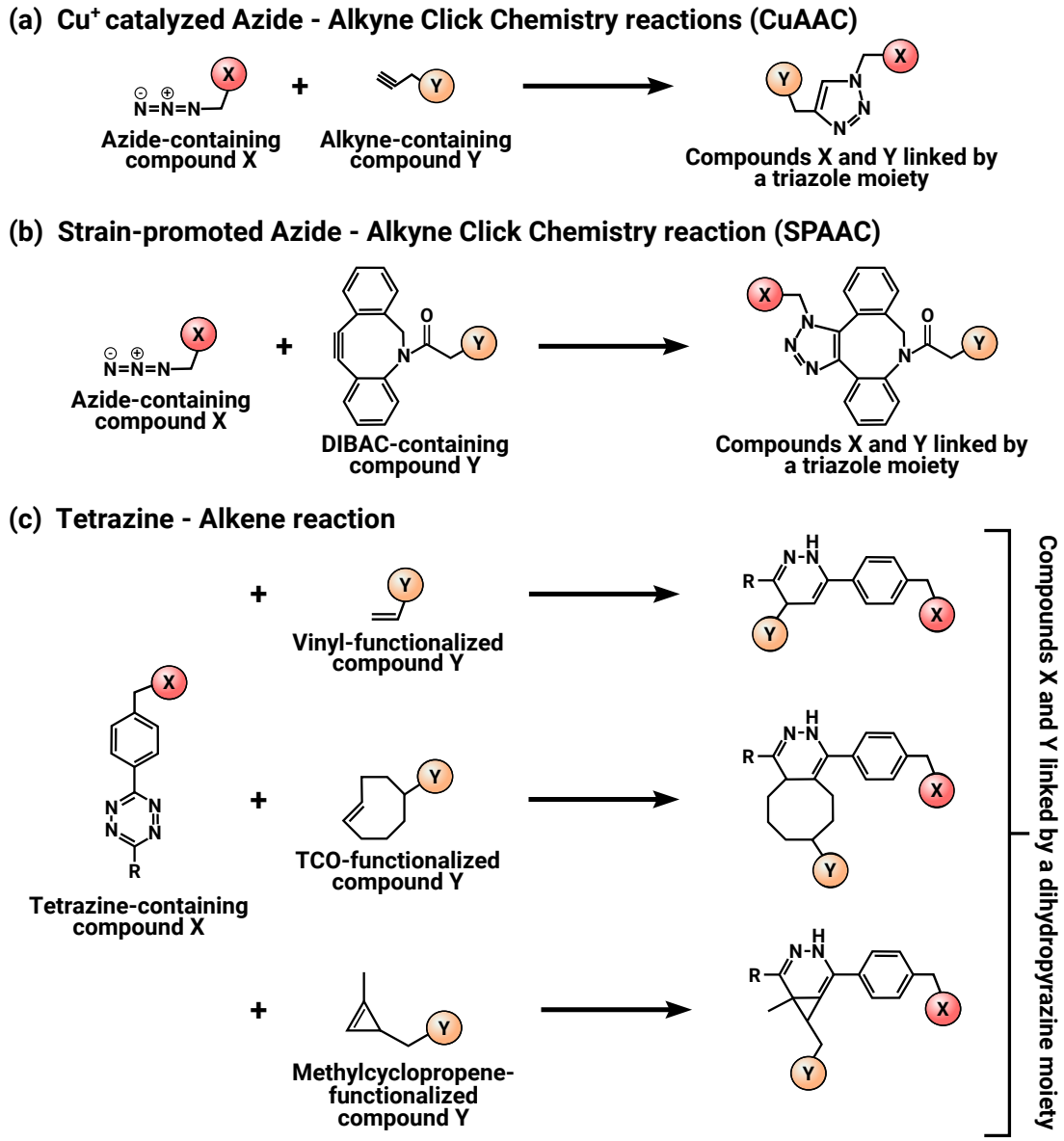

Figure 1.12 – Biocompatible click chemistry pairs. In this case, compound X or Y can be the probe of interest or a surface-bonded molecule. Reactions based on schemes provided by Jena Bioscience®[77].

1.5.2.f Coupling via photofunctionalization approaches

Another possibility consists in the use of photoactivable functionalities for probe immobilization. This approach is discussed with more details in Chapter 2 subsection 2.1.2. But in summary, two main strategies can be used, namely direct or indirect photofunctionalization (Figure 1.13).

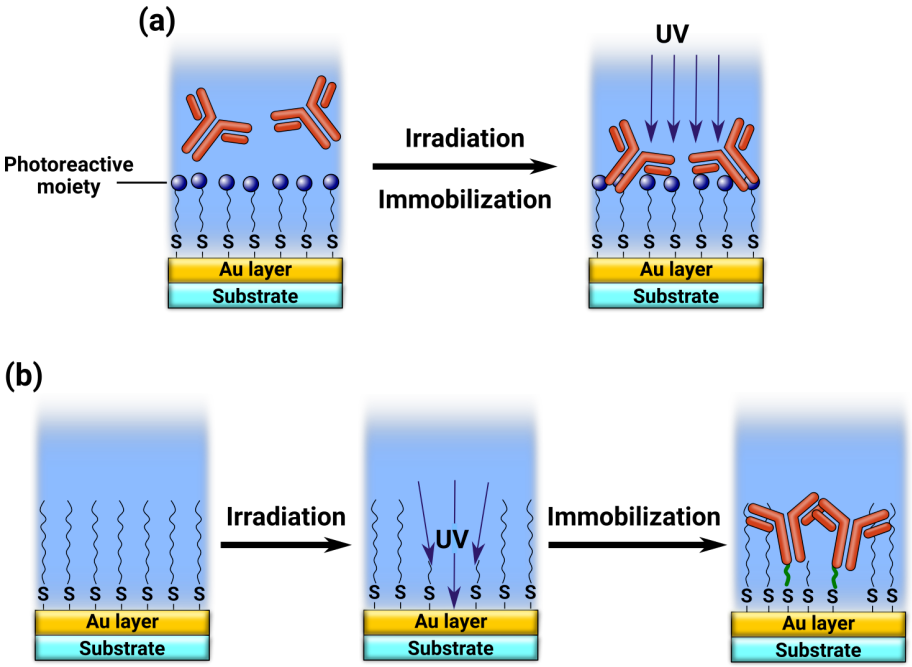

Figure 1.13 – Schematic representation of photofunctionalization methods. (a) Direct photofunctionalization where irradiation and immobilization occur simultaneously and (b) Indirect photofunctionalization where the processes are performed sequentially.

In direct photofunctionalization, light sensitive surfaces are prepared by SAMs containing photolabile moieties such as benzophenone, diazirine or nitrobenzy[98]. Upon irradiation at specific wavelengths, highly reactive intermediates are generated which can interact (non-specifically) with the biomolecules of interest.

For indirect photofunctionalization, the immobilization and the photoreaction steps occur at different moments avoiding direct irradiation of the biomolecules of interest. Photopatterning of surfaces and subsequent functionalization of unprotected zones is one of the most common strategies for this approach.

1.5.3 Bioaffinity-based immobilization of probes

Finally, indirect immobilization of probes can also be performed by using bioaffinity methods. In this case, biomolecules with site-specific activity to the probes (or to a compound coupled to the probes) are grafted on the gold surface. Then, different arraying methods (see Chapter 2 Section 2.1.1) can be employed to expose the grafted capturing molecules

to the probes/conjugated-probes of interest. Some examples include: streptavidin-biotin interactions, immobilization of His-tagged probes, capture of probes by grafted antibodies, capture of antibodies by grafted Protein A/G (5) and oligo-directed protein immobilization (some of which are illustrated in Figure 1.14)[42,66].

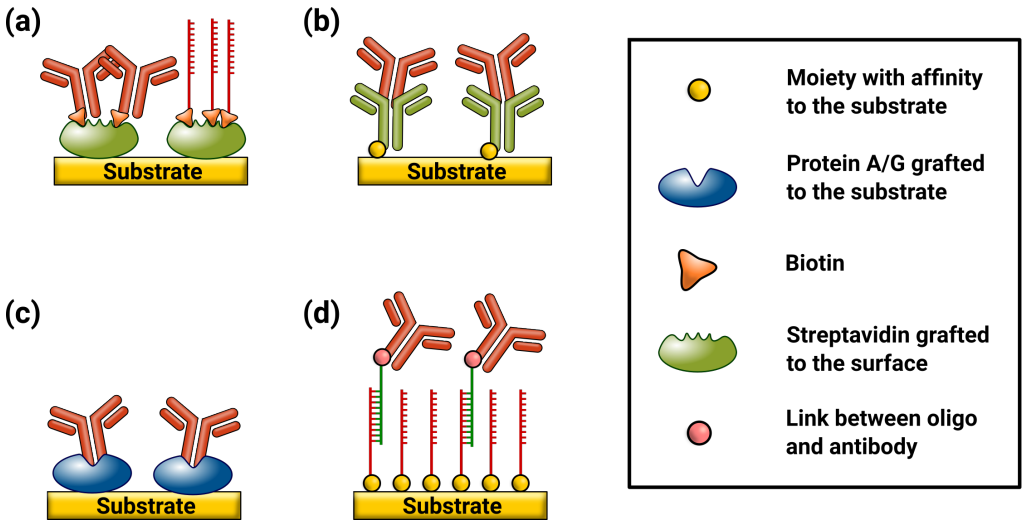

Figure 1.14 – Scheme representing some bioaffinity grafting strategies. (a) Biomolecule immobilization via streptavidin-biotin interaction; (b) Protein grafting via antibodies; (c) Antibody grafting via Protein A/G and (d) Oligo-assisted protein grafting.

1.6 Aim of this thesis

As it has been described, a vast amount of different chemical strategies can be used for the immobilization of desired probes over gold surface for the generation of SPR biochips. The selection of the appropriate method is directly linked to the nature of the probes to be grafted, the arraying procedure and the type SPR biochip to be produced.

During my PhD research, I explored multiple functionalization techniques for their implementation on three distinct SPR-based systems. Each one of these models presented an unique set of challenges, since the substrate showed either a planar, microstructured or nanostructured morphology composed of one or two different materials. Functionalization of such varied surfaces required the adaptation of different chemical approaches such as thiol and silane-based SAMs, pyrrole electropolymerization, photo-assisted functionalization, among others.

In this thesis, the main chapters are dedicated to a different SPR system, presenting an overview of the biosensing strategy, encountered challenges and the strategies used for their functionalization. The next chapter, Chapter 2, is dedicated to the formation of protein microarrays on standard non-structured (flat) gold surfaces via UV photo-assisted

(5). Recombinant bacterial protein created by combining four binding domains from Protein A and two binding domains from Protein G. It is able to bind to human IgG, IgA, IgE and IgM antibodies.[99,100]

indirect functionalization. Then, the following chapter, Chapter 3, focuses on the development and functionalization of a microstructured SPR biosensing device for real-time monitoring of cellular secretions. The fourth chapter explores the feasibility of multiplexed functionalization, via contact and non-contact methods, on nanostructured optical fibers with potential *in vivo* applications. Finally, Chapter 5 presents a general overview of the results obtained for each type of system while delving more into the advantages, limitations and future perspectives of the techniques developed in this manuscript.

References

[1] Bosch, M., Sánchez, A., Rojas, F., and Ojeda, C. (2007) Recent Development in Optical Fiber Biosensors. *Sensors 7*, 797–859.

[2] Vo-Dinh, T., and Cullum, B. (2000) Biosensors and biochips: advances in biological and medical diagnostics. *Fresenius' Journal of Analytical Chemistry 366*, 540–551.

[3] Grieshaber, D., MacKenzie, R., Vörös, J., and Reimhult, E. (2008) Electrochemical Biosensors - Sensor Principles and Architectures. *Sensors 8*, 1400–1458.

[4] Vidotti, M., Carvalhal, R. F., Mendes, R. K., Ferreira, D. C. M., and Kubota, L. T. (2011) Biosensors based on gold nanostructures. *Journal of the Brazilian Chemical Society 22*, 3–20.

[5] Chambers, J. P., Arulanandam, B. P., Matta, L. L., Weis, A., and Valdes, J. J. (2008) Biosensors based on gold nanostructures. *Current Issues in Molecular Biology 10*, 1–12.

[6] Heineman, W. R., and Jensen, W. B. (2006) Leland C. Clark Jr. (1918–2005). *Biosensors and Bioelectronics 21*, 1403–1404.

[7] Clark, L. C., and Lyons, C. (2006) Electrode systems for continuous monitoring in cardiovascular surgery. *Annals of the New York Academy of Sciences 102*, 29–45.

[8] Bhalla, N., Jolly, P., Formisano, N., and Estrela, P. (2016) Introduction to biosensors. *Essays In Biochemistry 60*, 1–8.

[9] Khansili, N., Rattu, G., and Krishna, P. M. (2018) Label-free optical biosensors for food and biological sensor applications. *Sensors and Actuators B: Chemical 265*, 35–49.

[10] Colás, J. J. *Dual-Mode Electro-photonic Silicon Biosensors*; Springer International Publishing, 2017; pp 7–35.

[11] Luo, X., and Davis, J. J. (2013) Electrical biosensors and the label free detection of protein disease biomarkers. *Chemical Society Reviews 42*, 5944.

[12] Damborsky, P., vitel, J., and Katrlik, J. (2016) Optical biosensors. *Essays In Biochemistry 60*, 91–100.

[13] Borisov, S. M., and Wolfbeis, O. S. (2008) Optical Biosensors. *Chemical Reviews 108*, 423–461.

[14] Lechuga, L. M. *Biosensors and Modern Biospecific Analytical Techniques*; Elsevier, 2005; pp 209–250.

[15] Jha, S. N. *Rapid Detection of Food Adulterants and Contaminants*; Elsevier, 2016; pp 125–145.

[16] Reddy, B., Salm, E., and Bashir, R. (2016) Electrical Chips for Biological Point-of-Care Detection. *Annual Review of Biomedical Engineering 18*, 329–355.

[17] Campuzano, S., Yáñez-Sedeño, P., and Pingarrón, J. (2017) Electrochemical Genosensing of Circulating Biomarkers. *Sensors 17*, 866.

[18] Wu, L., Ren, J., and Qu, X. (2014) Target-responsive DNA-capped nanocontainer used for fabricating universal detector and performing logic operations. *Nucleic Acids Research 42*, e160–e160.

[19] Chaubey, A., and Malhotra, B. (2002) Mediated biosensors. *Biosensors and Bioelectronics 17*, 441–456.

[20] Thévenot, D. R., Toth, K., Durst, R. A., and Wilson, G. S. (2001) Electrochemical biosensors: recommended definitions and classification1International Union of Pure and Applied Chemistry: Physical Chemistry Division, Commission I.7 (Biophysical Chemistry) Analytical Chemistry Division, Commission V.5 (Electroanalytical Chemistry).1. *Biosensors and Bioelectronics 16*, 121–131.

[21] Bantz, K. C., Meyer, A. F., Wittenberg, N. J., Im, H., Özge Kurtuluş, Lee, S. H., Lindquist, N. C., Oh, S.-H., and Haynes, C. L. (2011) Recent progress in SERS biosensing. *Physical Chemistry Chemical Physics 13*, 11551.

[22] Tripp, R. A., Dluhy, R. A., and Zhao, Y. (2008) Novel nanostructures for SERS biosensing. *Nano Today 3*, 31–37.

[23] Li, K., Wang, S., Wang, L., Yu, H., Jing, N., Xue, R., and Wang, Z. (2017) Fast and Sensitive Ellipsometry-Based Biosensing. *Sensors 18*, 15.

[24] Homola, J. *Springer Series on Chemical Sensors and Biosensors*; Springer Berlin Heidelberg, 2006; pp 3–44.

[25] Leung, A., Shankar, P. M., and Mutharasan, R. (2007) A review of fiber-optic biosensors. *Sensors and Actuators B: Chemical 125*, 688–703.

[26] Caucheteur, C., Guo, T., and Albert, J. (2015) Review of plasmonic fiber optic biochemical sensors: improving the limit of detection. *Analytical and Bioanalytical Chemistry 407*, 3883–3897.

[27] Ekgasit, S., Thammacharoen, C., Yu, F., and Knoll, W. (2004) Evanescent Field in Surface Plasmon Resonance and Surface Plasmon Field-Enhanced Fluorescence Spectroscopies. *Analytical Chemistry 76*, 2210–2219.

[28] Zeng, S., Baillargeat, D., Ho, H.-P., and Yong, K.-T. (2014) Nanomaterials enhanced surface plasmon resonance for biological and chemical sensing applications. *Chemical Society Reviews 43*, 3426.

[29] Homola, J., and Piliarik, M. *Springer Series on Chemical Sensors and Biosensors*; Springer Berlin Heidelberg, 2006; pp 45–67.

[30] Chen, P., Huang, N.-T., Chung, M.-T., Cornell, T. T., and Kurabayashi, K. (2015) Label-free cytokine micro- and nano-biosensing towards personalized medicine of systemic inflammatory disorders. *Advanced Drug Delivery Reviews 95*, 90–103.

[31] Born, M., Wolf, E., Bhatia, A. B., Clemmow, P. C., Gabor, D., Stokes, A. R., Taylor, A. M., Wayman, P. A., and Wilcock, W. L. *Principles of optics: electromagnetic theory of propagation, interference and diffraction of light*, 7th ed.; Cambridge University Press, 1999.

[32] Otto, A. (1968) Excitation of nonradiative surface plasma waves in silver by the method of frustrated total reflection. *Zeitschrift für Physik A Hadrons and nuclei 216*, 398–410.

[33] Kretschmann, E., and Raether, H. (1968) Notizen: Radiative Decay of Non Radiative Surface Plasmons Excited by Light. *Zeitschrift für Naturforschung A 23*.

[34] Schasfoort, R. B., and McWhirter, A. *Handbook of Surface Plasmon Resonance*; Royal Society of Chemistry, pp 35–80.

[35] Suzuki, A., Kondoh, J., Matsui, Y., Shiokawa, S., and Suzuki, K. (2005) Development of novel optical waveguide surface plasmon resonance (SPR) sensor with dual light emitting diodes. *Sensors and Actuators B: Chemical 106*, 383–387.

[36] Zhao, H., Gorshkova, I. I., Fu, G. L., and Schuck, P. (2013) A comparison of binding surfaces for SPR biosensing using an antibody–antigen system and affinity distribution analysis. *Methods 59*, 328–335.

[37] Newton, L., Slater, T., Clark, N., and Vijayaraghavan, A. (2013) Self assembled monolayers (SAMs) on metallic surfaces (gold and graphene) for electronic applications. *J. Mater. Chem. C 1*, 376–393.

[38] Nicosia, C., and Huskens, J. (2014) Reactive self-assembled monolayers: from surface functionalization to gradient formation. *Mater. Horiz. 1*, 32–45.

[39] da Silva, A. L. C. M., Gutierres, M. G., Thesing, A., Lattuada, R. M., and Ferreira, J. (2014) SPR Biosensors Based on Gold and Silver Nanoparticle Multilayer Films. *Journal of the Brazilian Chemical Society*

[40] Nuzzo, R. G., and Allara, D. L. (1983) Adsorption of bifunctional organic disulfides on gold surfaces. *Journal of the American Chemical Society 105*, 4481–4483.

[41] Crudden, C. M., Horton, J. H., Ebralidze, I. I., Zenkina, O. V., McLean, A. B., Drevniok, B., She, Z., Kraatz, H.-B., Mosey, N. J., Seki, T., Keske, E. C., Leake, J. D., Rousina-Webb, A., and Wu, G. (2014) Ultra stable self-assembled monolayers of N-heterocyclic carbenes on gold. *Nature Chemistry 6*, 409–414.

[42] Gedig, E. T. *Handbook of Surface Plasmon Resonance*; Royal Society of Chemistry, 2017; pp 171–254.

[43] Jewell, A. D., Tierney, H. L., and Sykes, E. C. H. (2010) Gently lifting gold's herringbone reconstruction: Trimethylphosphine on Au(111). *Physical Review B 82*.

[44] Leff, D. V., Brandt, L., and Heath, J. R. (1996) Synthesis and Characterization of Hydrophobic, Organically-Soluble Gold Nanocrystals Functionalized with Primary Amines. *Langmuir 12*, 4723–4730.

[45] Frasconi, M., Mazzei, F., and Ferri, T. (2010) Protein immobilization at gold–thiol surfaces and potential for biosensing. *Analytical and Bioanalytical Chemistry 398*, 1545–1564.

[46] Wahlgren, M. (1991) Protein adsorption to solid surfaces. *Trends in Biotechnology 9*, 201–208.

[47] Stuart, M. A. C. *Biopolymers at Interfaces*, 2nd ed.; Surfactant Science Series; CRC Press, 2003; Vol. 110; p 1–19.

[48] Billsten, P., Wahlgren, M., Arnebrant, T., McGuire, J., and Elwing, H. (1995) Structural Changes of T4 Lysozyme upon Adsorption to Silica Nanoparticles Measured by Circular Dichroism. *Journal of Colloid and Interface Science 175*, 77–82.

[49] Minton, A. P. (2001) Effects of Excluded Surface Area and Adsorbate Clustering on Surface Adsorption of Proteins. II. Kinetic Models. *Biophysical Journal 80*, 1641–1648.

[50] Butler, J., Ni, L., Nessler, R., Joshi, K., Suter, M., Rosenberg, B., Chang, J., Brown, W., and Cantarero, L. (1992) The physical and functional behavior of capture antibodies adsorbed on polystyrene. *Journal of Immunological Methods 150*, 77–90.

[51] Daniel, C., Roupioz, Y., Livache, T., and Buhot, A. (2015) On the use of aptamer microarrays as a platform for the exploration of human prothrombin/thrombin conversion. *Analytical Biochemistry 473*, 66–71.

[52] Melaine, F., Roupioz, Y., and Buhot, A. (2015) Gold Nanoparticles Surface Plasmon Resonance Enhanced Signal for the Detection of Small Molecules on Split-Aptamer Microarrays (Small Molecules Detection from Split-Aptamers). *Microarrays 4*, 41–52.

[53] Lombana, A., Raja, Z., Casale, S., Pradier, C.-M., Foulon, T., Ladram, A., and Humblot, V. (2014) Temporin-SHa peptides grafted on gold surfaces display antibacterial activity. *Journal of Peptide Science 20*, 563–569.

[54] Kim, S., Jang, L. K., Park, H. S., and Lee, J. Y. (2016) Electrochemical deposition of conductive and adhesive polypyrrole-dopamine films. *Scientific Reports 6*.

[55] Livache, T., Roget, A., Dejean, E., Barthet, C., Bidan, G., and Teoule, R. (1994) Preparation of a DNA matrix via an electrochemically directed copolymerization of pyrrole and oligonucleotides bearing a pyrrole group. *Nucleic Acids Research 22*, 2915–2921.

[56] Livache, T., Maillart, E., Lassalle, N., Mailley, P., Corso, B., Guedon, P., Roget, A., and Levy, Y. (2003) Polypyrrole based DNA hybridization assays: study of label free detection processes versus fluorescence on microchips. *Journal of Pharmaceutical and Biomedical Analysis 32*, 687–696.

[57] Bouguelia, S., Roupioz, Y., Slimani, S., Mondani, L., Casabona, M. G., Durmort, C., Vernet, T., Calemczuk, R., and Livache, T. (2013) On-chip microbial culture for the specific detection of very low levels of bacteria. *Lab on a Chip 13*, 4024.

[58] Suraniti, E., Sollier, E., Calemczuk, R., Livache, T., Marche, P. N., Villiers, M.-B., and Roupioz, Y. (2007) Real-time detection of lymphocytes binding on an antibody chip using SPR imaging. *Lab on a Chip 7*, 1206.

[59] Roupioz, Y., Berthet-Duroure, N., Leïchlé, T., Pourciel, J.-B., Mailley, P., Cortes, S., Villiers, M.-B., Marche, P. N., Livache, T., and Nicu, L. (2009) Electrochemical deposition: Small 13/2009. *Small 5*.

[60] Schweiger, B., Kim, J., Kim, Y., and Ulbricht, M. (2015) Electropolymerized Molecularly Imprinted Polypyrrole Film for Sensing of Clofibric Acid. *Sensors 15*, 4870–4889.

[61] Heinze, J., Frontana-Uribe, B. A., and Ludwigs, S. (2010) Electrochemistry of Conducting Polymers—Persistent Models and New Concepts†. *Chemical Reviews 110*, 4724–4771.

[62] Chi, Q., Zhang, J., Andersen, J. E. T., and Ulstrup, J. (2001) Ordered Assembly and Controlled Electron Transfer of the Blue Copper Protein Azurin at Gold (111) Single-Crystal Substrates. *The Journal of Physical Chemistry B 105*, 4669–4679.

[63] Murgida, D. H., and Hildebrandt, P. (2005) Redox and redox-coupled processes of heme proteins and enzymes at electrochemical interfaces. *Physical Chemistry Chemical Physics 7*, 3773.

[64] Fleming, B. D., Praporski, S., Bond, A. M., and Martin, L. L. (2008) Electrochemical Quartz Crystal Microbalance Study of Azurin Adsorption onto an Alkanethiol Self-Assembled Monolayer on Gold. *Langmuir 24*, 323–327.

[65] Gray, J. J. (2004) The interaction of proteins with solid surfaces. *Current Opinion in Structural Biology 14*, 110–115.

[66] Hermanson, G. T. *Bioconjugate Techniques*; Elsevier, 2013; pp 229–258.

[67] Johnsson, B., Löfås, S., and Lindquist, G. (1991) Immobilization of proteins to a carboxymethyldextran-modified gold surface for biospecific interaction analysis in surface plasmon resonance sensors. *Analytical Biochemistry 198*, 268–277.

[68] Peng, L., Calton, G. J., and Burnett, J. W. (1987) Effect of borohydride reduction on antibodies. *Applied Biochemistry and Biotechnology 14*, 91–99.

[69] Smyth, D., Blumenfeld, O., and Konigsberg, W. (1964) Reactions of N-ethylmaleimide with peptides and amino acids. *Biochemical Journal 91*, 589–595.

[70] Gorin, G., Martic, P., and Doughty, G. (1966) Kinetics of the reaction of N-ethylmaleimide with cysteine and some congeners. *Archives of Biochemistry and Biophysics 115*, 593–597.

[71] Partis, M. D., Griffiths, D. G., Roberts, G. C., and Beechey, R. B. (1983) Cross-linking of protein by ?-maleimido alkanoylN-hydroxysuccinimido esters. *Journal of Protein Chemistry 2*, 263–277.

[72] Heitz, J. R., Anderson, C. D., and Anderson, B. M. (1968) Inactivation of yeast alcohol dehydrogenase by N-alkylmaleimides. *Archives of Biochemistry and Biophysics 127*, 627–636.

[73] O'Shannessy, D. J., Brigham-Burke, M., and Peck, K. (1992) Immobilization chemistries suitable for use in the BIAcore surface plasmon resonance detector. *Analytical Biochemistry 205*, 132–136.

[74] Nie, J., Li, J.-P., Deng, H., and Pan, H.-C. (2015) Progress on Click Chemistry and Its Application in Chemical Sensors. *Chinese Journal of Analytical Chemistry 43*, 609–617.

[75] Kolb, H. C., Finn, M. G., and Sharpless, K. B. (2001) Click Chemistry: Diverse Chemical Function from a Few Good Reactions. *Angewandte Chemie International Edition 40*, 2004–2021.

[76] Jewett, J. C., and Bertozzi, C. R. (2010) Cu-free click cycloaddition reactions in chemical biology. *Chemical Society Reviews 39*, 1272.

[77] GmbH, J. B. Click Chemistry. `https://www.jenabioscience.com/click-chemistry`.

[78] Hong, V., Presolski, S., Ma, C., and Finn, M. (2009) Analysis and Optimization of Copper-Catalyzed Azide-Alkyne Cycloaddition for Bioconjugation. *Angewandte Chemie International Edition 48*, 9879–9883.

[79] Presolski, S. I., Hong, V. P., and Finn, M. Copper-Catalyzed Azide–Alkyne Click Chemistry for Bioconjugation. *Current Protocols in Chemical Biology 3*, 153–162.

[80] Barge, A., Tagliapietra, S., Binello, A., and Cravotto, G. (2011) Click Chemistry Under Microwave or Ultrasound Irradiation. *Current Organic Chemistry 15*, 189–203.

[81] Ess, D. H., Jones, G. O., and Houk, K. N. (2008) Transition States of Strain-Promoted Metal-Free Click Chemistry: 1, 3-Dipolar Cycloadditions of Phenyl Azide and Cyclooctynes. *Organic Letters 10*, 1633–1636.

[82] Subramanian, N., Sreemanthula, J. B., Balaji, B., Kanwar, J. R., Biswas, J., and Krishnakumar, S. (2014) A strain-promoted alkyne-azide cycloaddition (SPAAC) reaction of a novel EpCAM aptamer-fluorescent conjugate for imaging of cancer cells. *Chem. Commun. 50*, 11810–11813.

[83] Mbua, N. E., Guo, J., Wolfert, M. A., Steet, R., and Boons, G.-J. (2011) Strain-Promoted Alkyne-Azide Cycloadditions (SPAAC) Reveal New Features of Glycoconjugate Biosynthesis. *ChemBioChem 12*, 1912–1921.

[84] Baskin, J. M., Prescher, J. A., Laughlin, S. T., Agard, N. J., Chang, P. V., Miller, I. A., Lo, A., Codelli, J. A., and Bertozzi, C. R. (2007) Copper-free click chemistry for dynamic in vivo imaging. *Proceedings of the National Academy of Sciences 104*, 16793–16797.

[85] Codelli, J. A., Baskin, J. M., Agard, N. J., and Bertozzi, C. R. (2008) Second-Generation Difluorinated Cyclooctynes for Copper-Free Click Chemistry. *Journal of the American Chemical Society 130*, 11486–11493.

[86] Sletten, E. M., and Bertozzi, C. R. (2008) A Hydrophilic Azacyclooctyne for Cu-Free Click Chemistry. *Organic Letters 10*, 3097–3099.

[87] Ning, X., Guo, J., Wolfert, M., and Boons, G.-J. (2008) Visualizing Metabolically Labeled Glycoconjugates of Living Cells by Copper-Free and Fast Huisgen Cycloadditions. *Angewandte Chemie International Edition 47*, 2253–2255.

[88] Dommerholt, J., Schmidt, S., Temming, R., Hendriks, L. J. A., Rutjes, F. P. J. T., van Hest, J. C. M., Lefeber, D. J., Friedl, P., and van Delft, F. L. (2010) Readily Accessible Bicyclononynes for Bioorthogonal Labeling and Three-Dimensional Imaging of Living Cells. *Angewandte Chemie International Edition 49*, 9422–9425.

[89] Debets, M. F., van der Doelen, C. W. J., Rutjes, F. P. J. T., and van Delft, F. L. (2010) Azide: A Unique Dipole for Metal-Free Bioorthogonal Ligations. *ChemBioChem 11*, 1168–1184.

[90] Kuzmin, A., Poloukhtine, A., Wolfert, M. A., and Popik, V. V. (2010) Surface Functionalization Using Catalyst-Free Azide-Alkyne Cycloaddition. *Bioconjugate Chemistry 21*, 2076–2085.

[91] Campbell-Verduyn, L. S., Mirfeizi, L., Schoonen, A. K., Dierckx, R. A., Elsinga, P. H., and Feringa, B. L. (2011) Strain-Promoted Copper-Free "Click" Chemistry for 18F Radiolabeling of Bombesin. *Angewandte Chemie 123*, 11313–11316.

[92] Dommerholt, J., Rutjes, F. P. J. T., and van Delft, F. L. (2016) Strain-Promoted 1, 3-Dipolar Cycloaddition of Cycloalkynes and Organic Azides. *Topics in Current Chemistry 374*.

[93] Devaraj, N. K., Weissleder, R., and Hilderbrand, S. A. (2008) Tetrazine-Based Cycloadditions: Application to Pretargeted Live Cell Imaging. *Bioconjugate Chemistry 19*, 2297–2299.

[94] McKay, C. S., and Finn, M. (2014) Click Chemistry in Complex Mixtures: Bioorthogonal Bioconjugation. *Chemistry & Biology 21*, 1075–1101.

[95] Graziano, G. (2004) Rate enhancement of Diels–Alder reactions in aqueous solutions. *Journal of Physical Organic Chemistry 17*, 100–101.

[96] Blackman, M. L., Royzen, M., and Fox, J. M. (2008) Tetrazine Ligation: Fast Bioconjugation Based on Inverse-Electron-Demand Diels-Alder Reactivity. *Journal of the American Chemical Society 130*, 13518–13519.

[97] Lang, K., Davis, L., Wallace, S., Mahesh, M., Cox, D. J., Blackman, M. L., Fox, J. M., and Chin, J. W. (2012) Genetic Encoding of Bicyclononynes and trans-Cyclooctenes for Site-Specific Protein Labeling in Vitro and in Live Mammalian Cells via Rapid Fluorogenic Diels–Alder Reactions. *Journal of the American Chemical Society 134*, 10317–10320.

[98] MacKinnon, A. L., and Taunton, J. (2009) Target Identification by Diazirine Photo-Cross-linking and Click Chemistry. *Curr Protoc Chem Biol 1*, 55–73, 23667793[pmid].

[99] Eliasson, M., Olsson, A., Palmcrantz, E., Wiberg, K., Inganas, M., Guss, B., Lindberg, M., and Uhlen, M. (1988) Chimeric IgG-binding receptors engineered from staphylococcal protein A and streptococcal protein G. *J. Biol. Chem. 263*, 4323–4327.

[100] Rispens, T., and Vidarsson, G. *Antibody Fc*; Elsevier, 2014; pp 159–177.

2

Protein patterning via photo-assisted functionalization

Contents

2.1 Scientific context

2.1.1 Protein microarrays - production and challenges

Protein microarray technology is a versatile and powerful high-throughput tool that has been exploited for applications as diverse as clinical diagnosis of diseases and search for new biomarkers[1–6], drug screening[2,7], analysis of protein-biomolecule interactions[8,9], mapping of metabolic pathways[9], vaccine development[10] and immunoprofiling[11,12].

This technology can be classified on three main categories based on their intended application:

— **Functional microarrays:** These are employed to screen protein-molecule interactions (accounting for drug analysis, study of metabolic pathways, post-translational modifications, etc);

— **Analytical microarrays:** These systems graft proteins, with a known affinity to an analyte (such as antibodies) or the analyte of interest, on a substrate[13]. Assays are performed in order to quantify the amount of analyte/antibodies on a sample, evaluate specificity and affinity of antibodies, characterize protein activity, among others;

— **Reverse phase microarrays:** Conceived in 2001 by Paweletz et al.[14], in these systems the exact composition of the proteins grafted is unknown as it correspond to lysates (either from either tissues, cells or bodily fluids). These lysates are grafted on a the same array and then exposed to a single highly specific antibody allowing the comparison of relative protein expression on all samples[15].

By engineering the properties of the microarray, it is possible to optimize their sensitivity/specificity, perform high-throughput analysis and minimize sample consumption[6,11,16,17]. However, for achieving this, special attention has to be put into selection and implementation of the arraying method.

Compared with the initial stages of protein microarraying (based on physisorption of proteins deposited by manual[18] or automatic systems[19]), modern fabrication methods have significantly evolved becoming more complex and robust. Nevertheless, they still face multiple major challenges such as: (a) Microspot heterogeneity and inconsistent signal quantification, (b) low signal-to-noise ratio (caused by factors as complex as surface properties, cross-contamination, mass transport, etc), (c) poor control of the local and global conditions during fabrication (pH, temperature, drying effects), (d) low-yield and/or random grafting of the proteins and (e) damage of the probes (denaturation, reduced activity) during grafting and/or storage[11]. Since none of the available technologies can address all these issues, the selection of the fabrication method depends entirely on which parameters are the most critical for the application.

Traditionally, microarray fabrication methods can be categorized into two big groups, contact and non-contact approaches. Rather than providing an extensive review on each approach (which can already be found in the literature[1,9,11,16,20,21]), a brief overview of

the most popular fabrication methods will be presented (Figure 2.1).

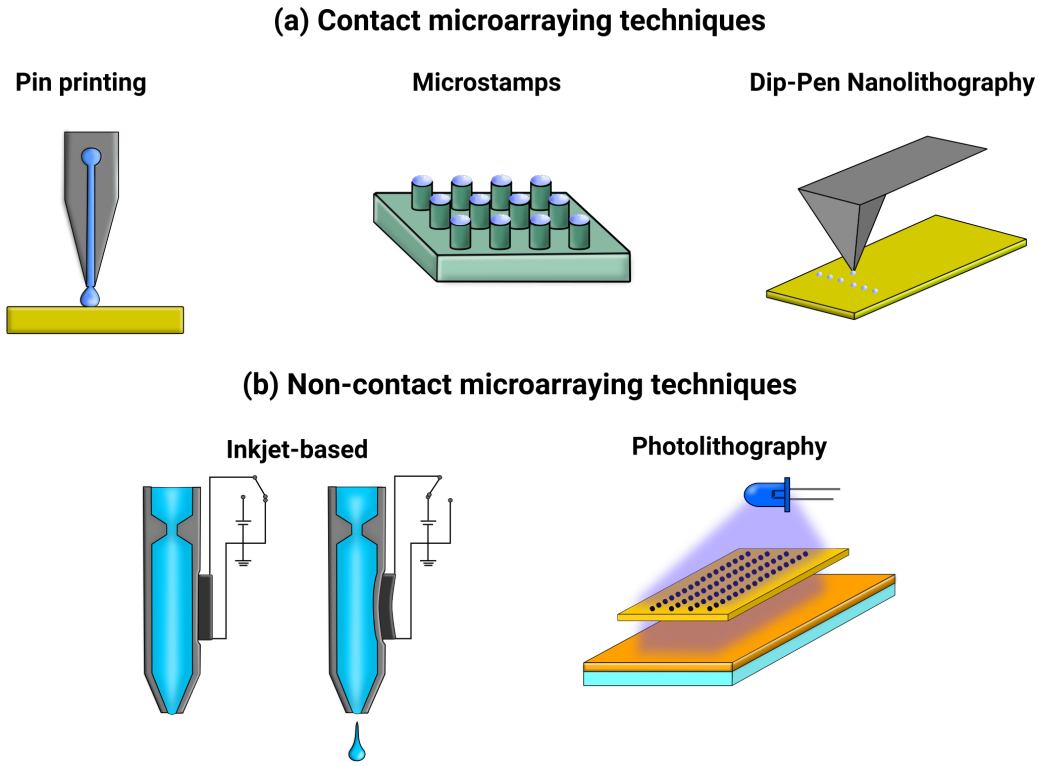

Figure 2.1 – Summary of existing protein arraying technologies. (a) Exemplifies some methods based on contact of the microarraying system with the substrate while (b) shows some non-contact technologies.

2.1.1.a Contact-based microarraying technologies

Pin printing: This technique uses different pin types (solid, split, quill, etc) to deliver droplets of proteins in aqueous solution on the desired surfaces[11,20,22]. Controlled droplet deposition relies on the regulating the surface energetics between of the solution, the substrate and the pin[20]. Hollow pin systems allow the spotting of numerous features before the need of re-immersion in the protein solution (recharging of the pins/sample loading), however, the spot size and deposited volume tend to decrease over subsequent prints. Moreover, the use of high viscosity additives (required to reduce evaporation rate) such as sugars, glycerol or polymers may cause clogging and also a greater risk of cross-contamination[23]. These issues can be solved by using solid pins which allow spotting of solutions with different viscosity, but require rinsing and recharging after each deposition[11]. Furthermore, due to its simple design (movement of the pin between deposition site, source reservoir and cleaning site), arraying in complex patterns usually requires long time of operation[11].

Microstamping: This technique employs the same fundamental basis as pin printing. It is a serial deposition method where stamps are loaded with the protein solution,

cleaned and re-loaded for new cycles. However, it differs with the previous technique in the fact that, this method is envisioned for parallel generation of many spots with the same protein[11]. These stamps are generally made of cross-linked elastomers, for example Polydimethylsiloxane (PDMS) with specific patterns defined by a mold fabricated by lithographic methods. It has the advantage that can be mass produced at very low costs, allowing stamps to be used just a single time eliminating cross-contamination issues[20]. Furthermore, it allows high throughput microarray production in short fabrication times[24]. However, alignment of the features, when using multiple stamps, can cause severe issues. Moreover, even if the creation of the stamps is very inexpensive, preparation of the molds in clean-room conditions results in elevated fees[24]. Also, although it is usually not the case for PDMS stamps, contamination of the substrate with surface-active components of the stamp and swelling of the elastomer can induce severe problems[25,26],

Dip-Pen Nanolithograpy (DPN): This technology employs a cantilever tip of Atomic Force Microscopy (AFM) to deliver drops of a protein solution to a substrate via a solvent meniscus[27]. The principle is similar to pin-printing, but it achieves lateral resolution in the nanometer range (up to 15 nm depending of the system[28]). In this sense, DPN has been broadly used for academic purposes but its clinical applications are still very limited[29]. Throughput issues (difficulties to pattern multiple proteins over "large" areas), fragility of the cantilevers and elevated costs and the fact that most optical detection devices are adapted for micrometric readings are some obstacles that limit further the translation of this technology into clinical usage[11,30].

A shared issue of all contact printing techniques is the risk of surface damage during the grafting. The following techniques avoid such problem since no contact exist between the arraying tool and the surface of the microarray.

2.1.1.b Non-contact microarraying technologies

Most non-contact printing techniques are based on the ejection of a protein solution as a droplet or stream through an orifice at a specific distance into the substrate surface[31]. This allows microarraying with high precision, in very short times and flexible in terms of patterns that can be created[32].

The sample ejection from the reservoir can be performed by inkjet (either piezoelectric or thermal-based), electrostatic or acoustic mechanisms[32]. However, inkjet systems are the most common.

Inkjet system: In this case, a change in the volume of the reservoir causes a rapid pressure change which in turn leads to the ejection of a droplet[11,33,34]. The change of pressure in the chamber causes shear rates in the order of 10^4 to 10^6 s^{-1} which can lead, in some cases, to protein unfolding and denaturation in the case of sensitive samples[32]. This technology often employs either a piezoelectric material or a resistor, however, the use of a resistor constitutes a simpler and more robust approach[32]. Thermal inkjet (resistor-based system) induces a fast heating of the liquid which generates a vapor bubble which pushes the protein solution through an orifice[11]. Initially there were some concerns regarding the effect of this fast heating over biomolecules, surprisingly, there is little evidence that

the molecules of the droplet are damaged by the heating pulse[32]. In general, both inkjet-based systems cover several of the deficiencies of contact techniques by having faster arraying times, facilitates multiplexing, are more versatile as its possible to create more complex arrays, minimizes cross-contamination and the reservoir volume is no longer an issue for this method. Nevertheless, inkjet systems are highly susceptible to viscosity changes. Re-calibration of ejection parameters has to be performed for different solutions with significant differences in their viscosity. Otherwise, spot quality, size, uniformity and volume will be dramatically affected. Furthermore, it is crucial to control the humidity of the environment to avoid evaporation of the small volumes deposited on the substrate.

Besides inkjet systems, non-contact lithography methods can be employed to create features where the proteins of interest can bind.

Electron-beam lithography: This is a maskless technique that allow generation of nanoscale features for patterning[11]. It can be applied to either cause cross-linking or reducing solubility of molecules previously added to the substrate (negative resist) or by degrading/increasing their solubility (positive resist)[35]. After rinsing, the surface is exposed to the protein solution in order to graft them in the desired patterns. It has advantages such as its remarkable lateral resolution (10^1 to 10^6 nm) and formation patterns in arbitrary shapes[35]. However, it requires clean-room facilities, expensive instrumentation, long operational times, multi-step processes and the process has to be done in vacuum which limits iterative patterning once proteins have been arrayed on the surface.

Photolithography/photoactivation: Similar to the previously described method, this one requires the addition of a layer of molecules on the surface of the substrate (either with photo-activable moieties or susceptible to degradation). The irradiation of the surface is usually done by exposure to ultraviolet light (UV) through a mask with the desired pattern[11]. It has the advantage that can be performed with relatively inexpensive devices, under biomolecule-friendly conditions allowing iterative cycles, can create numerous features per cycle and with high lateral resolutions[36].

As it has been previously mentioned, in contrast to other biomolecules (nucleic acids, peptides or sugars) proteins require a permanent hydrated environment to ensure their structural integrity and functionality. An ideal grafting procedure should be performed fully in an aqueous environment, however, this proves challenging if not impossible for most techniques. This reason makes photo-mediated strategies an highly attractive alternative for protein immobilization.

2.1.2 State of the art on photo-assisted protein arraying

Photochemistry has proven an extremely powerful tool specially since it can be performed either in dry or wet environments. For the latter, a varied array of organic solvents or aqueous solutions can be employed. Moreover, it has other desirable properties such as high selectivity, fast kinetics and versatility which have been exploited in fields as diverse as organic synthesis[37], polymer conjugation[38,39] and surface functionalization[40,41].

Research in photo-assisted functionalization of surfaces has focused on two main strategies: direct and indirect approaches. These mainly differ on whether or not the biomolecules to be grafted are irradiated during the process and directly depends on the chemistry used for the grafting. Among the mechanisms by which the process can occur, we can mention: grafting via radical reactions between a photosensitive surface and the biomolecules to be arrayed[42–44] (Figure 2.2a), destruction or removal of molecules on the irradiated zones revealing the bare substrate[44–46] (Figure 2.2b) and surfaces containing reactive functionalities protected by photocleavable groups[44,47,48] (Figure 2.2c).

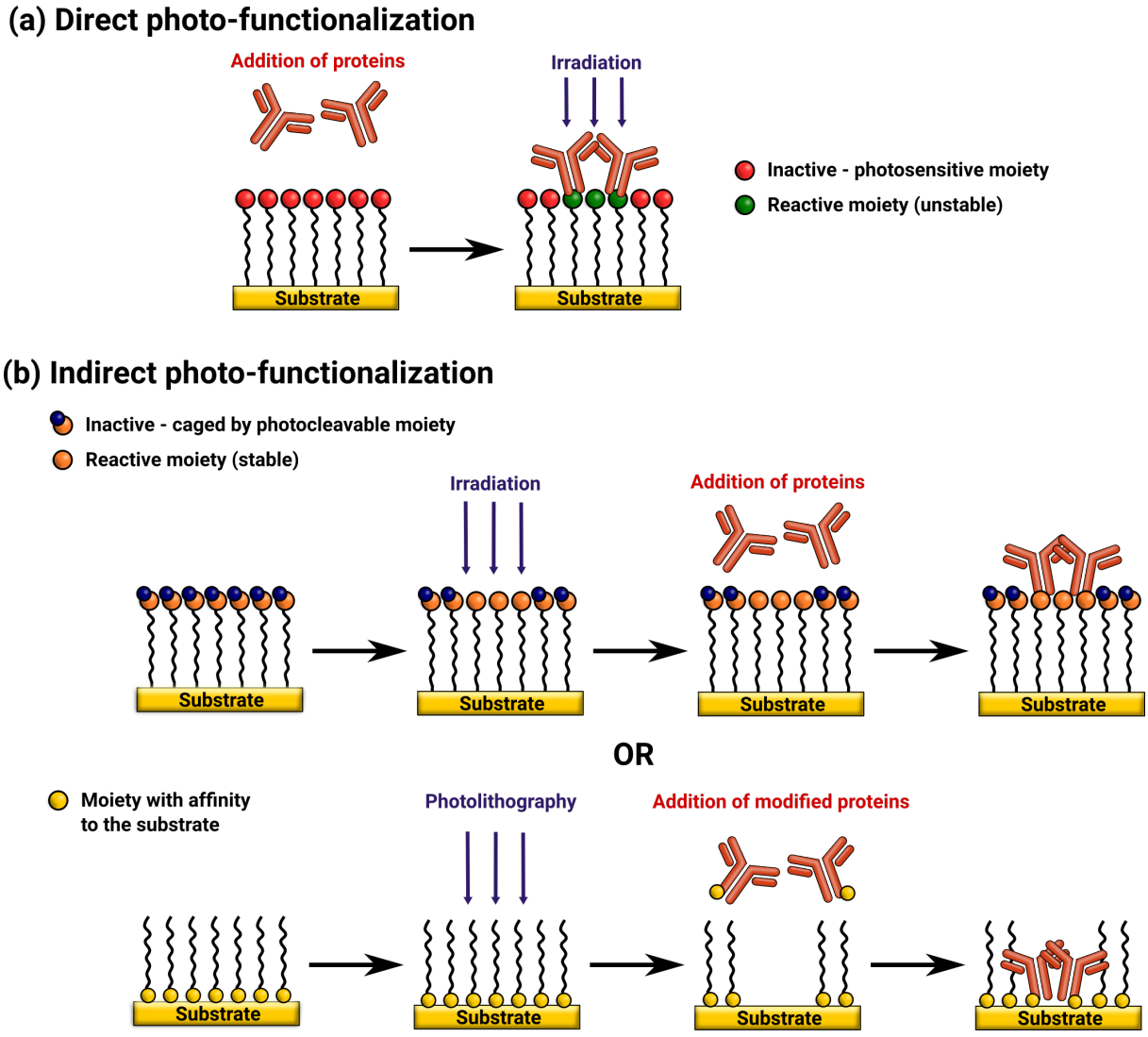

Figure 2.2 – Scheme describing main photo-functionalization approaches. (a) Shows direct functionalization where proteins and the surface are simultaneously irradiated and (b) demonstrates two examples of indirect photo-functionalization, the first one based on reactive moeities caged by photocleavable functionalities and the second one on photolithography.

2.1.2.a Direct photo-functionalization

Direct exposure of proteins to UV light can cause irreversible modifications, such as their cleavage into smaller polypeptides or cross-liking[49]. Even if this is not desirable, it is required when using compounds that form unstable intermediaries (for example, photogenerated radical species) on the substrate. Still, this type of systems are attractive since they do not require complex organic synthesis, they are straight-forward and they allow to capture unmodified proteins via covalent binding.

In their review, Delaittre et al.[41] describe numerous strategies that are employed for the generation of unstable moieties over surfaces. Although, these approaches focus on the grafting of polymers due to their inherent resistance to the irradiation conditions. Significant efforts have been made to perform such reactions in milder conditions (wavelengths >350 nm), but this typically requires the use of complex optical set-ups or additional reagents (i.e. metal complexes as catalysts)[40].

Photo-generation of carbon radicals became popular due to their high reaction rates and their ease of use[41]. They can be generated by photoinitiators[50] or photoredox catalysts[51,52], however their use can limit the resolution of the system due to radical diffusion. Another alternative is to incorporate photoreactive moieties on the surface. These groups are commonly found in protein crosslinking or labeling products and can be adapted for surface grafting. The most common photo-reactive groups[53] include benzophenone (Figure 2.3a), diazirine derivatives (Figure 2.3b) and phenyl azides (Figure 2.3c). Other methods, although less commonly used, are based on thiol-alkene (Figure 2.3d) and thiol-alkyne (Figure 2.3e) reactions[53]

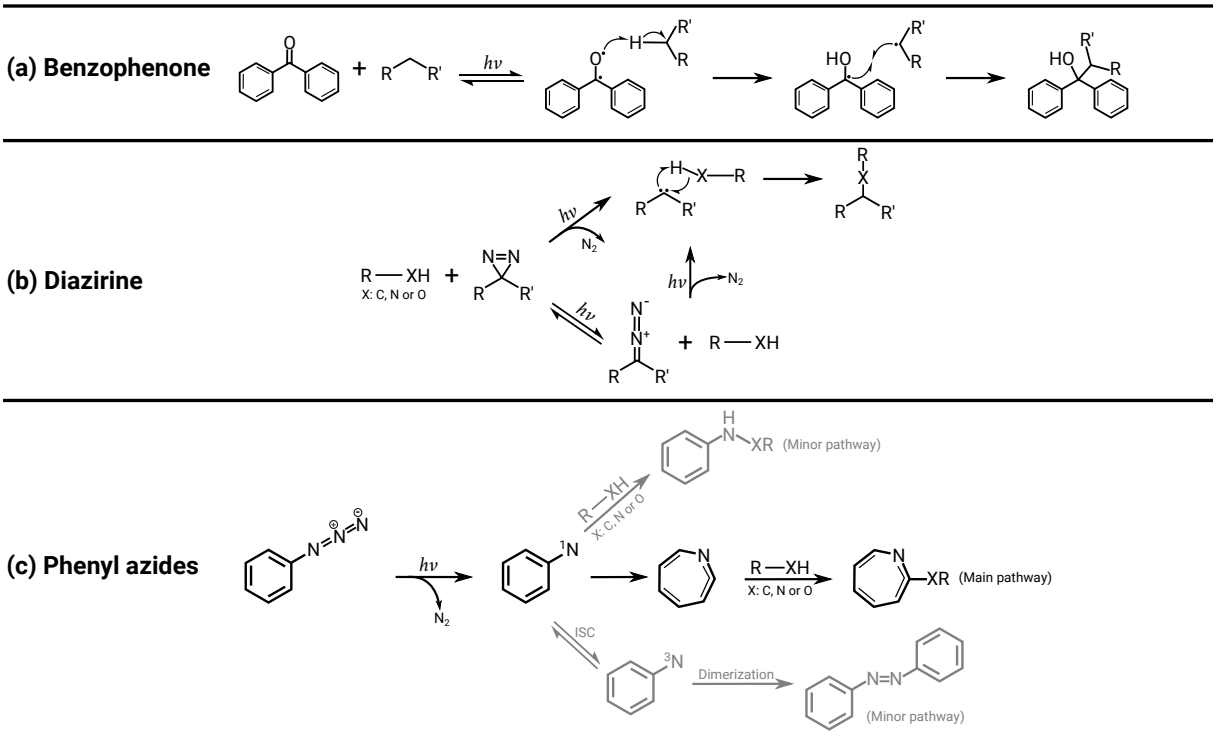

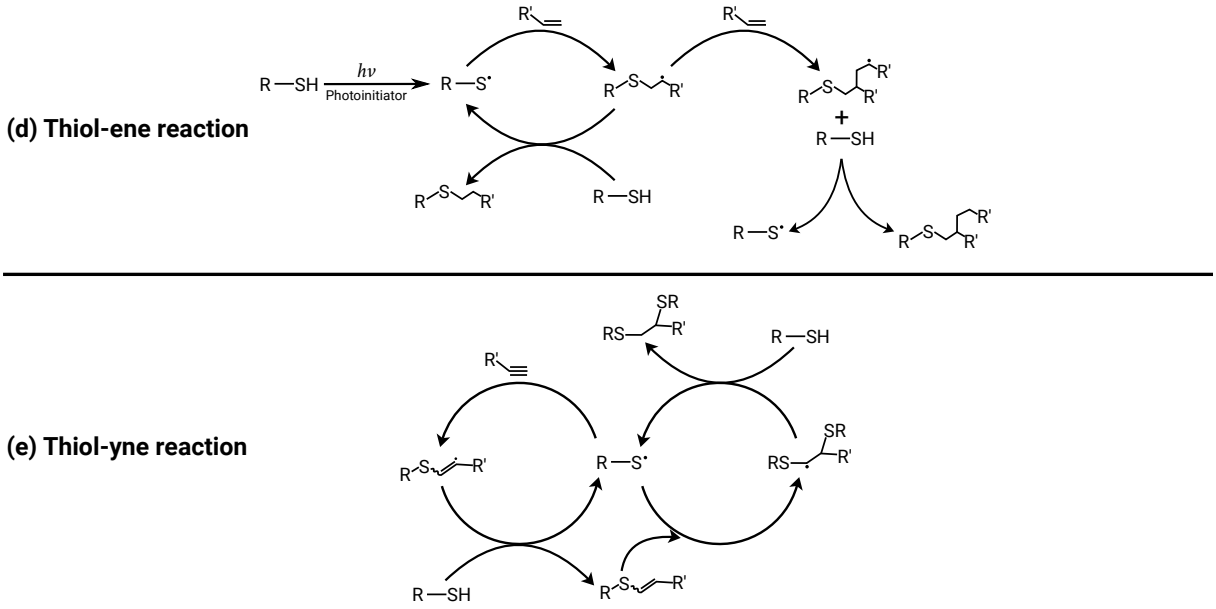

Figure 2.3 – Reaction schemes for several compounds used in direct functionalization. (a) Reaction of a benzophenone with R-H compounds via generation of a carbon-centered radical, (b) Reaction of a diazirine with a R-XH compound, formation of a diazo compound as a subproduct, (c) Multiple pathways of reactions with phenyl azide, after production of singlet nitrene (^{1}N) there can be: direct reaction with R-XH compounds, ring expansion and further reaction with R-XH compounds or intersystem crossing (ISC) to for triplet state (^{3}N) causing dimerization, (d) Thiol-alkene radical polymerization process and (e) Thiol-alkyne radical polymerization process. Schemes inspired from Preston and Wilson [54], Lowe et al. [55], Zuo et al. [56]

Benzophenones have reversible activation at ∼350 nm, are selective for insertion into C-H σ bonds due to the formation of a triplet carbonyl state, chemically stable (inert to most solvents) but are relatively bulky in size[53,57]. Besides their bulk, they require long irradiation times in order to be effective which can risk non-specific interactions[58]. Balakirev et al. [59] functionalized the inner wall of fused-silica capillaries with either oligonucleotides or a recombinant protein G via benzophenone derivatives while Delamarche et al. [60] performed the immobilization of antibodies on gold surfaces using another benzophenone derivative.

Diazirine derivatives form highly reactive carbenes when exposed to UV light in the range of 330-370 nm[61,62], are more stable than phenyl azides and have a relative small size (alkyl diazirines) avoiding steric issues[53].

Finally, phenyl azides are one of the most popular groups. They form a highly reactive nitrene intermediate when exposed to UV light (250-350 nm) which interacts with double bounds, inserts into C-H or N-H sites or reacts with a nucleophilic functionality after undergoing a ring expansion[53,62].

Other types of phototriggered radical coupling reactions are thiol-ene and thiol-yne radical

additions[41]. Both reactions rely on the generation of a carbon radical which, by hydrogen abstraction, creates a thiyl radical that can react with alkenes[55,63]. Examples of this methodology have been reported for grafting of organic compounds[41] while this technique has also used for protein modification in solution[64].

The team of Waldmann[65,66] reported the use of a photochemical coupling of olefins to thiols forming thioether bonds. This thiol-ene reaction was performed in buffered aqueous solution under mild UV conditions (365-405 nm). They performed numerous tests based either on direct grafting of proteins with olefin moeities or indirect arraying of streptavidin-modified proteins (by initial grafting biotinylated-olefins).

Another interesting reaction was presented by Lim and Lin[67] which developed a new bioorthogonal pair based on a photoinduced azirine-alkene cycloaddition. This reaction was highly specific, performed at neutral pH, room temperature, in ∼2 min and using biological friendly buffers. This reaction was performed in solution for biomolecule coupling but it could be adapted for protein grafting on surfaces. Unfortunately, the wavelength used in their work (302 nm) could cause damage to the biomolecules. Nevertheless, they suggest modifications such as placing auxochromic groups in the phenyl rings to tune the wavelength to 365 nm or even using two-photon 700 nm photoactivable azirines.

The group of Neves-Petersen[68–73] performed oriented grafting of immunoglobulins, enzymes and Bovine Serum Albumin (BSA) over thiol-reactive surfaces. This process was mediated by reduction of specific disulfide bridges by excitation of aromatic amino acids at 280 nm. In their work, the authors created an array of spots (25 µm in diameter) under aqueous conditions. However, more sensitive samples could suffer important loss of functionality under such harsh irradiation conditions (high energy wavelengths).

In a different approach, Yodmongkol et al.[74] described a process based on radical mediated cross-linking. Anti-human α-fetoprotein (AFP) was mixed with dimethylacrylamide (DMAA), methacryloyloxy benzophenone (MaBP), and Na-4-styrenesulfonate (SSNa) and droplets of 1.6 nl were deposited over a unmodified Poly-methyl methacrylate (PMMA) substrate. Irradiation by UV light (254 nm) caused the crosslinking of the solution trapping the antibody in the matrix. Fluorescence evaluation of the biochip showed that it was sensible to AFP in the range of 5 to 100 $ng.ml^{-1}$.

2.1.2.b Indirect photo-functionalization

In indirect photo-functionalization approaches the grafting step is decoupled from the photoreaction which is particularly advantageous when working with sensitive proteins. This can be performed by deprotecting caged reactive moeities or locally removing self-assembled monolayers from a surface allowing specific grafting on the deprotected areas (photolithography). Preparation of compounds with caged-photoreactive motifs usually results in tedious synthetic routes with low yields[41].

An interesting work was presented by Lee et al.[75], who grafted biologically active ligands (peptides in this case) by photodeprotection of a caged group. They made a SAM with an hydroquinone containing alkanethiol which was protected with a photolabile group (nitro-

veratryloxycarbonyl - NVOC). UV light (365 nm) was used through a photomask to generate patterns of the desired geometry, then, the hidroquinone was converted to quinone by mild electrochemical oxidation. These quinones could then react with oxyamine modified ligands. This conjugate could be reversed by applying a mild reductive potential, regenerating them to hydroquinones. This whole process did not affect the capture and release of cells, however, the long exposure times limits its applicability for other type of systems that require multiplexing. Similarly, Alonso et al.[44] created photosensitive silanes aimed for protein immobilization. These molecules contained tetraethylene glycol triethoxysilane with a terminal amino group which was protected by NVOC. Unfornately, in their method further modification steps with organic solvents had to be performed in order for the amino terminated surfaces to be adaptable for protein grafting which limits serial patterning of different proteins.

Leggett and his team performed a photodeprotection technique in order to remove protein-resistant moieties from the surface[76]. They synthesized nitrophenyl ethoxycarbonyl-protected amino propyl triethoxysilane (NPEOC-APTES). Exposure to UV light would remove the NPEOC component (which was conjugated with oligo ethylene glycol giving it protein resistant properties) allowing adsorption of fluorescent proteins on the deprotected surfaces.

Some examples of this photolithographic approach include the work by Lee et al.[77] which performed the arraying of extracellular matrix over glass surfaces. Silanized glass slides were spin coated with a positive photoresist and UV-irradiated in a specific pattern. Afterwards, the surface was exposed to solutions of common Extra Cellular Matrix (ECM) proteins (collagens I, II, and IV as well as laminin) allowing the attachment of hepatocytes in the desired patterns.

In another work, Mir et al.[36] created a DNA sensor, an immunosensor and an enzymatic sensor by UV photolithography. Their photoresist was based on a methacrylate copolymer with a photoacid generator sensitive at $\lambda > 300$ nm. Specific irradiation using a mask allowed patterning of the biomolecules of interest. Multiple cycles were performed on distinct zones allowing multiplex arraying. Removal of the whole photoresists was performed via brief UV exposure to the whole system. They found that the conditions for removal of the photoresist did not denatured the immobilized biomolecules.

Finally, Weber et al.[78] described the UV-mediated deterioration of polyethylene glycol terminated SAMs in an aqueous environment. This allowed them to tune the anti-fouling properties of the surface and thus increase the adhesion of BSA on the exposed areas. Nevertheless, such approach was not evaluated for immobilization of functional proteins.

2.2 Indirect photofunctionalization of non-structured gold surfaces

2.2.1 Proposed strategy

As for a vast number of biosensing devices, gold surfaces have become a standard substrate due to the relatively inert nature of gold in biological conditions as well as the fact that it supports a wide range of functionalization strategies (section 1.4 and section 1.5). Among them, thiol-gold interactions have become one of the most popular strategies[79].

This particular chemistry allows the formation of self assembled monolayers (SAMs) which have been reported to be easily modified by UV irradiation[80–83]. This feature can be further exploited for the production of protein microarrays. Nonetheless, most of the research done on photopatterning of thiol-based SAMs have been done on a gas phase[80–83] or direct exposure of proteins to the source of irradiation[68,69]. However, such processes significantly limit the use of this method due to the rapid loss of biological functionality under such harsh conditions.

Therefore, we developed an arraying procedure that could be performed under a fully liquid environment and that also avoids direct exposure of the proteins to UV light. Such method avoids protein denaturing due to drying effects as well as degradation caused by UV light (photolysis). This approach is based on the photochemical deprotection of gold surfaces (previously covered by thiol-based SAMs) prior to the spontaneous adsorption of thiolated proteins, all carried out in a microfluidic chamber (Figure 2.4). Such method gives access to a high spatio-temporal control of the patterns as well as a multiplex and serialized functionalization of the surface.

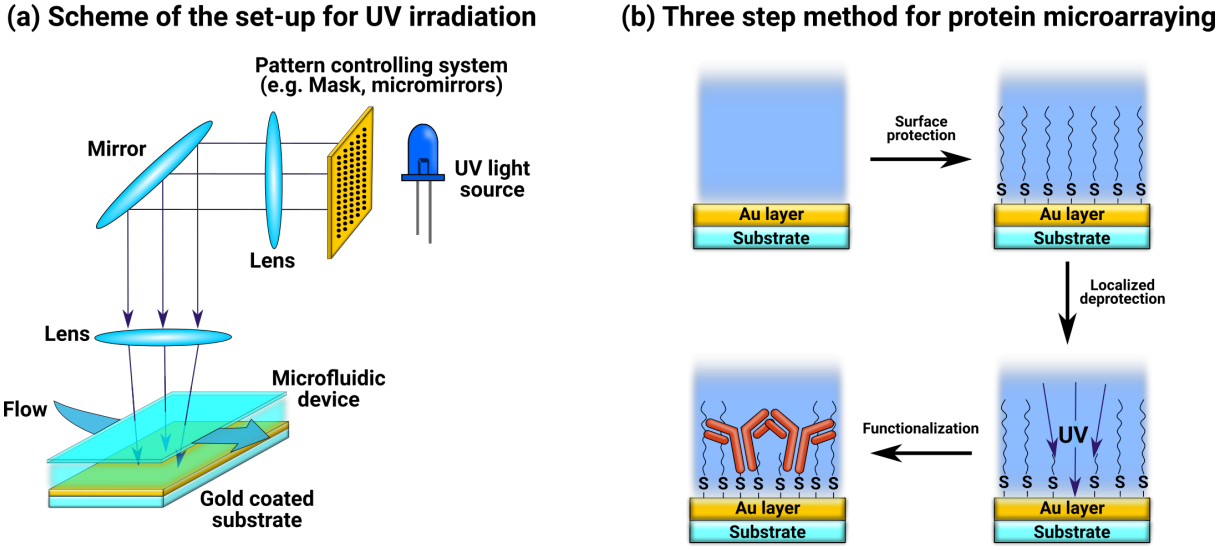

Figure 2.4 – Photodeprotection of gold surfaces in aqueous environment. (a) Scheme of the set-up used for the photopatterning of SAMs. (b) Formation of a protective layer using a thiol-based SAM, UV-assisted localized deprotection and protein patterning by spontaneous adsorption on gold.

2.2.2 Desorption of thiol-based SAMs using UV light

For the selection of the protective layer, we carried out a series of experiments using hydrophobic and hydrophilic thiolated compounds for forming SAMs. Afterwards we monitored their UV-mediated desorption kinetics via SPR.

Gold-coated SPR prisms were covered with one of two Poly Ethylene Glycol (PEG) derivatives: a long chain thiolated-PEG ($PEG_{2000}SH$, MW= 2000 Da), a short chain thiolated-PEG ($PEG_{350}SH$, MW= 350 Da); or one of three alkanethiols: 1-dodecanethiol ($CH_3(CH_2)_{11}SH$, MW= 202.4 Da), 2-methyl-2-propanethiol ($C(CH_3)_3SH$, MW= 90.2 Da) or 6-mercapto-1-hexanol ($HO(CH_2)_6SH$, MW= 134.2 Da) (refer to Annex A.1.1 for a detailed experimental procedure).

A homemade optical device was used during the Surface Plasmon Resonance Imaging (SPRi) assays (Figure 2.5). This hybrid set-up combined a SPR device with a commercial optical microscope allowing exposure of the samples to UV light while monitoring the SPR signal over time. The experimental conditions as well as information regarding the fluidic device used are in these assays are further detailed in Annex A.1.2.

(a) Scheme of hybrid SPRi + UV irradiation set-up **(b) Picture of real optical system**

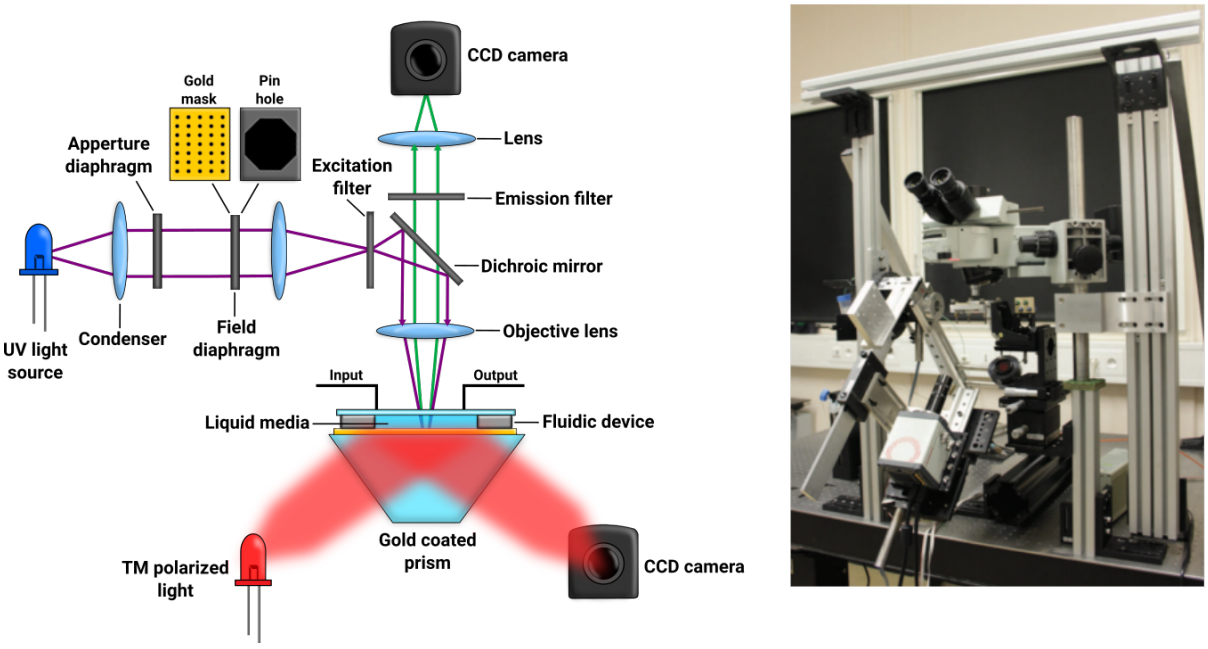

Figure 2.5 – Hybrid optical set-up for simultaneous UV irradiation and SPRi monitoring. (a) Basic explanatory scheme showing the main components of the system and (b) a picture of the device used during the assays.

During UV irradiation (performed with a high-pressure mercury lamp with an Olympus filter 330-385 nm), we observed a decrease in the signal intensity (which is a signature of loss of material under our setup conditions) only on PEG-based SAMs. Whereas, non PEG-based SAMs did not suffered a significant shift in their SPR signal (Figure 2.6). The difference in the magnitude of these signals (regarding the two PEG derivatives) could

be explained by an effect of the molecular weight and surface density. Since shifts in the SPR signal are caused by changes in the refractive index near the monitored surface, desorption of higher amounts of material would lead to a larger impact on the signal.

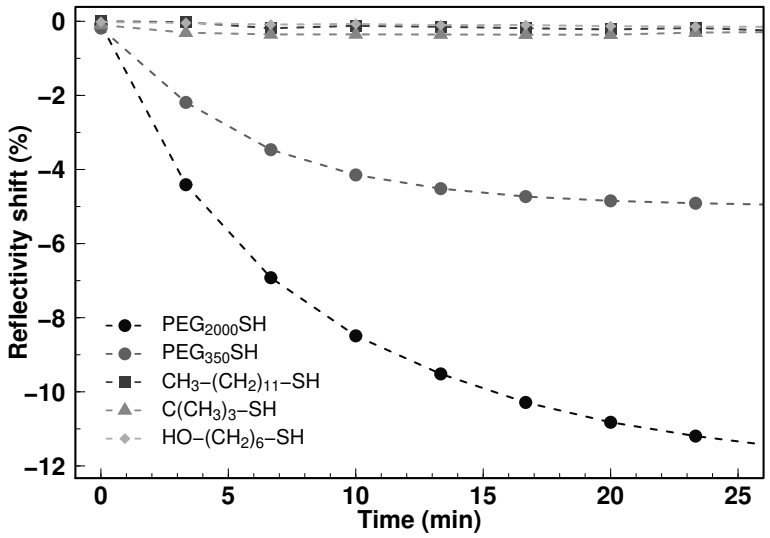

Figure 2.6 – SPR monitoring during UV irradiation of different SAMs: Polyethylene glycol ($PEG_{2000}SH$ and $PEG_{350}SH$), 1-dodecanethiol ($CH_3(CH_2)_{11}SH$), 2-methyl-2-propanethiol ($C(CH_3)_3SH$) and 6-mercapto-1-hexanol ($HO(CH_2)_6SH$).

Under our experimental conditions, contrary to what has been reported on alkanethiols using more energetic wavelengths and on air[80–83], there is no rupture of Au-S or C-S bonds of the thiolated molecules. Taking into account that only the compounds containing ether bonds (R-O-R') were affected by UV irradiation, we considered this phenomena might be a photodegradation process based on C-O cleavage.

2.2.3 Monitoring of adsorption/desorption kinetics via SPR

We explored further the desorption kinetics of PEG-based SAMs using SPR by performing multiple cycles of adsorption and UV-induced desorption. Each cycle consisted in the injection of the respective PEG solution (20 µM) to form a new SAM, then a stabilization time with Phosphate Buffered Saline (PBS) as running buffer and finally UV-irradiation of the SAM.

The results were surprising. We observed that the SPR signal, after UV irradiation, of $PEG_{350}SH$ SAMs did not return to the baseline level (Figure 2.7). This fact suggests that some material was left on the surface after each cycle. Furthermore, new injections of $PEG_{350}SH$ did not succeed to restore the SPR signal to its previous maximum level. A steady increase in the basal level with a constant decrease in the maximum value could be explained by partial degradation of the SAM.

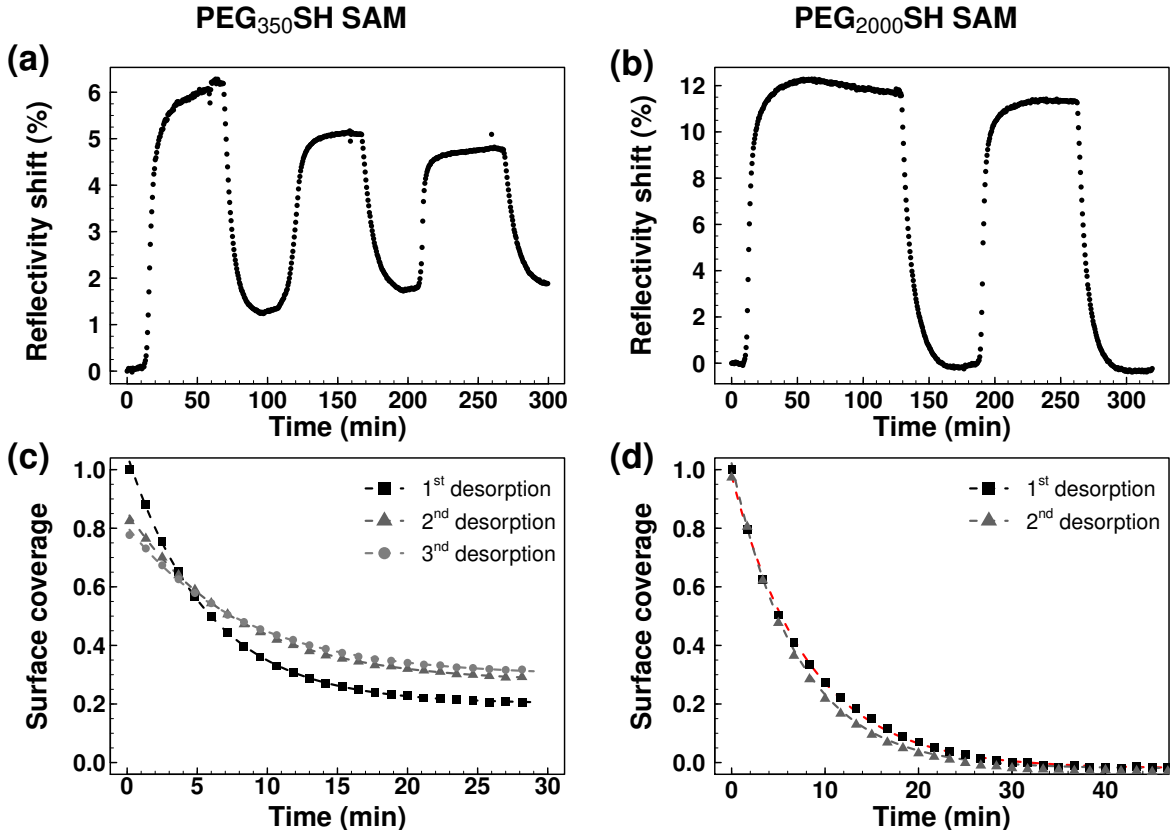

Figure 2.7 – Adsorption and UV-induced desorption kinetics of PEG-based SAMs followed by SPR. (a,b) SAM formation and UV-mediated desorption of (a) $PEG_{350}SH$ and (b) $PEG_{2000}SH$; (c,d) overlap of each UV-mediated desorption process for (c) $PEG_{350}SH$ and (d) $PEG_{2000}SH$ SAMs respectively. Data was normalized from 0% (reflectivity before first injection) to 100% coverage (reflectivity shift after first adsorption process).

To explain our results we hypothesized that the initial plateau during SAM formation was caused due to steric hindrance of the attached molecules and not due to complete saturation of binding sites to the gold surface. This is a valid assumption the maximum density of thiol-based SAMs require long incubation times, varying from minutes to hours up to days[84–87] even if the formation of the Au-S covalent bond occurs after ∼3 seconds[87].

Partial degradation of $PEG_{350}SH$ caused accumulation of mass on the surface (seen as a increment of the baseline) while simultaneously reducing the number of available sites for the attachment of new molecules (reducing the maximum obtainable number of molecules after each new adsorption cycle), as it is represented graphically on Figure 2.8a.

In case of $PEG_{2000}SH$ SAM, such phenomena were not observed on the performed cycles. Continuing with our previous explanation, compounds with larger hydrodynamic volume would cause higher steric effects leading to SAMs with fewer molecules per surface area. Degradation of such SAMs would reveal larger zones of gold previously blocked by steric effects. Since the amount of material left on the surface is significantly lower than for $PEG_{350}SH$ SAMs, adsorption of new $PEG_{2000}SH$ molecules would not be signifi-

cantly affected, at least not after only two cycles of SAM formation/removal as shown in Figure 2.8b.

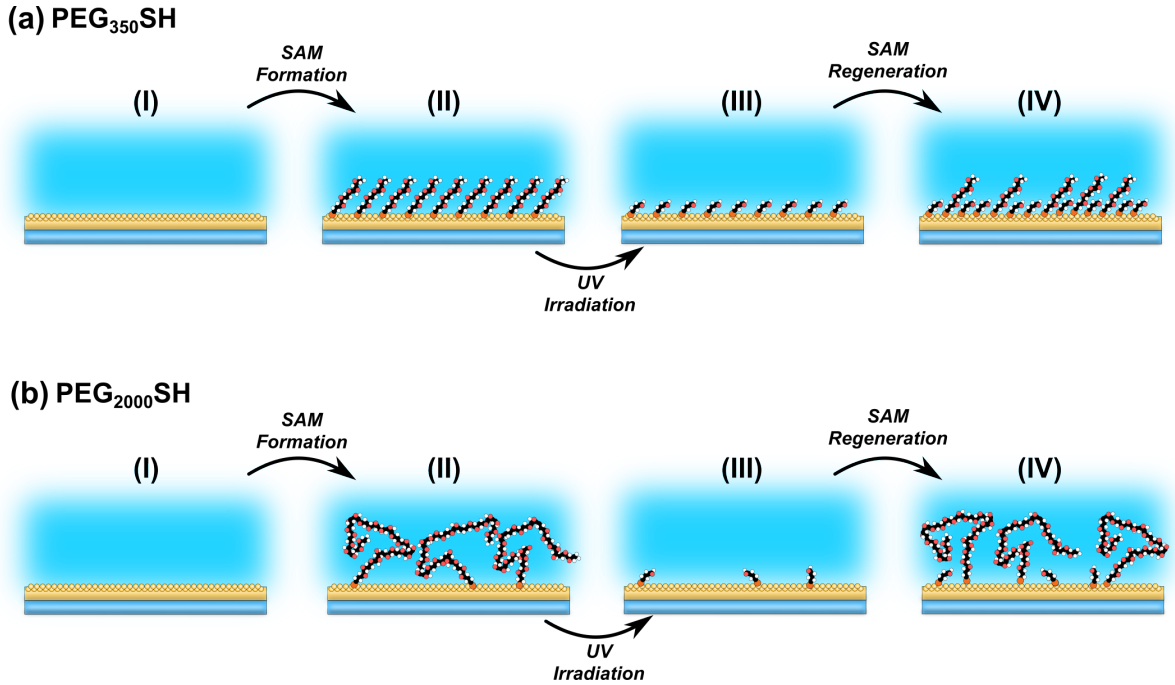

Figure 2.8 – Scheme of PEG adsorption/desorption cycles. For both PEG derivatives: (I) Initial stage of a bare gold surface, (II) Surface after SAM formation, (III) Surface after UV irradiation and (IV) Surface after injection of new thiolated molecules. In the case of $PEG_{350}SH$, the refractive index on the irradiated surface is higher on III than I, since fragments of PEG are left on the surface after irradiation. On the other hand, after SAM regeneration the refractive index is lower on IV than II due to a reduction in the net amount of material on the surface. This is not the case for $PEG_{2000}SH$ since the differences in refractive index are not as significant (I compared to III and II compared with IV).

Furthermore, our data are coherent with results reported by Legett and Zharnikov who performed experiments with similar compounds in air[88–91] and aqueous[78] environments. In their work, they explained a dependence on the wavelength with the rate of degradation of ethylene glycol chains while the alkanethiol part was primarily unaffected (as we observed while irradiating alkanethiols). Moreover, they noted the formation of sulfonates during UV irradiation (at a very small scale), indicating rupture of some Au-S bonds but at a considerably slower rate.

2.2.4 Goniometry experiments

Since SPR assays showed partial ($PEG_{350}SH$) and seemingly complete removal ($PEG_{2000}SH$) of the PEG-based SAMs during UV irradiation, we further characterize the system by performed contact angle measurements. If the PEG-based SAM is being degraded or

removed, we expected to observe a drastic change on the hydrophilicity of the irradiated surfaces.

In the case of $PEG_{2000}SH$ SAMs, if our previous explanation was correct, the contact angle with water should be similar (after UV irradiation) to that of a bare gold surface. Whereas, for $PEG_{350}SH$ SAMs, the surface would change its hydrophilicity based on the nature of the exposed moeities (either by becoming more hydrophobic or hydrophilic). To evaluate this, we measured the contact angles of water on the functionalized surfaces exposed to UV irradiation as well as those used as control (Figure 2.9).

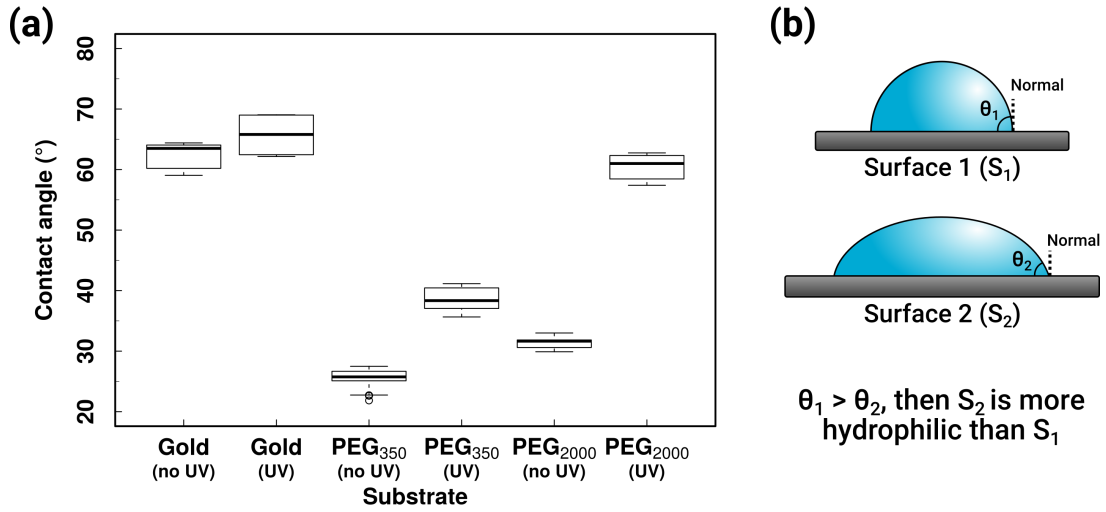

Figure 2.9 – Contact angle of water on functionalized surfaces. (a) Boxplot of measured contact angles for each SAM before and after UV irradiation. Lines inside the box represent that median value in the distribution. (b) Schematic representation of contact angles of water relative to hydrophilicity of a surface.

We noticed a significant shift in the contact angle of $PEG_{2000}SH$ SAMs after UV exposure (from 30°to 61°) which are very close to those of bare gold (63-65°). For $PEG_{350}SH$ SAMs, there was a less radical increase in the contact angle (from 26°to 38°). These new results were coherent with our previous hypothesis (Figure 2.8). Degradation of $PEG_{2000}SH$ unblocks large areas of unoccupied gold while $PEG_{350}SH$ SAM leaves a denser layer of material with unknown moieties which are relatively hydrophilic.

Interestingly, previous research by Weber et al.[78] and Ducker et al.[92] described the generation of hydrophilic moieties (C=O) upon UV irradiation of PEGylated surfaces. In their work, they used Infrared Reflection Absorption (IRRA) and X-ray Photoelectron Spectrometry (XPS) on PEG based SAMs before and after UV irradiation, observing an increase of C=O signal which can be ascribed to aldehyde moieties.

2.2.5 Action mechanism of the desorption process

UV desorption of thiol-based SAMs over gold have been extensively studied, yet most of the research has been done conducted on air[82,83,93,94]. The action mechanism for this

photo-oxidation process can be described as follows (Equation 2.1)[83].

$$X(CH_2)_nS{-}Au + \frac{3}{2}O_2 + e^- \longrightarrow X(CH_2)_nSO_3^- + Au \tag{2.1}$$

Equation 2.1 is based on the conversion of thiols to sulfonates ($R\text{-}SO_3^-$), which are easily removed or replaced. Rieley et al.[82] suggested two mechanisms for this process which are depicted graphically in Figure 2.10.

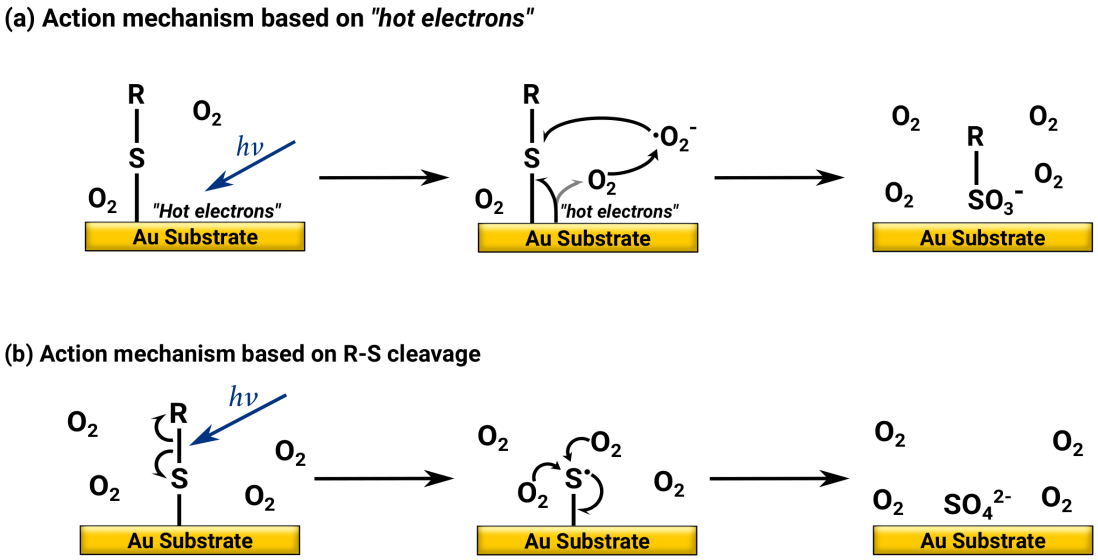

Figure 2.10 – Reported mechanisms for photooxidation of thiol-based SAMs. (a) UV excitation of "hot" electrons (electrons with sufficient kinetic energy to overcome the potential barrier required to break an interface state) from the metal to the adsorbate thiol or to a co-adsorbed oxygen in the surface forming superoxide radical ($\cdot O_2^-$); and (b) A mechanism similar to what has been observed in silver which involves a rupture of the R-S bond and then the oxidation of the chemisorbed sulfur to sulfate.

However, our results suggest that these mechanisms do not occur, at least when exposed to 365 nm, since we did not observed desorption in other thiol-based SAMs (as was shown in Figure 2.7).

Considering only dissociation energy (estimated from Luo and Luo[95]), the weaker bonds on the thiolated molecules grafted on gold would be Au-SH (253.6 $kJ.mol^{-1}$, corresponding to wavelengths $\leq$472 nm) and HS-R (307.9 $kJ.mol^{-1}$, corresponding to wavelengths $\leq$389 nm). However, we did not observed significant desorption/degradation in alkanethiols and just partial desorption on PEG which discards this process. The same applies for direct interaction of "hot electrons" with the adsorbate thiol, leaving generation of Reactive Oxygen Species (ROS) as a plausible explanation.

In the literature, very few research have been conducted regarding PEG-SH photo-irradiation in liquid phase. The most remarkable would be that of Weber et al.[78] which studied the degradation of oligoethylene glycol (OEG) in aqueous media. Strikingly, they reported that this phenomena can happen in absence of molecular oxygen. Nonetheless, under their

experimental conditions, it is extremely challenging to ensure total absence of chemisorbed oxygen on the surfaces or even in solution and due the use of highly energetic wavelengths (254 nm), direct photolysis of water $H_2O \longrightarrow H\cdot + HO\cdot$ could occur. Unfortunately, an in-depth mechanism of the process was not presented in this work.

To tackle such mystery, we decided to evaluate the literature regarding degradation of PEG in solution. Won et al.[96] described a radical mediated process for the degradation of PEG in aqueous solutions Figure 2.11.

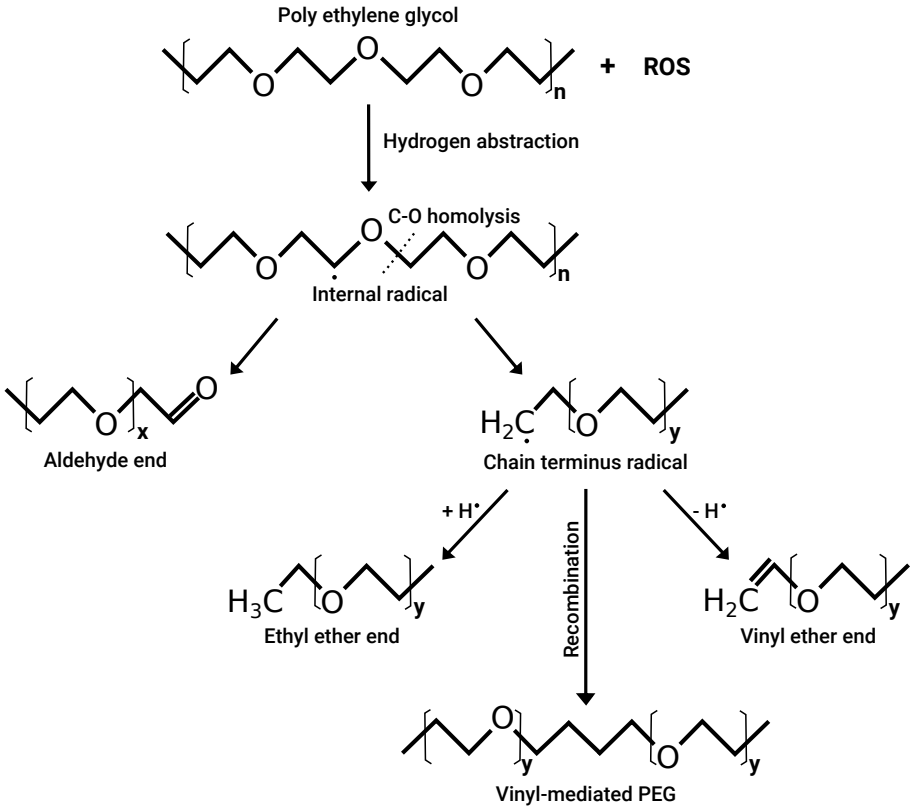

Figure 2.11 – Degradation of PEG via hydrogen abstraction. Mechanism adapted from Won et al.[96]

This mechanism is triggered by the removal of an hydrogen from a carbon atom in the ethylene glycol subunits. This generates an internal carbon centered radical which leads to a C-O homolysis leaving aldehyde ends such as the ones described by Weber et al.[78] and Ducker et al.[92].

Since ROS are known for causing hydrogen abstractions and can be generated by UV irradiation in aqueous media, we used Electron Paramagnetic Resonance (EPR) spectroscopy[97] to track the radical species produced during our procedure.

2.2.6 Evaluation of ROS on the desorption kinetics

Electron Paramagnetic Resonance (EPR), known as well as Electro Spin Resonance (ESR), shares the same fundamental principle as Nuclear Magnetic Resonance (NMR) since both techniques monitor the interaction of magnetic dipoles with an external magnetic field and electromagnetic radiation at a specific wavelength[98]. However, rather than the monitoring of nuclear state spins as NMR does, EPR (as its name implies) concerns with the electronic spin states caused by one or more unpaired electrons making it a suitable technique to explore radicalar mechanisms.

Yet, we had multiple concerns regarding the lower detection limit (LOD) of the EPR equipment as well as the stability of the radical species formed during the process. To solve the first issue, we compared the EPR spectra of a series of dilutions of a stable radical to determine the minimum concentration we could reliably detect under standard experimental conditions (Annex A.1.3)(Figure 2.12).

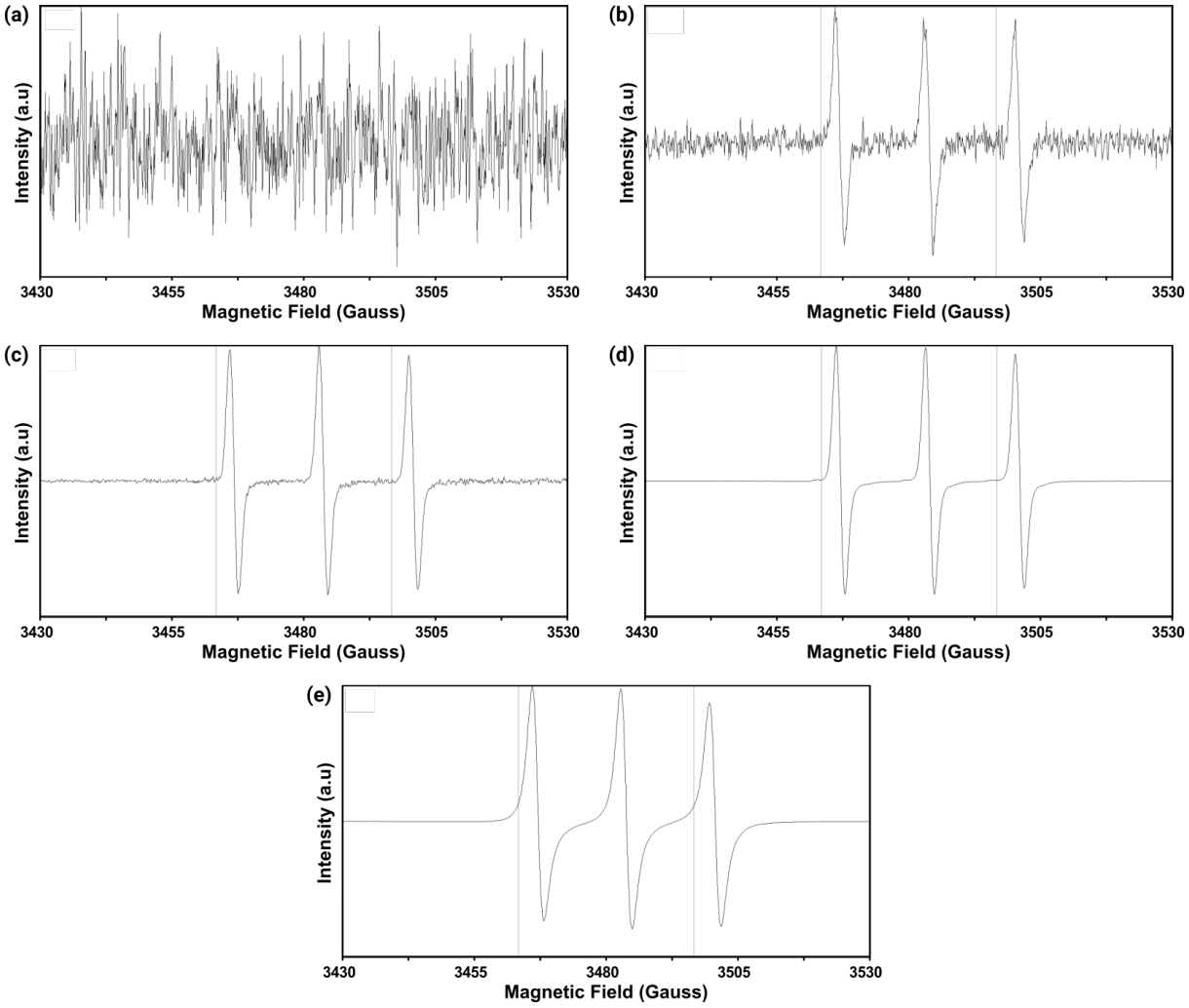

Figure 2.12 – EPR spectra of different concentrations of 4-Hydroxy-TEMPO: (A) 1 µM, (B) 10 µM, (C) 100 µM, (D) 1mM and (E) 10 mM.

A series of dilutions of the stable radical 4-Hydroxy-TEMPO (4 - Hydroxy - 2, 2, 6, 6 -tetramethyl piperidine 1-oxyl, also know as TEMPOL) were prepared in PBS at 10 mM, 1 mM, 100 µM, 10µM and 1µM. We were able to observe clear signals up to 10µM using 1 Gauss of modulation without additional accumulation cycles, below this concentration the signal:noise ratio was extremely low. Assuming a experimental limit in the range of 10 µM and a working volume of 30 µL, we calculated that about 1.8×10^{14} radicals were required for a detection. Such amount of "EPR active" molecules (compounds that contain unpaired electrons) represented a new challenge. Under our UV irradiation set-up, we could only irradiate small surfaces at a time and the process of collecting the sample without diluting it and measure it in a short period of time was extremely challenging. Therefore, we redesigned completely our assay. The new test involved the use of a concentrated solution ($\sim4.9\times10^{16}$ particles.L^{-1}) of 20 nm gold nanoparticles (AuNP).

Considering a surface density of $PEG_{2000}SH$ around 3.42 molecules.nm^{-2} (approximated from Xia et al.[99]), the use of AuNP dramatically increased the irradiated surface per volume of sample. Furthermore, this new study model allowed direct deposition of the sample on a quartz tube that could be irradiated immediately before the EPR measurements. This step significantly reduced the time for between the putative generation of radicals via UV irradiation and their potential detection.

Due to the short half-life of most radicals under aqueous conditions, we used the spin trap 5,5-dimethyl-1-pyrroline N-oxide (DMPO) which reacts covalently with radical products[100]. This reaction generates stable adducts that can be detected via EPR. We mixed the nanoparticle solution with DMPO and performed irradiation of the tube in a controlled environment for 1.75 min using a UV diode (365 nm). After irradiation, we recorded the EPR spectra and made a simulation with four possible radical species (Figure 2.13a), namely: a carbon centered radical (as suggested in Figure 2.11), degradation products of DMPO, hydroxyl radicals (main ROS expected from this type of process) and thiyl radicals (created by radicalization of the thiol moieties).

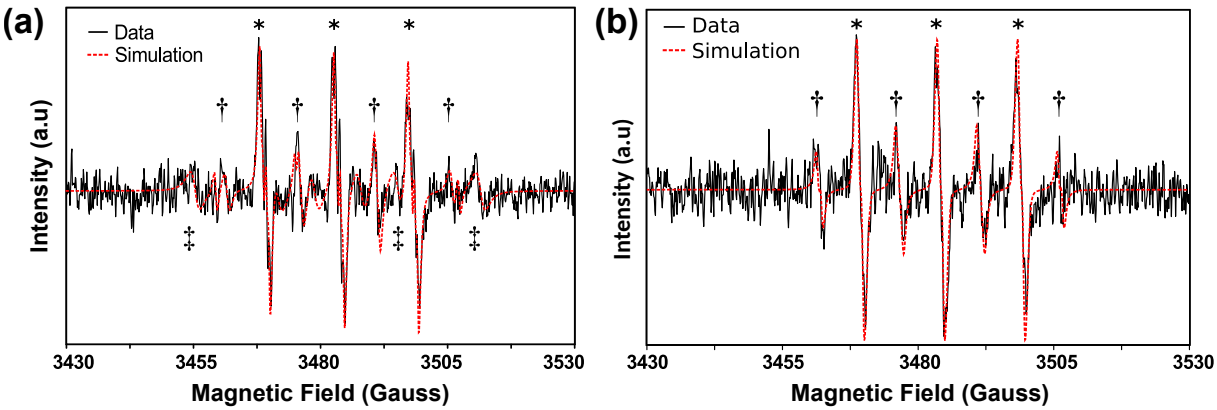

Figure 2.13 – EPR spectra of UV-irradiated PEGylated gold nanoparticles (AuNP). (a) PEG-AuNP in a DMPO solution and after UV-irradiation. (b) Spectra of the blank solution (PBS with DMPO solution but without AuNP). Solid black line corresponds to experimental spectrum while the red segmented line to the simulation of radicals (DMPO degradation products*, hydroxyl † and carbon centered radicals ‡).

The hyperfine couplings used for the first species were AN_0 = 16.3 G and AH_1= 23.5 G, closely resembling those observed for carbon centered radicals (R·)[101]. In the case of the second species, we used AN_0= 14.6 G, AH_1=1.13 G and AH_2=0.5 G which can be ascribed to oxidative degradation products of DMPO[100]. Hydroxyl radicals (OH·) were observed as a third species[100], presenting the hyperfine couplings AN = 14.5 G and AH_1 = 14.6 G. As for thiyl radicals (RS·)[102,103], we used AN = 15.7 and AH1 = 16.4.

The EPR signals from the simulated HO· and RS· were too weak and close to each other, preventing their proper identification. In the blank experiment (EPR spectra of an irradiated sample without nanoparticles, Figure 2.13b), we observed signals of hydroxyl radicals of similar magnitude excited at the same magnetic field intensities which suggests that the signals observed in Figure 2.13a correspond to hydroxyl radicals formed via UV irradiation of the solution.

2.2.7 Exploration of a possible photo-Fenton reaction

PEG degradation by hydroxyl radicals (in the presence of iron ions) has been reported via a photo-Fenton reaction[104]. As it was possible that unexpected traces of iron ions were present in our experimental conditions, we performed SPR assays to evaluate the effect of such process in PEG UV-mediated desorption kinetics.

We dissolved iron salts (either $FeSO_4$ or $FeCl_3$) and mixed them with our running buffer. The solutions were flowed on a microfluidic device during UV irradiation of a PEGylated gold surface. Instead of increasing the desorption rate, as it would be expected from a photo-Fenton process, the desorption was actually slower than in PBS (Figure 2.14).

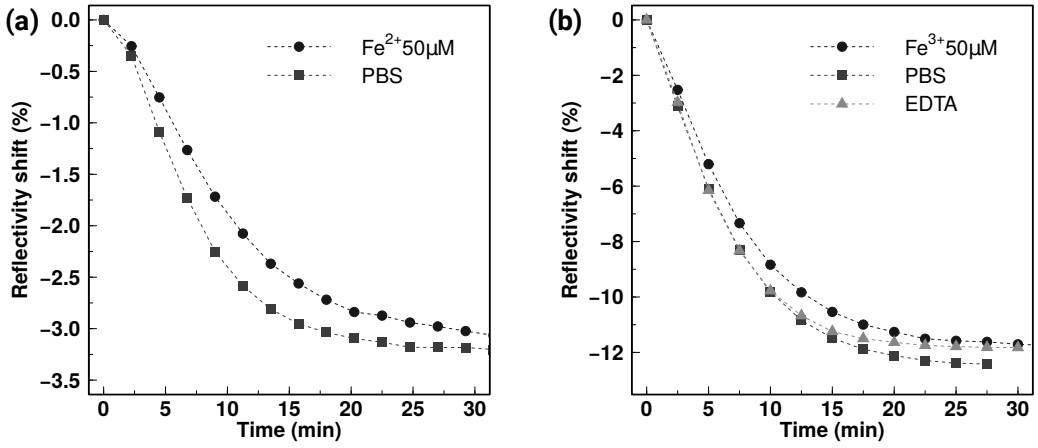

Figure 2.14 – Irradiation of $PEG_{2000}SH$ SAM exposed to UV light under (a) $FeSO_4$ flow compared to PBS and (b) $FeCl_3$ flow compared to PBS and EDTA.

This unexpected result could be ascribed to the formation of UV-absorbing complexes between iron ions and the dissolved oxygen[105]. Such complexes could have reduced the irradiation efficiency and/or decreasing the availability of oxygen accounting for the results. Nonetheless, Weber et al.[78] described that oxygen is not required for UV-mediated

PEG degradation in aqueous media. Even if that is the case and oxygen it is not required for degradation of the ethylene glycol units, its presence allows spontaneous desorption of SAMs due to oxidation of the thiol moieties which normally accelerates the desorption process.

In order to completely discard the hypothesis of a possible photo-Fenton effect, we performed a test using ethylene diamine tetra acetic acid (EDTA) as a cation chelating agent. Addition of EDTA solution did not affect the kinetics in any significant way compared to PBS suggesting that a photo-Fenton process does not need to be involved for the degradation to occur under our conditions.

2.2.8 Evaluation of ROS scavengers

Preliminary assays using hydrogen peroxide (0.25% v/v, which produces hydroxyl radicals when irradiated with UV light) showed a significant increase in the desorption rate of $PEG_{2000}SH$ SAMs (see Annex A.2.1). As ROS seemed to be able to mediate this process, we continued to explore their involvement. For such experiments, mannitol[106] (100 mM, reported to scavenge hydroxyl radicals) and sodium pyruvate[107,108] (10 mM, which prevents formation of hydrogen peroxide) were flowed during the UV irradiation process.

However, none of the scavengers had any significant effect on the desorption kinetics (Figure 2.15).

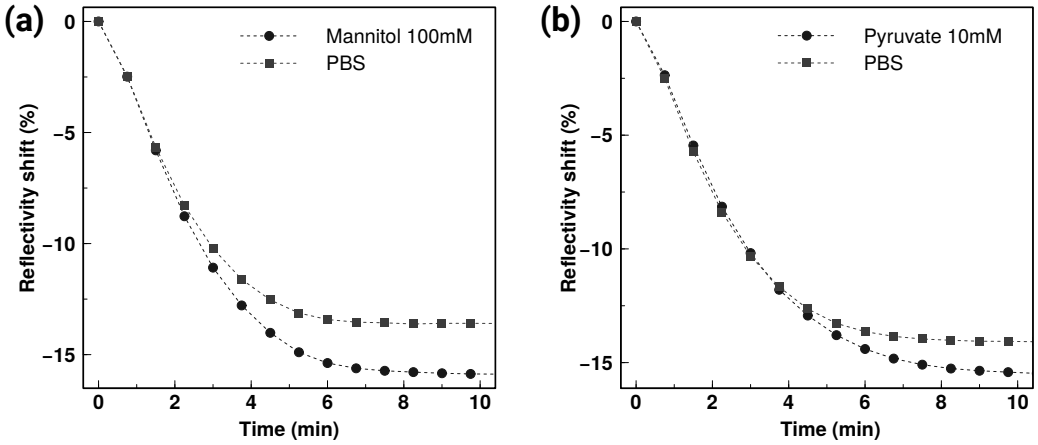

Figure 2.15 – Desorption kinetics of $PEG_{2000}SH$ when exposed to ROS scavengers. (a) Flow of a 100 mM mannitol solution and (b) flow of 10 mM Pyruvate solution.

These results suggest that, even if ROS may be involved in the PEG degradation mechanism, prevention of their formation in the bulk solution do not affect the desorption process.

2.2.9 Final remarks on the potential action mechanism

From EPR tests, we observed production of hydroxyl radicals but when we added ROS scavengers during the irradiation, there was no real effect on the desorption kinetics. It is possible that such radicals are generated in the environment nearby the SAM, reacting first with the PEG instead of the scavengers in solution. Another possibility is the direct photolysis of the R-O bonds which have a dissociation energy of 338.9 kJ.mol^{-1} (energy from wavelengths $\leq$ 353 nm, not so different from the ones used)[95]. Even if we could not find an in-depth explanation for the degradation mechanism, we obtained numerous clues about this phenomena. Namely, that the process most probably involves hydrogen abstraction and C-O homolysis. This statement would explain the presence of aldehyde moieties described in the literature[78,92] while also the partial degradation process we explained before based on SPR, EPR and goniometry assays.

2.3 Validation of the functionalization method

Considering the desorption kinetics assays, SAM regeneration experiments and goniometry results, we concluded that $PEG_{2000}SH$ SAMs were suitable as protective layers of gold surfaces. The next stage then consisted on evaluating the feasibility to generate microarrays using this method.

2.3.1 Detection of small molecules on a photopatterned microarray

Previous SPR experiments showed that it was possible to remove and regenerate $PEG_{2000}SH$ SAMs so we extended this surface chemistry method to similar biomolecules. In order to achieve this, a previous master student (Thanh Nguyen) created a mask by specific removal of the metallic surface on gold coated (50 nm thickness) glass slides.

This method required the use of a micro-controller system to direct the movement of a metallic needle into specific patterns while applying a bias voltage (15 V) between the gold layer and the needle. Once the needle was located in the desired location, it was lowered until contact resulting in a short circuit causing thermal bursting of the gold layer. This method created a grid of apertures with a pitch of 150 µm with an average aperture diameter of 40 µm (Figure 2.16a).

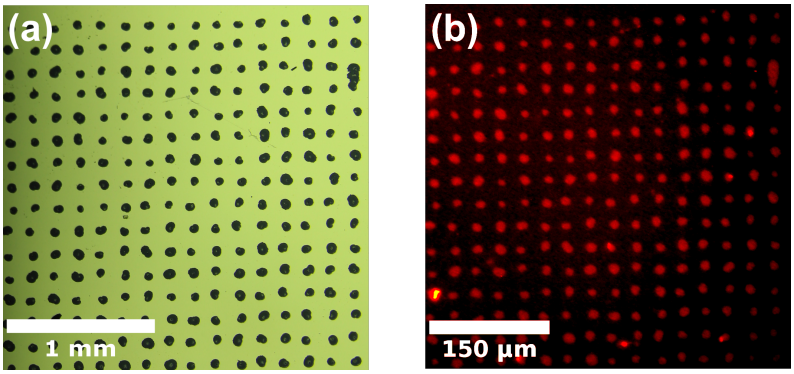

Figure 2.16 – Photopatterning of fluorescent molecules on a gold surface. (a) Grid created over a gold surface as a mask for UV irradiation. (b) Fluorescence image (20x objective) of photopatterned features functionalized with biotin-PEG-SH and revealed with SAPE.

We functionalized a gold surface with $PEG_{2000}SH$ SAM, which was then irradiated using previously described mask allowing selective photodegradation the SAM. The deprotected areas were then functionalized with a solution of biotinylated PEG-SH.

Afterwards, the surface was rinsed with PBS to remove unbounded and then incubated in a solution of a fluorescent protein (StreptAvidin-PhycoErythrin, SAPE). Thanks to the specific interaction between streptavidin and biotin moieties, fluorescent microscopy imaging of the surface showed labeling closely matching the pattern used for the UV irradiation (Figure 2.16b).

By image analysis we estimated a lateral resolution around 5 µm (width at half maximum) (Figure 2.17). We believe that this limit is caused mainly by optical imperfections in the illumination setup, but chemical diffusion processes may be involved as well.

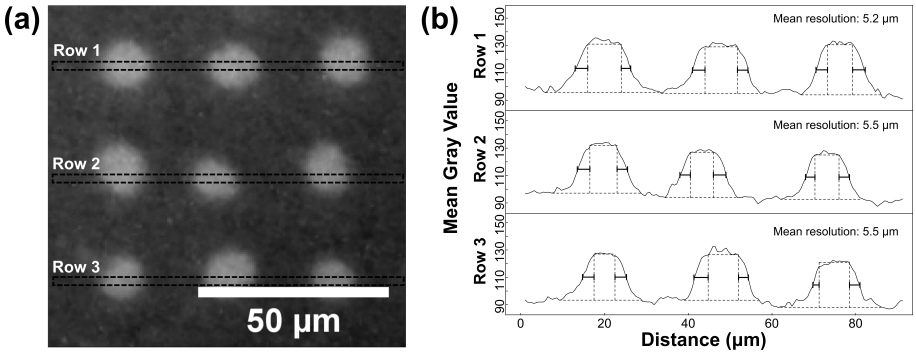

Figure 2.17 – Analysis of the lateral resolution of photo-assisted functionalization process. (a) Fluorescent image of features functionalized with thiolated Biotin-PEG after exposure to SAPE. (b) Mean gray value of selected regions corresponding to functionalized and non-functionalized areas.

2.3.2 Capture of individual cells on a photopatterned microarray

After the successful fabrication of a pattern with fluorescent molecules, we repeated the previous experiment but replacing the biotinylated-PEG-SH by thiolated antibodies (anti-human CD3-SH), specific to antigens anchored on the membrane of human T cells (Figure 2.18).

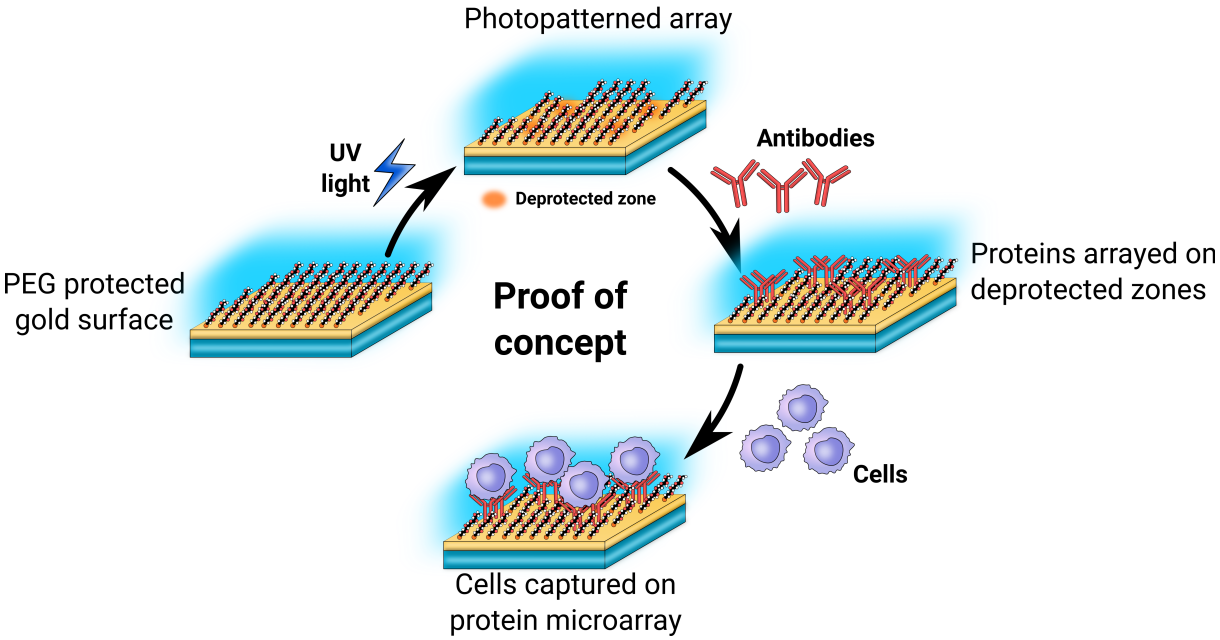

Figure 2.18 – Biological validation of indirect photo-assisted functionalization.

Once the photopatterning was performed, a solution with anti-human CD3-SH was injected in the microfluidic cell for 20 min. The surface was rinsed with PBS and then exposed to a suspension of Peripheral Blood Mononuclear Cells (PBMCs) previously obtained via density gradient separation from blood samples[109]. The surface was in contact with the solution of cells ($2x10^6$ cells.mL^{-1}) for 20 minutes, afterwards unbounded cells were gently washed away with PBS. Visualization via optical microscopy confirmed the efficient capture of multiple cells on each anti-CD3 micrometric motif (Figure 2.19a).

The feature size was easily adjusted by selecting an objective lens with higher magnification on the illuminating setup, giving access to motifs in the same size range of human lymphocytes (12-14 µm in diameter) (as shown in Figure 2.19b). Additional experiments were performed with thiolated rabbit immunoglobulins as a negative control. In this case, specific cell capture was not observed (Figure 2.19c).

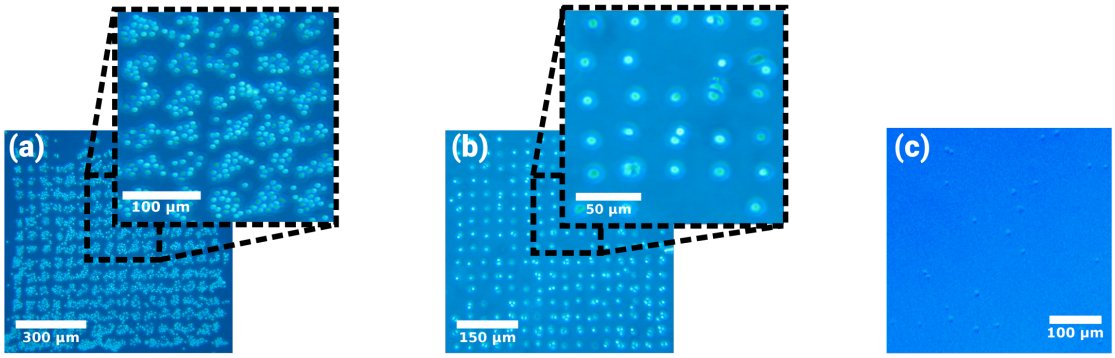

Figure 2.19 – UV-assisted protein patterning in aqueous conditions. (a) Patterns performed through a 10x objective and functionalized with anti-human CD3 had an average size around 50 µm allowing capture of multiple cells per feature; (b)Pattern performed through a 20x objective lens and functionalized with anti-human CD3 had an average size around 15-20 µm, allowing capture of individual cells on the protein array; (c) Negative control were grafting was performed using thiolated rabbit IgG instead of anti-human CD3, there was no specific capture of cells in this case.

Heterogeneity in the optical apertures of the mask affected directly the spot size. This led to variance in the number of captured cells per feature (as shown in Figure 2.20). Multiple cells were captured in a pattern matching the defects caused by improper alignment of the needle during mask fabrication. The variability in morphology and size of the apertures can be considerably improved by using a different fabrication method for the mask. A typical example is the use of photolithography which has been widely exploited for photomask microfabrication in the production of integrated circuits[110].

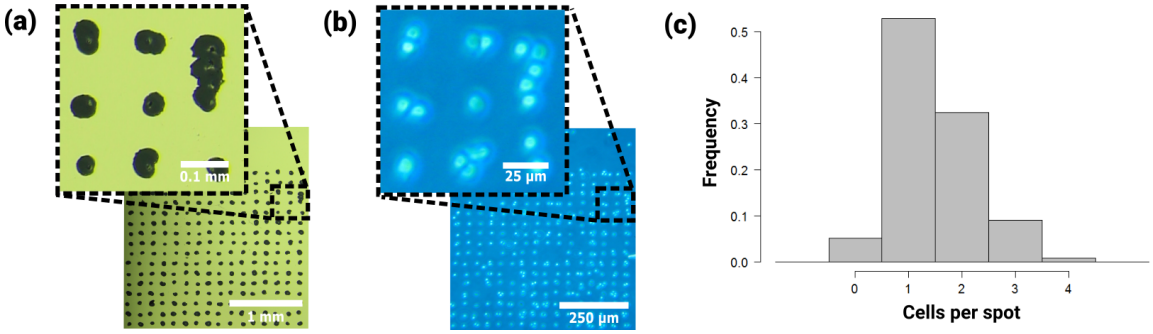

Figure 2.20 – Heterogeneity in photolithography mask account for multiple cells captured per spot on the protein array. (a) Grid created over a gold surface as a mask for UV irradiation; (b) cells captured on the same pattern made through the mask shown in (a); (c) Histogram of frequencies of cells per spot in the protein array. More than 50% of the spots contained a single cell, while near 35% contained two. Only 5% of the features were vacant after cell incubation.

2.4 Conclusions

We developed a UV photolithography process that is fully compatible with surface patterning of proteins. This strategy is based on degradation of PEG SAMs used as a protective layer. We analyzed the influence of numerous parameters in order to better understand the mechanics by which the process takes place. Even though an in-depth action mechanism was not found, we discovered relevant clues that demonstrate a process potentially mediated by C-O homolysis that is not triggered by a photo-Fenton reaction but could be caused by ROS generation and/or direct photolysis. Also, we observed a strong dependence on the surface density of the SAM (related to the molecular weight of the PEG derivative used). After selection of the adequate protective layer ($PEG_{2000}SH$), we fabricated protein microarrays that allowed the capture of individual cells.

The speed of the desorption process can be further improved by increasing the light intensity. However, the desorption step is not the limiting step for making highly multiplexed arrays. The slowest process is the formation of new thiol-gold SAMs which takes considerable time (dozens of minutes) to achieve low-surface density SAMs. Nevertheless, it is important to highlight that this process can be used to pattern any protein of interest over gold surfaces. By keeping a continuously liquid medium while avoiding direct exposure of proteins to UV light, it is possible to preserve the native functionality of delicate samples. Although it was not evaluated, this technique could be employed by sequential multiplexed functionalization of the surface. Such process would overcome limitations that are present in technologies based on micro-contact printing or micro-cantilevers such as low throughput, difficult operation and dryness[111] while allowing simple tuning of the feature size.

Finally, the method herein described is compatible with cell culture conditions, making it suitable for the development of biosensors for *in vitro* detection of cell secretions.

References

[1] Chandra, H., Reddy, P. J., and Srivastava, S. (2011) Protein microarrays and novel detection platforms. *Expert Review of Proteomics 8*, 61–79.

[2] Betzen, C., Alhamdani, M. S. S., Lueong, S., Schröder, C., Stang, A., and Hoheisel, J. D. (2015) Clinical proteomics: Promises, challenges and limitations of affinity arrays. *Proteomics - Clinical Applications 9*, 342–347.

[3] Driguez, P., Doolan, D. L., Molina, D. M., Loukas, A., Trieu, A., Felgner, P. L., and McManus, D. P. *Methods in Molecular Biology*; Springer New York, 2014; pp 221–233.

[4] Hu, B., Niu, X., Cheng, L., Yang, L.-N., Li, Q., Wang, Y., Tao, S.-C., and Zhou, S.-M. (2015) Discovering cancer biomarkers from clinical samples by protein microarrays. *Proteomics - Clinical Applications 9*, 98–110.

[5] Hinchliffe, T. E., Lin, Z.-T., and Wu, T. (2016) Protein arrays for biomarker discovery in lupus. *Proteomics - Clinical Applications 10*, 625–634.

[6] Yu, X., Petritis, B., and LaBaer, J. (2016) Advancing translational research with next-generation protein microarrays. *Proteomics 16*, 1238–1250.

[7] Pulito, C., Sacconi, A., Korita, E., Maidecchi, A., and Strano, S. *Methods in Molecular Biology*; Springer New York, 2016; pp 189–199.

[8] Phizicky, E., Bastiaens, P. I. H., Zhu, H., Snyder, M., and Fields, S. (2003) Protein analysis on a proteomic scale. *Nature 422*, 208–215.

[9] Sun, H., Chen, G. Y., and Yao, S. Q. (2013) Recent Advances in Microarray Technologies for Proteomics. *Chemistry & Biology 20*, 685–699.

[10] Natesan, M., and Ulrich, R. G. (2010) Protein Microarrays and Biomarkers of Infectious Disease. *International Journal of Molecular Sciences 11*, 5165–5183.

[11] Romanov, V., Davidoff, S. N., Miles, A. R., Grainger, D. W., Gale, B. K., and Brooks, B. D. (2014) A critical comparison of protein microarray fabrication technologies. *The Analyst 139*, 1303–1326.

[12] Li, B., Jiang, L., Song, Q., Yang, J., Chen, Z., Guo, Z., Zhou, D., Du, Z., Song, Y., Wang, J., Wang, H., Yu, S., Wang, J., and Yang, R. (2005) Protein Microarray for Profiling Antibody Responses to Yersinia pestis Live Vaccine. *Infection and Immunity 73*, 3734–3739.

[13] Haab, B. B., Dunham, M. J., and Brown, P. O. (2001) *Genome Biology 2*, research0004.1.

[14] Paweletz, C. P., Charboneau, L., Bichsel, V. E., Simone, N. L., Chen, T., Gillespie, J. W., Emmert-Buck, M. R., Roth, M. J., III, E. F. P., and Liotta, L. A. (2001) Reverse phase protein microarrays which capture disease progression show activation of pro-survival pathways at the cancer invasion front. *Oncogene 20*, 1981–1989.

[15] Huang, S., and Creighton, C. (2015) Reverse phase protein arrays in signaling pathways: a data integration perspective. *Drug Design, Development and Therapy* 3519.

[16] Sutandy, F. R., Qian, J., Chen, C.-S., and Zhu, H. (2013) Overview of Protein Microarrays. *Current Protocols in Protein Science 72*, 27.1.1–27.1.16.

[17] Aguilar-Mahecha, A., Hassan, S., Ferrario, C., and Basik, M. (2006) Microarrays as Validation Strategies in Clinical Samples: Tissue and Protein Microarrays. *OMICS: A Journal of Integrative Biology 10*, 311–326.

[18] Chang, T.-W. (1983) Binding of cells to matrixes of distinct antibodies coated on solid surface. *Journal of Immunological Methods 65*, 217–223.

[19] MacBeath, G., and Schreiber, S. L. (2000) Printing Proteins as Microarrays for High-Throughput Function Determination. *Science 289*, 1760–1763.

[20] Barbulovic-Nad, I., Lucente, M., Sun, Y., Zhang, M., Wheeler, A. R., and Bussmann, M. (2006) Bio-Microarray Fabrication Techniques—A Review. *Critical Reviews in Biotechnology 26*, 237–259.

[21] Hall, D. A., Ptacek, J., and Snyder, M. (2007) Protein microarray technology. *Mechanisms of Ageing and Development 128*, 161–167.

[22] Kusnezow, W., and Hoheisel, J. D. (2003) Solid supports for microarray immunoassays. *Journal of Molecular Recognition 16*, 165–176.

[23] Wu, P., and Grainger, D. W. (2006) Comparison of Hydroxylated Print Additives on Antibody Microarray Performance. *Journal of Proteome Research 5*, 2956–2965.

[24] Tseng, F.-G., Ho, C.-E., Su, C.-J., Chen, Y.-F., Huang, H., and Chieng, C.-C. Characterization of simultaneous protein microarray formation by discrete micro stamper on surfaces of different wettabilities. 2005 IEEE International Conference on Robotics and Biomimetics - ROBIO. 2005.

[25] Akbulut, O., Yu, A. A., and Stellacci, F. (2010) Fabrication of biomolecular devices via supramolecular contact-based approaches. *Chem. Soc. Rev. 39*, 30–37.

[26] Kaufmann, T., and Ravoo, B. J. (2010) Stamps, inks and substrates: polymers in microcontact printing. *Polymer Chemistry 1*, 371.

[27] Lee, M., Kang, D.-K., Yang, H.-K., Park, K.-H., Choe, S. Y., Kang, C., Chang, S.-I., Han, M. H., and Kang, I.-C. (2006) Protein nanoarray on Prolinker™ surface constructed by atomic force microscopy dip-pen nanolithography for analysis of protein interaction. *Proteomics 6*, 1094–1103.

[28] Wu, C.-C., Reinhoudt, D. N., Otto, C., Subramaniam, V., and Velders, A. H. (2011) Strategies for Patterning Biomolecules with Dip-Pen Nanolithography. *Small 7*, 989–1002.

[29] Salaita, K., Wang, Y., and Mirkin, C. A. (2007) Applications of dip-pen nanolithography. *Nature Nanotechnology 2*, 145–155.

[30] Zheng, Z., Daniel, W., Giam, L., Huo, F., Senesi, A., Zheng, G., and Mirkin, C. (2009) Multiplexed Protein Arrays Enabled by Polymer Pen Lithography: Addressing the Inking Challenge. *Angewandte Chemie International Edition 48*, 7626–7629.

[31] Li, D., Ed. *Encyclopedia of Microfluidics and Nanofluidics*; Springer US, 2008.

[32] Ihalainen, P., Määttänen, A., and Sandler, N. (2015) Printing technologies for biomolecule and cell-based applications. *International Journal of Pharmaceutics 494*, 585–592.

[33] Fujita, S., Onuki-Nagasaki, R., Fukuda, J., Enomoto, J., Yamaguchi, S., and Miyake, M. (2013) Development of super-dense transfected cell microarrays generated by piezoelectric inkjet printing. *Lab Chip 13*, 77–80.

[34] Allain, L. R., Stratis-Cullum, D. N., and Vo-Dinh, T. (2004) Investigation of microfabrication of biological sample arrays using piezoelectric and bubble-jet printing technologies. *Analytica Chimica Acta 518*, 77–85.

[35] Kolodziej, C. M., and Maynard, H. D. (2012) Electron-Beam Lithography for Patterning Biomolecules at the Micron and Nanometer Scale. *Chemistry of Materials 24*, 774–780.

[36] Mir, M., Dondapati, S. K., Duarte, M. V., Chatzichristidi, M., Misiakos, K., Petrou, P., Kakabakos, S. E., Argitis, P., and Katakis, I. (2010) Electrochemical biosensor microarray functionalized by means of biomolecule friendly photolithography. *Biosensors and Bioelectronics 25*, 2115–2121.

[37] Hoffmann, N. (2008) Photochemical Reactions as Key Steps in Organic Synthesis. *Chemical Reviews 108*, 1052–1103.

[38] Delaittre, G., Guimard, N. K., and Barner-Kowollik, C. (2015) Cycloadditions in Modern Polymer Chemistry. *Accounts of Chemical Research 48*, 1296–1307.

[39] Chatani, S., Kloxin, C. J., and Bowman, C. N. (2014) The power of light in polymer science: photochemical processes to manipulate polymer formation, structure, and properties. *Polym. Chem. 5*, 2187–2201.

[40] Claus, T. K., Telitel, S., Welle, A., Bastmeyer, M., Vogt, A. P., Delaittre, G., and Barner-Kowollik, C. (2017) Light-driven reversible surface functionalization with anthracenes: visible light writing and mild UV erasing. *Chemical Communications 53*, 1599–1602.

[41] Delaittre, G., Goldmann, A. S., Mueller, J. O., and Barner-Kowollik, C. (2015) Efficient Photochemical Approaches for Spatially Resolved Surface Functionalization. *Angewandte Chemie International Edition 54*, 11388–11403.

[42] Fodor, S., Read, J., Pirrung, M., Stryer, L., Lu, A., and Solas, D. (1991) Light-directed, spatially addressable parallel chemical synthesis. *Science 251*, 767–773.

[43] Sabanayagam, C. R., Smith, C. L., and Cantor, C. R. (2000) Oligonucleotide immobilization on micropatterned streptavidin surfaces. *Nucleic Acids Res 28*, e33–e33.

[44] Alonso, J. M., Reichel, A., Piehler, J., and del Campo, A. (2008) Photopatterned Surfaces for Site-Specific and Functional Immobilization of Proteins. *Langmuir 24*, 448–457.

[45] Dulcey, C., Georger, J., Krauthamer, V., Stenger, D., Fare, T., and Calvert, J. (1991) Deep UV photochemistry of chemisorbed monolayers: patterned coplanar molecular assemblies. *Science 252*, 551–554.

[46] Tarlov, M. J., Burgess, D. R. F., and Gillen, G. (1993) UV photopatterning of alkanethiolate monolayers self-assembled on gold and silver. *Journal of the American Chemical Society 115*, 5305–5306.

[47] Critchley, K., Jeyadevan, J. P., Fukushima, H., Ishida, M., Shimoda, T., Bushby, R. J., and Evans, S. D. (2005) A Mild Photoactivated Hydrophilic/Hydrophobic Switch. *Langmuir 21*, 4554–4561.

[48] Dendane, N., Hoang, A., Guillard, L., Defrancq, E., Vinet, F., and Dumy, P. (2007) Efficient Surface Patterning of Oligonucleotides Inside a Glass Capillary through Oxime Bond Formation. *Bioconjugate Chemistry 18*, 671–676.

[49] Yamazoe, H., Uemura, T., and Tanabe, T. (2008) Facile Cell Patterning on an Albumin-Coated Surface. *Langmuir 24*, 8402–8404.

[50] Fouassier, J. P., and Lalevée, J. *Photoinitiators for Polymer Synthesis*; Wiley-VCH Verlag GmbH & Co. KGaA, 2012.

[51] Tucker, J. W., and Stephenson, C. R. J. (2012) Shining Light on Photoredox Catalysis: Theory and Synthetic Applications. *The Journal of Organic Chemistry 77*, 1617–1622.

[52] Prier, C. K., Rankic, D. A., and MacMillan, D. W. C. (2013) Visible Light Photoredox Catalysis with Transition Metal Complexes: Applications in Organic Synthesis. *Chemical Reviews 113*, 5322–5363.

[53] MacKinnon, A. L., and Taunton, J. (2009) Target Identification by Diazirine Photo-Cross-linking and Click Chemistry. *Curr Protoc Chem Biol 1*, 55–73, 23667793[pmid].

[54] Preston, G. W., and Wilson, A. J. (2013) Photo-induced covalent cross-linking for the analysis of biomolecular interactions. *Chemical Society Reviews 42*, 3289.

[55] Lowe, A. B., Hoyle, C. E., and Bowman, C. N. (2010) Thiol-yne click chemistry: A powerful and versatile methodology for materials synthesis. *Journal of Materials Chemistry 20*, 4745.

[56] Zuo, Y., Lu, H., Xue, L., Wang, X., Ning, L., and Feng, S. (2014) Preparation and characterization of luminescent silicone elastomer by thiol–ene "click" chemistry. *J. Mater. Chem. C 2*, 2724–2734.

[57] Dorman, G., and Prestwich, G. D. (1994) Benzophenone Photophores in Biochemistry. *Biochemistry 33*, 5661–5673.

[58] Dubinsky, L., Krom, B. P., and Meijler, M. M. (2012) Diazirine based photoaffinity labeling. *Bioorganic & Medicinal Chemistry 20*, 554–570.

[59] Balakirev, M. Y., Porte, S., Vernaz-Gris, M., Berger, M., Arié, J.-P., Fouqué, B., and Chatelain, F. (2005) Photochemical Patterning of Biological Molecules Inside a Glass Capillary. *Analytical Chemistry 77*, 5474–5479.

[60] Delamarche, E., Sundarababu, G., Biebuyck, H., Michel, B., Gerber, C., Sigrist, H., Wolf, H., Ringsdorf, H., Xanthopoulos, N., and Mathieu, H. J. (1996) Immobilization of Antibodies on a Photoactive Self-Assembled Monolayer on Gold. *Langmuir 12*, 1997–2006.

[61] MacKinnon, A. L., Garrison, J. L., Hegde, R. S., and Taunton, J. (2007) Photo-Leucine Incorporation Reveals the Target of a Cyclodepsipeptide Inhibitor of Cotranslational Translocation. *Journal of the American Chemical Society 129*, 14560–14561.

[62] Hermanson, G. T. *Bioconjugate Techniques*; Elsevier, 2013; pp 299–339.

[63] Hoyle, C., and Bowman, C. (2010) Thiol-Ene Click Chemistry. *Angewandte Chemie International Edition 49*, 1540–1573.

[64] Wang, Y., Bruno, B. J., Cornillie, S., Nogieira, J. M., Chen, D., Cheatham, T. E., Lim, C. S., and Chou, D. H.-C. (2017) Application of Thiol-yne/Thiol-ene Reactions for Peptide and Protein Macrocyclizations. *Chemistry - A European Journal 23*, 7087–7092.

[65] Jonkheijm, P., Weinrich, D., Köhn, M., Engelkamp, H., Christianen, P., Kuhlmann, J., Maan, J., Nüsse, D., Schroeder, H., Wacker, R., Breinbauer, R., Niemeyer, C., and Waldmann, H. (2008) Photochemical Surface Patterning by the Thiol-Ene Reaction. *Angewandte Chemie International Edition 47*, 4421–4424.

[66] Jonkheijm, P., Weinrich, D., Schröder, H., Niemeyer, C., and Waldmann, H. (2008) Chemical Strategies for Generating Protein Biochips. *Angewandte Chemie International Edition 47*, 9618–9647.

[67] Lim, R. K. V., and Lin, Q. (2010) Azirine ligation: fast and selective protein conjugation via photoinduced azirine–alkene cycloaddition. *Chemical Communications 46*, 7993.

[68] Duroux, M., Gurevich, L., Neves-Petersen, M. T., Skovsen, E., Duroux, L., and Petersen, S. B. (2007) Using light to bioactivate surfaces: A new way of creating oriented, active immunobiosensors. *Applied Surface Science 254*, 1126–1130.

[69] Duroux, M., Skovsen, E., Neves-Petersen, M. T., Duroux, L., Gurevich, L., and Petersen, S. B. (2007) Light-induced immobilisation of biomolecules as an attractive alternative to microdroplet dispensing-based arraying technologies. *Proteomics 7*, 3491–3499.

[70] Parracino, A., Neves-Petersen, M. T., di Gennaro, A. K., Pettersson, K., Lövgren, T., and Petersen, S. B. (2010) Arraying prostate specific antigen PSA and Fab anti-PSA using light-assisted molecular immobilization technology. *Protein Science 19*, 1751–1759.

[71] Parracino, A., Gajula, G. P., di Gennaro, A. K., Correia, M., Neves-Petersen, M. T., Rafaelsen, J., and Petersen, S. B. (2011) Photonic immobilization of bsa for nanobiomedical applications: creation of high density microarrays and superparamagnetic bioconjugates. *Biotechnology and Bioengineering 108*, 999–1010.

[72] Petersen, S. B., di Gennaro, A. K., Neves-Petersen, M. T., Skovsen, E., and Parracino, A. (2010) Immobilization of biomolecules onto surfaces according to ultraviolet light diffraction patterns. *Applied Optics 49*, 5344.

[73] Skovsen, E., Kold, A. B., Neves-Petersen, M. T., and Petersen, S. B. (2009) Photonic immobilization of high-density protein arrays using Fourier optics. *PROTEOMICS 9*, 3945–3948.

[74] Yodmongkol, S., Sutapun, B., Praphanphoj, V., Srikhirin, T., Brandstetter, T., and Rühe, J. (2016) Fabrication of protein microarrays for alpha fetoprotein detection by using a rapid photo-immobilization process. *Sensing and Bio-Sensing Research 7*, 95–99.

[75] Lee, E.-J., Chan, E. W. L., and Yousaf, M. N. (2009) Spatio-Temporal Control of Cell Coculture Interactions on Surfaces. *ChemBioChem 10*, 1648–1653.

[76] Zubir, O. E., Xia, S., Ducker, R. E., Wang, L., Mullin, N., Cartron, M. L., Cadby, A. J., Hobbs, J. K., Hunter, C. N., and Leggett, G. J. (2017) From Monochrome to Technicolor: Simple Generic Approaches to Multicomponent Protein Nanopatterning Using Siloxanes with Photoremovable Protein-Resistant Protecting Groups. *Langmuir 33*, 8829–8837.

[77] Lee, J. Y., Shah, S. S., Zimmer, C. C., yu Liu, G., and Revzin, A. (2008) Use of Photolithography to Encode Cell Adhesive Domains into Protein Microarrays. *Langmuir 24*, 2232–2239.

[78] Weber, T., Meyerbröker, N., Hira, N. K., Zharnikov, M., and Terfort, A. (2014) UV-mediated tuning of surface biorepulsivity in aqueous environment. *Chem. Commun. 50*, 4325–4327.

[79] Frasconi, M., Mazzei, F., and Ferri, T. (2010) Protein immobilization at gold–thiol surfaces and potential for biosensing. *Analytical and Bioanalytical Chemistry 398*, 1545–1564.

[80] Mu, X., Gao, A., Wang, D., and Yang, P. (2015) Self-Assembled Monolayer-Assisted Negative Lithography. *Langmuir 31*, 2922–2930.

[81] Zhang, Y., Terrill, R. H., and Bohn, P. W. (1999) Ultraviolet Photochemistry and ex Situ Ozonolysis of Alkanethiol Self-Assembled Monolayers on Gold. *Chemistry of Materials 11*, 2191–2198.

[82] Rieley, H., Price, N. J., Smith, T. L., and Yang, S. (1996) Photo-oxidation and photo-reduction in alkylthiol monolayers self-assembled on gold. *Journal of the Chemical Society, Faraday Transactions 92*, 3629.

[83] Brewer, N. J., Janusz, S., Critchley, K., Evans, S. D., and Leggett, G. J. (2005) Photooxidation of Self-Assembled Monolayers by Exposure to Light of Wavelength 254 nm: A Static SIMS Study. *The Journal of Physical Chemistry B 109*, 11247–11256.

[84] Peterlinz, K. A., and Georgiadis, R. (1996) In Situ Kinetics of Self-Assembly by Surface Plasmon Resonance Spectroscopy. *Langmuir 12*, 4731–4740.

[85] Rouhana, L. L., Moussallem, M. D., and Schlenoff, J. B. (2011) Adsorption of Short-Chain Thiols and Disulfides onto Gold under Defined Mass Transport Conditions: Coverage, Kinetics, and Mechanism. *Journal of the American Chemical Society 133*, 16080–16091.

[86] Love, J. C., Estroff, L. A., Kriebel, J. K., Nuzzo, R. G., and Whitesides, G. M. (2005) Self-Assembled Monolayers of Thiolates on Metals as a Form of Nanotechnology. *Chemical Reviews 105*, 1103–1170.

[87] Xue, Y., Li, X., Li, H., and Zhang, W. (2014) Quantifying thiol–gold interactions towards the efficient strength control. *Nature Communications 5*.

[88] Khan, M. N., and Zharnikov, M. (2013) Fabrication of ssDNA/Oligo(ethylene glycol) Monolayers and Patterns by Exchange Reaction Promoted by Ultraviolet Light Irradiation. *The Journal of Physical Chemistry C 117*, 24883–24893.

[89] Jeyachandran, Y. L., Weber, T., Terfort, A., and Zharnikov, M. (2013) Application of Long Wavelength Ultraviolet Radiation for Modification and Patterning of Protein-Repelling Monolayers. *The Journal of Physical Chemistry C 117*, 5824–5830.

[90] Jeyachandran, Y. L., Meyerbröker, N., Terfort, A., and Zharnikov, M. (2015) Maskless Ultraviolet Projection Lithography with a Biorepelling Monomolecular Resist. *The Journal of Physical Chemistry C 119*, 494–501.

[91] Montague, M., Ducker, R. E., Chong, K. S. L., Manning, R. J., Rutten, F. J. M., Davies, M. C., and Leggett, G. J. (2007) Fabrication of Biomolecular Nanostructures by Scanning Near-Field Photolithography of Oligo(ethylene glycol)-Terminated Self-Assembled Monolayers. *Langmuir 23*, 7328–7337.

[92] Ducker, R. E., Janusz, S., Sun, S., and Leggett, G. J. (2007) One-Step Photochemical Introduction of Nanopatterned Protein-Binding Functionalities to Oligo(ethylene glycol)-Terminated Self-Assembled Monolayers. *Journal of the American Chemical Society 129*, 14842–14843.

[93] Huang, J., and Hemminger, J. C. (1993) Photooxidation of thiols in self-assembled monolayers on gold. *Journal of the American Chemical Society 115*, 3342–3343.

[94] Choi, H.-S., Kang, Y., Lee, H., and Lee, C. (2007) Photopatterning of gold and copper surfaces by using self-assembled monolayers. *Current Applied Physics 7*, 522–527.

[95] Luo, Y.-R., and Luo, Y.-R. *Comprehensive handbook of chemical bond energies*; CRC Press: Boca Raton, 2007.

[96] Won, Y. S., Cho, D., Kim, Y., Lee, J., and Park, S. S. (2010) Degradation of poly(ethylene glycol) by electrolysis during the Cu electroplating: A combined experimental and density functional theory study. *Journal of Applied Polymer Science 117*, 2083–2089.

[97] Rowlands, C. C., and Murphy, D. M. *Encyclopedia of Spectroscopy and Spectrometry*; Elsevier, 2017; pp 173–179.

[98] Roessler, M. M., and Salvadori, E. (2018) Principles and applications of EPR spectroscopy in the chemical sciences. *Chemical Society Reviews 47*, 2534–2553.

[99] Xia, X., Yang, M., Wang, Y., Zheng, Y., Li, Q., Chen, J., and Xia, Y. (2011) Quantifying the Coverage Density of Poly(ethylene glycol) Chains on the Surface of Gold Nanostructures. *ACS Nano 6*, 512–522.

[100] Buettner, G. R. (1987) Spin Trapping: ESR parameters of spin adducts 1474 1528V. *Free Radical Biology and Medicine 3*, 259–303.

[101] Sinha, B. K. (1984) Metabolic activation of procarbazine. *Biochemical Pharmacology 33*, 2777–2781.

[102] Ross, D., and Moldeus, P. (1985) Generation of reactive species and fate of thiols during peroxidase-catalyzed metabolic activation of aromatic amines and phenols. *Environ Health Perspect 64*, 253–257, 3007092[pmid].

[103] Davies, M. J., Forni, L. G., and Shuter, S. L. (1987) Electron spin resonance and pulse radiolysis studies on the spin trapping of sulphur-centered radicals. *Chemico-Biological Interactions 61*, 177–188.

[104] Giroto, J. A., Teixeira, A. C. S. C., Nascimento, C. A. O., and Guardani, R. (2010) Degradation of Poly(ethylene glycol) in Aqueous Solution by Photo-Fenton and H $_2$ O $_2$ /UV Processes. *Industrial & Engineering Chemistry Research 49*, 3200–3206.

[105] Loures, C. C., Alcântara, M. A., Izário Filho, H. J., Teixeira, A., Silva, F. T., Paiva, T. C., and Samanamud, G. R. (2013) Advanced oxidative degradation processes: fundamentals and applications. *International Review of Chemical Engineering 5*, 102–120.

[106] Shen, B., Jensen, R. G., and Bohnert, H. J. (1997) Mannitol protects against oxidation by hydroxyl radicals. *Plant Physiology 115*, 527–532.

[107] Desagher, S., Glowinski, J., and Prémont, J. (1997) Pyruvate protects neurons against hydrogen peroxide-induced toxicity. *Journal of Neuroscience 17*, 9060–9067.

[108] Troxell, B., Zhang, J.-J., Bourret, T. J., Zeng, M. Y., Blum, J., Gherardini, F., Hassan, H. M., and Yang, X. F. (2014) Pyruvate Protects Pathogenic Spirochetes from H2O2 Killing. *PLoS ONE 9*, e84625.

[109] Whiteside, T. L., Berardi, R. S., and Rabin, B. S. (1975) Quantitation of Human Peripheral Blood T and B Lymphocytes. *International Archives of Allergy and Immunology 48*, 731–738.

[110] Rizvi, S. *Handbook of Photomask Manufacturing Technology*, 1st ed.; CRC Press, 2005.

[111] Roupioz, Y., Berthet-Duroure, N., Leïchlé, T., Pourciel, J.-B., Mailley, P., Cortes, S., Villiers, M.-B., Marche, P. N., Livache, T., and Nicu, L. (2009) Individual Blood-Cell Capture and 2D Organization on Microarrays. *Small 5*, 1493–1497.

3

Functionalization of microstructured surfaces for *in vitro* detection of cell secretions

Contents

3.1 Scientific context

A plethora of biologically relevant processes depend directly on the effective secretion of biomolecules. Such compounds are critical in the adaptation and survival of uni- and multicellular organisms and can exert a wide range of functions, ranging from regulatory/communication purposes (quorum sensing molecules, neurotransmitters, cytokines, hormones, etc) to structural functions (extracellular matrix, collagen, polysaccharides, etc).

An in-depth knowledge of the mechanisms by which these processes take place would lead to major advances in medicine (*e.g.* novel biomarkers and therapeutic targets), food industry (avoiding biofilm formation[1]) and basic research (*e.g.* plant-to-plant communication[2,3], developmental biology[4], study of immune response[5]).

Specifically, a great amount of effort has been focused on the study of cytokines and chemokines. These are soluble proteins that are secreted by a wide variety of cells to modulate the body's response to injuries and infection[6]. This group of proteins vary in their function as well as in their molecular weight which ranges from 6 to 70 kDa[7].

They act in a highly localized way as mediators and modulators of immunological responses, cell-to-cell communication, inflammatory stimuli, hematopoietic development, among others[8]. The physiological effects of cytokines commonly rely on their relative concentration[9] as well as in their sequential release[10]. Furthermore, some cytokines are pleiotropic which relates to their ability to address several target causing different responses[11]. This creates extremely complex interactions with additive, synergistic and even antagonistic effects as well as induced secretion of cytokines by another[7].

Due to this fact, it is important to recognize that the physiological responses caused by them are related to a network of interactions[12,13] (as represented by Figure 3.1).

However, the ephemeral nature of cytokines as well as their presence in very low concentrations (femto to picomolar levels)[15] makes their detection very challenging. Drastic increases in their concentration has been related to inflammation and ailment progression, for which they are widely used as biomarkers to monitor the effects of treatments as well as to predict progression of diseases[16,17].

In their comprehensive review, Stenken and Poschenrieder[7] provided an overview of some relevant diseases and the role that cytokines display on them as is the case for: Alzheimer[18,19], asthma[20,21], alloreactivity[22], colon cancer[23,24], lung cancer[25], atherosclerosis[26,27], cardiovascular diseases[28,29], depression[30,31], infection by Human Immunodeficiency Virus (HIV)[32,33], sepsis[34,35], Parkinson's disease[36,37], rheumatoid arthritis[38] and autoimmune diseases[39,40].

The widespread involvement of cytokines in such diseases make particularly interesting their real-time monitoring, which in turn would lead to earlier diagnosis as well as more effective treatments[41,42]. However, analysis of such intricate systems requires the creation of novel sensing technologies.

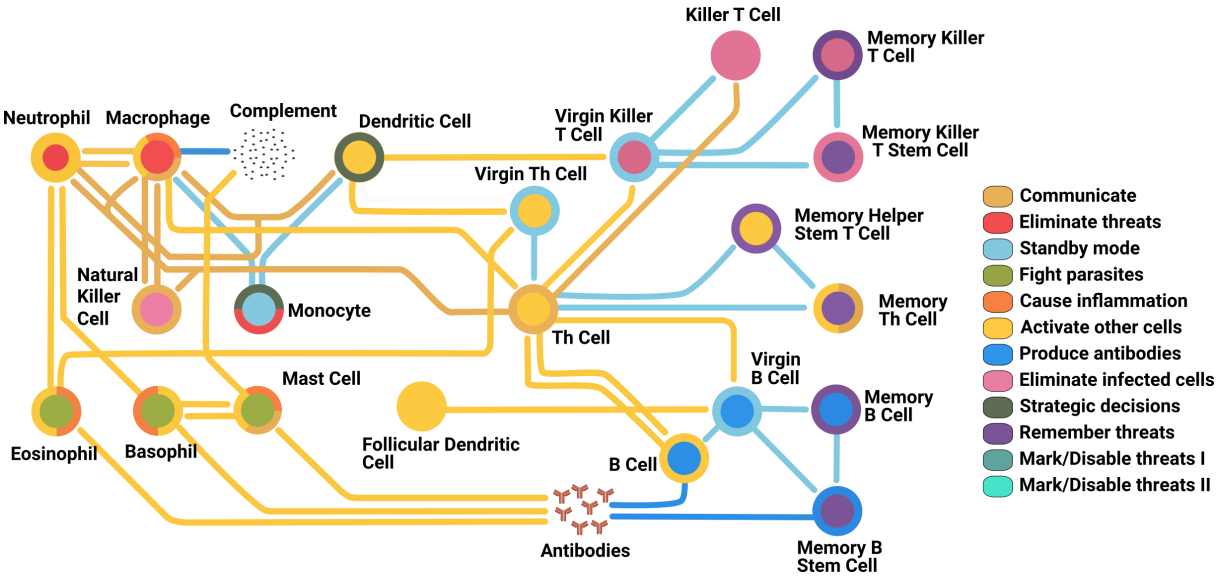

Figure 3.1 – Simplified scheme for cell-to-cell interactions during immune response. Different colors represent the main functions performed by each cell type while the paths indicate their direct interactions via cytokines/chemokines secretion. Modified from Dettmer et al. [14]

3.1.1 Biosensing cytokine secretion

Among the traditional methods for cytokine analysis one can mention: Enzyme Linked ImmunoAssays (ELISA) [43], ELISPOT [44] and indirect methods for cytokine expression such as Polymerase Chain Reaction (PCR) [45].

ELISA is considered as the standard method for cytokine measurements being widely used for biomedical research as well as in clinical laboratories [43]. The typical assay involves an antibody sandwich strategy. Specific antibodies are grafted on the bottom of a well where they capture the antigen of interest, then a secondary antibody linked with an enzyme is used for the detection. This system is commercially provided by numerous vendors for a large number of cytokines. Nevertheless, ELISA has numerous weaknesses such as a huge dependence on the quality of the antibodies and skills/experience of the user [43,46]. Furthermore, it only allows quantification of one cytokine at a time (from the same aliquot), it is common to find discrepancies in results from different ELISA tests, it analyzes the secretions of whole cell populations (this assumes that there is an uniform response when that is not necessarily the case) and has a relatively narrow dynamic range (which refers to the range where there is a linear relationship between analyte concentration and observed signal) compared with other technologies (for traditional ELISAs, it is in the order of 2 to 3-logs) [43,47,48].

ELISPOT has a similar principle to ELISA, but in this case, single cell suspensions, rather than cell lysates, are added to wells with a membrane that has been previously coated with cytokine capturing antibodies [49]. When the cells are stimulated, the secreted cytokines are captured by surrounding antibodies and accumulate locally. Then, cell lysis is induced

and the surface of the wells is exposed to secondary antibodies coupled with an alkaline phosphatase that produces a colored precipitate in presence of a specific substrates such as BCIP/NBT (5-Bromo-4-Chloro-3-Indolyl Phosphate in conjunction with Nitro Blue Tetrazolium)[49]. Estimation of the amount of active cells in a population can be performed by correlating the amount of purple/blue dots with the total number of cells deposited on the surface, allowing the study of functional heterogeneity[50]. Modification of ELISPOT by using fluorophores on the secondary antibody allows simultaneous detection of a few cytokines[51]. However, the maximum number of cytokines that can be evaluated is limited to the overlapping in the spectra of the fluorophores.

Methods based on PCR have the advantage of having a wide linear dynamic range, sensitive at very low level of abundance of the target mRNA and can be used for a variety of different applications[52,53]. However, even if there is, often, a correlation between the amount of mRNA produced and the levels of secreted active cytokines, this indirect method does not provide accurate estimations of the cytokines in the samples (*e.g.* over-expression required due to short-life of a cytokine, slow secretion rate, etc).

Recently, other technologies including flow cytometric bead assays and micropatterned arrays have been gaining popularity. Flow cytometric multiplex arrays (known as bead-based multiplex assays) is currently one of the most commonly used formats[43]. Commercial solutions from BD Bioscience (Cytometric Bead Array - CBA) and Luminex (Multi-Analyte Profiling - xMAP) use sets of micrometric beads that are discriminated by flow cytometry[43]. Multiple sets of beads can be used and each coated with specific capture antibodies. By using a sandwich strategy, the addition of secondary antibodies tagged with fluorophores/chromophores allows detection of multiple analytes in the same sample. Based on the chromogenic/fluorogenic emission and the size of the beads, it is possible to discriminate up to 25 analytes for some commercial systems to nearly 100 for customized systems[43]. Furthermore, these platforms require microliter volume samples and have a wide dynamic range in their sensitivity[43,54].

As with bead-based immunoassays, a great amount of effort was focused on the development of antibody microarrays[43]. As described in Chapter 2, protein microarrays offer excellent high-throughput analysis requiring low sample volumes, thus making them suitable for multiplex cytokine analysis. An interesting example of commercial protein microarrays for cytokine detection is presented by Pawlak et al.[55]. Different sets of antibodies were spotted on their proprietary substrate via ink-jet microarraying. By using a sandwich strategy with biotinylated secondary antibodies and streptavidin/Cy-5, simultaneous detection of human IL-1β, IL-2, IL-4, IL-6, IL-12, IL-13, TNF-α and IFN-γ was achieved. Similar examples are described by Mustafa et al.[56] in their review regarding antibody microarrays for secretome profiling. While they found vast discrepancies among the performance of different systems, they show that this approach surpasses by far standard assays, such as ELISA, in terms of throughput and cost.

3.1.2 Biosensors/biochips for multiplex detection of cytokines

ELISA, the standard system for cytokine measurement, usually requires very long incubation times as well as extensive workflows[7]. Due to the biological relevance of cytokines, a vast amount of transduction platforms for their detection can be found in the literature. Those devices employ either electrochemical, magnetic, mechanical, acoustic or optical transduction systems. Nevertheless, multiplex detection of cytokines has been mainly described using electrochemical and optical approaches, being the use of optical techniques the most common strategy. In this manuscript, an overview of some remarkable examples will be provided. For a more extensive review please refer to Chen et al.[57].

3.1.2.a Common approaches for multiplex detection of cytokines

In the case of electrochemical biosensing, signal generation occurs due to changes in potential, impedance or current between a series of electrodes[58]. An example of electrochemical biochips used for cytokine detection include the work of Baraket et al.[59]. They created an impedance-based sensor by grafting monoclonal anti-human IL-10 and IL-1β on the electrodes and detected both cytokines at low concentrations (ranging from 1 to 15 pg.mL^{-1}, corresponding to femtomolar levels). Another interesting example was presented by Kongsuphol et al.[60]. They were able to measure the concentration of 4 cytokines (IL-6, IFN-γ, TNF-α and IL-8) from only 10 µL of sample. This was achieved by creating Miniaturized Electrophoresis Electrochemical Protein Sensor (MEEPS) with a dynamic range for detection between 10 ng.mL^{-1} to 20 µg.mL^{-1} (around 0.5 nM to 1 µM) (Figure 3.2). The use of Field-Effect Transistors (FETs) is also common for cytokine, it has been reported the detection for IL-6, IL-8 and TNF-α at femtomolar concentrations[61,62] .

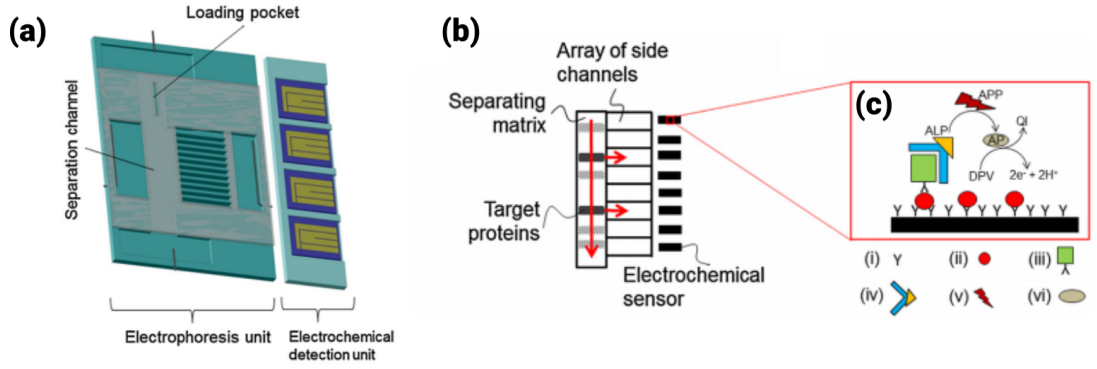

Figure 3.2 – MEEPS for multiplexed protein detections developed by Kongsuphol et al.[60]. (a) Scheme comprising an electrophoresis separation system and an electrochemical sensor; (b) Proteins flow through a separating matrix and are transferred into an array of side channels leading to the sensors and (c) Sandwich immunoassay: (i) capture antibody, (ii) target, (iii) Antibody-biotin, (iv) streptavidin-alkaline phosphatase (ALP), (v) AminoPhenyl Phosphate (APP) and (vi) aminophenol (AP). AP is oxidized on the surface of the electrode to quinoeimine (QI), which can be measured via Differential Pulse Voltammetry (DPV).

In the case of optical based methods, a variety of solutions have been developed based on either fluorescence, chemiluminiscence, use of optical resonators or plasmonic effects. Among the available literature, Zhu et al.[63] presented one of the first examples of a microdevice able to capture specific subsets of T-cells from small volumes of human blood and directly determine their secretion profile. Features containing either anti-human CD3 or anti-human CD8 where positioned near areas with antibodies specific to IL-2 and IFN-γ. After cell activation, evaluation of the secretions was performed using a sandwich strategy with fluorescent labeled secondary antibodies.

Lu et al.[64] took a different approach by creating a relatively simple platform consisting of an array of subnanoliter microchambers. Such micro-chambers were able to confine single cells and, when coupled with high-density antibody barcode microarrays, allowed highly multiplex protein detection over a thousand of single cells in parallel. A few years later, the same team[65] improved their system allowing the simultaneous detection of 42 immune effector proteins secreted from single cells. This study represented at the moment the highest record for a multiplex cytokine detection on single-cells (Figure 3.3). Furthermore, this study also demonstrated that cell populations, with seemingly identical phenotypes, can present relevant heterogeneity at functional and cell behavior levels.

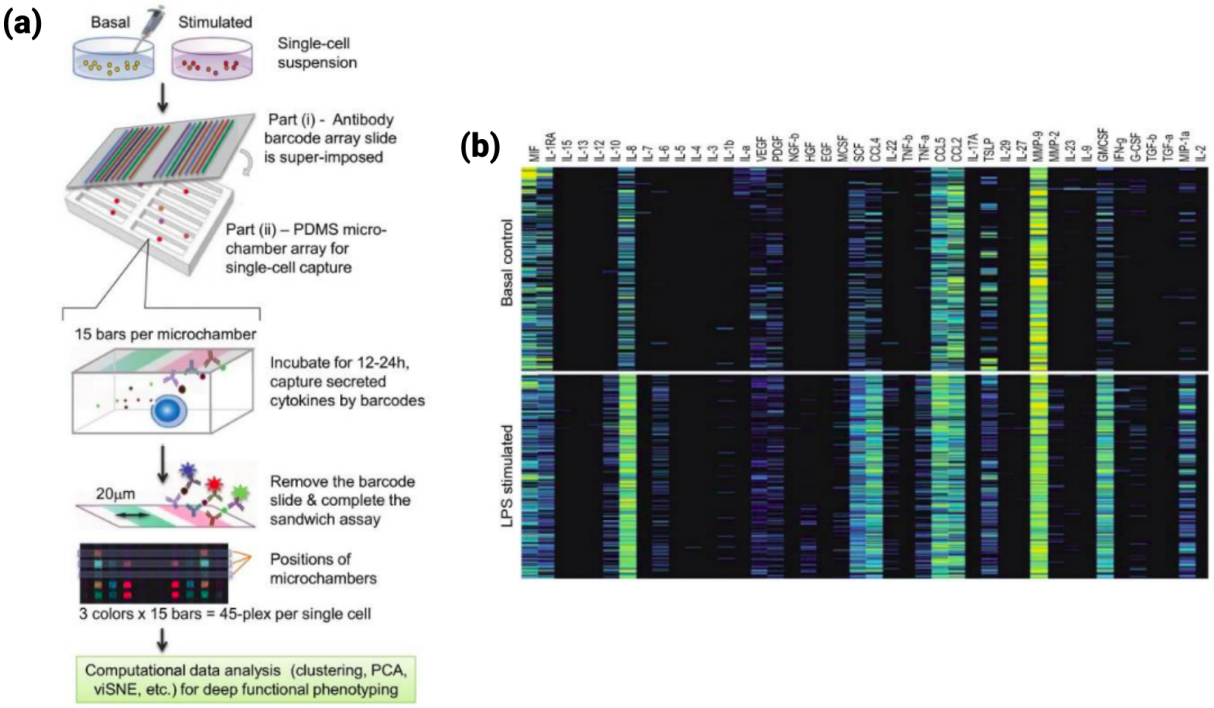

Figure 3.3 – Fluorescence assay developed by Lu et al.[65] for the function profiling of 42 immune effectors on single cells. (a) Workflow of high-throughput profiling of single cells and (b) Representative heat maps (basal vs. stimulated) showing single-cell protein profiles measured on macrophages, in which each row represents a complete protein profile from a single cell and each column a protein of interest.

Another interesting example of fluorescent-based systems is presented by Cohen et al.[66],

they reached femtomolar limits of detection for seven rat cytokines in serum. Their system was based on Single Molecule Arrays (SiMoA) allowing detection in serum below the limit of detection of conventional immunoassays.

Regarding the use of optical microresonators, Luchansky and Bailey[67] achieved picomolar sensitivity of IL-2 and IL-8 secreted by Jurkat cells using a sandwich immunoassay on silicon photonic microring resonators. Later, the same group optimized the system for simultaneous analysis of IL-2, IL-4, IL-5, and TNF-α from primary Th0, Th1 and Th2 susbsets of $CD4^+$ T cells with picomolar sensitivity and in just 5 min of analysis (of exposure to a secondary antibody)[68] (Figure 3.4). Although the use of a sandwich strategy to increase the sensitivity turned this approach into an end-point method, optical microresonators have the potential of being used for real-time measurements[69,70] but their implementation into biochip-like systems remains challenging as they usually require complex microfabrication methods[71].

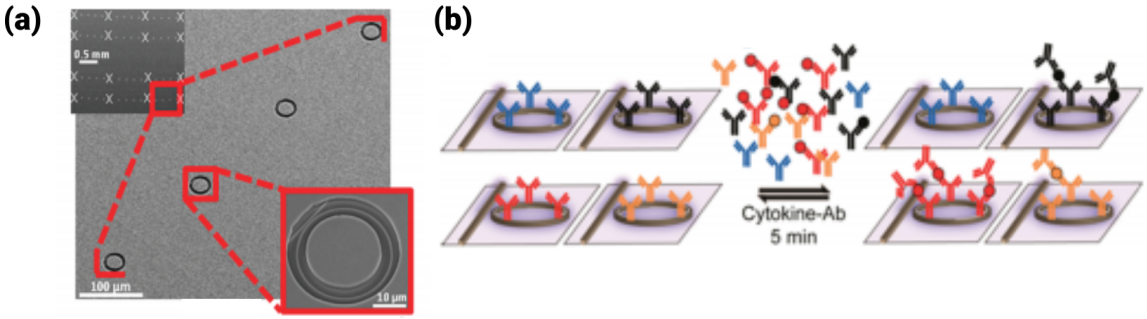

Figure 3.4 – Microring resonator arrays developed by Luchansky and Bailey[68] for multiplexed sandwich immunoassays. (a) SEM images depicting a silicon photonic microring resonator chip with an array of 64 rings and (b) Arrays of microrings functionalized with capture antibodies for various cytokines. Secondary antibodies are used to enhance the signal.

In the case of Surface Enhanced Raman Scattering (SERS), picomolar sensitivity in blood samples was achieved for IL-6, IL-8 and IL-18 by Kamińska et al.[72]. Kamińska et al.[72] used two approaches, named parallel and simultaneous, based on a sandwich SERS immunoassay which is shown in Figure 3.5. One main disadvantage of SERS consists in the difficulty in interpreting the results as the signal enhancement can cause non-relevant Raman bands[73]. Moreover, this approach is limited by the amount of different Raman reporters that can be simultaneously used without overlapping in their SERS signal.

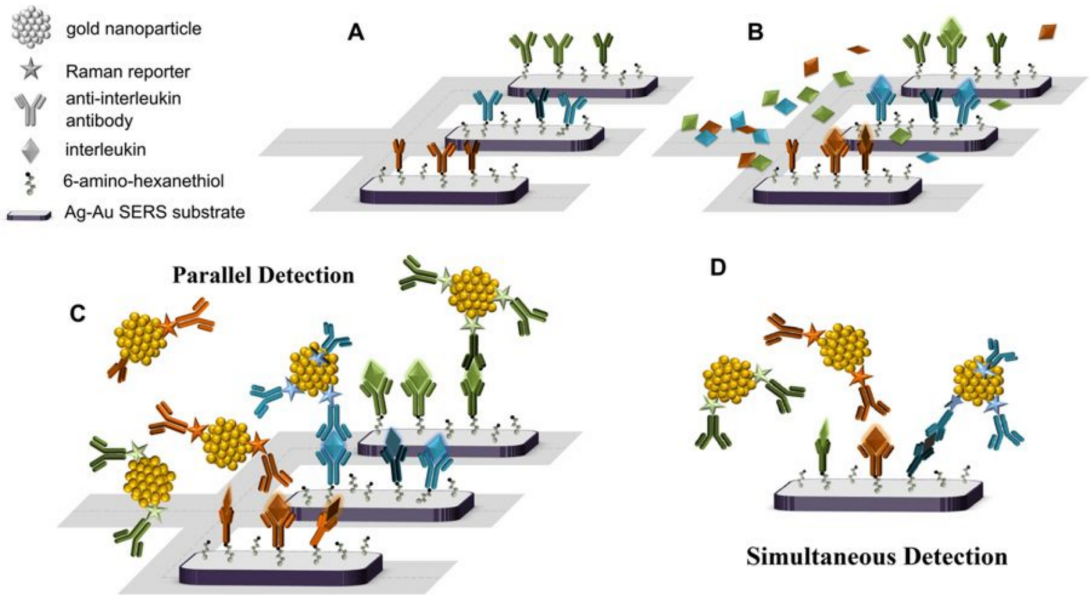

Figure 3.5 – SERS-based multiplex immunoassays for cytokine analysis developed by Kamińska et al.[72]. (A-C) Parallel approach based on use of specific zones for recognizing each cytokine, where in (A) addition of antibodies to the substrate, (B) Injection of the sample and (C) Addition of the nanoshells for sandwich SERS immunoassay. (D) Simultaneous cytokine detection by functionalizing the same substrate with different antibodies. Identification is achieved by employing nanoshells with different Raman reporters, hence obtaining specific SERS spectra based on the cytokines present in the sample.

Yet, all the previously described approaches to multiplex cytokine detection share a major drawback. These techniques consist on end-point measurements, requiring the repetition of the assays with different samples for each time point of interest in order to estimate the secretion kinetics. Besides the ability of simultaneously measure multiple cytokines, real-time information is extremely valuable for a variety of physiological conditions[74]. Since the immune response acts as a networked system, fluctuations in the concentration of one cytokine can, often, induce changes in the presence of multiple others for which multiplex and real-time sensing systems are required[74].

3.1.2.b SPR-based approaches for multiplex sensing of cytokines

In this sense, Surface Plasmon Resonance (SPR) is a powerful tool for cytokine detection. As explained in Chapter 1 section 1.2, SPR is a versatile, label-free, real-time technique for analysis of biomolecular interactions. Conventional systems (ELISA, ELISPOT), as well as most of the methods described before, rely on end-point quantification of cytokines. While this approach may be desired for some applications, it is not suitable for the continuous monitoring of cell secretions. Nevertheless, the use of SPR for cytokine analysis is less common than fluorescence-based assays, due to sensitivity issues[75]. The sensitivity for conventional SPR systems is usually in the range of 10^{-7} - 10^{-6} refractive index units (RIU) corresponding to detection limits in nanomolar range while many clinical settings

require cytokine detection at femto- to picomolar concentrations[57,76].

Battaglia et al.[77] were one of the first to report the use of a SPR device for multiplex cytokine detection in physiologically-relevant samples. Using a fiber-optic SPR system, they achieved measurements of IL-1β, IL-6 and TNF-α in culture media. Other teams have focused on increasing the sensitivity of their SPR systems via sandwich strategies with nanoparticles or other structures[78,79], surface nanostructuring for Localized Surface Plasmon Resonance (LSPR)[57], multi-domain aptamers[80] and using engineered proteins for optimizing immobilization of the probes[81]. Another possibility is the trapping of the cells on zones surrounded by the probes of interest. Milgram et al.[82] demonstrated that, by this approach, it is possible to detect cell secretions in minutes thanks to a high local protein concentration nearby the cells, before their dilution in the bulk medium.

This approach also suffers from an important drawback, the lack of intrinsic selectivity. The penetration depth of the SPR evanescent field is much larger than the size of the target biomolecules, causing the system to be susceptible to any fluctuations in the Refractive Index (RI) of the bulk[57,83]. Regarding *in vitro* culture of cells, these fluctuations may be caused by the attachment of the cells, local modifications in the chemical composition of the culture media (due to nutrient consumption and waste release), secretion of other molecules (*e.g.* extracellular matrix components) and cell debris. Such events would cause a larger RI shift than the capturing of the targeted secretions, leading to extremely low signal-to-noise ratios (Figure 3.6).

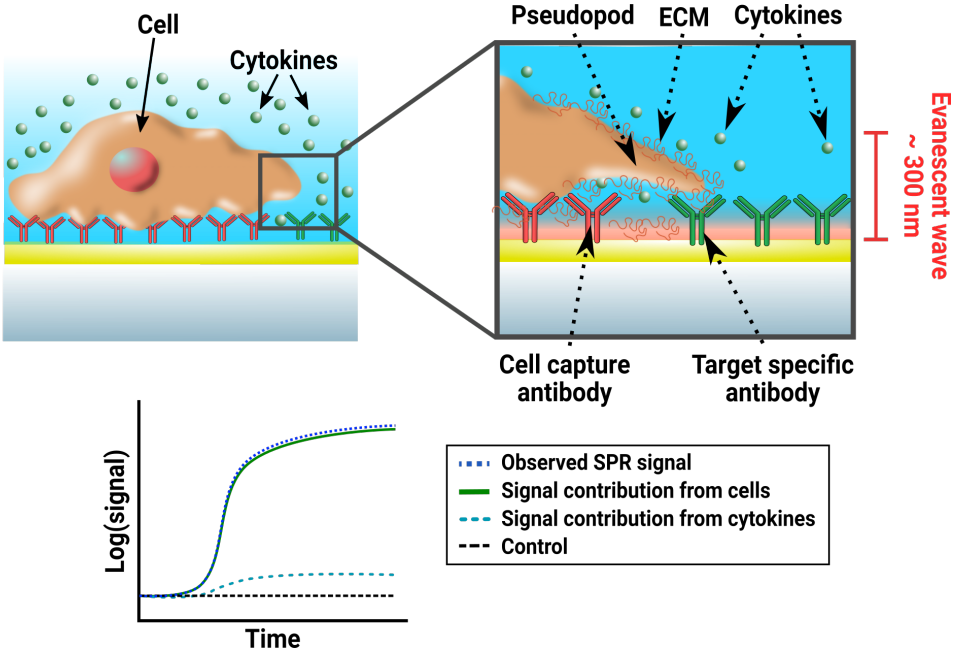

Figure 3.6 – Low signal-to-noise ratio during SPR monitoring of cells and their secretions. RI fluctuations caused by cells are several orders of magnitude higher than that those coming from their secretions, masking detection of the latter. In this case, the observed SPR signal of a secreting cell would be almost identical to that of a non-secreting cell as cytokine's contribution to the SPR is almost negligible.

To address this issue, our group, Chimie pour la Reconnaissance et l'Etude d'Assemblages

Biologists (CREAB), have developed several strategies to reduce the non-specific SPR signals caused by the cells. These strategies are based on applying different structures over the gold layer to separate the cells from sensing surface while still allowing diffusion of their secretions. Once outside the range of the evanescent field, cell-derive SPR signals would be suppressed while their secretions can still be captured by the probes grafted on the gold layer.

3.1.3 Modified SPR biochips for *in vitro* assays

In order to achieve simultaneous SPR detection of cells and their secretions, our team has evaluated different approaches such as the formation of hydrogels on the gold layer, generation of micropillars and the use of monolayers of microspheres (microbeads) over the sensing surface.

3.1.3.a Hydrogel-based systems:

Hydrogels were evaluated as a simple method to create an environment of controlled thickness over the gold surface, setting the cells outside the evanescent field. Due to their reticulated nature, small molecules (such as cytokines) can diffuse through the pores of the network reaching the sensing surface where they can be captured by specific probes (Figure 3.7).

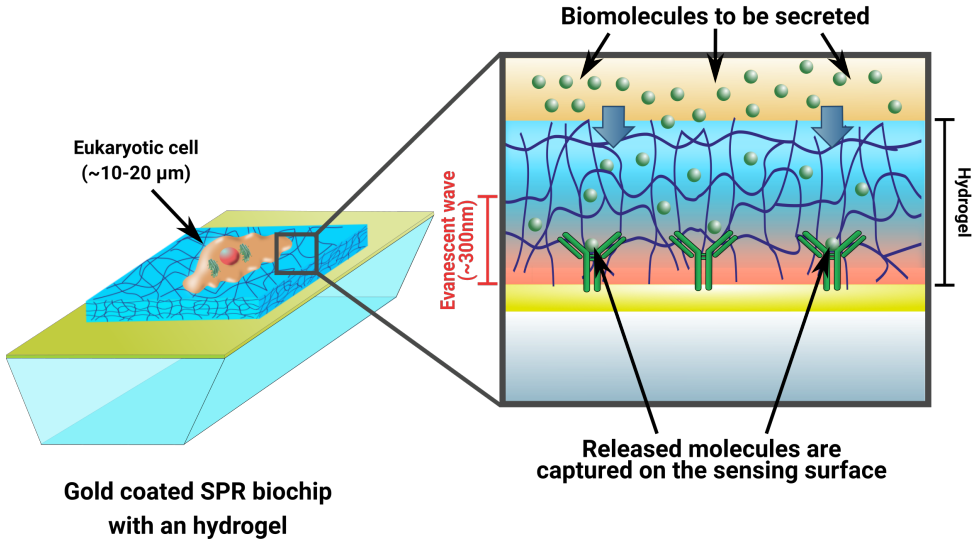

Figure 3.7 – Basic scheme of an hydrogel used as a spacer system for *in vitro* culture of cells over a SPR prisms.

Hydrogels based on sodium alginate, agarose 1% and poly(allylamine) were evaluated. Besides having a simple fabrication process, hydrogels provide an anti-fouling surface reducing non-specific attachment of proteins, the pore size can be easily regulated depending

on the crosslinking parameters and they provide an hydrated environment compatible with *in vitro* cell culture.

However, this strategy led to important levels of SPR-noise caused by the swelling of the hydrogels. Furthermore, localized functionalization of the hydrogel in order to capture specific subsets of a mixed cell population would prove to be challenging.

3.1.3.b Micropillars

Another approach was the production of micropillars by using Focused Ion Beam (FIB) lithography of a resin, SU-8, over silicon substrates. Similar to the hydrogel, the principle consisted in using the resin-based micropillars as spacers between the sensing zone and the cells (Figure 3.8). The surface was etched leaving pillars of 300 nm of height and ∼50 nm diameter with a pitch of 400 nm among them.

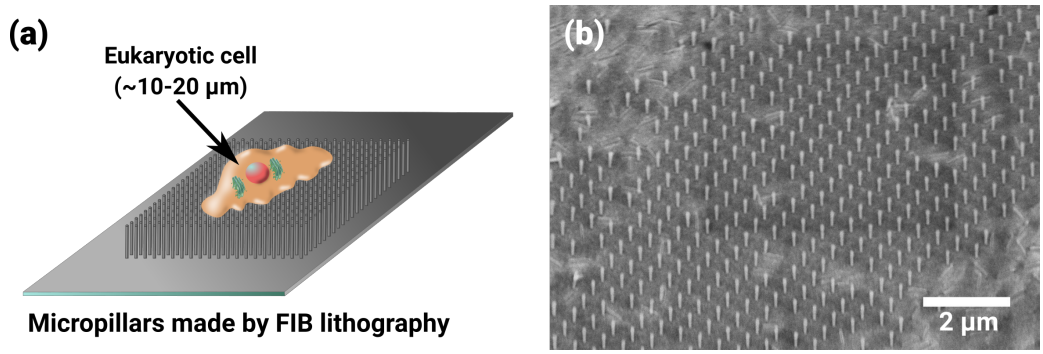

Figure 3.8 – Micropillars as a spacer system for *in vitro* culture of cells.

This strategy presented numerous liabilities that undermined their use on a sensing system. Among them, the main issues consisted on low mechanical resistance of the micropillars (which are easily damaged by cells or handling of the system) as well as in extremely long fabrication times. As the patterning time of millimetric areas is in the order of hours (1-10 $mm^2.h^{-1}$), the surface covered by the micropillars on each biochip was extremely small, limiting the utility of this approach.

3.2 Microbead-based microarrays for biosensing

3.2.1 Micrometric spheres as a spacing system

A highly promising alternative to micropillars and hydrogels consisted in the use of a monolayer of silica microspheres. Their spherical morphology is of particular interest as it minimizes the contact area with the gold surface and with neighboring beads. As they occupy a relatively small area of the sensing surface, large gold regions are available for functionalization with the probes of interest. Moreover, the microbeads are organized on

the surface in such a way that creates small "pore-like" structures among neighboring microbeads, allowing diffusion of molecules through the monolayer.

As an example, in the case of ⌀: 1 µm spheres, the microbeads constitute a spacing system that keeps the cells outside the evanescent field (typically in the range of a few hundreds of nanometers depending of the wavelength used). The "pores" in the resulting compact arrangement of the monolayer would have an estimated area of 0.04 µm^2, which should be small enough to avoid cell access to the gold layer and large enough to not hinder diffusion of small molecules to the sensing surface (Figure 3.9a).

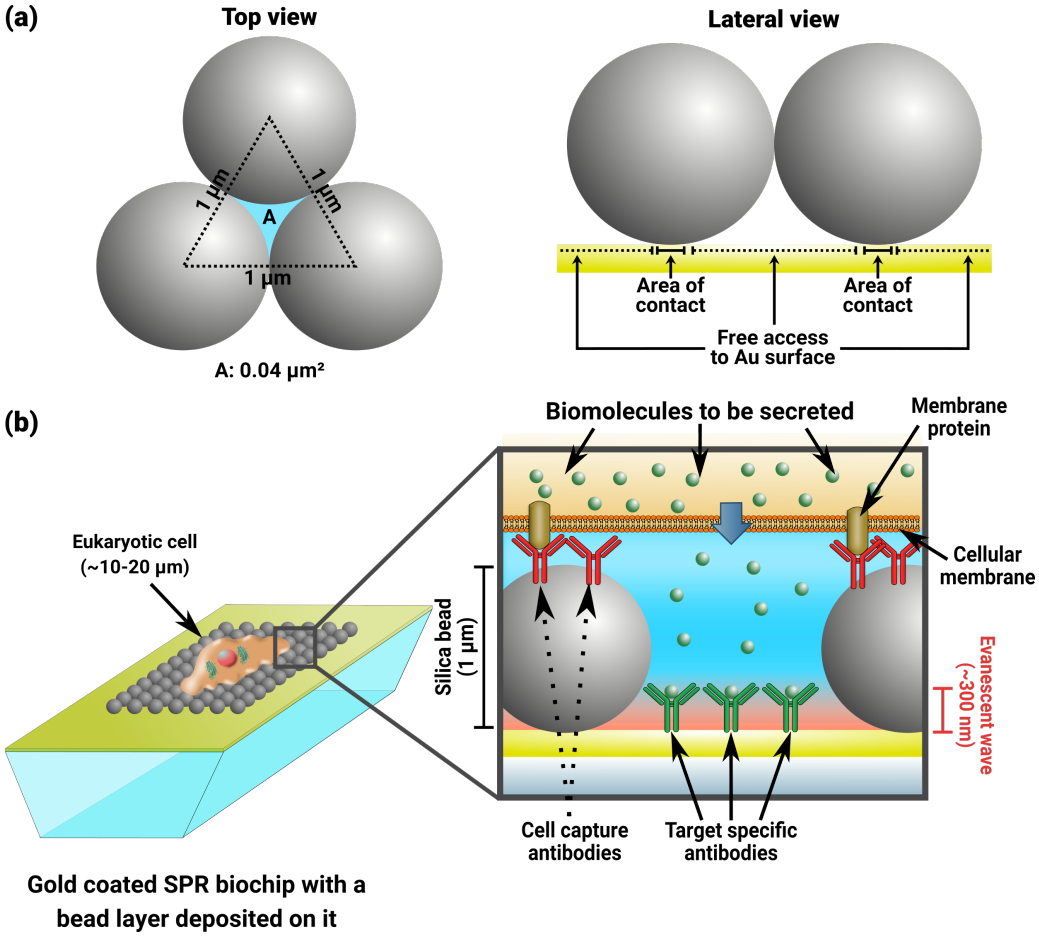

Figure 3.9 – Microbeads as a spacer system for *in vitro* culture of cells over a SPR biochip. (a) Pore-like structures formed due to the arrangement of the microbeads on the gold surface and (b) Schematic representation of the microbead-based SPR system under cell culture conditions.

Furthermore, silica microbeads are a relatively cheap and mass-produced material with well known chemical properties[84]. On their surface, the microbeads present silanol moieties that can be easily exploited for further chemical functionalization. Additionally, one of our partners, Olivier Dellea (LITEN-CEA Grenoble), has a strong expertise in the deposition of these materials over large surfaces and on a multitude of substrates. Therefore, in terms of fabrication times, the production of this type of microstructuring

of the surface was drastically faster than the micropillar approach.

Bead deposition over the different gold coated substrates was performed by our partner, Olivier Dellea, via the Boostream® process[85] (Figure 3.10). This method employs a liquid phase on a slope where the particles are dispensed, causing the hydrodynamic forces to arrange the particles as a film on the liquid. Then, the substrate of interest is set in contact with the monolayer of particles and withdraw from the liquid causing capillary bridges that transfer the particles into the substrate[85].

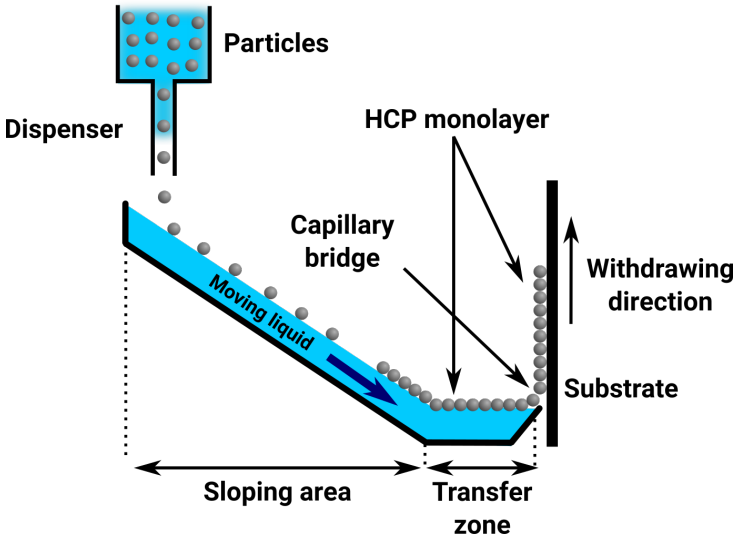

Figure 3.10 – Basic configuration of the Boostream® process. Uniform size particles form a Hexagonal Close-Packed (HCP) monolayer on the surface. Modified from Dellea et al. [85].

Preliminary assays performed by a previous post-doctoral researcher (Cyril Herrier) showed that cells could be deposited over the microbead monolayer as it can be seen in the SEM images (Figure 3.11).

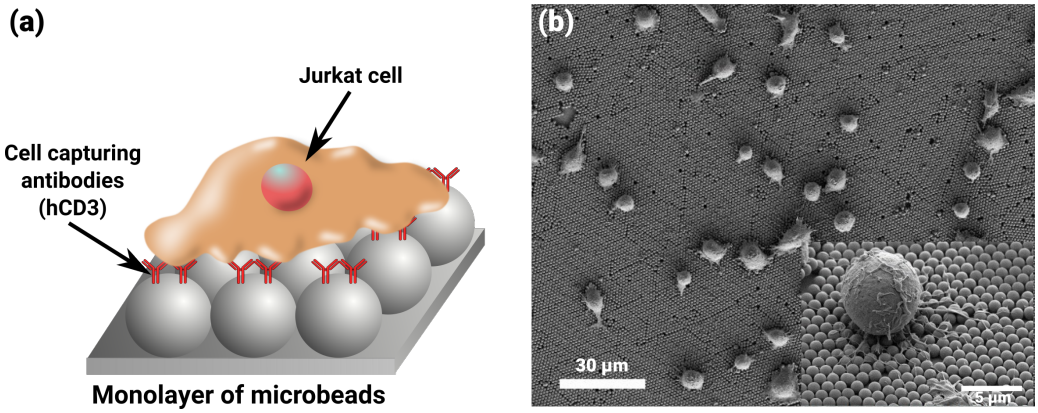

Figure 3.11 – Jurkat cells over microbeads covered surface. (a) Scheme illustrating capturing of cells over the monolayer of microspheres and (b) SEM images done by Cyril Herrier of Jurkat cells captured on the microbead surface.

3.2.2 Stability of silica microbead on the sensing device

3.2.2.a Mechanical stability of microbead-based system

However, deposition of the beads without chemical bonding to the surface limited their mechanical stability during handling and processing of the substrates. To reduce issues related to bead displacement/removal, Cyril Herrier developed a chemical method to ensure the stability of the monolayer. Briefly, the gold surfaces are plasma treated and then immersed in a solution of 3-mercapto-propyl-trimethoxy silane forming a SAM (further details can be found in Annex A.1.6).

The SAM left a surface with exposed alkoxy silane functionalities which are able to react with silanol moieties on the microbead's outer layer, forming a covalent bond after a dehydration stage (Figure 3.12).

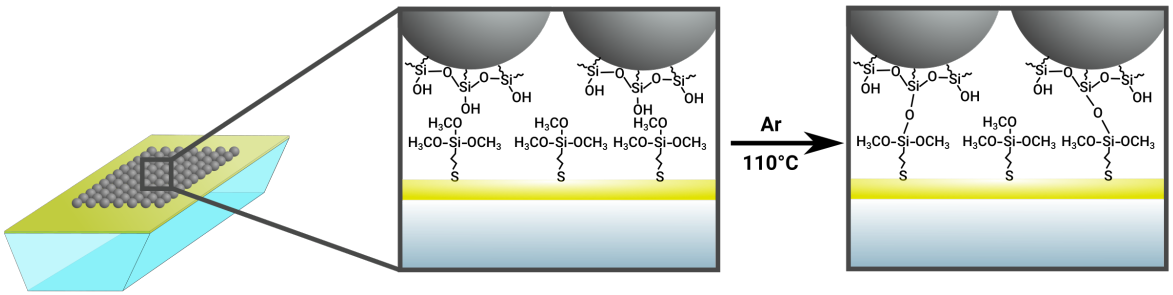

Figure 3.12 – Silane functionalization of gold surfaces for improving mechanical stability of the microbead layer.

3.2.2.b Chemical stability of silica microbeads in aqueous media

The chemical linkage to the gold surface improved the mechanical stability of the monolayers, thus facilitating their manipulation and operation as biosensors. However, soon after we faced a considerably direr problem related to the dissolution of the microbeads in biologically relevant media. Preliminary SPR assays, done by Cyril Herrier, showed a persistent negative drift while using PBS on the prisms modified with microbeads.

To evaluate the chemical stability of the system, we exposed the silica microbeads to common aqueous media used in biological experiments, namely PBS and a standard culture media for mammalian cells (Roswell Park Memorial Institute medium, RPMI 1640).

For the assays, the microbeads were deposited over of silicon substrate by the Boostream® process. We proceeded to disinfect the surface by rinsing them gently with ethanol 70% to reduce the risk of bacteria/yeast contamination (which would induce changes in the chemical composition of the medium). Afterwards, the substrates were dried under sterile conditions and immersed in either PBS or RPMI 1640 (supplemented with PeniStrepto and 10% Fetal Bovine Serum). To mimic standard cell culture conditions, all the sub-

strates were incubated at 37 ℃ in a 5% CO_2 atmosphere for varying time periods. . Finally, the samples were gently rinsed with distilled water and coated with platinum via Precise Etching Coating System (PECS) before their visualization on Scanning Electron Microscopy (SEM) (Figure 3.13).

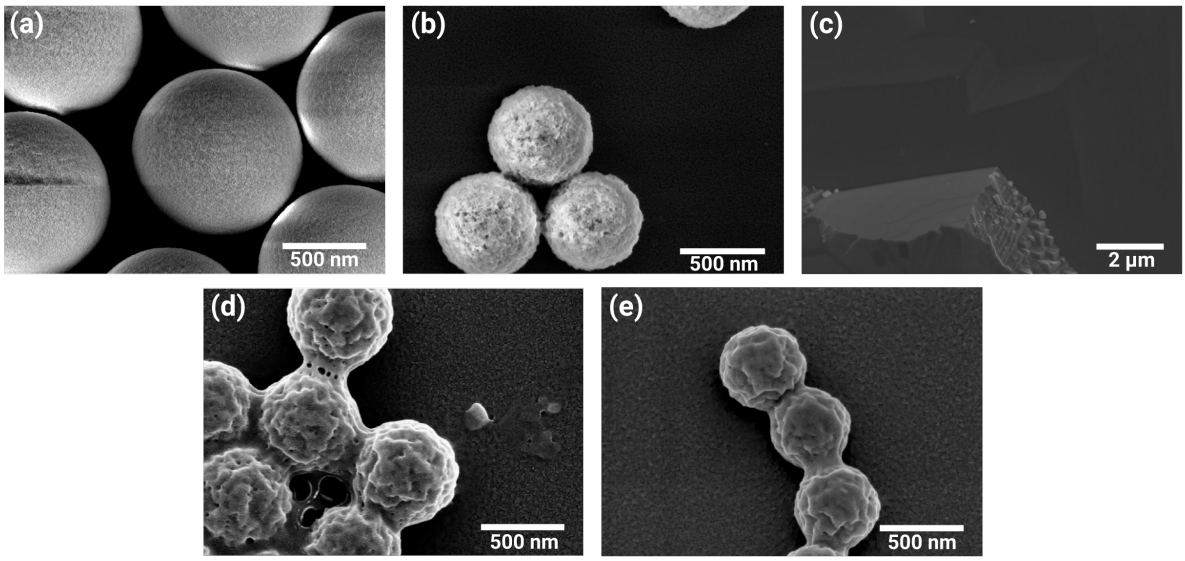

Figure 3.13 – Degradation of silica microbeads (1 µm diameter) after exposure to: (a) No aqueous media (control); (b) PBS for 24h; (c) PBS for 48h; (d) RPMI 1640 for 24h and (e) RPMI 1640 for 48h. In the case of image (c), no microbeads were observed (only the silicon substrate). To show that it was not a localized phenomenon, a larger field of view was used demonstrating the lack of microbeads in this area.

The size of the silica particles decreased by ∼40% after 24h of exposure to either solution while after 48h there was no observable beads on the sample immersed in PBS suggesting their complete dissolution. To understand these results, we took a look at the theory behind the degradation of silica-based structures. In aqueous solutions, the hydrolysis of silanes as well as the condensation of siloxane bonds are directly dependent of the pH[84,86]. Either acidic or basic conditions can catalyze the hydrolysis of Si-OR bonds but at near neutral pH (as in our conditions, pH buffered to 7.4) the hydrolysis rate(Equation 3.1) is at its lowest while condensation (Equation 3.2) is favored[86] and so, during our experimental conditions, the silica structures should not suffer any significant degradation.

$$HO^- + HO{-}Si(OR)_3 \rightleftharpoons H_2O + {-}O{-}Si(OR)_3 \tag{3.1}$$

$$Si(OR)_3{-}O^- + HO{-}Si(OR)_3 \rightleftharpoons Si(OR)_3{-}O{-}Si(OR)_3 + HO^- \tag{3.2}$$

When immersed in pure water, it has been reported[87] that mesoporous silica dissolves extremely slowly, at rates between 7 to 120 nm.year^{-1}. However, degradation of silica films in PBS at neutral pH has been previously observed[88]. PBS is composed of NaCl (137 mM), KCl (2.7 mM), Na_2HPO_4 (10 mM) and KH_2PO_4 (1.8 mM). Marshall and Warakomski[89] evaluated the solubility of amorphous silica in water in presence of 10 different salts

at varying concentrations, including NaCl and KCl. They observed a decrease in the solubility of the silica in presence of all the evaluated salts and thus, we could ascribe the dissolution of silica to the presence of phosphate ions.

Surprisingly, Bass et al.[88] suggest in their work that the silica dissolution was caused by the pH (which was neutral in this case) and not the presence of phosphates at relatively high concentrations. They support this claim by presenting experiments using a phosphate-free buffer (1 M tris-(hydroxy-methyl)-amino-methane, known as Tris buffer) at pH 7.3 obtaining similar results to those of PBS. Nevertheless, they omitted an extremely important fact, that is, the effect of amino-containing compounds such as Tris. Due to the basicity of amino functionalities (pK_a ~10)[90], these moieties are able to remove a proton from water molecules[84]. Such event promotes the formation of Zwitterion-like molecules on the silica surface enabling a nucleophilic attack from water molecules to the silicon atom[84,91].

Furthermore, Neofotistou and Demadis[92] suggest that amino-rich compounds can stabilize monomeric silica units and slow silicic acid polycondensation, promoting further hydrolysis[91]. Considering this mechanism, silica dissolution in aqueous media can be promoted by weak bases at neutral pH, which is the case for Tris and also for phosphate ions (which act as weak bases since with pK_a of 12.67 for HPO_4^{2-} and 7.21 for $H_2PO_4^{-}$)[90] as described in Figure 3.14.

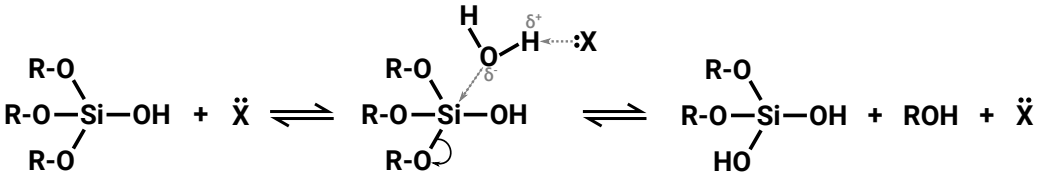

Figure 3.14 – Proposed general base-catalyzed mechanism for silica hydrolysis where Ẍ is a base. Modified from Abou-El-Sherbini et al.[84].

He et al.[93] described the degradation behavior of mesoporous silica in presence of Simulated Body Fluid (SBF), which is a salt solution usually buffered by Tris. In their work, they proposed a three stage degradation procedure consisting in:

— A fast degradation stage during the first 2 h of exposure caused by "strong ionic corrosion" of the SBF. Although, rather than the "corrosion" process suggested by them, silica is dissolved by the effect of phosphate ions and Tris buffer as described in Figure 3.14;

— A constant degradation phase at a much slower rate due to the deposition of calcium/magnesium ions adsorbed on the inner surface of the pore channels of the beads (as first seen by Marshall and Warakomski[89]). Interaction between these cations allows the formation of insoluble calcium/magnesium silicates which effectively passivate the surface slowing down the dissolution of the silica;

— A day-scale degradation due to incomplete coverage of the calcium/magnesium silicate layer and a constant dissolution via diffusion of silicon species across the passivating layer.

Coherently with their results, when we exposed the microbeads to RPMI (which is a cell culture media rich in amino-containing compounds but also in calcium and magnesium salts) we noticed the appearance of interconnecting structures between the degraded beads (Figure 3.13d-e). Such structures can be ascribed to the formation of insoluble silicate layer that passivated the surface slowing down the hydrolysis process.

However, when the beads were exposed to PBS (which do not contain neither calcium nor magnesium salts), no passivating layer is formed. A direct consequence of this was that the beads were stuck in the first stage of fast degradation. In fact, as the siloxane network is hydrolyzed, the outer layer becomes more porous (Figure 3.13b) leading to an increase in the surface area and thus, of the hydrolysis rate until complete dissolution (Figure 3.13c).

To prevent/reduce silica degradation in biological media, several strategies could be applied: (a) functionalization of the microbeads with PEG or organosilanes which would reduce the amount of free silanol groups and thus the hydrolysis rate[94,95]; (b) formation of a passivating layer by immersion of the beads on concentrated solutions of calcium/magnesium salts[89,96,97]; (c) selection of another material (polystyrene, poly-methylmethacrylate, alginate, etc) or (d) thermal treatment of the beads reducing pore size and amount of free silanol groups by their condensation into siloxanes[98,99].

In the case of the first two strategies, such extensive surface modification could hinder our ability to couple biomolecules of interest on the surface of the beads. While a whole new approach for microbead attachment and functionalization would have to be envisioned if another material was selected (added to potential immunoreactivity of the materials[100–103] limiting its *in vitro* applications).

Due to the limitations of the other strategies, thermal treatment of the microbeads was selected as the most promising stabilization method. This approach is based in the fact that calcination of silica promotes the formation of siloxanes (Equation 3.3) via condensation of the exposed silanol groups. Furthermore, this process leads to a reduction of the pore size, and therefore the surface area, limiting the hydrolysis rates[96].

$$\mathrm{Si(OR)_3{-}OH + HO{-}Si(OR)_3 \xrightarrow{\Delta} Si(OR)_3{-}O{-}Si(OR)_3 + H_2O} \tag{3.3}$$

Since hydrolysis reactions are inhibited in pure silica due to the high connectivity of the glass network[96], we expected that a reduction in the silanol groups, as well as in the total surface area, would drastically decrease the degradation rate. With this goal in mind, we evaluated two different thermal treatment procedures for thermal stabilization of the microbeads: classical sintering and a Fluidized Bed Reactor (FBR).

FBR employs a porous system to support the solid substrates inside a chamber[104]. A fluid (either gas or liquid) is then passed through this support system. By regulating the flow rate, fluidization of the substrates (which refers to a state when the force of the flow balances out the weight of the substrate) can be achieved. This allows the generation of a uniform temperature gradients allowing an homogeneous treatment of the silica microbeads (Figure 3.15).

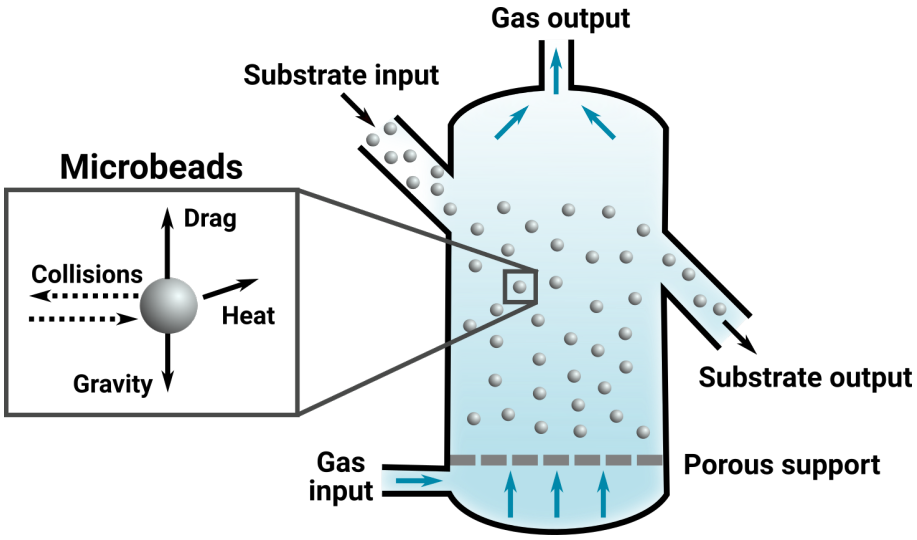

Figure 3.15 – Scheme of a fluidized bed reactor. Illustration based on a image with a Creative Commons License in Wikimedia Commons.

Sintering of silica microbeads has been widely studied[99,105,106]. Furthermore, this process has also been used for improving the optical properties of silica microspheres[98]. On the other hand, the use of a FBR with silica microspheres has been reported for a variety of purposes[107–109] but so far not for reducing their hydrolysis rate in aqueous media.

3.2.2.c Evaluation of thermally stabilized microbeads

In collaboration with our partner, we performed both thermal treatments as well as the bead deposition over silicon substrates. For FBR-approach, the beads were treated for 2 h at 800 ℃ before their deposition. In the case of sintering, the microspheres were first deposited on the substrate and then calcinated in an oven for 1 h at 800 ℃. Both treatments were carried out under an atmosphere of normal (environmental) air.

The samples were then tested for their stability, as previously described (page 75), by their incubation into conic tubes with either sterile PBS or culture media. Based on SEM visualization, for both thermal treatments, the microbeads showed no sign of degradation even after 48 h of immersion in culture media (as shown in Figure 3.16).

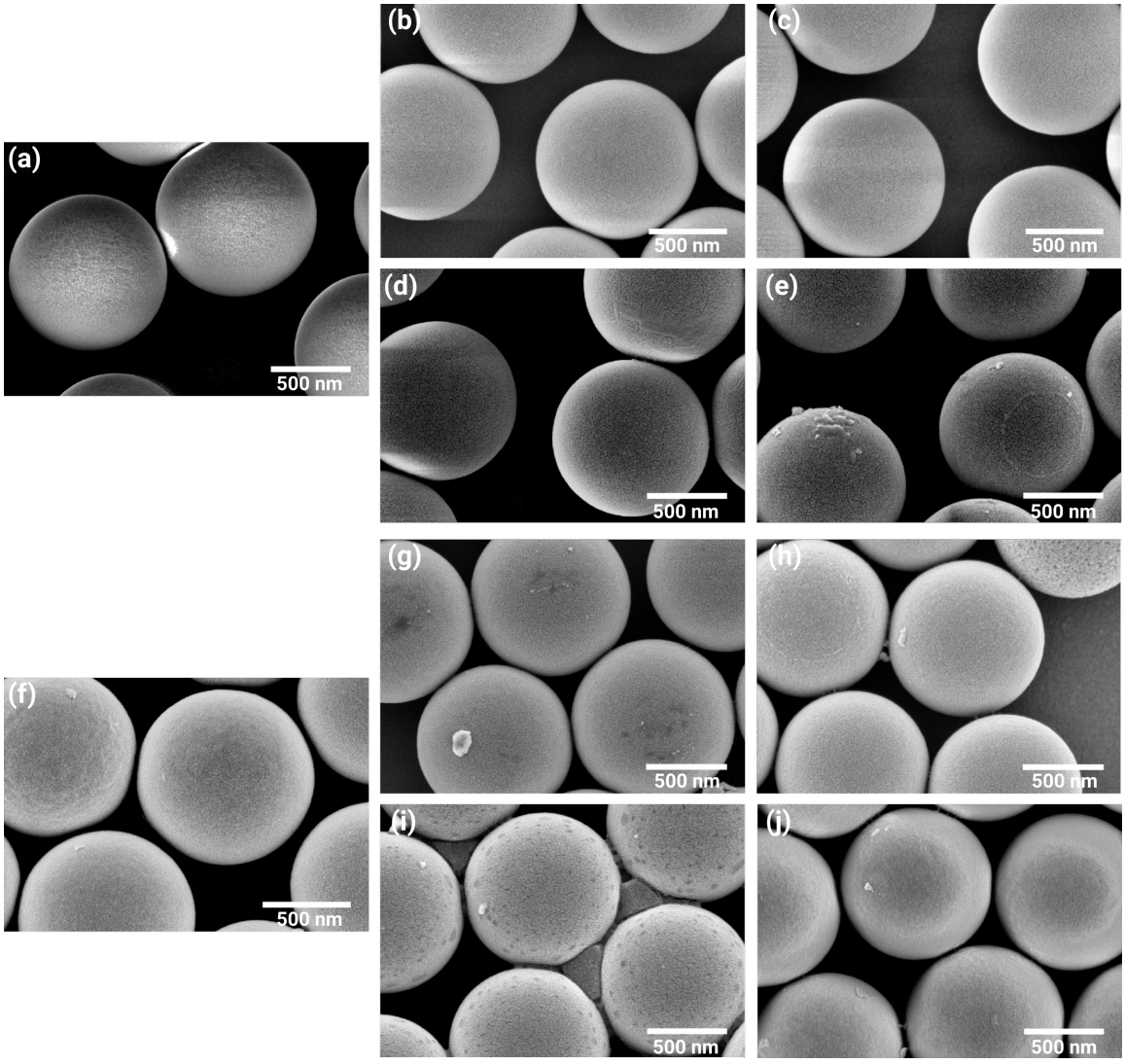

Figure 3.16 – SEM images of thermally treated 1 µm silica beads after exposure to: (a,f) No aqueous media (control); (b,g) 24h in PBS; (c,h) 48h in PBS; (d,i) 24h in RPMI and (e,j) 48h in RPMI. (a-e) Correspond to sintered beads while (f-j) to those treated by FBR.

Based on the SEM images, both thermal stabilization methods seemed suitable for the stabilization of the microbeads. However, we selected FBR since direct sintering of the microbeads on the prisms would negatively impact the gold layer. Then, a new batch of FBR-treated beads was deposited over Horiba gold-coated prisms and evaluated as before. For our liquid phase, we employed RPMI 1640 as it is a multipurpose and widely used medium for the culture of numerous cell types. In this case, the medium was supplemented with 10% Fetal Bovine Serum, PeniStrepto and HEPES. The latter was added as to regulate the pH of the medium as it was not possible to control the CO_2 concentration in our SPR system. For RPMI (as well as many other culture media), the pH strongly depends of the amount of CO_2 in the atmosphere as it contains a sodium bicarbonate ($NaHCO_3$) buffer (as illustrated in Figure 3.17.

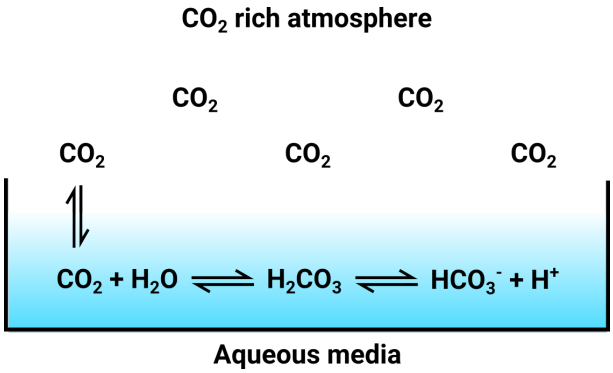

Figure 3.17 – Graphical representation of pH regulation by a bicarbonate buffer in aqueous media. CO_2 dissolves freely reacting with water to form carbonic acid while sodium bicarbonate dissociates into sodium and bicarbonate ions. By increasing the concentration of bicarbonate ions, the equilibrium is driven to the left avoiding acidification of the media[110].

Strikingly, SEM imaging showed heterogeneous degradation of the microbeads in the prism (Figure 3.18). Around a third of all the microbeads showed signs of hydrolysis while others were seemingly stable. It is possible that during the FBR treatment of the new batch of microbeads, the material experienced non-uniform thermal gradients leading to a mixture of stable with unstable microspheres.

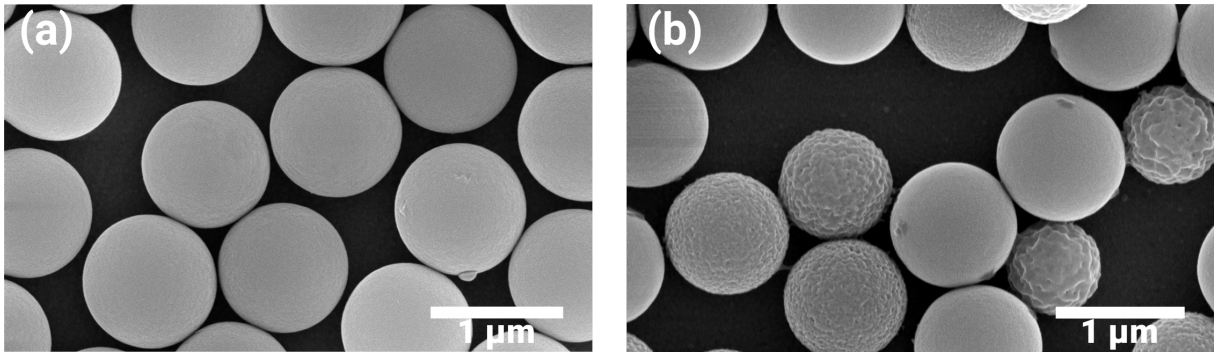

Figure 3.18 – SEM images of FBR treated microbeads exposed to culture media. (a) Sample used as a control (not exposed to culture media) and (b) sample immersed in culture media for 36h.

We no longer had access to the FBR to prepare a new batch of samples. Therefore, our partner prepared another set of microbeads but stabilized via sintering under different parameters (12 h at 800 ℃) and then deposited over gold prisms. The microbeads were further functionalized with MPTS which provided a platform for biomolecule coupling as it will be explain in Section 3.2.4.

SPR monitoring of these microbeads was performed in presence of supplemented RPMI 1640 at 37 ℃. This time, no degradation was observed contrary to a similar tests performed on microbeads stabilized by FBR (Figure 3.19). In the case of the sintered microbeads, there was a positive drift in the order of 3% of reflectivity over 50 h of incubation

probably due to protein attachment on the surfaces.

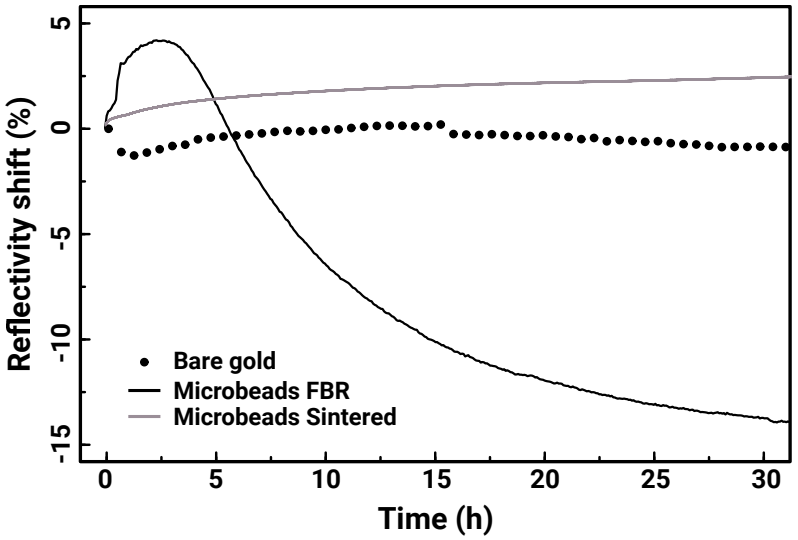

Figure 3.19 – SPR monitoring of stabilized microbeads by FBR or sintering (12 h at 800℃ + MPTS treatment), exposed to culture media RPMI 1640.

From our evaluations, we can conclude that sintering for 12 h at 800 ℃ was the most efficient treatment to avoid silica degradation. By increasing the reticulation in the silica network (due to condensation of silanols into siloxanes), the microbeads became resistant to hydrolysis even after 50 h of incubation in culture media.

3.2.3 Optical properties of microbead-based system

Once we obtained a stable system, we characterized the optical properties of the microbead layer using the hybrid SPRi set-up described in the previous chapter (Chapter 2, Figure 2.5). For microbeads presenting a monodisperse diameter, deposition via the Boostream® process resulted in the formation of crystalline domains on the gold surfaces generating an iridescence phenomenon as observed in Figure 3.20a. This light scattering effect caused problems related to signal heterogeneity over the surface during SPR imaging. However, after the thermal treatment, the microbeads experienced small changes in their surface morphology and size disrupting the iridescence effect but also giving a more homogeneous SPR signal (Figure 3.20b).

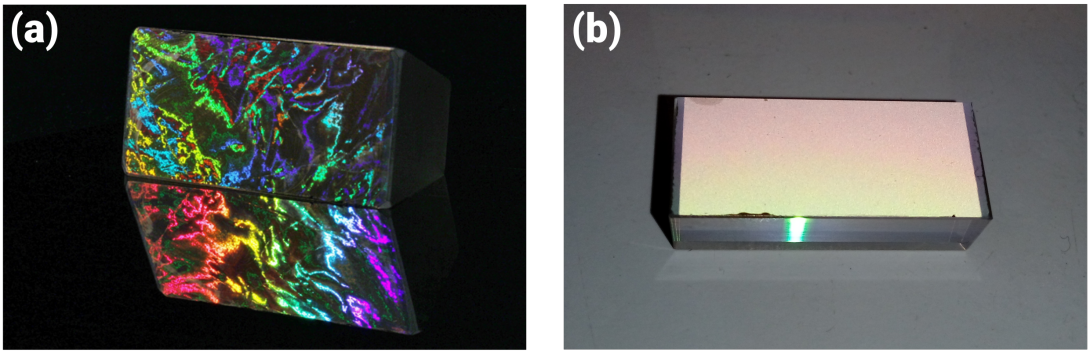

Figure 3.20 – Silica microspheres (⌀: 1 µm) deposited over Horiba gold coated prisms illuminated with non-collimated white light. (a) Non-thermal treated microbeads showing an iridescence effect on the surface (image taken by Cyril Herrier) and (b) thermal treated microbeads.

Mechanical removal of the microbead layer in some areas allowed us to obtain a reference surface ("bare gold"). We used a microfluidic device to regulate the input of culture media and then, we made reflectivity measurements employing a 735 nm LED as SPR light source. The surface with microbeads exhibited two valleys in the signal instead of the typical single valley corresponding to the SPR phenomena (Figure 3.21).

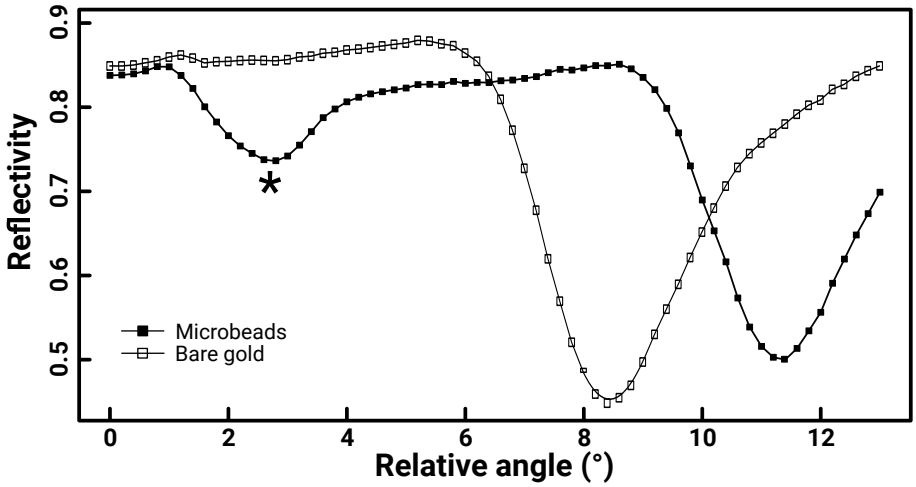

Figure 3.21 – Plasmon curves of surfaces with and without microbeads in culture media (RPMI 1640). The SPR angle on gold (surface without microbeads) was set as 0°. In case of the WGM phenomena, the valley associated to this optical effect are marked with an asterisk (*).

This new valley, represented by an asterisk (*) in Figure 3.21, might correspond to the generation of a resonance mode on the silica microspheres, namely Whispering Gallery Mode (WGM). WGM is a process exploited by optical microresonators and it is traditionally produced by using prisms to couple light into microspheres[111–114]. Moreover, generation of WGM has been described as a result of surface plasmons[115]. On silica microspheres, this phenomena presents a modal field intensity distribution concentrated

near the dielectric-air interface[116] (as illustrated in Figure 3.22).

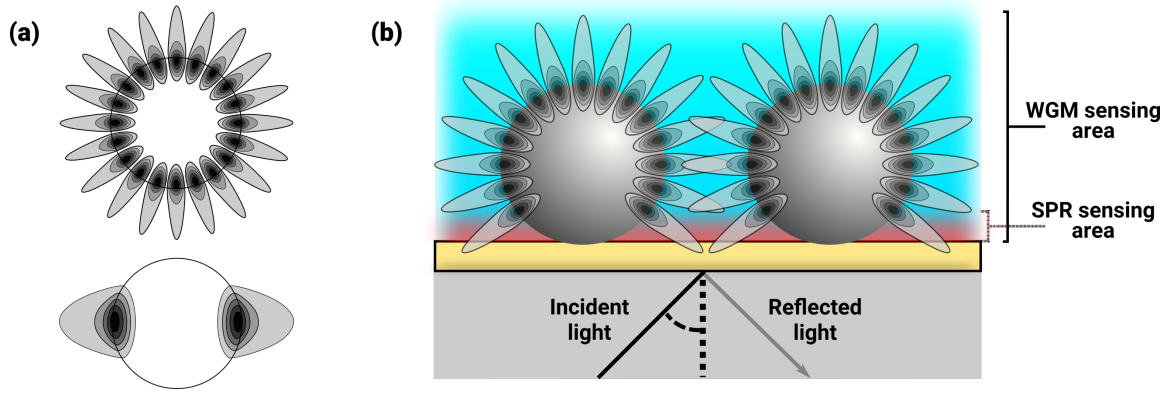

Figure 3.22 – Scheme illustrating the WGM in silica microspheres. (a) Near-field intensity portraits of WGM on silica microspheres. Redrawn from Benson et al.[111]; (b) Scheme of WGM and SPR sensing on the surface of the prism.

WGM phenomena is able to probe the surroundings of the microbeads (>1 µm from the metal) while SPR can be used for monitoring the surface of the metal (∼ 200 nm from the metal layer). Therefore, the use of these two phenomena operating at different modes can be applied for simultaneous detection of cells and their secretions.

In our hybrid SPRi set-up, it is already possible to perform dual monitoring of cells (via conventional microscopy) while performing SPR for detecting their secretions. However, cell sensing by WGM offers new benefits as it shows only the cells in direct contact with the surface (which can be difficult to distinguish via optical microscopy during the first stages of cell adhesion/capture). Furthermore, it might be able to detect some cell secretions imperceptible by conventional microscopy (*e.g.* extracellular matrix in adherent cells) and could also help future miniaturization of the system. This last aspect is relevant as optical microscopy is used to correlate the position of the cells with the SPR responses and it requires addition of a set of lenses, mirrors and another CDD camera whereas WGM could provide similar information by just adding an additional diode to the system.

In its simplest form, dual WMG/SPR monitoring requires the use of two light sources which, under our experimental setup, would need to fulfill two conditions: (a) the incident angles of both sources must be positioned in the sensitive range for each phenomena and (b) the light reflected on the prism from both light sources have to be inside the field of view of the detector device (CCD camera). Both conditions could be easily achieved if the desired incident angles for each phenomena overlap or are relatively close to each other (in our setup that would be a difference <10° for example) for a specific pair of wavelengths (Figure 3.23).

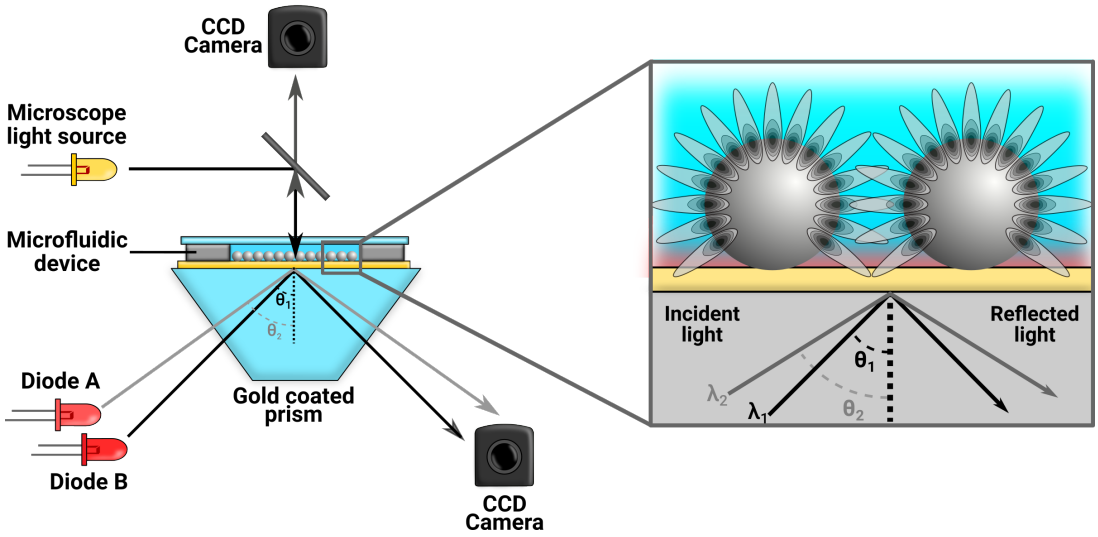

Figure 3.23 – Theoretical scheme of an optical setup for dual WMG/SPR monitoring. Two diodes of "compatible wavelengths" are used for exciting the WGM and the SPR phenomena simultaneously. The incidence angles for both diodes are <10° apart from each other and set to the optimal sensitivity for each phenomena. The scheme also shows a simplified diagram of the elements used during optical microscopy. On the right, a zoom on the sensing region shows excitation of surface plasmons in the gold layer and generation of the whispering gallery mode on the microbeads.

In order to select a pair of "compatible wavelengths", we performed reflectivity measurements at distinct angles of incidence for several wavelengths (Figure 3.24). While doing so we observed some interesting facts: (a) by increasing the wavelength the distance between the WGM and SPR angles decreased and (b) while the SPR angle was very dependent of the wavelength, the WGM angle was considerably less affected by it (the shift in angle per nanometer was one order of magnitude inferior for WGM than for SPR). Based on such observations, a dual device should include a 850 nm light source for SPR imaging while one inferior or equal to 625 nm for WGM.

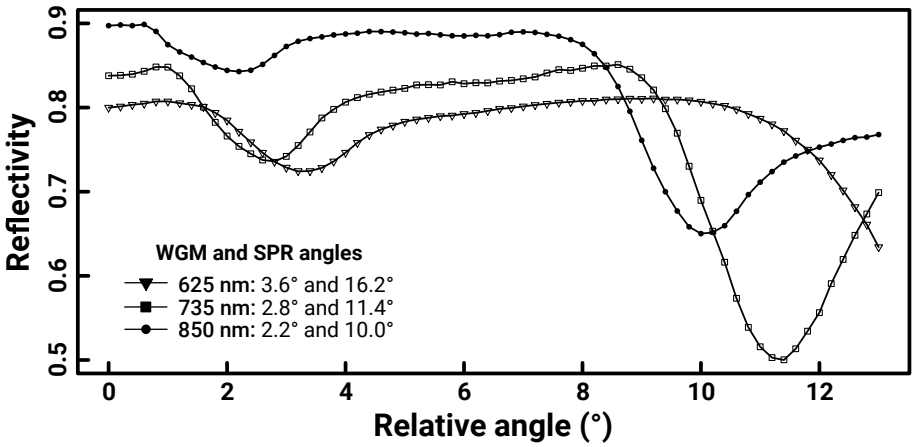

Figure 3.24 – Angle interrogation of the microstructured prisms at different wavelengths in RPMI 1640.

Afterwards, we evaluated the efficiency of the microbead monolayer to supress the cell-derived SPR response of individual cells as well as the possibility of detecting those cells using WGM. On new microbead-modified prisms, a microfluidic device with thermoregulation (set at 25 ℃) allowed flowing different media into the system. After addition of culture media (supplemented RPMI 1640), SPR and WGM images were taken at different wavelengths (625 nm, 735 nm and 850 nm). Then, adherent cells (pancreatic rat insulinoma cell line RIN-m, described in detail on subsubsection 3.2.5.a) were added at a concentration of 1.6x10^5 cells.mL^{-1} and incubated for 24 h in culture media. At the end of the incubation period, new images were recorded at the same angles and wavelengths employed at the beginning of the assay (Figure 3.25).

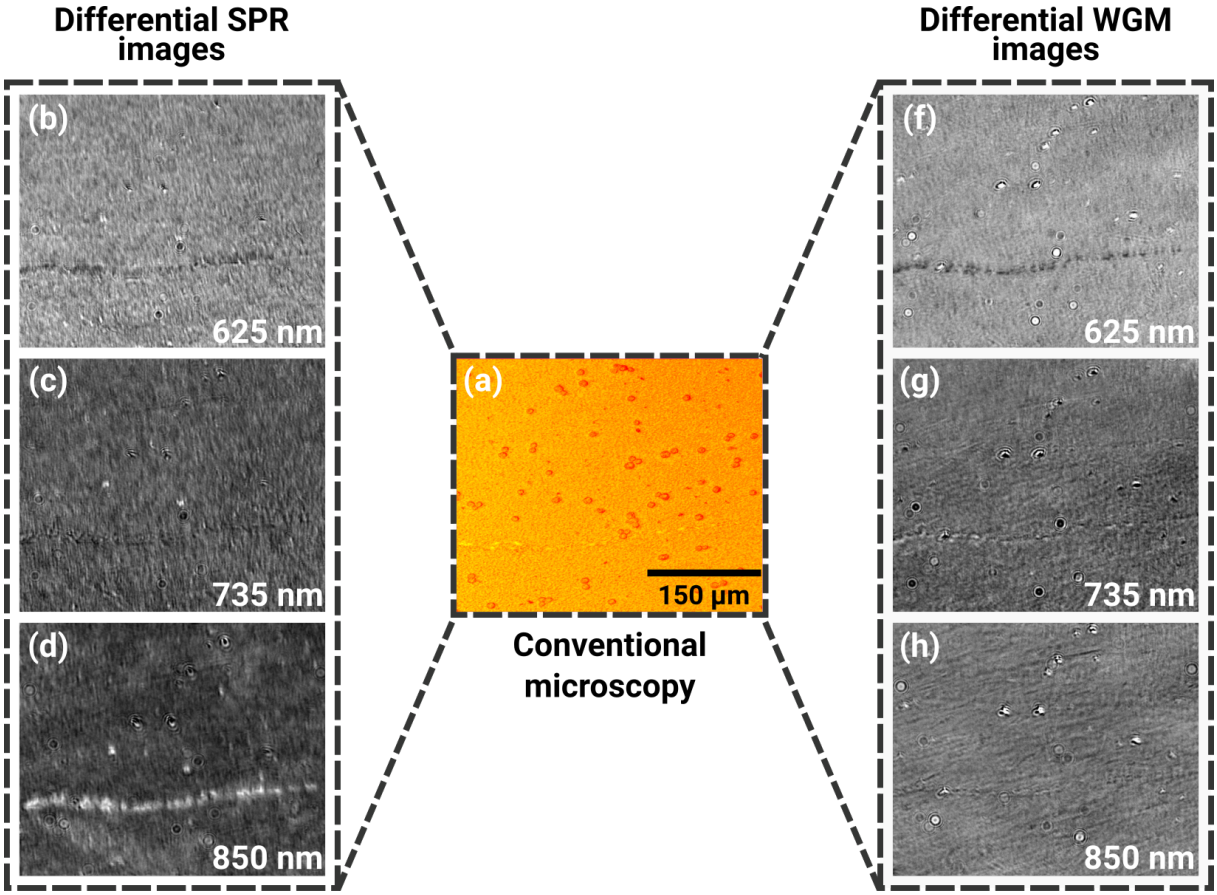

Figure 3.25 – Visualization of RIN-m cells after 24h of incubation by SPR, WGM and conventional microscopy. (a) Image taken by conventional microscopy; (b-d) SPR differential images at different wavelengths; (f-h) WGM differential images at different wavelengths. ImageJ[117,118] was used for the analysis of the images.

The pictures captured by conventional optical microscopy were used as a template for the alignment of the SPR and WGM images. Afterwards, a differential image for each phenomena at different wavelengths was generated. The alignment of all the images allowed to estimate the corresponding position of the cells (seen by optical microscopy) on the SPR and WGM differential images. These results indicate that the microbead system was effectively separating the cells from the sensing region as mostly no cell-induced SPR

response was observed. On the other hand, the WGM differential images showed signals in the position corresponding to cells suggesting that WGM can be effectively used for cell detection on our setup.

3.2.4 Orthogonal chemistry functionalization of surfaces

Afterwards, the next step consisted on the development of orthogonal functionalization methods allowing the capture of the target cells on the microbeads and detection of cell secretions on the gold surface. With this goal in mind, we employed two different strategies: (a) Electropolymerization to functionalize the gold surface with bioreceptors specific to cell secretions and (b) Thiol-maleimide reaction for the indirect functionalization of the silica microspheres.

3.2.4.a Functionalization of gold surfaces by electropolymerization

In this case, the biomolecules of interest (with available primary amines) are conjugated with pyrrole via N-hydroxysuccinimide (NHS)/amino reaction (procedure described in Annex A.1.5). After their purification, the pyrrole-coupled biomolecules are mixed with free pyrrole in electropolymerization buffer (solution with a high content of electrolytes). Deposition of the mixture is done by a micropipette whose movement is regulated by a microcontroller[119]. By using a platinum wire inside the micropipette's tip, and making electrical contact with the gold surface, it is possible to apply electric potential difference in a localized way. This generates co-polymerization of the pyrrole-conjugated molecules with the free pyrrole attaching them on defined positions at the gold surface (Figure 3.26) via the mechanism described in Chapter 1 section 1.4.2.

It is important to highlight that the gold surface was already functionalized with MPTS via thiol-gold chemistry (page 74). However, this does not affect the formation of a polypyrrole film as the S-Au bonds, in the spotted area, are cleaved via a reductive voltammetric desorption[120] during the electropolymerization process.

When applying a difference in the electric potential, the desorption of the thiols as well as the polymerization of the pyrrole moieties occur at a much faster rate than the re-adsorption of the thiolated compounds on the gold surface[120]. Therefore, the MPTS-SAM is effectively removed while grafting pyrrole-containing biomolecules. Additionally, the microbead layer in the electropolymerized zones does not show evident perturbations to its mechanical stability. This fact may be explained by a stabilizing effect caused by lateral forces with neighboring beads and/or some level of fixation in the polypyrrole film.

Considering that our research team has extensive experience in electropolymerization of pyrrole over gold surfaces[121–124], we focused our effort on evaluating the possibility to perform a two step reaction (silanol-silane and thiol-maleimide reactions) for grafting proteins over silica surfaces.

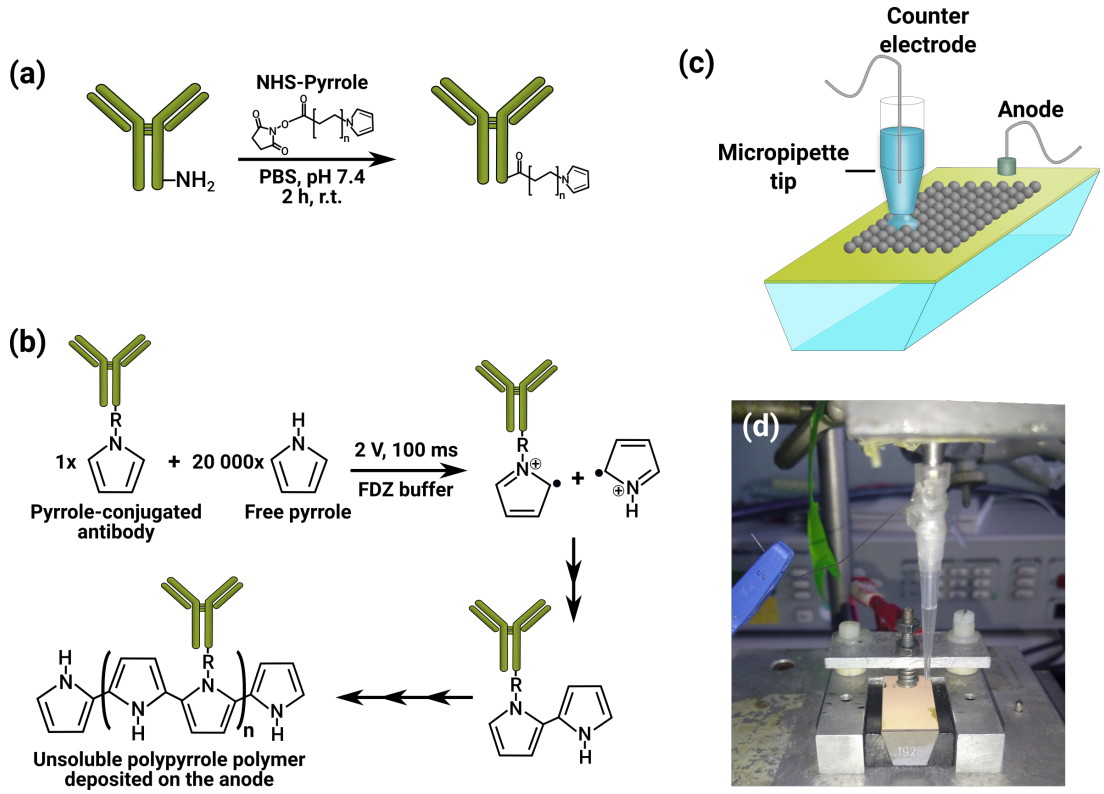

Figure 3.26 – Functionalization of gold surface by electropolymerization. (a) Antibodies are coupled with pyrrole via a NHS-amino reaction; (b) A mixture of 20 molar equivalents of free-pyrrole per pyrrole-conjugated antibody is prepared. A difference in potential induces polymerization of the free-pyrrole molecules with the pyrrole containing antibodies, creating a thin film on the gold layer; (c) Scheme depicting the electropolymerization system and (d) Picture of the actual electropolymerization system.

3.2.4.b Two-step functionalization of silica surfaces via silane-silanol and thiol-maleimide reactions

Biofunctionalization on silica surfaces was performed via a two-step procedure. This method consisted on the initial formation of a SAM over the silica by the heterobifunctional compound MPTS. In this case, the silica surface is exposed overnight at room temperature to a 30 mM MPTS solution prepared in toluene. The SAM is produced by a condensation reaction between the silanol (HO-Si- on the bead surface) and silane (R-O-Si- in MPTS) moieties as described in Equation 3.2 (in this case, the equilibrium is driven towards the formation of siloxanes (-Si-O-Si-) as the inverse reaction is much slower[86] and hydrolysis does not occur due to the lack of water molecules in the media). The formation of a MPTS-SAM via formation of siloxanes leaves a surface rich with sulfhydryl functionalities (-SH).

Separately, maleimide moieties are introduced into the biomolecules of interest via a NHS/amino reaction (Chapter 1 section 1.5.2.a). Finally, grafting of the biomolecules on the MPTS-functionalized silica surfaces occurs thanks to an alkylation reaction be-

tween the maleimide (on the biomolecules) and thiol (on the surface) functionalities (as described in Chapter 1 section 1.5.2.c). Similar to the electropolymerization procedure, we can employ a semi-automatic arraying method for a controlled deposition of solution containing the maleimide-coupled biomolecules over the surface of interest (Figure 3.27).

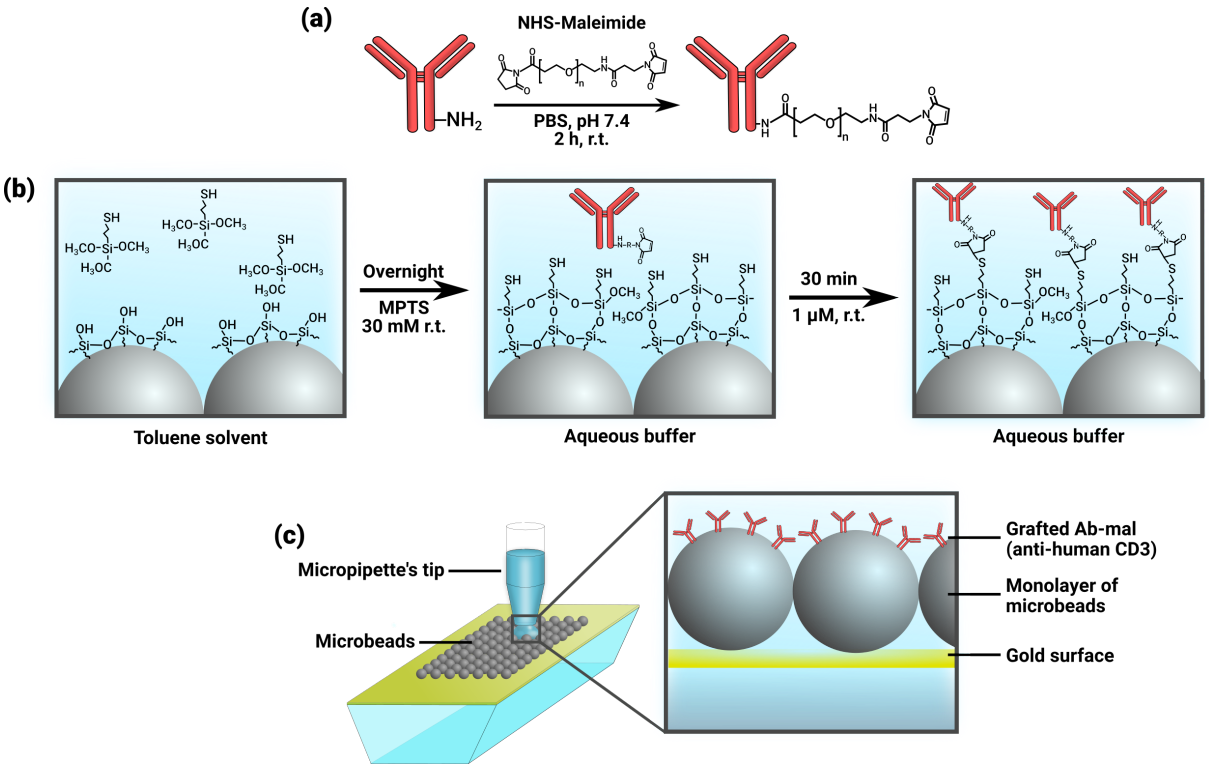

Figure 3.27 – Functionalization of silica surface by silane-silanol and thiol-maleimide reactions. (a) Maleimide moieties are introduced into antibodies via NHS-amino chemistry; (b) A MPTS-based SAM is created on the surface of the microbeads by silane-silanol interaction, then the modified antibodies are grafted on the thiol-exposed surface via a thiol-maleimide reaction which forms a thioether bond; (c) Localized deposition using a microcontroller system of droplets containing the maleimide-conjugated antibodies.

To assess this method, we produced maleimide-coupled antibodies (Ab-Mal) by reacting anti-human CD3 (mouse origin) with NHS-maleimide (biocoupling procedures are detailed in Annex A.1.5). Ab-mal were then spotted at 1 µM over a glass slide previously functionalized with MPTS (immersion overnight in a 30 mM MPTS/toluene solution). The slide was incubated for 30 min at r.t. in a humid chamber (relative humidity ~85%) before rinsing with PBS. Then, free thiol moieties were blocked by immersion on a maleimidohexanoic acid solution (5 mM for 15 min) and rinsed with PBS-T (PBS + Tween20® 0.02%).

Finally, fluorescence imaging was performed after exposure to anti-mouse IgG antibodies coupled with biotin (13 nM for 15 min) followed by SAPE 10% (v/v). Fluorescence spots were observed only in the regions exposed to maleimide-conjugated antibodies (as seen in Figure 3.28), validating the functionalization approach.

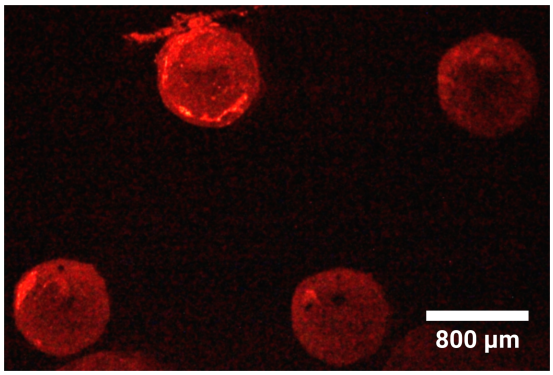

Figure 3.28 – Fluorescence control of the two-step biofunctionalization over a glass slide. Fluorescent spots correspond to grafted anti-human CD3 mouse-produced antibodies visualized by biotinylated anti-mouse IgG + SAPE.

3.2.4.c Dual functionalization of microstructured prisms

We performed dual functionalization in two stages. First, pyrrole-conjugated antibodies (Rabbit IgG-pyr) were spotted via electropolymerization on the gold surface. Then, as before, we used Ab-mal (anti-human CD3 from mice) for the grafting on the microbeads as illustrated in Figure 3.29 (experimental procedure is described in Annex A.1.6).

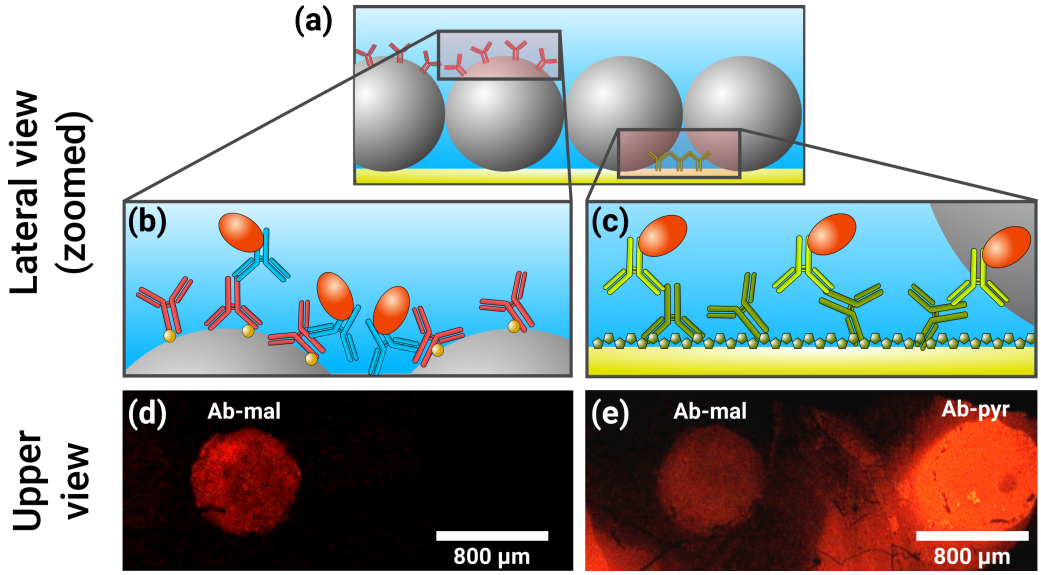

Figure 3.29 – Fluorescence evaluation of orthogonal functionalization strategies. (a) Scheme showing localized functionalization of the microbeads and the gold surface; (b) On the of silica microbeads, Ab-mal (maleimide conjugated anti-human CD3 antibodies, produced in mice) were immobilized via thiol-maleimide chemistry. Biotinylated anti-mouse IgG and SAPE were used for their visualization; (c) At the gold surface, Ab-pyr (pyrrolated IgG antibodies, produced in rabbit) were arrayed via electropolymerization. visualization was done by biotinylated anti-rabbit IgG and SAPE; (d) Fluorescence revelation of Ab-mal over the microstructured surface and (e) Fluorescence revelation of both, Ab-mal and Ab-pyr, in the same microstructured prism.

Evaluation of the functionalization on the microbeads was performed by covering the surface with biotinylated anti-mouse IgG followed by SAPE 10% (v/v). Fluorescense was observed only in the spots exposed to the maleimide-coupled antibodies (Figure 3.29d). Afterwards, the effective electropolymerization of pyrrole containing antibodies on the gold surface was evaluated by adding biotinylated anti-Rabbit IgG and SAPE. Strong fluorescence was observed on the areas where electropolymerization was performed (Figure 3.29e), while spots from the previous step could also be seen confirming specific protein grafting on both surfaces.

For our next step we evaluated the functionality of the grafted proteins. On a microbead-modified prism, spots of Ab-mal, either mouse produced anti-human CD3 or anti-human CD8, were arrayed on the microbeads. Then we grafted rabbit IgG by electropolymerization on the gold surface. As in Chapter 2, Peripheral Blood Mononuclear Cells (PBMCs) were used for evaluating cell capturing.

PBMCs are constituted by 70% to 90% lymphocytes, of which around 70-85 % are $CD3^+$ and roughly the 33.3% of $CD3^+$ cells are $CD8^+$ [125]. This would translate in considerable less cells attached to anti-$CD8^+$ spots on the biochip compared to anti-$CD3^+$. PBMCs were concentrated to 3×10^6 cells.mL^{-1} in sterile PBS. During 1 h, each 15 min 100 µL of the cell solution was added to the biochip and left at room temperature in a humid chamber. Afterwards, gently washes with PBS were performed until non-specific adsorption of cells was no longer observed (Figure 3.30).

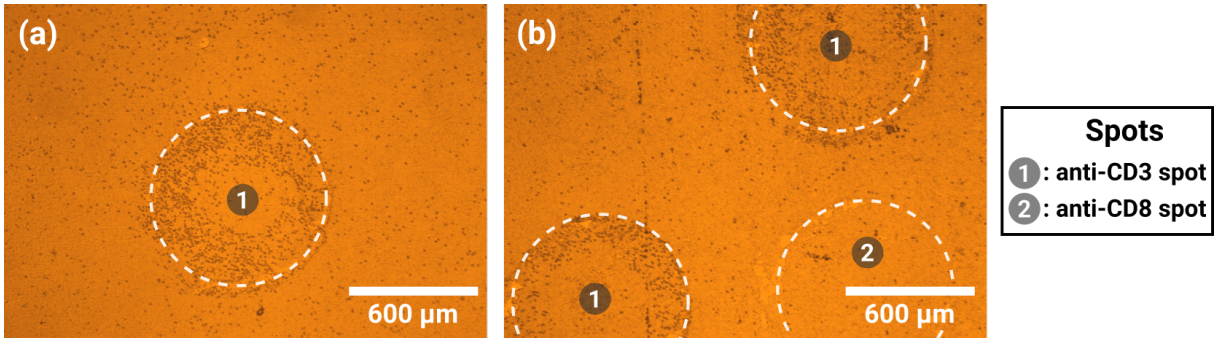

Figure 3.30 – Optical microscopy images of $CD3^+$ cells captured on the surface of the biochip. Images taken with a 10x objective. (a) Cells captured in a single anti-human CD3 spot and (b) Cells captured in two anti-human CD3 spots while no cells are observed on the anti-human CD8 spot.

Only CD3 spots showed signs of specific cell capture which was not unexpected as the amount of CD8+ cells is considerably inferior in normal PBMC populations. Interestingly, we observed that the cells, rather than being uniformly distributed on each feature, were predominantly located at the borders of each spot (Figure 3.30).

Considering that the spotting solution for the Ab-mal did not contained glycerol, this peculiarity could be caused by a gradual drying of the deposited droplets. These ring patterns are commonly observed when drops of colloidal suspensions or solutions of non-volatile compounds evaporate and are commonly referred as "coffee stains" [126–129]. Eral et al. [128] described that this phenomenon is caused when the three-phase contact line (the

boundary of the droplet at the solid, vapor and liquid phases) does not recedes during evaporation but gets pinned at defects on the surface (Figure 3.31).

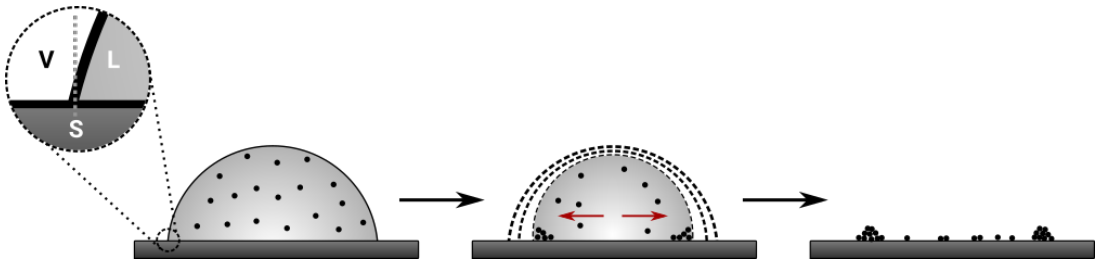

Figure 3.31 – Schematic of the drop evaporation process. Image modified from Eral et al.[128].

As the drop tries to maintain its shape while having a pinned contact line, an outward flow within the droplet is generated[128]. This flow transports more solute at the contact line, increasing its concentration at the margins while decreasing it in the center[128]. This phenomenon has been reported during microarraying of biochips[130,131]. In our case, the higher concentrations of Ab-mal at the droplet border increased the frequency of interactions between the maleimide moieties and the available thiols, leading to a radial gradient in the amount of immobilized antibodies. Optimization for the spotting of Ab-mal should be performed by evaluating the cell capture uniformity on features made at varying antibody and glycerol concentrations.

Besides evaluating the functionality of the grafted anti-human CD3, we performed fluorescence revelation of the features made by the two spotting methods. Firstly, detection of the electropolymerized rabbit IgG (Ab-pyr) was performed by exposing the surface to biotinylated anti-rabbit IgG (a 13 nM solution for 15 min) and then SAPE 10% (v/v) for 20 min (Figure 3.32). After rinsing the surface, fluorescence imaging confirmed the presence of rabbit IgG on the gold surface (Figure 3.32d). However, the spots presented an atypical morphology (much larger than expected and not clearly defined). Such irregularities could be ascribed to long contact times (in the order of ≥ 3 seconds) of the spotting solution with the microstructured surface before applying a voltage. Due to capillarity, the liquid can expand among the microbeads incurring in variations of the spot size. Such issue can be easily overcome by applying a voltage as soon as the drop enters in contact with the gold surface.

Finally, fluorescence revelation of Ab-mal (via biotinylated anti-mouse IgG + SAPE 10% under similar conditions at those previously employed) confirmed the presence of the grafted antibodies. Fluorescence results added to cell capture experiments showed the effectiveness of our two-step method for silica biofunctionalization as the proteins could be immobilized while retaining their biological functionality.

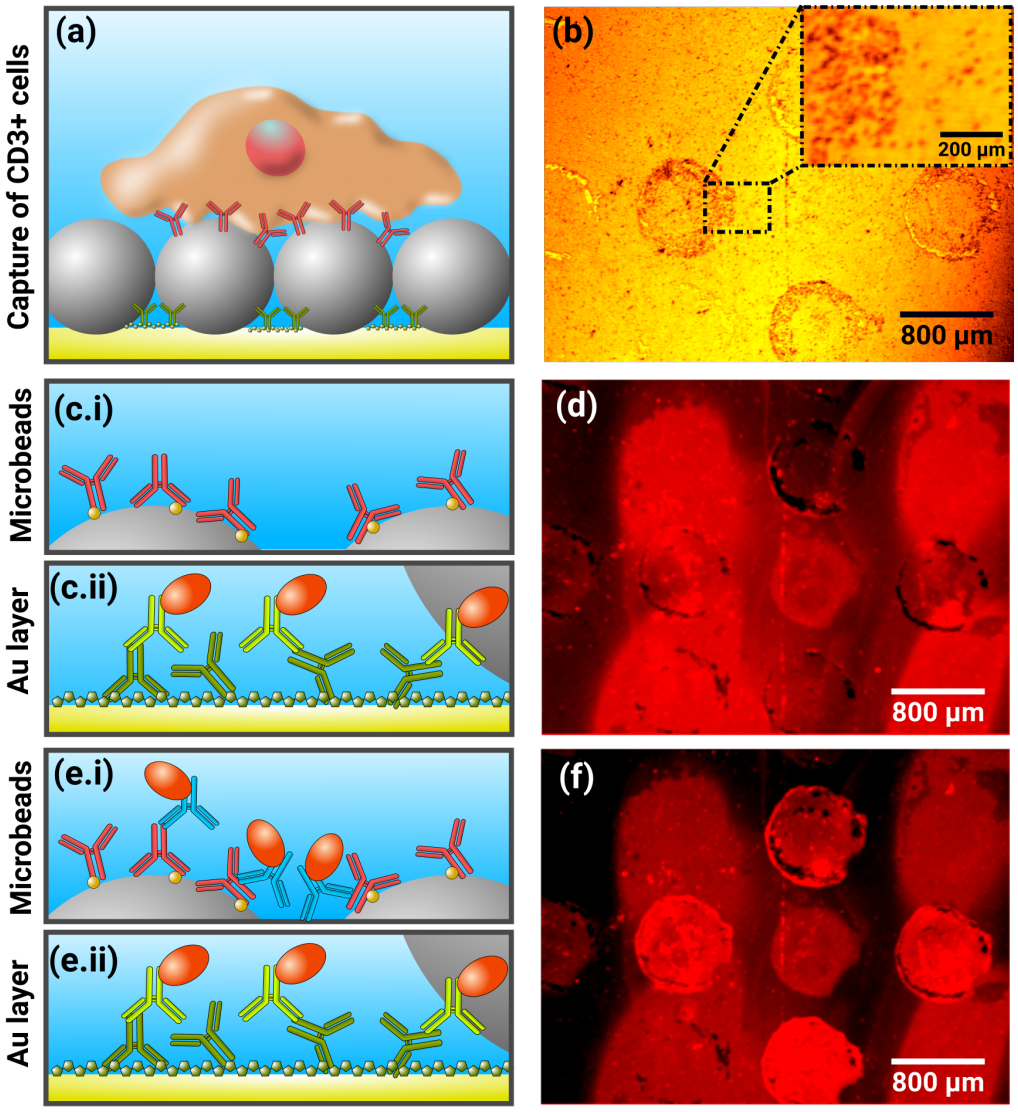

Figure 3.32 – Validation of orthogonal functionalization over silica and gold surfaces. First, PBMCs were captured by the anti-human CD3 antibodies grafted on the microbead surface as seen in the (a) schematic illustration and (b) optical microscopy image. Afterwards, confirmation of the grafting via electropolymerization of rabbit IgG was performed by exposing the surface to anti-rabbit IgG and SAPE 10%. In this case, the spots corresponding to (c.i) functionalization on the microbeads did not show specific fluorescence while the ((c.ii, d) electropolymerized regions were fluorescent. Finally, the surface was exposed to anti-mouse IgG and SAPE allowing detection of the (e.i, f) Ab-mal antibodies on the silica surfaces.

3.2.4.d SPR monitoring of cells on the microstructured biochip

After fluorescent validation of the grafting methods, we evaluated our microstructured biochip using SPR. For the assays we used the hybrid SPR setup described earlier in Chapter 2 with the same microfluidic chamber. Tests consisted in manually injecting a

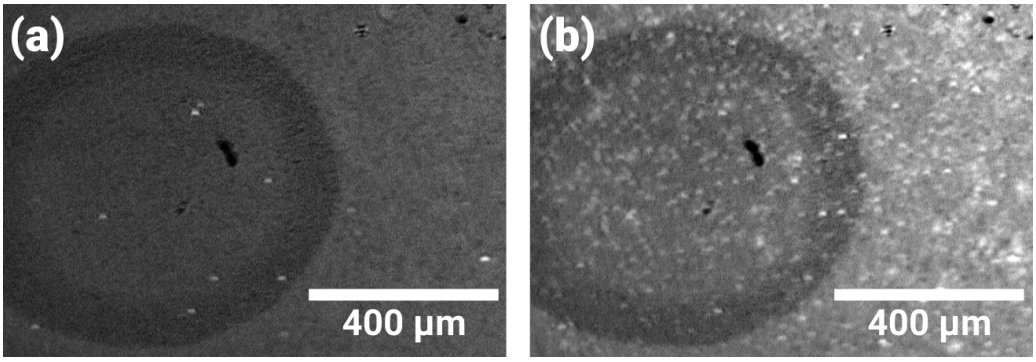

Figure 3.33 – SPRi differential images of the microstructured biochip showing one spot functionalized with Ab-mal (anti-human CD3) after (a) 10 min and (b) 90 min of cell sedimentation. Bright spots correspond to PBMCs sedimented on the surface.

solution of PMBCs ($\sim 3\times10^6$cells.mL^{-1} in PBS) into the microfluidic chamber, then the system was left in static conditions to allow cell sedimentation while constant monitoring was done via SPR at room temperature (625 nm as a SPR light source).

Contrary to the results obtained in the previous test with non-functionalized beads and using a different type of cells, we observed clear SPR responses derived from cell attachment on the surface after 10 minutes of sedimentation (Figure 3.33). This difference might be caused by some destabilizing effect of the functionalization/washing steps over the microbead monolayer or caused by difference behavior of the evaluated cells. PBMCs can exhibit some levels of phagocytic activity[132] which could disrupt the monolayer of microspheres leading to shifts in the SPR signal.

For further analysis, we selected ∼100 regions of interest (ROIs) corresponding to zones with and without cells. Monitoring of these zones showed that the microbeads not functionalized with Ab-mal (just passivated with maleimidohexanoic acid) were more susceptible to bulk and localized changes in the refractive index (Figure 3.34). This was not surprising as the interrogation angle selected was optimized for sensitivity of the non-functionalized beads (although all the ROIs shared almost identically plasmonic profiles). The bulk shift in the refractive index, caused by flowing the cell-containing solution, induced a generalized increase of ∼4% in the reflectivity. Using this as a baseline, we can observe that the attachment of the cells on the microbead layer induced an average (n=50) reflectivity shift of just ∼2%. This was very encouraging as previous tests using conventional Horiba prisms (without microstructuration) showed that the SPR response caused by the attachment of the cells directly on the gold was in the order of +10-15% reflectivity shift. This result proves a >5-7 fold reduction in the "unwanted" SPR response caused by the cells which was the main objective of the microstructuration of the biochip.

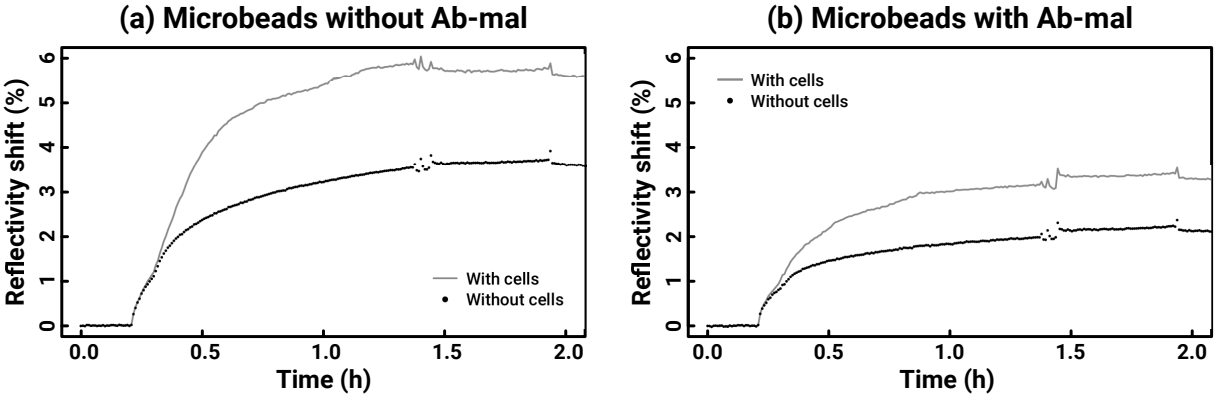

Figure 3.34 – Average cell-derived (N=50) SPR response of the microstructured system on (a) zones without Ab-mal coupling and (b) on Ab-mal spots.

On the other hand, an interesting fact is that we did not observed specific capture of $CD3^+$ cells. Once the cells sedimented on the surface it was not possible to effectively remove non-specifically attached cells by just manually flowing buffer into the system, this resulted in a relatively homogeneous distribution of cells over the whole surface of the biochip. Such issue might be related to the geometry of the fluidic sytem, the liquid chamber consisted in an oval reservoir of $\sim$ 3 mm height x 2 cm length x 0.8 cm width. As the liquid input/output had a 0.75 mm inner diameter, there would be a relatively large (possibly a few dozen micrometers in height) "static layer" on the surface. This "static layer" is not directly affected by perturbations in the flow rate on the "flowing layer" of the liquid and so, once the cells passed the threshold from one layer to the other, modifications in the flow rate would not succeed to remove the attached cells.

3.2.4.e SPR detection of biomolecules on the microstructured biochip

Successful SPR detection of molecules released in the media was observed when either anti-rat or anti-rabbit IgG were added on the microfluidics (Figure 3.35), reaching similar levels to the expected signal of non-modified prisms (bare gold surfaces).

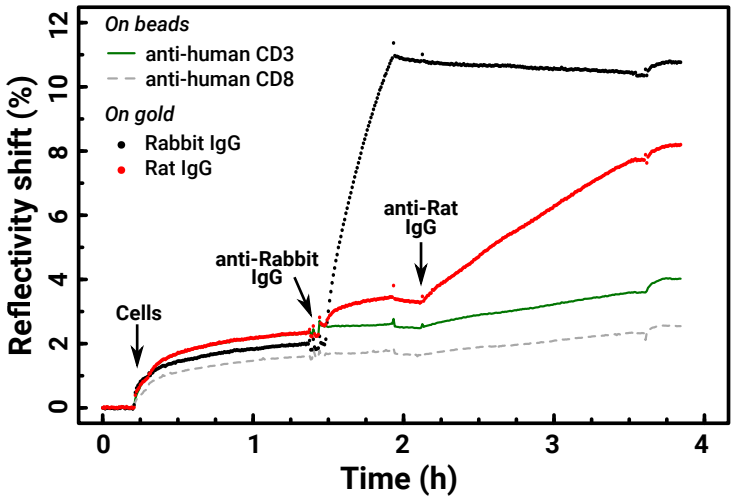

Figure 3.35 – Average SPR response of the multiple grafted features during the assay. Arrows indicate the injection of different solutions containing either cells, rabbit IgG or rat IgG to the liquid chamber of the system.

3.2.5 Cellular models for *in vitro* assays

Once we assessed the feasibility of performing SPR biomolecule detection on the microstructured biochip and have an estimation of the cell-derived noise, we characterized the secretion levels of several cellular models for their potential SPR analysis of their secretions.

3.2.5.a Description of the cellular models to be used

During our assays, we employed different types of cells which can be classified into two main subgroups, namely adherent and non-adherent cells. Adherent cells, or anchorage dependent cells, are those who require a attachment to a substrate for their growth, proliferation and general survival[133]. Whereas, non-adherent cells (anchorage independent) can perform all their functions in suspension[133]. Most cell types are normally anchorage dependent (*e.g.* hepatocytes, endo- and epithelial cells, neurons, etc) while hematopoietic, sexual cells and some tumoral cells are examples of non-adherent cells[133].

Another relevant classification of the cellular models is based on their immediate origin. This creates two subgroups known as: primary cells and cell lines. The concept of "primary cells" refers to cells extracted from the donor organism and that have not being previously cultured *in vitro*[133]. They are more sensitive to environmental conditions, requiring specific culture media, and have a limited life span (which greatly varies among cell types as well as from donor to donor)[133]. Once a primary culture is subcultured (or passaged), it becomes a "cell line"[133].

Cell lines can be subgrouped into finite or continuous lines, which differ in the maximum amount of population doublings that the cell line can sustain before senescence (which refers to cellular aging/deterioration)[133]. For finite cell lines, this number oscillates be-

tween 20 to 80 doublings while continuous lines, which have become immortal, can escape from this senescence control[133]. The possibility of subculturing and characterizing specific cell lines is highly appealing, nevertheless, serial passage induces important genotypic and phenotypic variations which leads to poor representation of the behavior of primary cells[134].

We characterized the secretion profile of different types of cells (either primary cells or cell lines, adherent or non-adherent). This in order to determine the feasibility of using them as cellular models for *in vitro* detection of their secretions by our microstructured SPR biochip. With this aim, we evaluated:

RIN-m cell line: Rat insulinoma-derived cell line (RIN-m ATCC®CRL-2057™) was used as a model for adherent cells. Normal cell function of adherent cells is linked to their attachment on a surface via secretion of extracellular matrix proteins (ECM proteins). Previously, we evaluated the cell-induced SPR response using non-adherent cells. However, the secretion of ECM proteins added to potential mobility on the surface makes this cell line an interesting model for evaluating the microstructured system. Furthermore, this cell line constitutively secretes insulin[135] which could be used as a standard analyte on our SPR system.

PBMCs: Human Peripheral Blood Mononuclear Cells, known as PBMCs, are primary cells isolated from human peripheral blood samples by a density gradient centrifugation using Ficoll-Histopaque. PBMCs include lymphocytes, monocytes and dendritic cells[125]. Typically, they are constituted by 1-2% dendritic cells, 10-20% monocytes and between 70-90% lymphocytes[125]. From which, 5-10% are B-cells, 5-20% Natural Killer cells (NK cells) and 70-85% T-cells (which express the co-receptor CD3 in their membranes). $CD3^+$ cells can be further divided into two subsets: roughly a 66.6% of $CD4^+$ and $\sim$33.3% $CD8^+$ cells[125]. Contrary to RIN-m cells, PBMCs lack anchorage dependence, reducing the risks to alter the microstructures on the surface of our biochip. Furthermore, secretion of different cytokines (e.g. IL-2, IFN-γ and TNF-α) can be chemically stimulated by supplementing their culture media with: plant lectins, LipoPolySaccharides (LPS), Phorbol 12-Myristate 13-Acetate (PMA)/Ionomycin, Purified Protein Derivative of Tuberculin (PPD) and/or anti-CD3, anti-CD28 antibodies[136].

THP-1 cell line: Derived from a human leukemic monocyte cell line (ATCC®TIB-202™), these cells are another non-adherent model that we evaluated. THP-1 cells do not present any surface nor cytoplasmatic immunoglobulins (making their capture on the biochip challenging) and can be differentiated into macrophages by stimulation with PMA[137,138]. Further stimulation (with LPS for example) promotes the secretion of multiple cytokines and chemokines including IL-6, TNF-α and Macrophage Inflammatory Proteins (MIP)[138,139].

Table 3.1 – Summary of the main characteristics displayed by the evaluated cellular models.

Name	Type	Adherent	Specie	Secretions	Requires activation
RIN-m	Cell line	Yes	Rat	Insulin and somastostatin	No
PBMC	Primary	No	Human	Multiple cytokines including: IFN-γ, IL (from 1 to 10), TNF-α, etc.	Yes. Typically PMA/Ionomycin
THP-1	Cell line	No	Human	Multiple cytokines including: TNF-α, IFN-γ, MIP-1α, MIP-1β, etc.	Yes. Differentiation with PMA Activation with LPS + R848

3.2.5.b Determination of secretion profiles for each cell-line

RIN-m cell line: Evaluation of insulin secretion by RIN-m cells was based on the method designed by Müller[140]. A more detailed procedure is described in Annex A.1.8. Briefly, cells were seeded into multiwell plates, until their attachment. Then, the metabolic activity of the cells was reset by incubating them in a glucose-free buffer for 30 min. Then, the supernatants are replaced by a buffer with high glucose concentration (25 mM) and then, the cells are incubated at 37 ℃ 5% relative humidity. The supernatants were collected at different intervals and stored at -20 ℃ until analyzed by ELISA (Figure 3.36).

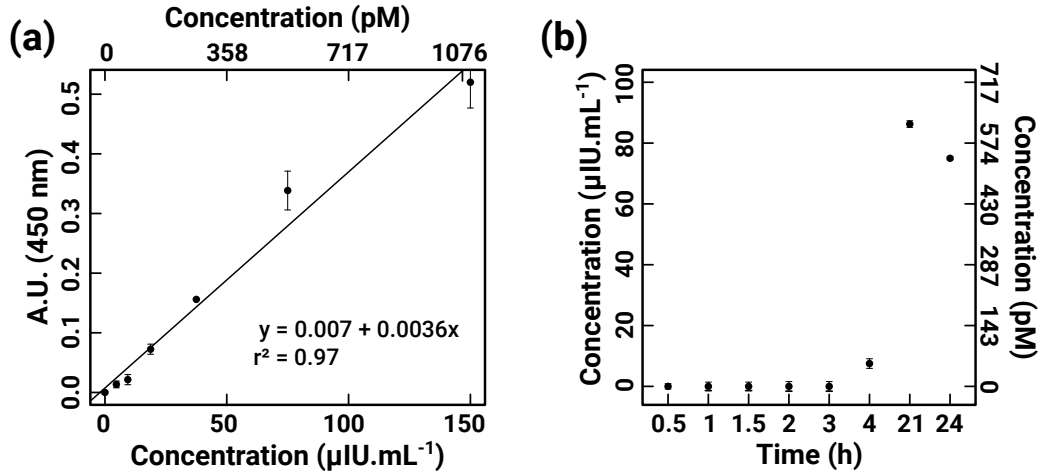

Figure 3.36 – ELISA analysis of insulin secretions by RIN-m cells on high glucose media. (a) Calibration curve with insulin standard; (b) Estimated concentrations of secreted insulin of 1x10^6 cells in 1 mL of culture media at different incubation times.

Secretion of insulin by RIN-m cells has been reported to reach concentrations between 1-1.7 nM for 10^6 cells after 24h of culture[141]. Yet, the same authors indicate that these levels can vary greatly from clone to clone. Our experiments showed a concentration of 0.6 nM for similar culture conditions (culture media, number of cells and incubation time). This level of insulin secretion is considerably low compared to other insulinoma

cell lines such as RINm5F (10 nM of insulin under the same conditions)[142] and INS-1 (15-200 nM)[143,144]. The relatively low insulin secretion by RIN-M cells may be caused by somastostatin which is a potent inhibitor of insulin secretion and it is also secreted by this cell line[145].

PBMCs: We proceeded then to evaluate the secretion profile of PBMCs after been activated by PMA / Ionomycin (Annex A.1.9). Specifically, we focused on IL-2 and IFN-γ secretion. IL-2 role on the immune response is mainly related to its effects on lymphocytes where it promotes T-cell growth, increase NK cytolytic activity, induces differentiation of T-cells and mediates activation-induced cell death[146,147].

On the other hand, IFN-γ is involved in numerous processes for tumor control as well as in the defense against intracellular pathogens (specially viruses)[148]. Some of its functions, as described by Schroder et al.[149] in their review, include: up-regulation of pathogen recognition, antigen processing and presentation, antiviral response, inhibition of cell proliferation, induction of apoptosis, immunomodulation, leukocyte trafficking and activation of antimicrobial effector functions.

Briefly, cells were pre-cultured and then activated in PMA/Ionomycin (100 ng.mL^{-1} and 500 ng.mL^{-1} respectively) supplemented AIM-V media (fully-defined serum-free media for immunological studies). Cells were seeded into 96-multiwell plates (200 µL, 4.8×10^5 cells per well). After incubation at 37 ℃ on a 5% CO_2 atmosphere with 85% relative humidity, supernatants were collected at specific times and frozen until ELISAs were performed for quantification of IL-2 and IFN-γ (Figure 3.37).

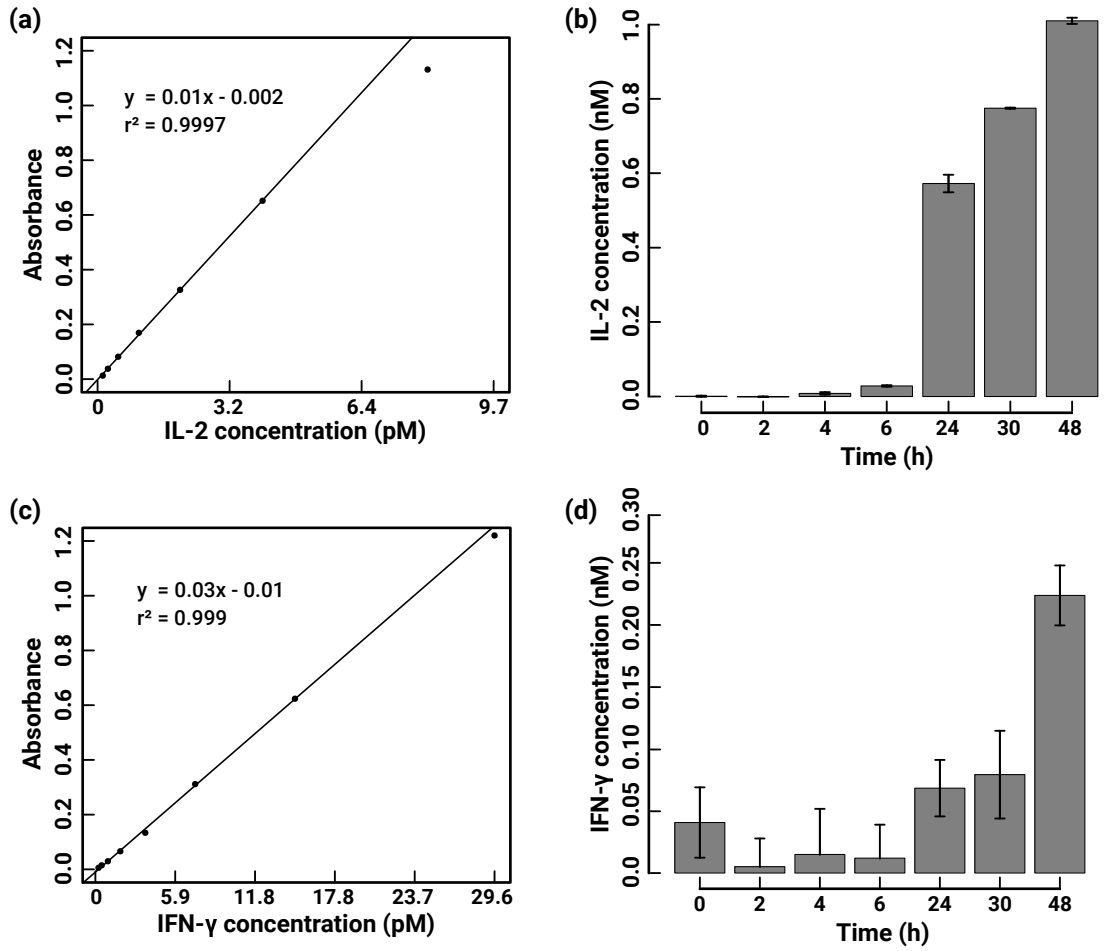

Figure 3.37 – ELISA quantification at different times of intra and extracellular of IL-2 and IFN-γ of 4.8×10^{-1}cells.well^{-1}. Error bars correspond to one standard deviation. Calibration reference curves for (a) IL-2 and (c) IFN-γ. Quantification of (b) IL-2 and (d) IFN-γ on the samples.

Activation of PBMC is traditionally performed at cell concentrations ranging from 0.5-2×10^6 cells per milliliter[150]. In our tests, we employed the lower limit and observed similar results to those of the literature regarding the secretion levels of PBMC (with cultures of 1×10^6 cells per well)[151]. The fact that we obtain the same bulk cytokine concentration while using about half the amount of cells may be produced by some sort of regulation mechanism for cytokine release. Such mechanism would not be limited by the amount of secreting cells but rather by the bulk cytokine concentration. Such hypothesis is plausible as it was stated in section 3.1 that the relative cytokine concentration in the medium is able to regulate the production of others.

A comparison of the different cytokine levels from activated PBMC (PMA/Ionomycin, 10^6 cells mL^{-1} and after 20h) is presented in Table 3.2.

Based on the results reported by Collins[151] as well as on our experiments, we expected that

Table 3.2 – Secretion levels of different cytokines before and after PMA/Ionomycin stimulation of PBMC. Adapted from Collins[151].

		Stimulated		**Basal**	
Cytokine	*MW (g.mol^{-1})*	*Conc. (pg.mL^{-1})*	*Conc. (pM)*	*Conc. (pg.mL^{-1})*	*Conc. (pM)*
IFN-γ	1.7×10^4	5243	308	<2	0.12
IL-1a	1.8×10^4	<2.0	<0.1	17.9	1.0
IL-2	1.5×10^4	12500	833	<0.5	0.03
IL-3	1.7×10^4	134	8	<2.0	<0.1
IL-4	$1.\times10^4$	85	5.6	<0.5	<0.03
IL-6	2.5×10^4	375	15	6.4	0.26
IL-8	1.1×10^4	1440	130	730	66.36
IL-10	1.8×10^4	127	7.0	8.0	0.4
TNF-α	1.7×10^4	5100	300.00	1.4	0.08
GM-CSF	1.5×10^4	2310	158	33.7	2.3

PBMC would secreted IL-2 and IFN-γ at concentrations ranging from pico to nanomolar levels after 48h of activation.

THP-1 cell line Finally, we activated THP-1 cells to determine their secretion profile, specifically, TNF-α release. This cytokine has a vast amount of homeostatic and pathogenic functions including: organogenesis and tissue regeneration, induction of necrosis in tumors, inflammation, recruitment of inflammatory cells, activation of vascular endothelium, tissue degeneration among many others[152].

For the assays, cells were differentiated into macrophages by exposing them to RPMI + PMA (10 ng.mL^{-1}), then seeded into multiwell plates and activated with AIM-V + LPS (0.1 µg.mL^{-1}) + R848 (0.2 µg.mL^{-1}), detailed process in Annex A.1.10. As in previous assays, the culture media was recollected at specific incubation times and frozen until their quantification via ELISA (Figure 3.38).

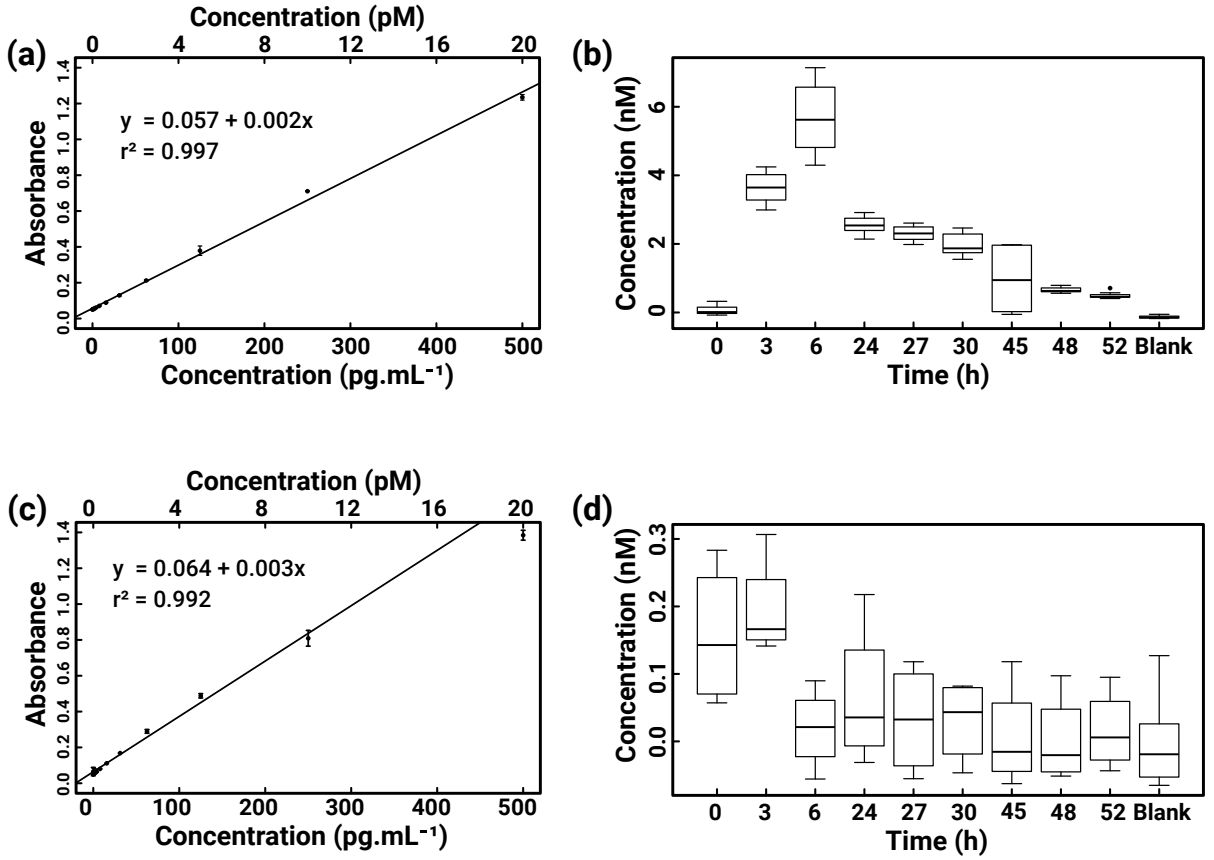

Figure 3.38 – TNF-α quantification on THP-1 cells via ELISA. (a,c) Calibration curve for activated and non-activated sample respectively; (b) Quantification of TNF-α present in culture media of activated cells at different incubation times and (d) Quantification of TNF-α on culture media of non-activated cells.

On non-activated cells, TNF-α levels were negligible while activated cells produced relatively high concentrations (higher amount of the secreted molecule compared with PBMCs and RIN-m cells) after just 3 h of incubation (Figure 3.38) decaying after 24 h. Therefore, it is possible that the maximum TNF-α concentration in the media might have been reached between 6-24 h of incubation. Considering the ephemeral nature of cytokines, this concentration profile was not unexpected. As mentioned before, TNF-α mediates numerous processes in macrophages, being consumed/degraded in the process while its secretion rate decreases over time.

After the profiling of our cellular models, we observed the highest secretion levels on THP-1 cells where release of TNF-α (MW: $\sim$17 kDa) reached $\geq$ 6 nM in just 6 h after activation. Followed by PBMCs whose IFN-γ (MW: $\sim$17 kDa) and IL-2 (MW: $\sim$15 kDa) secretion levels after 48 h were in the range of 0.2 nM and 1 nM respectively. Lastly, RIN-m cells showed insulin (MW: $\sim$5.8 kDa) release levels of 0.6 nM after 24 h of culture. Considering that SPR is a technique based on fluctuations of the refractive index near the sensing surface, nano and subnanomolar concentrations of low-molecular mass molecules would cause very slight shifts in the refractive index, making their detection

quite challenging. For this reason, we proceeded to evaluate the lower limit of detection (LOD) for the different secretions using SPR.

3.2.5.c SPR detection of insulin, IFN-γ and IL-2 using antibodies

To determine the LOD of our SPR system, we monitored the SPR response after exposing a conventional SPR biochip to increasing concentrations of reference solutions of insulin, IFN-γ and IL-2, in a range from 100 pM to 10 nM. For this, Horiba prisms were electrospotted with pyrrole-conjugated antibodies (anti-human IFN-γ, anti-human IL-2, anti-rat insulin and anti-human CD28).

The prisms were set into SPR set-up (diode 680 nm as light source) with a microfluidic system fed by a pump. Experiments were set at 25 ℃ with a continuous flow of PBS at 2.5 µL.s^{-1} with a 500 µL injection loop. First, the prisms were passivated by injection of a 1% (m/v) solution of Bovine Serum Albumin (BSA). Then, injections of the respective analytes (prepared by dissolving lyophilized ELISA standards for IFN-γ and IL-2 or dilution of a concentrated mother solution in the case of insulin) were flowed through the system at increasing concentrations (Figure 3.39).

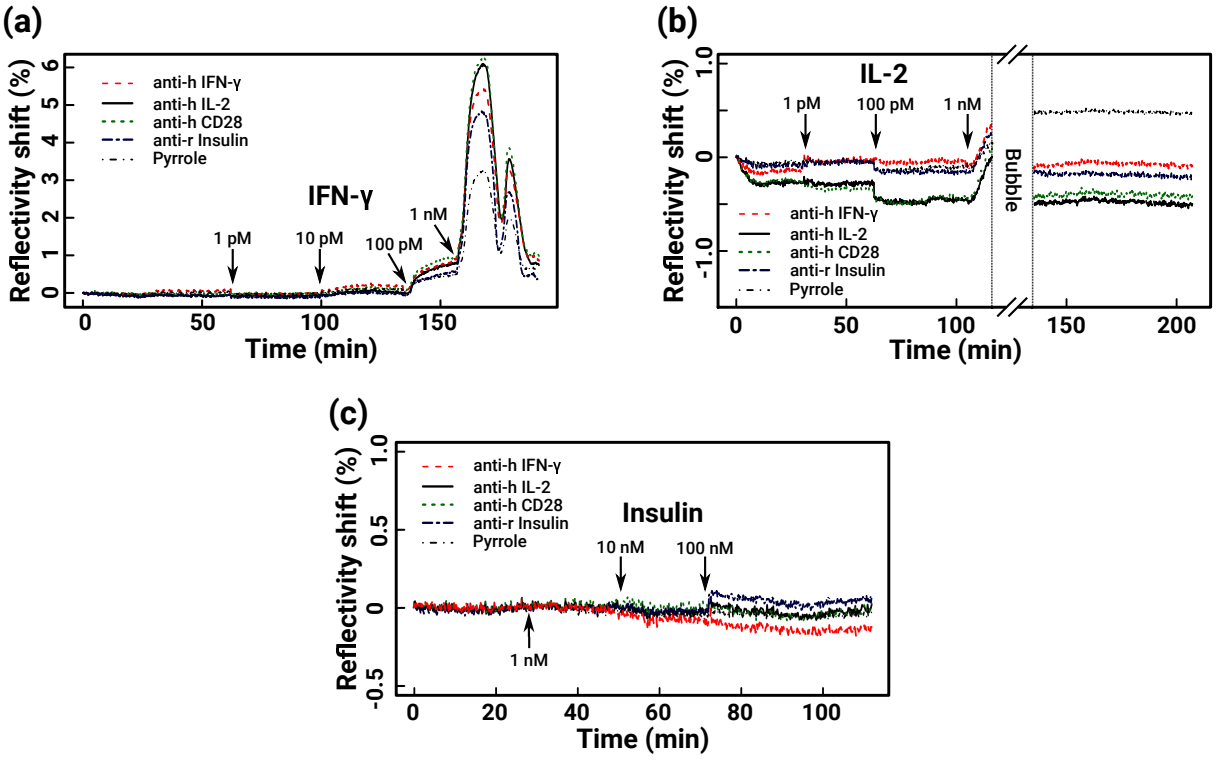

Figure 3.39 – Average SPR responses at different concentrations of (a) IFN-γ, (b) IL-2 and (c) insulin on protein microarrays.

In the case of IFN-γ, the standard solution had a carrier protein, BSA, at very high concentrations (1% m/v) which caused the big reflectivity shifts observed in Figure 3.39a.

However, as it was the case for the rest of analytes, no specific signal was observed at the evaluated concentrations.

Considering the lack of specificity, we used ELISA as a quality control method to validate that the pyrrolated antibodies employed for cytokine detection were biologically active. Multiwell plates were coated with anti-mouse CD45 (which was going to substitute CD28 as negative control), anti-human IL-2 and IFN-γ antibodies (unmodified and pyrrole-conjugated).

Functionality of the antibodies was confirmed as seen in Figure 3.40. Coupling with pyrrole did not alter their performance and all showed to be highly specific by no reacting with a mismatched cytokine.

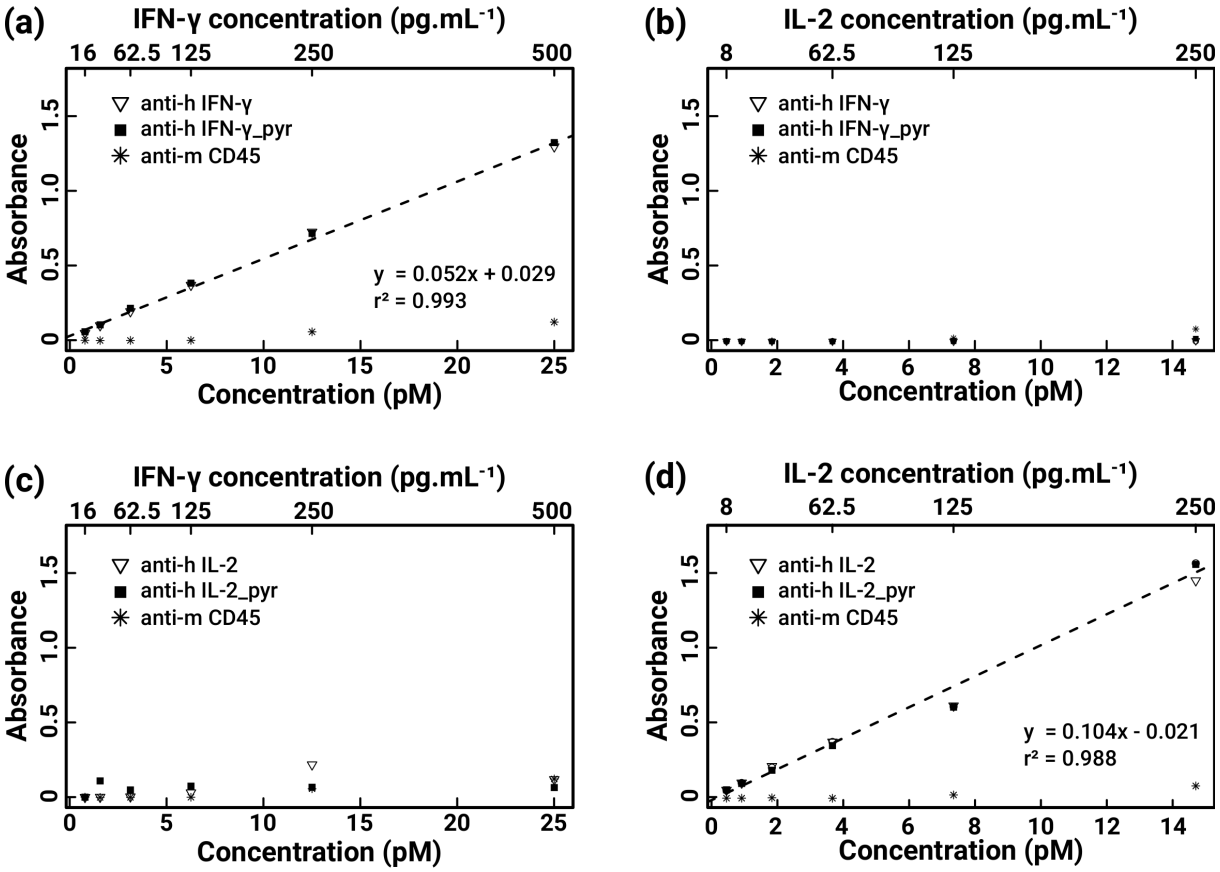

Figure 3.40 – ELISA evaluation of pyrrole-conjugated and unmodified anti-human IFN-γ, anti-human IL-2 and anti-mouse CD45. Curves correspond to: (a) anti IFN-γ exposed to IFN-γ; (b) anti IFN-γ exposed to IL-2; (c) anti IL-2 exposed to IFN-γ and (d) anti IL-2 exposed to IL-2. In all cases, anti-mouse CD45 was used as negative control.

From these control experiments we can conclude that the functionality of the antibodies was not compromised during pyrrole-coupling, and the grafting procedure should not have affected them considerably (as described by Grosjean et al.[119]). Therefore, the detection issues to the LOD of our setup requiring the use of more concentrated standards. With our sensing system, voluminous and massive molecules (IgG antibodies with MW $\sim$150 kDa)

are used for the capture of small proteins (5-17 kDa in these cases). Due to the large size of these probes, antibodies have low grafting densities leading to the attachment of just a few molecules of the analyte per unit area, translating into to negligible SPR responses. By using smaller probes, higher surface densities can be achieved. This translates into the capture of more analytes per surface unit, hence increasing the sensitivity of the system.

Based on this, we decided to evaluate the use smaller probes for cytokine detection (Figure 3.41). Several molecules could be used for this purpose such as antigen-binding fragments (Fab)[153], nanobodies[154] and aptamers[155]. More precisely, we selected the latter due to their intrinsic stability, chemical versatility and ease of production. By switching from an antibody (∼150 kDa) to an aptamer (∼10 kDa) model, we would expect considerably higher grafting densities leading to an increment in the number of target molecules captured on the biochip surface.

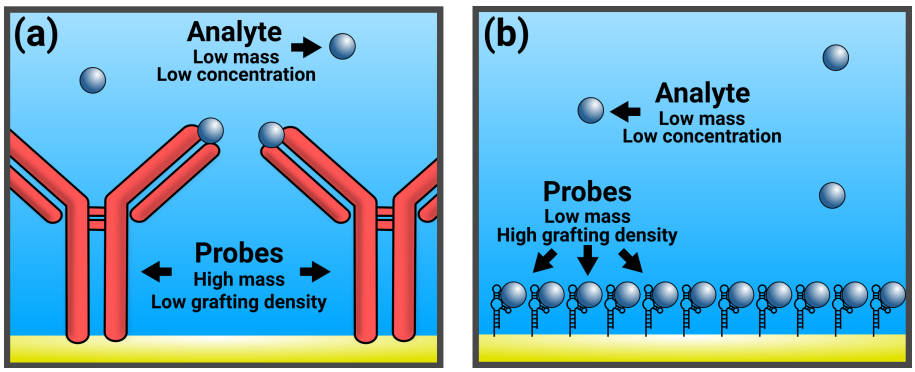

Figure 3.41 – Graphical representation of the size effect of the probes in the grafting density.

3.2.5.d SPR detection of IFN-γ and TNF-α using aptamers

Aptamers are oligonucleotide sequences that, similarly to antibodies, are able to bind to specific targets. They can be selected by a process called SELEX (Systemic Evolution of Ligands by EXponential enrichment)[156]. This process is based on cycles of selection and amplification using large pools of different oligonucleotides (> trillion of distinct sequences) which bind with different affinities to a target under specific parameters[155]. The molecules are submitted to mild denaturing to select the ones with higher affinity which are then modified and amplified repeating the cycle until the desired level of affinity is achieved.

Compared to antibodies, aptamers have numerous advantages such as simpler and cheaper production, low inter-batch variability, reversible denaturing and chemical simplicity which facilitates their use in numerous applications[155]. Furthermore, their use to develop aptasensors (sensors which employes aptamers as probes) for cytokine detection have been steadily growing[80,157–163].

We selected two DNA-based aptamers, from the literature, for the detection of IFN-γ[158,159,164] and TNF-α[165]. These oligonucleotides were synthesized with a terminal amino

moiety which allowed further chemical modifications (e.g. biotinylation, coupling with thiol or with pyrrole).

Some of the properties of these aptamers are described in Table 3.3.

Table 3.3 – Description of the oligonucleotides used during the assays.

Oligonucleotide	**Sequence**	**Length (bp)**	**T_m (℃)**	**M.W. ($g.mol^{-1}$)**
TNF-α apt.	5′-NH_2-C_6-TGGTGGATGGCGCAGTCGGCGACAA-3′	25	68.6	7788.1
IFN-γ apt.	5′-GGGGTTGGTTGTGTTGGGTGTTGTGTCCAACCCC-C_6-NH_2-3′	34	69.2	10558.8
Zip6c (control)	5′-GACCGGTATGCGACCTGGTATGCG-C_6-NH_2-3′	24	57.4	7606.1

First, we added thiol moieties to the aptamers via NHS/NH_2 chemistry. Then, solutions of the thiolated aptamers were prepared in K_2HPO_4 1 M buffer with $PEG_{2000}SH$ to form mixed SAMs avoiding potential steric hindrance between the aptamers. These spotting conditions were inspired from the work[166] of Camille Daniel, a former doctoral student in our lab. To select the optimal ratio oligo:$PEG_{2000}SH$, three different solutions were prepared: 20 µM oligo / 10 µM PEG (2:1), 10 µM oligo / 10 µM PEG (1:1) and 10 µM oligo / 20 µM PEG (1:2). Biochips were produced by functionalizing Horiba SPR prisms with the different solutions using the spotting robot sciFLEXARRAYER from SCIENION (procedure in Annex A.1.1).

The same SPR system was employed (light source 680 nm) with a fluidic system fed by a pump (200 µL injection loop, constant flow of 2.5 $\mu L.s^{-1}$) and temperature set at 25 ℃. PBS-T (PBS + Tween20 0.05% v/v) was used as running buffer.

Correct grafting of the oligos was verified by injection of their corresponding complementary strands (cDNA). Once this was confirmed, the cDNA were removed by addition of NaOH 50 mM. The surface was then passivated with an injection of BSA 1% (m/v). Standard solutions of carrier-free TNF-α in the range of 5-250 nM were added followed by the IFN-γ standards, from 50-1000 nM, as seen in Figure 3.42.

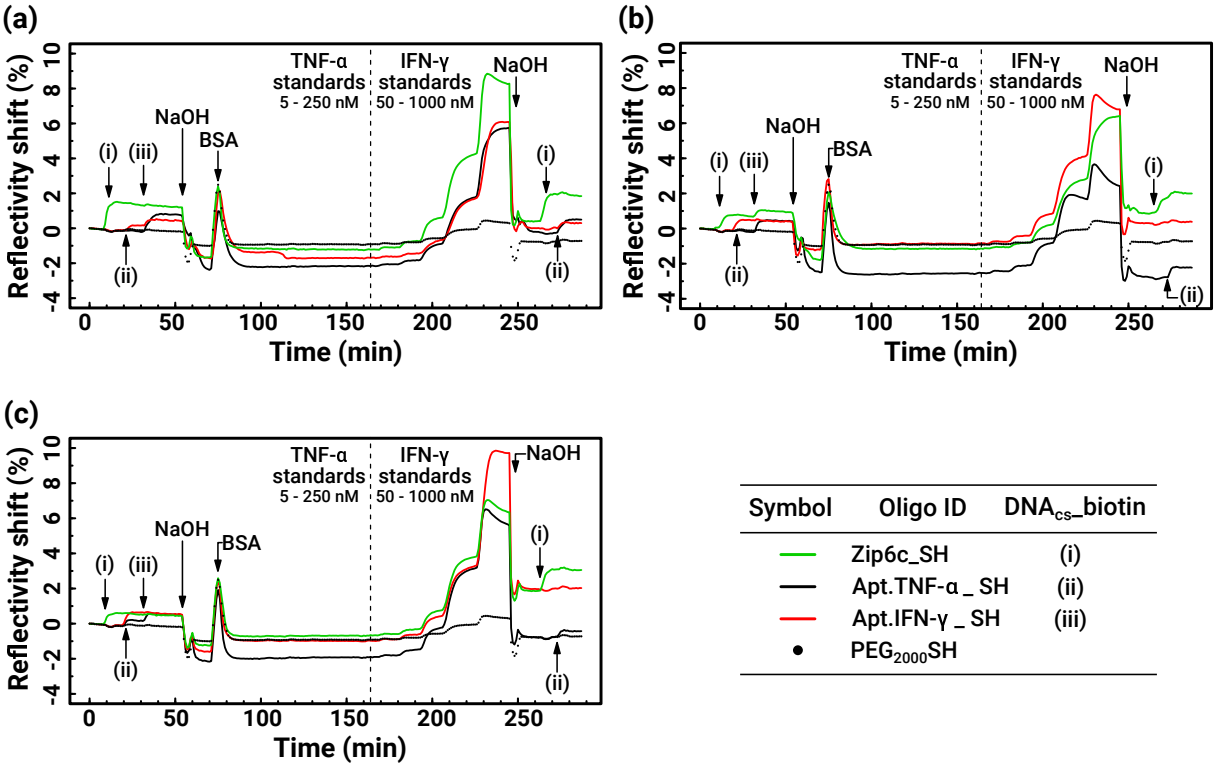

Figure 3.42 – SPR responses for each probe corresponding to thiolated aptamers or Zip6 grafted at different concentrations. The graphs correspond to Oligo:PEG molar ratios of: (a) 2:1, (b) 1:1 and (c) 1:2.

No detection of TNF-α was observed on any of the grafted probes, whereas, all the probes showed significant SPR responses when exposed to IFN-γ at 50 nM and above. This was unexpected as analysis of the IFN-γ peptidic sequence using ScanProsite[167] showed no potential DNA binding sites that might explain such behavior. In their work[158,159,164], the team directed by Revzin did not evaluate the affinity of IFN-γ towards different DNA sequences grafted on their sensor. As their sensors were based on fluctuations in the redox potential, possible attachment of IFN-γ to the probes would not affect their system as long as IFN-γ binding does not alter significantly the distance between the redox label and the surface.

As it was unclear if the lack of specific SPR response was caused by the LOD of our system or biological inactivity of our probes (aptamers), we evaluated the affinity of the aptamers to their corresponding cytokines by an ELISA-like procedure. For this Aptamer-Based ELISA (ABELISA), we modified the aptamers with either maleimide or biotin functionalities in order to employ multiple detection approaches. Then we proceeded to the grafting of the antigens (either TNF-α or IFN-γ) by incubation with a basic buffer (pH $\sim$9.6). Such conditions allow hydrophobic interactions between the plastic surface and hydrophobic pockets of the proteins, incurring in a passive adsorption process as described in Chapter 1 section 1.4.1. Further addition of the corresponding biotinylated aptamer (or biotinylated antibody to verify proper antigen grafting) was performed followed by avidin-

conjugated horseradish peroxidase (HRP-avidin). Lastly, the use of TetraMethylBenzidine (TMB) as substrate for the peroxidase allowed us to confirm recognition of the cytokines by our probes (Figure 3.43).

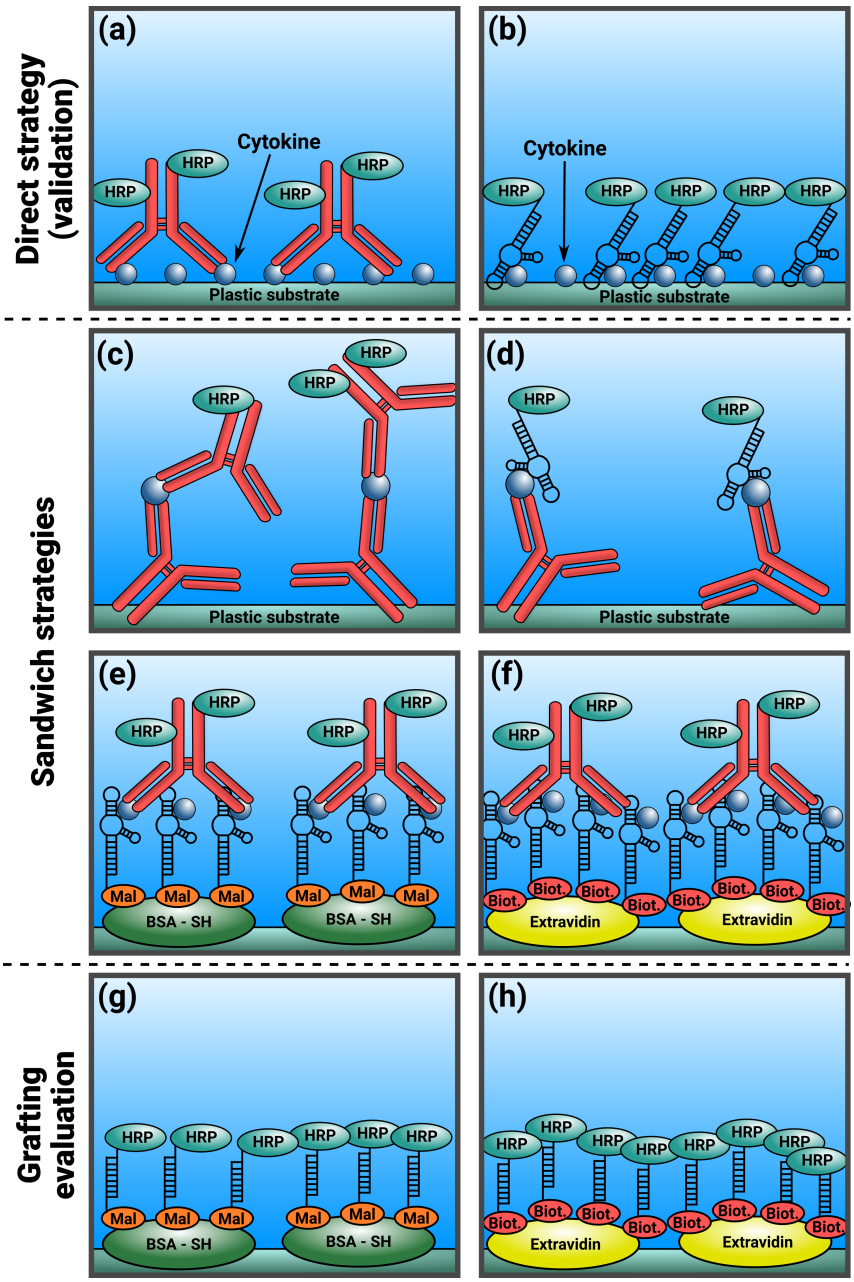

Figure 3.43 – Different approaches performed for an Aptamer-Based ELISA (ABELISA). (a) Direct detection with HRP-conjugated antibodies; (b) Direct detection with HRP-conjugated aptamers; (c) Traditional ELISA sandwich assay (Ab-Ab); (d) Antibody-Aptamer sandwich (Ab-Apt); (e) Aptamer-Antibody (Apt-Ab) sandwich, grafting via maleimide-thiol; (f) Aptamer-Antibody (Apt-Ab) sandwich, grafting via biotin-extravidin; (g-h) Hybridization with DNAcs. In all the cases, the grafting of the first layer of proteins occurs via hydrophobic interactions with the plastic surface.

Coherently with the previous SPR results, the TNF-α aptamer did not react with TNF-α. This was surprising as Orava et al.[165] showed effective SPR detection of TNF-α in solution using this aptamer. A possible explanation for might be provided by the work of Nübel et al.[168]. They highlight that aptamers designed against TNF-α tend to have little affinity for the protein *in vitro* as the binding of the aptamers is strongly correlated to the equilibrium between the monomeric and homotrimeric forms of TNF-α, which can be easily perturbed. Due to this reason, we dropped the use of this oligo and focused on the study of the IFN-γ aptamer as this one showed a strong signal when used for direct detection of IFN-γ (Figure 3.44).

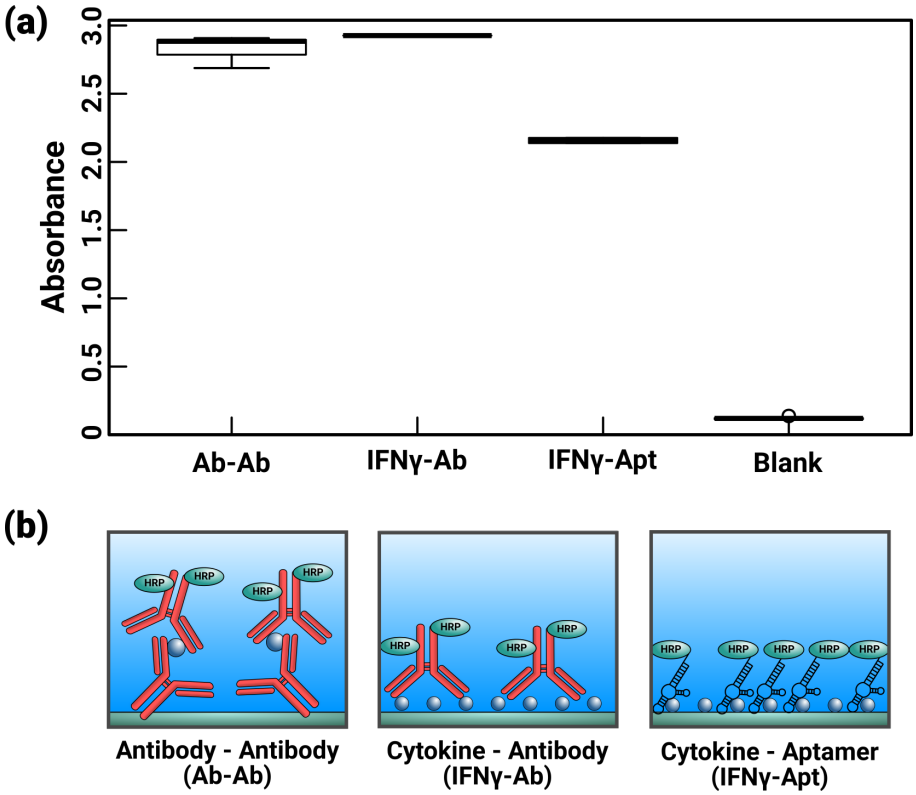

Figure 3.44 – Validation of aptamers via ABELISA. (a) Absorbance measurements of traditional indirect (sandwich) ELISA as well as of direct method using antibodies or aptamers for the detection of IFN-γ and (b) Graphical illustration of the approaches used in (a).

We then evaluated the feasibility of a sandwich assay using aptamers and antibodies via another ABELISA as illustrated in Figure 3.43d-f. The ability to use antibodies at the end of the SPR experiments would aid to confirm cytokine capturing by amplifying the SPR signal. However, we were unsure if the antibody recognition site would be blocked by the aptamer or if the binding with the antibody would cause cytokine release by the aptamer. To answer this questions, we performed the grafting of either antibodies or aptamers on the plastic surface of ELISA plates. The immobilization of the antibodies was performed via hydropobic interactions, as previously stated, yet, this method was not feasible for immobilizing the oligonucleotides. To circumvent this, we evaluated two different

strategies for grafted the aptamers on the ELISA plates. First, we coated the microplate wells, via hydrophobic interactions, with either thiolated Bovine Serum Albumin (BSA-SH) or Extravidin® (which is a highly stable modified version of avidin which presents elevated affinity for biotin). Via NHS reactions (Chapter 1 section 1.5.2.a), we introduced either maleimide or biotin moieties on the aptamer allowing their immobilization on the BSA-SH or Extravidin coated surfaces via an alkylation reaction of maleimides with thiols (Chapter 1 section 1.5.2.c) or Biotin-extravidin affinity (Chapter 1 section 1.5.3). Once the surface was functionalized with the probes of interest, we follow the steps of a conventional ELISA by adding serial dilutions of IFN-γ and then incubation with the detection biomolecule (either a biotinylated aptamer or antibody) which resulted in the data shown in Figure 3.45.

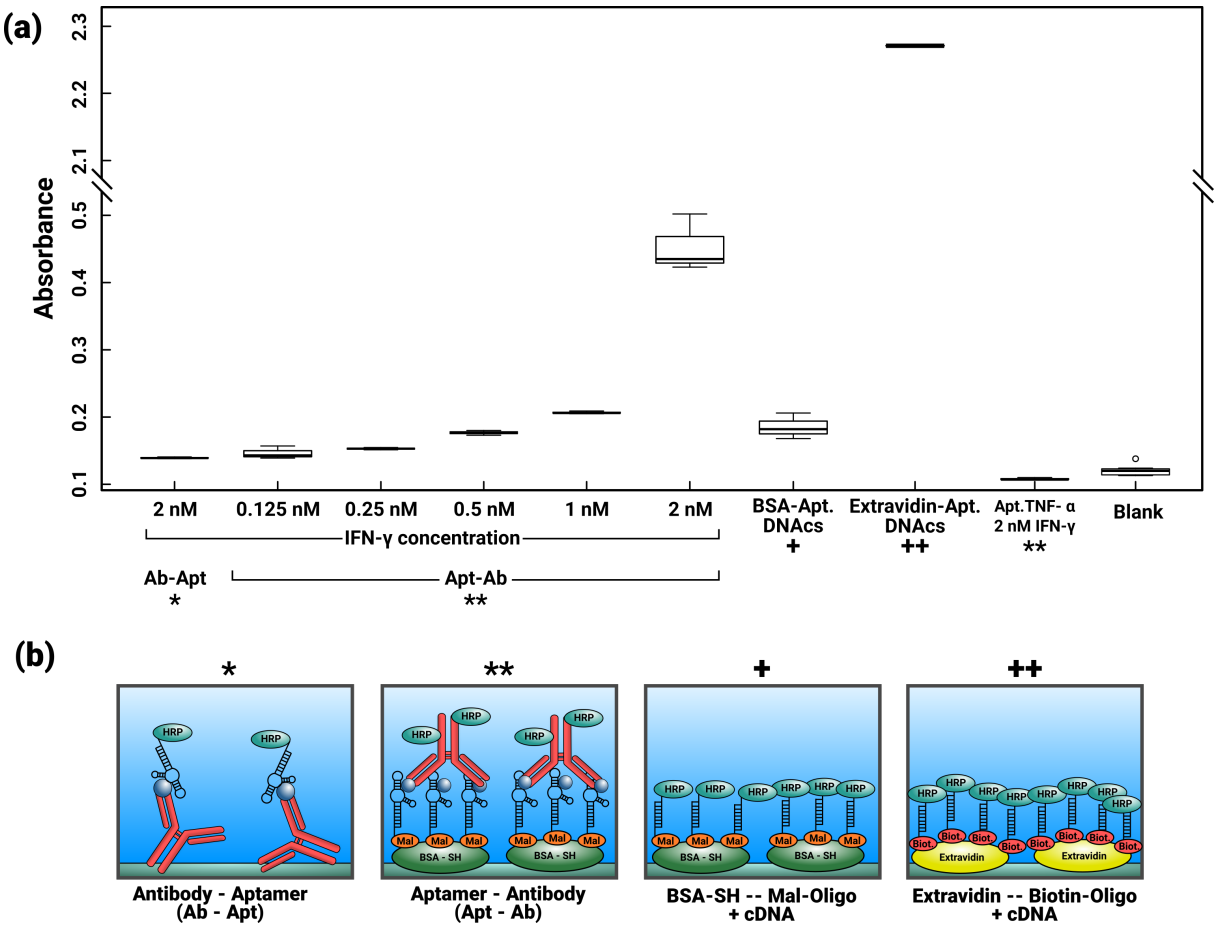

Figure 3.45 – ABELISA evaluation of sandwich strategies for IFN-γ detection. (a) Colorimetric results obtained from the different strategies and (b) Graphical representation of the coating methods employed for each measurement.

The sandwich strategy where antibodies were grafted on the surface and aptamers were used as the detection molecule (Ab-Apt approach, Figure 3.43d) was no different than the blank even when exposed to the highest concentration (2 nM) of IFN-γ (Figure 3.45). This strategy cause a masking of the aptamer binding site to the IFN-γ after the later is captured by the antibodies. However, in the reverse approach (BSA-SH mediated grafting

of aptamers while using detection antibodies, Apt-Ab method as shown in Figure 3.43e) we observed higher colorimetric signals as the concentration of IFN-γ increased, demonstrating that this approach can be used for sandwich detection of this cytokine.

To compare the grafting method of the oligos (either by BSA-SH or Extravidin), we substituted IFN-γ by biotinylated-cDNA. In this case, oligonucleotide immobilization mediated by Extravidin-biotin interactions was considerably superior as the colorimetric signal obtained was 1 order of magnitude higher than for the thiol-maleimide strategy.

Theoretically, BSA contains 59 lysine residues from which 30-35 primary amines are sterically available for reacting with a crosslinker[169]. After conjugation with NHS-thiol, we expected to have numerous available binding sites compared to Extravidin, which has only 4 biotin binding sites. Several hypothesis were made to explain such a marked difference. The first one is based on the reaction kinetics of thiol-maleimide versus avidin-biotin. Even though the thiol-maleimide reaction occurs relatively fast in solution[170], solid-liquid phase reactions take considerably longer times for which the low oligo-maleimide concentrations (0.1 µM) would require more than 60 min of incubation for binding efficiently to BSA-SH. Another explanation could be that the thiol moieties from BSA became sterically unaccessible after immobilization of the protein on the plastic surface. As it has been extensively reported, some biomolecules suffer extensive conformational changes during hydrophobic-based adsorption (Chapter 1 section 1.4.1). If that was the case for BSA, it is possible that a smaller than expected amount of thiols is available for interacting with the maleimide-conjugated oligos.

In any case, as Extravidin-mediated grafting of oligos proved to be extremely efficient, we could employ this strategy for the biding of the aptamer on the SPR biochips. Nevertheless, due to time constraints, such experiments were not performed.

3.3 Conclusions

To summarize, in this chapter we focused on the development and functionalization of a SPR biochip for *in vitro* study of cells and their secretions. This biochip was based on a monolayer of silica microspheres that created a physical barrier between the cells and the sensing region of the SPR.

We faced numerous challenges including the degradation of the microstructures under aqueous media used for biological assays. We overcame this issue by a thermal treatment of the silica microbeads which reduced the pore size and the amount of free silanol moieties in the surface, decreasing significantly the hydrolysis rate. These microspheres conferred our biochips a new optical property, namely the appearance of whispering gallery waves. We successfully used of this optical mode for the detection of cells deposited on the monolayer, yet, further evaluations and instrument optimization should be performed in order to exploit it. More importantly, we observed either total or partial suppression of cell-derived SPR noise in the system with microbeads. In the case of partial suppression, when employing PBMCs, cell attachment induced a reflectivity shift between 1-3% in the system with microbeads which considerably lower than the typical 10-15% when cells

attach directly on the gold surface.

Moreover, we successfully employed two orthogonal approaches for the functionalization of the silica microbeads and the gold surface. Coupling of cell capturing antibodies was performed over the silica surfaces using maleimide-thiol interactions. Fluorescence validation followed by capturing of PBMCs showed that the method is efficient and it could be further optimized by regulating concentrations and incubation times. The gold surface was functionalized via electropolymerization. As with the functionalization of the microbeads, the effective arraying of proteins was evaluated via fluorescence. SPR imaging was used afterwards demonstrating the possibility to perform SPR measurements on this microstructured system.

Finally, we characterized multiple cellular models (RIN-m, THP-1 and PBMCs) in terms of their secretion profile. One of our biological models, the RIN-m cell line, produced subnanomolar amounts of insulin (a 5.8 kDa protein even smaller than cytokines) after 24 h of incubation. Such levels of secretion for a low-molecular weight species made this cell line a complex model for the study of cell secretions via SPR. Among the other models, the THP-1 cell line was the most promising as it secreted $\sim$ 6 nM of TNF-α (a $\sim$15 kDa cytokine) in less than 6 h after its activation. As the expected bulk concentrations of the secreted biomolecules were in the pico to nanomolar range, we evaluated the lower limit of detection of our SPR system. This proved to be considerably more complex than expected. During our first assays, we monitored the SPR response over immunomicroarrays while flowing different standard solutions of the analytes. However, we did not observed any specific response. Yet, the aptamers were not as efficient as it was reported in the literature.

We developed different ELISA-like assays to evaluate the functionality of the selected aptamers. We found that the TNF-α aptamer was not reacting at all while the INF-γ presented a strong interaction with its cytokine. Furthermore, we found that Extravidin-mediated grafting of oligos could be an interesting approach for our system.

In overall, we developed a microstructured SPR biochip which is able to reduce the cell-derive signals while also detects biomolecule interactions via SPR. Orthogonal functionalization methods were evaluated and validated. However, sensitivity of the system may be a major issue. For this, optimization of the grafting method (either direct electropolymerization of pyrrole-conjugated aptamers or Extravidin-mediated immobilization) have to be performed as well as new SELEX in order to obtain more efficient aptamers.

Finally, even if this approach still requires a significant amount of work to achieve ideal *in vitro* detection of cell secretions, we consider this strategy as a viable option worth exploring for the development of novel biosensing technologies.

References

[1] Srey, S., Jahid, I. K., and Ha, S.-D. (2013) Biofilm formation in food industries: A food safety concern. *Food Control 31*, 572–585.

[2] Ueda, H., Kikuta, Y., and Matsuda, K. (2012) Plant communication. *Plant Signaling & Behavior 7*, 222–226.

[3] Coppola, M., Cascone, P., Madonna, V., Lelio, I. D., Esposito, F., Avitabile, C., Romanelli, A., Guerrieri, E., Vitiello, A., Pennacchio, F., Rao, R., and Corrado, G. (2017) Plant-to-plant communication triggered by systemin primes anti-herbivore resistance in tomato. *Scientific Reports 7*.

[4] Kaliyappan, K., Palanisamy, M., Govindarajan, R., and Duraiyan, J. (2012) Microarray and its applications. *Journal of Pharmacy and Bioallied Sciences 4*, 310.

[5] Ryu, W.-S. *Molecular Virology of Human Pathogenic Viruses*; Elsevier, 2017; pp 63–82.

[6] Stanley, A. C., and Lacy, P. (2010) Pathways for Cytokine Secretion. *Physiology 25*, 218–229.

[7] Stenken, J. A., and Poschenrieder, A. J. (2015) Bioanalytical chemistry of cytokines – A review. *Analytica Chimica Acta 853*, 95–115.

[8] Lefkowitz, D. L., and Lefkowitz, S. S. (2001) Macrophage-neutrophil interaction: A paradigm for chronic inflammation revisited. *Immunology and Cell Biology 79*, 502–506.

[9] Wakita, T., Shintani, F., Yagi, G., Asai, M., and Nozawa, S. (2001) Combination of inflammatory cytokines increases nitrite and nitrate levels in the paraventricular nucleus of conscious rats. *Brain Research 905*, 12–20.

[10] Han, Q., Bagheri, N., Bradshaw, E. M., Hafler, D. A., Lauffenburger, D. A., and Love, J. C. (2011) Polyfunctional responses by human T cells result from sequential release of cytokines. *Proceedings of the National Academy of Sciences 109*, 1607–1612.

[11] Gordon, S., Fraser, I., Nath, D., Hughes, D., and Clarke, S. (1992) Macrophages in tissues and in vitro. *Current Opinion in Immunology 4*, 25–32.

[12] Balkwill, F., and Burke, F. (1989) The cytokine network. *Immunology Today 10*, 299–304.

[13] Schmitz, M. L., Weber, A., Roxlau, T., Gaestel, M., and Kracht, M. (2011) Signal integration, crosstalk mechanisms and networks in the function of inflammatory cytokines. *Biochimica et Biophysica Acta (BBA) - Molecular Cell Research 1813*, 2165–2175.

[14] Dettmer, P. et al. The Immune System Explained I - Bacteria Infection. `https://youtu.be/zQGOcOUBi6s?t=57`.

[15] Schenk, T., Irth, H., Marko-Varga, G., Edholm, L.-E., Tjaden, U., and van der Greef, J. (2001) Potential of on-line micro-LC immunochemical detection in the bioanalysis of cytokines. *Journal of Pharmaceutical and Biomedical Analysis 26*, 975–985.

[16] Bienvenu, J., Monneret, G., Fabien, N., and Revillard, J. P. (2000) The Clinical Usefulness of the Measurement of Cytokines. *Clinical Chemistry and Laboratory Medicine 38*.

[17] Dinarello, C. A. (2000) Proinflammatory Cytokines. *Chest 118*, 503–508.

[18] Zheng, C., Zhou, X.-W., and Wang, J.-Z. (2016) The dual roles of cytokines in Alzheimer's disease: update on interleukins, TNF-α, TGF-β and IFN-γ. *Translational Neurodegeneration 5*.

[19] Rubio-Perez, J. M., and Morillas-Ruiz, J. M. (2012) A Review: Inflammatory Process in Alzheimer's Disease, Role of Cytokines. *The Scientific World Journal 2012*, 1–15.

[20] Renauld, J.-C. (2001) New insights into the role of cytokines in asthma. *Journal of Clinical Pathology 54*, 577–589.

[21] Kips, J. C. (2001) Cytokines in asthma. *European Respiratory Journal 18*, 24–33.

[22] Brunet, M. (2012) Cytokines as predictive biomarkers of alloreactivity. *Clinica Chimica Acta 413*, 1354–1358.

[23] Krzystek-Korpacka, M., Diakowska, D., Kapturkiewicz, B., Bębenek, M., and Gamian, A. (2013) Profiles of circulating inflammatory cytokines in colorectal cancer (CRC), high cancer risk conditions, and health are distinct. Possible implications for CRC screening and surveillance. *Cancer Letters 337*, 107–114.

[24] Mager, L. F., Wasmer, M.-H., Rau, T. T., and Krebs, P. (2016) Cytokine-Induced Modulation of Colorectal Cancer. *Frontiers in Oncology 6*.

[25] Neuner, A., Schindel, M., Wildenberg, U., Muley, T., Lahm, H., and Fischer, J. (2001) Cytokine secretion: clinical relevance of immunosuppression in non-small cell lung cancer. *Lung Cancer 34*, S79–S82.

[26] Ramji, D. P., and Davies, T. S. (2015) Cytokines in atherosclerosis: Key players in all stages of disease and promising therapeutic targets. *Cytokine & Growth Factor Reviews 26*, 673–685.

[27] Moss, J. W., and Ramji, D. P. (2016) Cytokines: roles in atherosclerosis disease progression and potential therapeutic targets. *Future Medicinal Chemistry 8*, 1317–1330.

[28] Ito, T., and Ikeda, U. (2003) Inflammatory Cytokines and Cardiovascular Disease. *Current Drug Target -Inflammation & Allergy 2*, 257–265.

[29] Kofler, S., Nickel, T., and Weis, M. (2005) Role of cytokines in cardiovascular diseases: a focus on endothelial responses to inflammation. *Clinical Science 108*, 205–213.

[30] Felger, J., and Lotrich, F. (2013) Inflammatory cytokines in depression: Neurobiological mechanisms and therapeutic implications. *Neuroscience 246*, 199–229.

[31] Farooq, R. K., Asghar, K., Kanwal, S., and Zulqernain, A. (2016) Role of inflammatory cytokines in depression: Focus on interleukin-1β. *Biomedical Reports 6*, 15–20.

[32] Reuter, M. A., Pombo, C., and Betts, M. R. (2012) Cytokine production and dysregulation in HIV pathogenesis: Lessons for development of therapeutics and vaccines. *Cytokine & Growth Factor Reviews 23*, 181–191.

[33] Kedzierska, K., and Crowe, S. M. (2001) Cytokines and HIV-1: Interactions and Clinical Implications. *Antiviral Chemistry and Chemotherapy 12*, 133–150.

[34] Schulte, W., Bernhagen, J., and Bucala, R. (2013) Cytokines in Sepsis: Potent Immunoregulators and Potential Therapeutic Targets—An Updated View. *Mediators of Inflammation 2013*, 1–16.

[35] Chaudhry, H., Zhou, J., Zhong, Y., Mustafa Ali, M., McGuire, F., Nagarkatti, P., and Nagarkatti, M. (2013) Role of Cytokines as a Double-edged Sword in Sepsis. *27*, 669–84.

[36] Sadek, H. L. (2014) The Inflammatory Cytokines in the Pathogenesis of Parkinson's Disease. *Journal of Alzheimer's Disease & Parkinsonism 04*.

[37] Alcalay, R. N. (2016) Cytokines as Potential Biomarkers of Parkinson Disease. *JAMA Neurology 73*, 1282.

[38] McInnes, I. B., and Schett, G. (2007) Cytokines in the pathogenesis of rheumatoid arthritis. *Nature Reviews Immunology 7*, 429–442.

[39] Moudgil, K. D., and Choubey, D. (2011) Cytokines in Autoimmunity: Role in Induction, Regulation, and Treatment. *Journal of Interferon & Cytokine Research 31*, 695–703.

[40] Zvezdanovic, L., Djordjevic, V., Cosic, V., Cvetkovic, T., Kundalic, S., and Stankovic, A. (2006) The significance of cytokines in diagnosis of autoimmune diseases. *Jugoslovenska medicinska biohemija 25*, 363–372.

[41] Striz, I., Brabcova, E., Kolesar, L., and Sekerkova, A. (2014) Cytokine networking of innate immunity cells: a potential target of therapy. *Clinical Science 126*, 593–612.

[42] Schett, G., Elewaut, D., McInnes, I. B., Dayer, J.-M., and Neurath, M. F. (2013) How Cytokine Networks Fuel Inflammation: Toward a cytokine-based disease taxonomy. *Nature Medicine 19*, 822–824.

[43] Leng, S. X., McElhaney, J. E., Walston, J. D., Xie, D., Fedarko, N. S., and Kuchel, G. A. (2008) ELISA and multiplex technologies for cytokine measurement in inflammation and aging research. *J. Gerontol. A Biol. Sci. Med. Sci. 63*, 879–884.

[44] Dennis, K. (2008) ELISPOT Assay to Detect Cytokine-Secreting Murine and Human Cells. *Current Protocols in Immunology 83*, 6.19.1–6.19.9.

[45] Forlenza, M., Kaiser, T., Savelkoul, H. F. J., and Wiegertjes, G. F. *Methods in Molecular Biology*; Humana Press, 2011; pp 7–23.

[46] Aziz, N., Nishanian, P., Mitsuyasu, R., Detels, R., and Fahey, J. L. (1999) Variables that affect assays for plasma cytokines and soluble activation markers. *Clin. Diagn. Lab. Immunol. 6*, 89–95.

[47] Martins, T. B., Pasi, B. M., Pickering, J. W., Jaskowski, T. D., Litwin, C. M., and Hill, H. R. (2002) Determination of Cytokine Responses Using a Multiplexed Fluorescent Microsphere Immunoassay. *American Journal of Clinical Pathology 118*, 346–353.

[48] Valentina, M., Jan, F., Peder, N. L., Bo, Z., Hongjie, D., and Pernille, K. (2015) Cytokine detection and simultaneous assessment of rheumatoid factor interference in human serum and synovial fluid using high-sensitivity protein arrays on plasmonic gold chips. *BMC Biotechnology 15*.

[49] Yssel, H., Wijdenes, J., de Waal Malefyt, R., Mathieu, J.-F., and Pène, J. *Immunology of Infection*; Elsevier, 2010; pp 439–496.

[50] Sandberg, J. K., Fast, N. M., and Nixon, D. F. (2001) Functional Heterogeneity of Cytokines and Cytolytic Effector Molecules in Human $CD8^+$ T Lymphocytes. *The Journal of Immunology 167*, 181–187.

[51] Janetzki, S., Rueger, M., and Dillenbeck, T. (2014) Stepping up ELISpot: Multi-Level Analysis in FluoroSpot Assays. *Cells 3*, 1102–1115.

[52] Carding, S. R., Lu, D., and Bottomly, K. (1992) A polymerase chain reaction assay for the detection and quantitation of cytokine gene expression in small numbers of cells. *Journal of Immunological Methods 151*, 277–287.

[53] Plotnikova, M. A., Klotchenko, S. A., and Vasin, A. V. (2016) Development of a multiplex quantitative PCR assay for the analysis of human cytokine gene expression in influenza A virus-infected cells. *Journal of Immunological Methods 430*, 51–55.

[54] Castillo, L., and MacCallum, D. M. *Host-Fungus Interactions*; Humana Press, 2012; pp 425–434.

[55] Pawlak, M., Schick, E., Bopp, M. A., Schneider, M. J., Oroszlan, P., and Ehrat, M. (2002) Zeptosens' protein microarrays: A novel high performance microarray platform for low abundance protein analysis. *Proteomics 2*, 383.

[56] Mustafa, S. A., Hoheisel, J. D., and Alhamdani, M. S. S. (2011) Secretome profiling with antibody microarrays. *Molecular BioSystems 7*, 1795.

[57] Chen, P., Huang, N.-T., Chung, M.-T., Cornell, T. T., and Kurabayashi, K. (2015) Label-free cytokine micro- and nano-biosensing towards personalized medicine of systemic inflammatory disorders. *Advanced Drug Delivery Reviews 95*, 90–103.

[58] Reddy, B., Salm, E., and Bashir, R. (2016) Electrical Chips for Biological Point-of-Care Detection. *Annual Review of Biomedical Engineering 18*, 329–355.

[59] Baraket, A., Lee, M., Zine, N., Sigaud, M., Bausells, J., and Errachid, A. (2017) A fully integrated electrochemical biosensor platform fabrication process for cytokines detection. *Biosensors and Bioelectronics 93*, 170–175.

[60] Kongsuphol, P., Lee, G. C., Arya, S. K., Chiam, S. Y., and Park, M. K. (2017) Miniaturized electrophoresis electrochemical protein sensor (MEEPS) for multiplexed protein detections. *Sensors and Actuators B: Chemical 244*, 823–830.

[61] Pui, T.-S., Agarwal, A., Ye, F., Huang, Y., and Chen, P. (2011) Nanoelectronic detection of triggered secretion of pro-inflammatory cytokines using CMOS compatible silicon nanowires. *Biosensors and Bioelectronics 26*, 2746–2750.

[62] Hakim, M. M. A., Lombardini, M., Sun, K., Giustiniano, F., Roach, P. L., Davies, D. E., Howarth, P. H., de Planque, M. R. R., Morgan, H., and Ashburn, P. (2012) Thin Film Polycrystalline Silicon Nanowire Biosensors. *Nano Letters 12*, 1868–1872.

[63] Zhu, H., Stybayeva, G., Macal, M., Ramanculov, E., George, M. D., Dandekar, S., and Revzin, A. (2008) A microdevice for multiplexed detection of T-cell-secreted cytokines. *Lab on a Chip 8*, 2197.

[64] Lu, Y., Chen, J. J., Mu, L., Xue, Q., Wu, Y., Wu, P.-H., Li, J., Vortmeyer, A. O., Miller-Jensen, K., Wirtz, D., and Fan, R. (2013) High-Throughput Secretomic Analysis of Single Cells to Assess Functional Cellular Heterogeneity. *Analytical Chemistry 85*, 2548–2556.

[65] Lu, Y., Xue, Q., Eisele, M. R., Sulistijo, E. S., Brower, K., Han, L., ad David Amir, E., Pe'er, D., Miller-Jensen, K., and Fan, R. (2015) Highly multiplexed profiling of single-cell effector functions reveals deep functional heterogeneity in response to pathogenic ligands. *Proceedings of the National Academy of Sciences 112*, E607–E615.

[66] Cohen, L., Xie, L., Xylas, M. E., and Walt, D. R. (2018) Single Molecule Arrays for ultra-sensitive detection of rat cytokines in serum. *Journal of Immunological Methods 452*, 20–25.

[67] Luchansky, M. S., and Bailey, R. C. (2010) Silicon Photonic Microring Resonators for Quantitative Cytokine Detection and T-Cell Secretion Analysis. *Analytical Chemistry 82*, 1975–1981.

[68] Luchansky, M. S., and Bailey, R. C. (2011) Rapid, Multiparameter Profiling of Cellular Secretion Using Silicon Photonic Microring Resonator Arrays. *Journal of the American Chemical Society 133*, 20500–20506.

[69] Knittel, J., Chow, J. H., Gray, M. B., Taylor, M. A., and Bowen, W. P. (2013) Ultrasensitive real-time measurement of dissipation and dispersion in a whispering-gallery mode microresonator. *Optics Letters 38*, 1915.

[70] Armani, A. M., Fraser, S. E., and Vahala, K. J. Label-free, single molecule detection of cytokines using optical microcavities. LEOS 2007 - IEEE Lasers and Electro-Optics Society Annual Meeting Conference Proceedings. 2007.

[71] Zhang, C., Cocking, A., Freeman, E., Liu, Z., and Tadigadapa, S. Whispering gallery mode based on-chip glass microbubble resonator for thermal sensing. 2017 19th International Conference on Solid-State Sensors, Actuators and Microsystems (TRANSDUCERS). 2017.

[72] Kamińska, A., Winkler, K., Kowalska, A., Witkowska, E., Szymborski, T., Janeczek, A., and Waluk, J. (2017) SERS-based Immunoassay in a Microfluidic System for the Multiplexed Recognition of Interleukins from Blood Plasma: Towards Picogram Detection. *Scientific Reports 7*.

[73] Luna, A. *Encyclopedia of Spectroscopy and Spectrometry*; Elsevier, 2017; pp 919–923.

[74] Liu, G., Qi, M., Hutchinson, M. R., Yang, G., and Goldys, E. M. (2016) Recent advances in cytokine detection by immunosensing. *Biosensors and Bioelectronics 79*, 810–821.

[75] Albala, J. S. *BioMEMS and Biomedical Nanotechnology*; Springer US, pp 127–136.

[76] Homola, J. (2008) Surface Plasmon Resonance Sensors for Detection of Chemical and Biological Species. *Chemical Reviews 108*, 462–493.

[77] Battaglia, T. M., Masson, J.-F., Sierks, M. R., Beaudoin, S. P., Rogers, J., Foster, K. N., Holloway, G. A., and Booksh, K. S. (2005) Quantification of Cytokines Involved in Wound Healing Using Surface Plasmon Resonance. *Analytical Chemistry 77*, 7016–7023.

[78] Yang, C.-Y., Brooks, E., Li, Y., Denny, P., Ho, C.-M., Qi, F., Shi, W., Wolinsky, L., Wu, B., Wong, D. T. W., and Montemagno, C. D. (2005) Detection of picomolar levels of interleukin-8 in human saliva by SPR. *Lab on a Chip 5*, 1017.

[79] Martinez-Perdiguero, J., Retolaza, A., Bujanda, L., and Merino, S. (2014) Surface plasmon resonance immunoassay for the detection of the TNFα biomarker in human serum. *Talanta 119*, 492–497.

[80] Chuang, T.-L., Chang, C.-C., Chu-Su, Y., Wei, S.-C., hong Zhao, X., Hsueh, P.-R., and Lin, C.-W. (2014) Disposable surface plasmon resonance aptasensor with membrane-based sample handling design for quantitative interferon-gamma detection. *Lab Chip 14*, 2968–2977.

[81] Šípová, H., Ševců, V., Kuchař, M., Ahmad, J., Mikulecký, P., Osička, R., Malý, P., and Homola, J. (2012) Surface plasmon resonance biosensor based on engineered proteins for direct detection of interferon-gamma in diluted blood plasma. *Sensors and Actuators B: Chemical 174*, 306–311.

[82] Milgram, S., Cortes, S., Villiers, M.-B., Marche, P., Buhot, A., Livache, T., and Roupioz, Y. (2011) On chip real time monitoring of B-cells hybridoma secretion of immunoglobulin. *Biosensors and Bioelectronics 26*, 2728–2732.

[83] Tudos, A. J., and Schasfoort, R. B. *Handbook of Surface Plasmon Resonance*; Royal Society of Chemistry, pp 1–14.

[84] Abou-El-Sherbini, K. S., Weidler, P. G., Schiel, D., Amr, M. H. A., Niemann, H., El-Dafrawy, S., and Höll, W. H. (2014) Stabilization of Silica Gel against Hydrolysis by Doping with F^- or Zr(IV). *Green and Sustainable Chemistry 04*, 24–32.

[85] Dellea, O., Shavdina, O., Fugier, P., Coronel, P., Ollier, E., and Désage, S.-F. *Precision Assembly Technologies and Systems*; Springer Berlin Heidelberg, 2014; pp 107–117.

[86] Wu, S.-H., Mou, C.-Y., and Lin, H.-P. (2013) Synthesis of mesoporous silica nanoparticles. *Chemical Society Reviews 42*, 3862.

[87] Gouze, B., Cambedouzou, J., Parrès-Maynadié, S., and Rébiscoul, D. (2014) How hexagonal mesoporous silica evolves in water on short and long term: Role of pore size and silica wall porosity. *Microporous and Mesoporous Materials 183*, 168–176.

[88] Bass, J. D., Grosso, D., Boissiere, C., Belamie, E., Coradin, T., and Sanchez, C. (2007) Stability of Mesoporous Oxide and Mixed Metal Oxide Materials under Biologically Relevant Conditions. *Chemistry of Materials 19*, 4349–4356.

[89] Marshall, W. L., and Warakomski, J. M. (1980) Amorphous silica solubilities—II. Effect of aqueous salt solutions at 25°C. *Geochimica et Cosmochimica Acta 44*, 915–924.

[90] Lide, D. R. *CRC Handbook of Chemistry and Physics, 90th Edition (CRC Handbook of Chemistry & Physics)*; CRC Press, 2009.

[91] Yang, S.-A., Choi, S., Jeon, S. M., and Yu, J. (2018) Silica nanoparticle stability in biological media revisited. *Scientific Reports 8*.

[92] Neofotistou, E., and Demadis, K. D. (2004) Silica scale inhibition by polyaminoamide STARBURST® dendrimers. *Colloids and Surfaces A: Physicochemical and Engineering Aspects 242*, 213–216.

[93] He, Q., Shi, J., Zhu, M., Chen, Y., and Chen, F. (2010) The three-stage in vitro degradation behavior of mesoporous silica in simulated body fluid. *Microporous and Mesoporous Materials 131*, 314–320.

[94] Cauda, V., Schlossbauer, A., and Bein, T. (2010) Bio-degradation study of colloidal mesoporous silica nanoparticles: Effect of surface functionalization with organo-silanes and poly(ethylene glycol). *Microporous and Mesoporous Materials 132*, 60–71.

[95] Godin, B., Gu, J., Serda, R. E., Bhavane, R., Tasciotti, E., Chiappini, C., Liu, X., Tanaka, T., Decuzzi, P., and Ferrari, M. (2010) Tailoring the degradation kinetics of mesoporous silicon structures through PEGylation. *Journal of Biomedical Materials Research Part A 9999A*, NA–NA.

[96] Li, X., Zhang, L., Dong, X., Liang, J., and Shi, J. (2007) Preparation of mesoporous calcium doped silica spheres with narrow size dispersion and their drug loading and degradation behavior. *Microporous and Mesoporous Materials 102*, 151–158.

[97] Lin, Q., Xu, Z., Lan, X., Ni, Y., and Lu, C. (2011) The reactivity of nano silica with calcium hydroxide. *Journal of Biomedical Materials Research Part B: Applied Biomaterials 99B*, 239–246.

[98] Kuai, S., Zhang, Y., Truong, V.-V., and Hu, X. (2002) Improvement of optical properties of silica colloidal crystals by sintering. *Applied Physics A 74*, 89–90.

[99] Silencieux, F., Bouchoucha, M., Mercier, O., Turgeon, S., Chevallier, P., Kleitz, F., and Fortin, M.-A. (2015) Mesoporous Silica Nanoparticles under Sintering Conditions: A Quantitative Study. *Langmuir 31*, 13011–13021.

[100] Gamvrellis, A., Gloster, S., Jefferies, M., Mottram, P. L., Smooker, P., Plebanski, M., and Scheerlinck, J.-P. Y. (2013) Characterisation of local immune responses induced by a novel nano-particle based carrier-adjuvant in sheep. *Veterinary Immunology and Immunopathology 155*, 21–29.

[101] Bratlie, K. M., Dang, T. T., Lyle, S., Nahrendorf, M., Weissleder, R., Langer, R., and Anderson, D. G. (2010) Rapid Biocompatibility Analysis of Materials via In Vivo Fluorescence Imaging of Mouse Models. *PLoS ONE 5*, e10032.

[102] Trindade, M. C. D., Lind, M., Goodman, S. B., Maloney, W. J., Schurman, D. J., and Smith, R. L. (1999) Interferon-gamma exacerbates polymethylmethacrylate particle-induced interleukin-6 release by human monocyte/macrophagesin vitro. *Journal of Biomedical Materials Research 47*, 1–7.

[103] Rakshit, D. S., Ly, K., Sengupta, T. K., Nestor, B. J., Sculco, T. P., Ivashkiv, L. B., and Purdue, P. E. (2006) Wear Debris Inhibition of Anti-Osteoclastogenic Signaling by Interleukin-6 and Interferon- : Mechanistic Insights and Implications for Periprosthetic Osteolysis. *The Journal of Bone & Joint Surgery 88*, 788–799.

[104] Howard, J. R. *Fluidized Bed Technology*; 1989.

[105] Milne, S. J., Patel, M., and Dickinson, E. (1993) Experimental studies of particle packing and sintering behaviour of monosize and bimodal spherical silica powders. *Journal of the European Ceramic Society 11*, 1–7.

[106] Lesaine, A., Bonamy, D., Gauthier, G., Rountree, C. L., and Lazarus, V. (2018) Highly porous layers of silica nanospheres sintered by drying: scaling up of the elastic properties of the beads to the macroscopic mechanical properties. *Soft Matter 14*, 3987–3997.

[107] Weber, S., Briens, C., Berruti, F., Chan, E., and Gray, M. (2006) Agglomerate stability in fluidized beds of glass beads and silica sand. *Powder Technology 165*, 115–127.

[108] Quevedo, J., Pfeffer, R., Shen, Y., Dave, R., Nakamura, H., and Watano, S. (2006) Fluidization of nanoagglomerates in a rotating fluidized bed. *AIChE Journal 52*, 2401–2412.

[109] Clemente, A., Balas, F., Lobera, M. P., Irusta, S., and Santamaria, J. (2013) Fluidized Bed Generation of Stable Silica Nanoparticle Aerosols. *Aerosol Science and Technology 47*, 867–874.

[110] Mortimer, D., and Mortimer, S. T. In *Culture Media, Solutions, and Systems in Human ART*; Quinn, P., Ed.; Cambridge University Press, pp 47–67.

[111] Benson, T. M., Boriskina, S. V., Sewell, P., Vukovic, A., Greedy, S. C., and Nosich, A. I. *Frontiers in Planar Lightwave Circuit Technology*; Kluwer Academic Publishers, pp 39–70.

[112] Gorodetsky, M. L., Savchenkov, A. A., and Ilchenko, V. S. (1996) Ultimate Q of optical microsphere resonators. *Optics Letters 21*, 453.

[113] Vernooy, D. W., Furusawa, A., Georgiades, N. P., Ilchenko, V. S., and Kimble, H. J. (1998) Cavity QED with high-Qwhispering gallery modes. *Physical Review A 57*, R2293–R2296.

[114] Vernooy, D. W., Ilchenko, V. S., Mabuchi, H., Streed, E. W., and Kimble, H. J. (1998) High-Q measurements of fused-silica microspheres in the near infrared. *Optics Letters 23*, 247.

[115] Min, B., Ostby, E., Sorger, V., Ulin-Avila, E., Yang, L., Zhang, X., and Vahala, K. (2009) High-Q surface-plasmon-polariton whispering-gallery microcavity. *Nature 457*, 455–458.

[116] Sun, L., Chen, Z., Ren, Q., Yu, K., Bai, L., Zhou, W., Xiong, H., Zhu, Z. Q., and Shen, X. (2008) Direct Observation of Whispering Gallery Mode Polaritons and their Dispersion in a ZnO Tapered Microcavity. *Physical Review Letters 100*.

[117] Schindelin, J. et al. (2012) Fiji: an open-source platform for biological-image analysis. *Nature Methods 9*, 676–682.

[118] Schneider, C. A., Rasband, W. S., and Eliceiri, K. W. (2012) NIH Image to ImageJ: 25 years of image analysis. *Nature Methods 9*, 671–675.

[119] Grosjean, L., Cherif, B., Mercey, E., Roget, A., Levy, Y., Marche, P. N., Villiers, M.-B., and Livache, T. (2005) A polypyrrole protein microarray for antibody–antigen interaction studies using a label-free detection process. *Analytical Biochemistry 347*, 193–200.

[120] Lee, L. Y. S., and Lennox, R. B. (2007) Electrochemical Desorption ofn-Alkylthiol SAMs on Polycrystalline Gold: Studies Using A Ferrocenylalkylthiol Probe†. *Langmuir 23*, 292–296.

[121] Bouguelia, S., Roupioz, Y., Slimani, S., Mondani, L., Casabona, M. G., Durmort, C., Vernet, T., Calemczuk, R., and Livache, T. (2013) On-chip microbial culture for the specific detection of very low levels of bacteria. *Lab on a Chip 13*, 4024.

[122] Livache, T., Maillart, E., Lassalle, N., Mailley, P., Corso, B., Guedon, P., Roget, A., and Levy, Y. (2003) Polypyrrole based DNA hybridization assays: study of label free detection processes versus fluorescence on microchips. *Journal of Pharmaceutical and Biomedical Analysis 32*, 687–696.

[123] Suraniti, E., Sollier, E., Calemczuk, R., Livache, T., Marche, P. N., Villiers, M.-B., and Roupioz, Y. (2007) Real-time detection of lymphocytes binding on an antibody chip using SPR imaging. *Lab on a Chip 7*, 1206.

[124] Roupioz, Y., Berthet-Duroure, N., Leïchlé, T., Pourciel, J.-B., Mailley, P., Cortes, S., Villiers, M.-B., Marche, P. N., Livache, T., and Nicu, L. (2009) Electrochemical deposition: Small 13/2009. *Small 5*, NA–NA.

[125] Kleiveland, C. R. *The Impact of Food Bioactives on Health*; Springer International Publishing, 2015; pp 161–167.

[126] Deegan, R. D., Bakajin, O., Dupont, T. F., Huber, G., Nagel, S. R., and Witten, T. A. (1997) *Nature 389*, 827–829.

[127] Adachi, E., Dimitrov, A. S., and Nagayama, K. (1995) Stripe Patterns Formed on a Glass Surface during Droplet Evaporation. *Langmuir 11*, 1057–1060.

[128] Eral, H. B., Augustine, D. M., Duits, M. H. G., and Mugele, F. (2011) Suppressing the coffee stain effect: how to control colloidal self-assembly in evaporating drops using electrowetting. *Soft Matter 7*, 4954.

[129] Deegan, R. D., Bakajin, O., Dupont, T. F., Huber, G., Nagel, S. R., and Witten, T. A. (2000) Contact line deposits in an evaporating drop. *Physical Review E 62*, 756–765.

[130] Blossey, R., and Bosio, A. (2002) Contact Line Deposits on cDNA Microarrays: A "Twin-Spot Effect". *Langmuir 18*, 2952–2954.

[131] McHale, G. (2007) Surface free energy and microarray deposition technology. *The Analyst 132*, 192.

[132] Djaldetti, M., and Bessler, H. (2014) Mononuclear cells phagocytic activity affects the crosstalk between immune and cancer cells. *Biomedicine & Pharmacotherapy 68*, 679–683.

[133] Freshney, R. I. *Culture of Animal Cells*; John Wiley & Sons, Inc., 2010.

[134] Kaur, G., and Dufour, J. M. (2012) Cell lines. *Spermatogenesis 2*, 1–5.

[135] Oie, H. K., Gazdar, A. F., Minna, J. D., Weir, G. C., and Baylin, S. B. (1983) Clonal Analysis of Insulin and Somatostatin Secretion and L-Dopa Decarboxylase Expression by a Rat Islet Cell Tumor. *Endocrinology 112*, 1070–1075.

[136] Ai, W., Li, H., Song, N., Li, L., and Chen, H. (2013) Optimal Method to Stimulate Cytokine Production and Its Use in Immunotoxicity Assessment. *International Journal of Environmental Research and Public Health 10*, 3834–3842.

[137] Tsuchiya, S., Yamabe, M., Yamaguchi, Y., Kobayashi, Y., Konno, T., and Tada, K. (1980) Establishment and characterization of a human acute monocytic leukemia cell line (THP-1). *International Journal of Cancer 26*, 171–176.

[138] Bosshart, H., and Heinzelmann, M. (2016) THP-1 cells as a model for human monocytes. *Annals of Translational Medicine 4*, 438–438.

[139] da Silva Sousa-Vasconcelos, P., da Silva Seguins, W., de Souza Luz, E., and de Pinho/, R. T. (2015) Pattern of cytokine and chemokine production by THP-1 derived macrophages in response to live or heat-killed Mycobacterium bovis bacillus Calmette-Guérin Moreau strain. *Memórias do Instituto Oswaldo Cruz 110*, 809–813.

[140] Müller, G. *Drug Discovery and Evaluation: Pharmacological Assays*; Springer International Publishing, 2016; pp 3029–3057.

[141] Gazdar, A. F., Chick, W. L., Oie, H. K., Sims, H. L., King, D. L., Weir, G. C., and Lauris, V. (1980) Continuous, clonal, insulin- and somatostatin-secreting cell lines established from a transplantable rat islet cell tumor. *Proceedings of the National Academy of Sciences 77*, 3519–3523.

[142] Subash-Babu, P., Ignacimuthu, S., and Alshatwi, A. (2015) Nymphayol increases glucose-stimulated insulin secretion by RIN-5F cells and GLUT4-mediated insulin sensitization in type 2 diabetic rat liver. *Chemico-Biological Interactions 226*, 72–81.

[143] Asfari, M., Janjic, D., Meda, P., Li, G., Halban, P. A., and Wollheim, C. B. (1992) Establishment of 2-mercaptoethanol-dependent differentiated insulin-secreting cell lines. *Endocrinology 130*, 167–178.

[144] Hamid, M., McCluskey, J. T., McClenaghan, N. H., and Flatt, P. R. (2002) Comparison of the secretory properties of four insulin secreting cell lines. *Endocrine Research 28*, 35–47.

[145] Aspinwall, C. A., Lakey, J. R., and Kennedy, R. T. (1999) Insulin-stimulated insulin secretion in single pancreatic beta cells. *The Journal of Biological Chemistry 274*, 6360–6365.

[146] Liao, W., Lin, J.-X., and Leonard, W. J. (2011) IL-2 family cytokines: new insights into the complex roles of IL-2 as a broad regulator of T helper cell differentiation. *Current Opinion in Immunology 23*, 598–604.

[147] Gaffen, S., and Liu, K. (2004) Overview of interleukin-2 function, production and clinical applications. *Cytokine 28*, 109–123.

[148] Schoenborn, J. R., and Wilson, C. B. *Advances in Immunology*; Elsevier, 2007; pp 41–101.

[149] Schroder, K., Hertzog, P. J., Ravasi, T., and Hume, D. A. (2003) Interferon-γ: an overview of signals, mechanisms and functions. *Journal of Leukocyte Biology 75*, 163–189.

[150] Riedhammer, C., Halbritter, D., and Weissert, R. *Methods in Molecular Biology*; Springer New York, 2014; pp 53–61.

[151] Collins, D. P. (2000) Cytokine and cytokine receptor expression as a biological indicator of immune activation: important considerations in the development of in vitro model systems. *Journal of Immunological Methods 243*, 125–145.

[152] Kalliolias, G. D., and Ivashkiv, L. B. (2015) TNF biology, pathogenic mechanisms and emerging therapeutic strategies. *Nature Reviews Rheumatology 12*, 49–62.

[153] Sharma, S., Byrne, H., and O'Kennedy, R. J. (2016) Antibodies and antibody-derived analytical biosensors. *Essays In Biochemistry 60*, 9–18.

[154] Hassanzadeh-Ghassabeh, G., Devoogdt, N., Pauw, P. D., Vincke, C., and Muyldermans, S. (2013) Nanobodies and their potential applications. *Nanomedicine 8*, 1013–1026.

[155] Dunn, M. R., Jimenez, R. M., and Chaput, J. C. (2017) Analysis of aptamer discovery and technology. *Nature Reviews Chemistry 1*, 0076.

[156] Tuerk, C., and Gold, L. (1990) Systematic evolution of ligands by exponential enrichment: RNA ligands to bacteriophage T4 DNA polymerase. *Science 249*, 505–510.

[157] Liu, Y., Zhou, Q., and Revzin, A. (2013) An aptasensor for electrochemical detection of tumor necrosis factor in human blood. *The Analyst 138*, 4321.

[158] Liu, Y., Kwa, T., and Revzin, A. (2012) Simultaneous detection of cell-secreted TNF-α and IFN-γ using micropatterned aptamer-modified electrodes. *Biomaterials 33*, 7347–7355.

[159] Liu, Y., Liu, Y., Matharu, Z., Rahimian, A., and Revzin, A. (2015) Detecting multiple cell-secreted cytokines from the same aptamer-functionalized electrode. *Biosensors and Bioelectronics 64*, 43–50.

[160] Liu, Y., Rahimian, A., Krylyuk, S., Vu, T., Crulhas, B., Stybayeva, G., Imanbekova, M., Shin, D.-S., Davydov, A., and Revzin, A. (2017) Nanowire Aptasensors for Electrochemical Detection of Cell-Secreted Cytokines. *ACS Sensors 2*, 1644–1652.

[161] Kumar, L. S. S., Wang, X., Hagen, J., Naik, R., Papautsky, I., and Heikenfeld, J. (2016) Label free nano-aptasensor for interleukin-6 in protein-dilute bio fluids such as sweat. *Analytical Methods 8*, 3440–3444.

[162] Farid, S., Meshik, X., Choi, M., Mukherjee, S., Lan, Y., Parikh, D., Poduri, S., Baterdene, U., Huang, C.-E., Wang, Y. Y., Burke, P., Dutta, M., and Stroscio, M. A. (2015) Detection of Interferon gamma using graphene and aptamer based FET-like electrochemical biosensor. *Biosensors and Bioelectronics 71*, 294–299.

[163] Hashim, S. N., Tsuchiya, A., Kamiya, N., and Sando, S. (2015) A Single Fluorophore-labeled Aptamer Sensor for the Detection of Interferon Gamma. *Chemistry Letters 44*, 1670–1672.

[164] Liu, Y., Tuleouva, N., Ramanculov, E., and Revzin, A. (2010) Aptamer-Based Electrochemical Biosensor for Interferon Gamma Detection. *Analytical Chemistry 82*, 8131–8136.

[165] Orava, E. W., Jarvik, N., Shek, Y. L., Sidhu, S. S., and Gariépy, J. (2013) A Short DNA Aptamer That Recognizes TNFα and Blocks Its Activity *in Vitro*. *ACS Chemical Biology 8*, 170–178.

[166] Daniel, C. Aptamer biochip : Exploration of an alternative detection technique. Theses, Université de Grenoble, 2013.

[167] de Castro, E., Sigrist, C. J. A., Gattiker, A., Bulliard, V., Langendijk-Genevaux, P. S., Gasteiger, E., Bairoch, A., and Hulo, N. (2006) ScanProsite: detection of PROSITE signature matches and ProRule-associated functional and structural residues in proteins. *Nucleic Acids Research 34*, W362–W365.

[168] Nübel, C., Appel, B., Hospach, I., Mai, M., Krasteva, N., Nelles, G., Petruschka, L., and Müller, S. (2016) Challenges and Opportunities in the Development of Aptamers for TNFα. *Applied Biochemistry and Biotechnology 179*, 398–414.

[169] Scientific, T. F. Imject BSA (in PBS). `http://www.thermofisher.com/order/catalog/product/77110`.

[170] Northrop, B. H., Frayne, S. H., and Choudhary, U. (2015) Thiol–maleimide "click" chemistry: evaluating the influence of solvent, initiator, and thiol on the reaction mechanism, kinetics, and selectivity. *Polymer Chemistry 6*, 3415–3430.

4

Nanostructured optical fibers as potential *in vivo* sensing systems

Contents

4.1 Scientific context

Even before their widespread use for data communications, optical fibers have been extensively exploited in medicine[1,2]. This is specially the case for endoscopy, where they provide a suitable platform for minimally invasive procedures as they are non-toxic, very thin and flexible, chemically inert under physiological conditions and can be easily sterilized by standard methods[2–4].

However, their clinical uses are not limited only to their use as illuminating devices. By employing lasers with higher output power, it is possible to cut or ablate tissues in an extremely localized manner[2]. Moreover, their immunity to high intensity electromagnetic fields, radiofrequences and microwave signals, permits their use for real-time monitoring of patients during Magnetic Resonance Imaging (MRI), Computed Tomography (CT) or Positron Emission Tomography (PET) scans without risks of an electric shock, contrary to conventional electronic devices[2,5].

Other features such as their excellent light propagation and relatively low costs, make optical fibers a suitable transduction element for biosensing[6] (Figure 4.1). On this regard, sensors based on optical fibers (known as Fiber-Optic Sensors or FOS) have already been developed as researching tools for *in vivo* and *ex vivo* studies involving pathogen detection[7–9], protein kinetics[10,11], biofilm formation[12,13], diagnosis/monitoring of diseases[6,14,15].

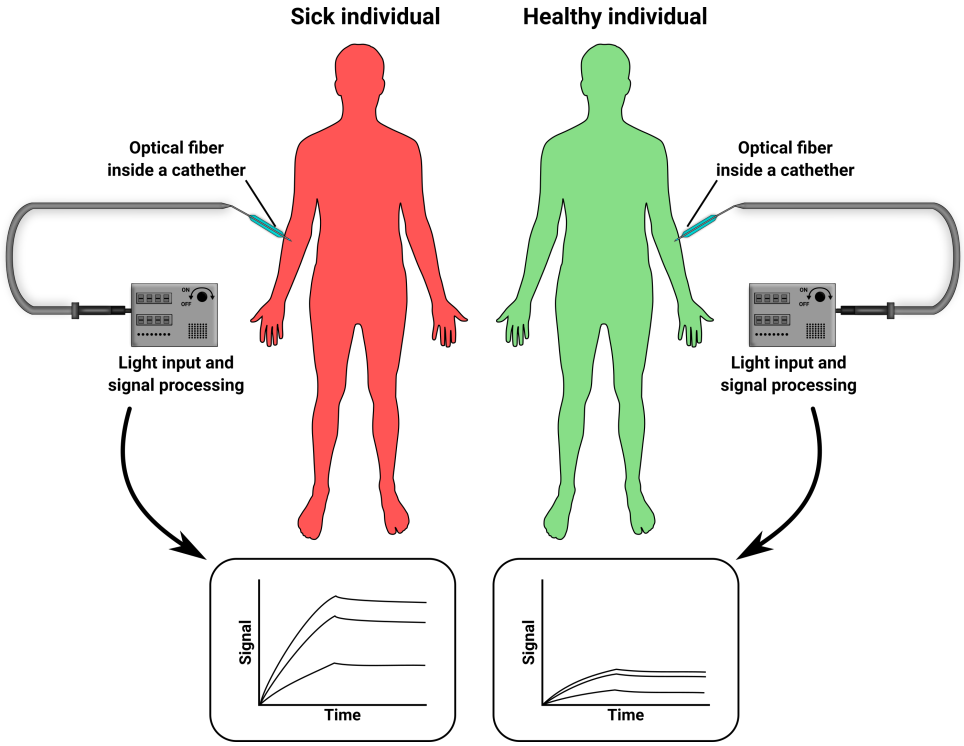

Figure 4.1 – Illustration of fiber-optic biosensors for point-of-care testing of two individuals (one of which presents a medical condition).

4.1.1 Light transmission in optical fibers

Before we continue talking about the use of optical fibers as sensors, we should introduce some basic functional aspects of optical fibers. However, as an in-depth explanation regarding the physics of light propagation inside the optical fibers is out of the scope of this PhD thesis, we will only present a brief overview of its main principles. For further details, please refer to Hasegawa[16] (whose review describes the basis of information transfer in optical fibers), Senior[17] (specifically Chapter 2, regarding the basis of light propagation) and Leung et al.[18] (review focused on the principles behind fiber-optic sensors).

Briefly, optical fibers are a type of waveguide (a structure that guides electromagnetic waves by limiting its propagation to 1-2 dimensions). They are typically composed by two elements: a core and a cladding. In its simplest form, the core consists of a high optical index material located at the center of the optical fiber, surrounding it is the cladding which presents a slightly lower optical index. Following Snell's law (Equation 1.1), as described in Chapter 1 section 1.2.1, if light enters in the core at an incident angle (θ_i) larger than the critical angle (θ_c, defined as the angle whose refraction is 90°), it will experience the phenomenon of Total Internal Reflection (TIR) allowing its propagation through the fiber[18].

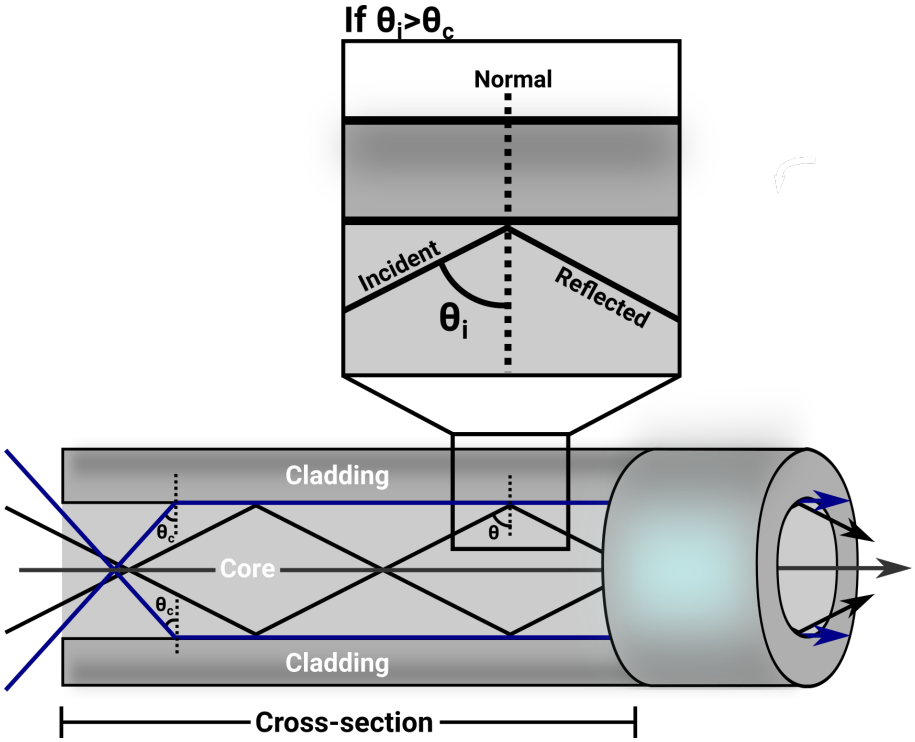

Figure 4.2 – Graphical representation of the phenomenon of Total Internal Reflection (TIR) through an optical fiber.

The way that light propagates vastly depends on the type of fiber that is being used. As there is an enormous amount of different optical fibers, we will limit our discussion to three types which have been designed for light transmission (passive fibers) and not for

signal amplification (active fibers).

In the case of passive fibers (illustrated in Figure 4.3), we can mention[18]:

— **Step-index fibers:** These fibers are characterized by a constant refractive index in the core (and the cladding)[18]. Their fabrication is relatively simple and these fibers are commonly used on most commercial applications.

— **Graded-index fibers:** These exhibit a gradual decrease in the RI from the center axis outwards[18]. This structure results in a reduced attenuation (which is the loss of intensity over the transmitted distance) but with a more complex and costly fabrication compared to step-index fibers.

— **Photonic crystal fibers (PCF):** In this case, the cladding is composed by air holes arrayed into a photonic crystal[19]. Photonic crystals are periodic structures able to control the transmission of light. By controlling the separation between the air holes and their diameter, it is possible to strictly regulate which wavelengths can: propagate into the crystal structure, be transmitted via reflection inside the core or being trapped[20]. Furthermore, the core can be composed either by a solid material (solid-core PCFs) or an air hole (hollow-core PCFs) in the center of the photonic crystal[19]. Theoretically, the PCFs present the lower attenuation from the three types of fibers[19], but, due to their complexity, their use of PCFs for sensing applications has not been widely explored.

Based on parameters such as the diameter of the cores, the wavelength of the propagated light and the refractive index of the core-cladding system, light can be transmitted in single or multiple ways[16]. These ways or paths of propagation are called modes. In the case of Single-Mode Fibers (SMF), the small diameter of the cores allow only one mode of propagation of the light making them efficient for high frequency data transmission as they present lower attenuation (as there is no real reflection since light follows an almost linear trajectory)[18]. In contrast, in Multi-Mode Fibers (MMF) light can travel in many possible ways through the cores[18] for which they are used for illumination purposes or short-distance transmission of light at high intensity (such as in laser-based cutting devices).

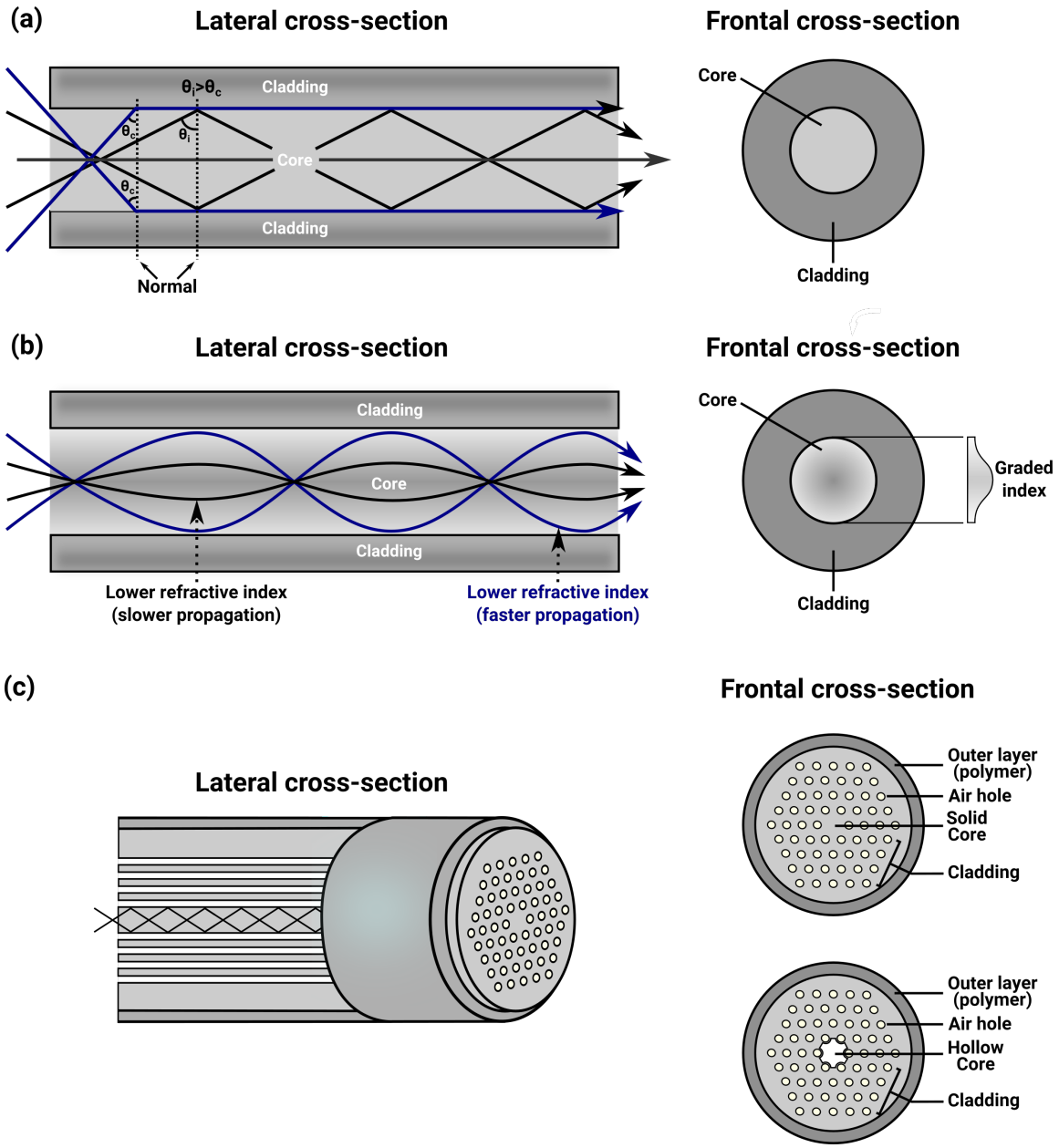

Figure 4.3 – Schematic representation of (a) Step-index, (b) graded-index and (c) photonic crystal optical fibers.

4.1.2 Fiber-Optic Sensors (FOS)

So far, the descriptions and applications that we have mentioned about optical fibers are based on the fact that they have been designed for efficient transmission of light. However, in order to be efficiently transmitted, the light has to avoid external interference and so, the cores are relatively isolated from the environment except at their end-faces which work as input/output points.

Considering that the light propagating through the core of a fiber is isolated from the

environment, the use of optical fibers as sensing devices can seem a little bit paradoxical as such application requires interaction of the light with the surroundings. Nonetheless, the development of sensors based on optical fibers can be achieved by different strategies, one of which, evanescent field-based sensors, consists in exploiting an interesting feature of the light under TIR.

Light propagating via TIR is composed by two different components: a guided wave and an evanescent wave (Figure 4.4). The guided wave corresponds to the light reflected back into the core by TIR while the evanescent wave is the result of the penetration, outside the boundary of the core, of the electric and magnetic fields of the reflected light[18]. This evanescent wave (called evanescent field as well) exponentially decays as it penetrates the media outside the core. Since the evanescent wave is a product from the electromagnetic fields of the incident light, fluctuations in the refractive index inside the evanescent field will shift the critical angle for TIR and so, the intensity of the light reflected to the core.

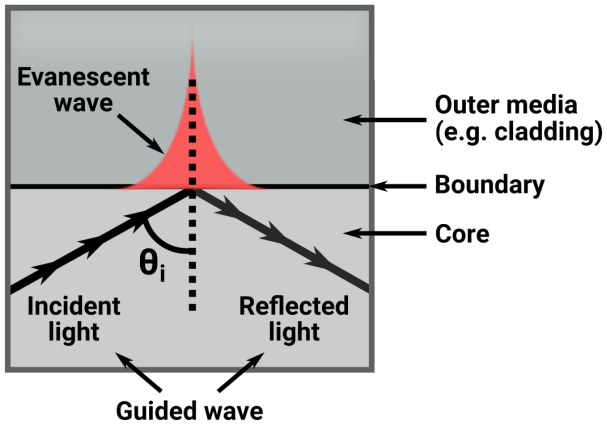

Figure 4.4 – Evanescent field at the core-cladding interface as light undergoes TIR.

Sensors based on optical fibers (commonly referred as Fiber-Optic Sensors, FOS) can be produced by using this phenomena either directly or with a signal amplification method.

4.1.2.a Non-amplified sensitivity

In case of non-amplified FOS, the sensing can be performed either at the end-face or in the lateral face of the fiber.

In the case of sensing at the end-face, intensity shifts in the retroreflected light are monitored based on fluctuations in the refractive index of the environment nearby one of the terminal faces. However, this method is rarely used without an amplification strategy as the changes in retroreflected light intensity are very slight.

On the other hand, lateral sensing can be performed by removing (totally or partially) the cladding of the fiber. Under such conditions, the external media (either air or a liquid solution) will act as a cladding and fluctuations in its RI will affect the propagation of the light. This method provides a larger surface of interaction as it depends only on the

unclad zone while the end-face approach is limited by the diameter of the core (usually in micrometric range). Unfortunately, the cladding provides mechanical resistance to the fiber and so, unclad fibers are extremely fragile and prone to breakage.

4.1.2.b Amplified sensitivity

Thin film coatings have become a widely used method for improving the sensitivity and even providing some range of selectivity to FOS[21]. Some of these functional coatings can interact with specific analytes providing a measurable signal such as the evanescent-field FOS created by Matsuo et al.[22]. In their work, they deposited a thin layer of an organic dye, TetraBromo Phenol Blue (TBPB), over the core of optical fibers. When the analyte (albumin) combines with TBPB, the optical absortion spectrum of this dye changes. As the film is inside the penetration range of the evanescent field, a measurable shift in the propagation of the guided wave occurs.

Other examples of functional films allows the monitoring of hydrogen[23], oxygen[24,25], humidity[26,27], among several others[28]. However, we will focus on metallic films as they allow the use of Surface Plasmon Resonance (SPR) which is an extensively used technique in our research team.

As explained in Chapter 1 section 1.2, this phenomenon occurs due to the excitation of Surface Plasmon Polaritons (SPPs) at the metal-liquid/air interface by the evanescent wave created at the core-metal interface due to TIR of incident light (Chapter 1 Figure 1.3). For this excitation to occur, specific coupling conditions (related to the wavelength, type of metal, thickness of the metal layer, refractive index of the air/liquid medium, etc) have to be achieved. These coupling conditions are highly sensitive to fluctuations in the refractive index of the medium probed by the SPP's evanescent field, causing sharp dips in the light intensity[29].

4.1.3 Configurations of SPR-based FOS

Diverse configurations for SPR-based FOS have been designed and described in the literature. Each system has different properties focused either on improving the sensitivity, accuracy, repeatability and/or the limit of detection (LOD)[29]. As for non-amplified sensing methods, SPR-based FOS can also be used for either lateral or end-face sensing. Based on this, we can categorize them as: (a) geometry-modified lateral sensing, (b) grating-assisted lateral sensing and (c) end-face sensing. In Figure 4.5 some representative examples are graphically depicted.

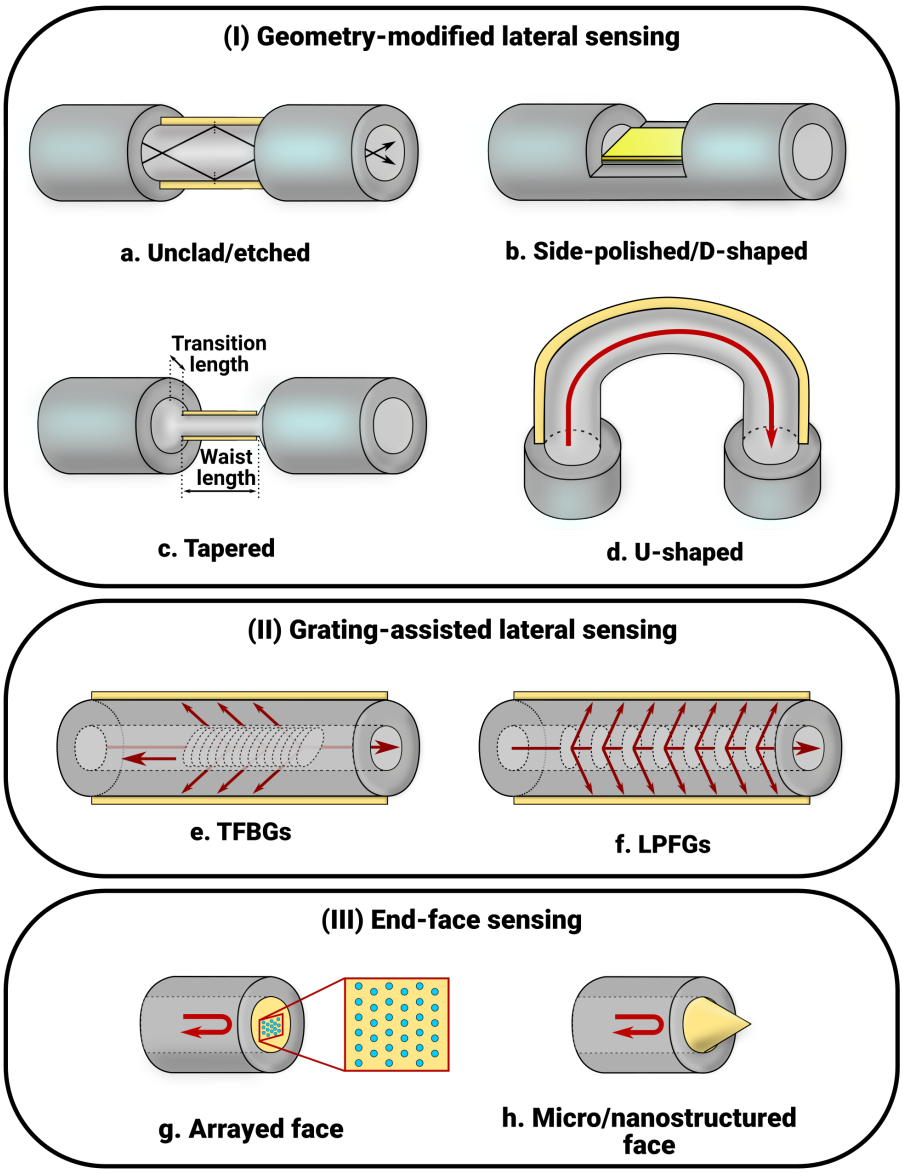

Figure 4.5 – Different SPR-based FOS configurations. (I) Geometry-modified lateral sensing: (a) unclad/etched fibers, (b) side-polished/D-shaped fiber, (c) tapered fiber, (d) U-shaped fiber; (II) Grating-assisted lateral sensing: (e) LPFGs, (f) TFBGs; and (III) End-face sensing: (g) arrayed face, (h) micro/nanostructured face. Modified from Caucheteur et al.[30]

4.1.3.a Geometry-modified lateral sensing

The simplest configuration of this category is based on the removal of the cladding (partial or complete) via chemical etching or side-polishing (Figure 4.5a,b). Since cladding removal drastically reduces the mechanical resistance of the fibers, this technique is usually done on cores with rather large diameters (200-600 µm)[30–32]. A variant of this approach consists in the localized removal of the cladding using a laser source, this treatment exposes only

a narrow strip of the core where the metal can be deposited[30]. In this case, even when using multimode fibers, only a narrow range of incidence angles are able to generate SPR phenomena. However, the use of such small detection areas makes these sensors highly susceptible to background noise.

Another configuration is that of tapered fibers (Figure 4.5c). These can be produced by gently stretching the fiber during intense heating. Such process makes the fibers thinner on some regions which can be unclad and metallized[30]. In the tapered zones, the magnitude of the evanescent field is increased making the system more sensitive[18].

A different way to increase the evanescent field can be done through the bending of the optical fiber[33,34]. Commonly this is done by creating a U-shaped probe as shown in Figure 4.5d. These fibers present an evanescent field with greater penetration depth and the great advantage of having the input and output almost at the same location, facilitating the monitoring[18,34].

Finally, other configurations, such as hetero-core structures, are possible as well but less commonly employed[30].

4.1.3.b Grating-assisted lateral sensing

Contrary to the previous examples, grating-assisted FOS do not require the fibers to be unclad and so, preserve the mechanical integrity of the fiber. For the generation of the SPR phenomena, these fibers contain photo-patterned gratings on the core which are able to diffract part of the light directly into the cladding where it can interact with the metallic layer[30]. In Figure 4.5, two different types of these fibers are shown: (e) Tilted Fiber Bragg Gratings (TFBGs) and (f) Long Period Fiber Gratings (LPFGs). Both types present distinct characteristics that have been reviewed elsewhere[30,35].

4.1.3.c End-face sensing

In contrast to most of the previous configurations (except for U-shaped fibers), end-face sensing provides an attractive advantage for *in vivo* monitoring. By using one terminal face for probing while the other serves as input/output of the light, the sampling becomes considerably more practical. Furthermore, by reducing the contact zone to only the end-face, the sensing procedure is assured to be minimally invasive while the risk of breakage or cleavage of the fiber inside the organism is negligible.

Some strategies for end-face monitoring consist in the use of nano-patterning technologies[30]. These methods create an array of metallic structures in the FOS terminal face generating a Localized Surface Plasmon Resonance (LSPR) phenomenon. These structures can be either nanoparticles[36], nanodots[37], apertures on a metallic films[38] or hybrid metallo-dielectric structures[39].

Another approach is the use of tapered tips. These structures can be formed either by mechanical stretching or chemical etching. In case of mechanical stretching, the process is similar to the tapered fibers described before. However, instead of gradually stretching

until reaching a constant thickness, these fibers are stretched until the end becomes a peak[18].

4.2 Conception of a nanostructured fiber-bundle SPR-based biochip

The previous compilation of configurations are just some examples of the most common FOS systems, however, in the literature there are numerous variations and completely different approaches to those presented so far[40–45].

All these systems can be used as Fiber-Optic BioSensors (FOBS) by immobilizing a bioreceptor into the metallic layer. Nevertheless, as described in Chapter 3.1, many relevant clinical conditions require the simultaneous analysis of multiple targets, a feature that the configurations described so far are unable to perform.

Regarding this problematic, the use of multi-core fiber bundles is a highly promising solution. These fiber bundles combine several independent fibers into a single one with multiple cores. Then, each core can act as an individual end-face based sensor and, by multiplexed functionalization, Fiber-Optic BioChips (FOBC) can be developed (Figure 4.6).

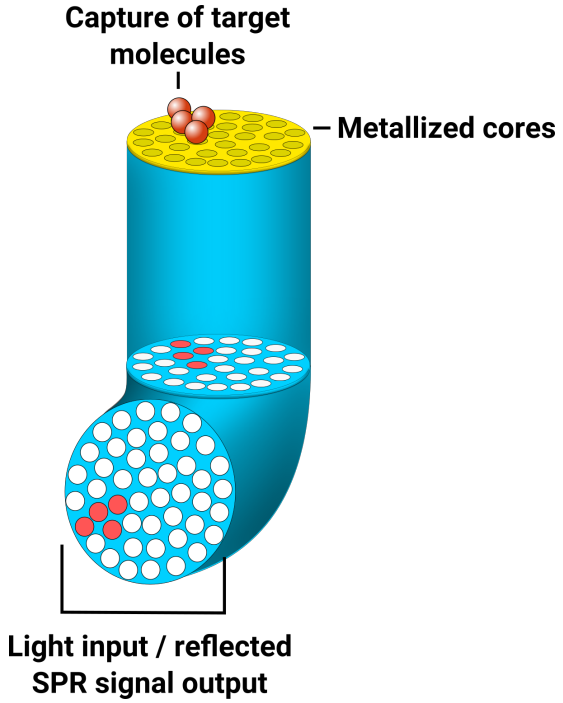

Figure 4.6 – Representation of SPR FOBS on a metallized multicore fiber-bundle.

Using this principle, our research team, in collaboration with several partners at Institut des Sciences Moléculaires (ISM, Bordeaux), Laboratoire d'analyse et d'architecture des systèmes (LAAS, Toulouse) and Institute for Advanced Biosciences (IAB, Grenoble),

decided to develop an optical platform for multiplexed analysis via an ANR (Agence Nationale de la Recherche) project called MOLY (MOLecular endoscopY for remote *in vivo* diagnosis) and constituted the thesis[46] of a former doctoral student from our laboratory, Karim Vindas.

4.2.1 Characteristics of the optical fiber-bundles

The optical fibers used for this project consisted in a bundle of SUMITOMO graded-index fibers which contained 6000 individual cores (Figure 4.7a). As there was some level of heterogeneity in the core size, some cores presented a single propagation mode while others allowed 2-3 modes.

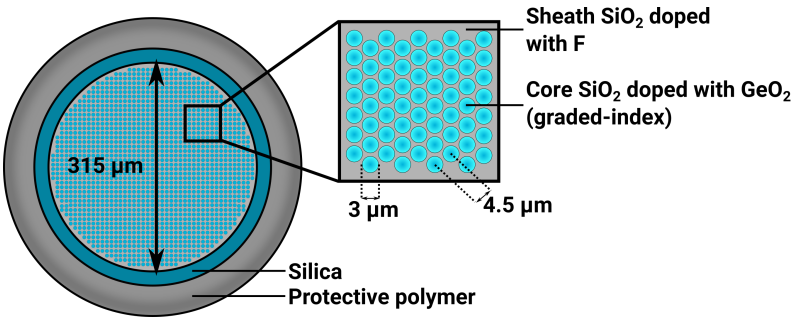

Figure 4.7 – Scheme of a SUMITOMO fiber-bundle before nanostructuration.

Since each core had the capability of acting as an independent sensor, this approach easily surpassed the, theoretical, multiplexing capabilities of the other configurations.

4.2.2 Nanostructuration via chemical etching

However, in order to increase the sensitivity of the system as mentioned in Section 4.1.3.c, the terminal face of the cores required to be modified. For this structuring, our partners exposed the terminal face of the fiber to buffered oxide etch (an etching buffer using a 40% solution of ammonium fluoride (NH_4F), hydrofluoric acid at 48% (HF) and water in a 5:1:1 volume ratio) which dissolves the siloxanes as well as the germanium oxides as described by the next set of reactions[47,48].

$$SiO_2 + 6\,HF \longrightarrow H_2SiF_6 + 2\,H_2O \tag{4.1}$$

$$H_2SiF_6 + 2\,NH_3 \longrightarrow (NH_4)_2SiF_6 \tag{4.2}$$

$$GeO_2 + 6\,HF \longrightarrow H_2GeF_6 + 2\,H_2O \tag{4.3}$$

$$H_2GeF_6 + 2\,NH_3 \longrightarrow (NH_4)_2GeF_6 \tag{4.4}$$

Reactions 4.1 and 4.2 describe the overall attack to silica (SiO_2) by the hydrofluoric acid followed by the ammonia (NH_3). Whereas, reactions 4.1 and 4.2 describe the attack to the germanium oxide. However, the mechanisms underlying these reactions involve several

steps and intermediate species[49]. The first of which is the dissociation of HF in aqueous solution.

$$HF \longrightarrow H^+ + F^- \tag{4.5}$$

Then, F^- anions can interact with un-dissociated acid HF molecules (reaction 4.6) forming bifluoride anions (HF^{2-}) which are considered as the main species responsible for the attack to the silica matrix[49] as described by reaction 4.7 .

$$HF + F^- \longrightarrow {HF_2}^- \tag{4.6}$$

$$SiO_2 + 3\,{HF_2}^- + H^+ \longrightarrow {SiF_6}^{2-} + 2\,H_2O \tag{4.7}$$

The etching solution contains high concentration of ammonium fluoride. At low concentrations it speeds up the etching rate since its dissociation in water (reaction 4.8) generates abundant F^- anions which can react with un-dissociated HF.

$$NH_4F \longrightarrow NH^{4+} + F^- \tag{4.8}$$

Nevertheless, at elevated molar ratios, it slows down the dissolution process by two mechanisms. First, the ${NH_4}^+$ cations interact with the ${HF_2}^-$ avoiding the attack on the silica by this specie[50] and secondly by increasing the pH, which makes the attack by the remaining HF considerably slower[51]. Interesting, due to solubility differences between $(NH_4)_2SiF_6$ and $(NH_4)_2GeF_6$ (on reactions 4.2 and 4.4), a faster dissolution rate of the cladding occurs leading to different micro- and nanostructures by adapting the concentration of the reagents as well as the etching time[52–56] (Figure 4.8).

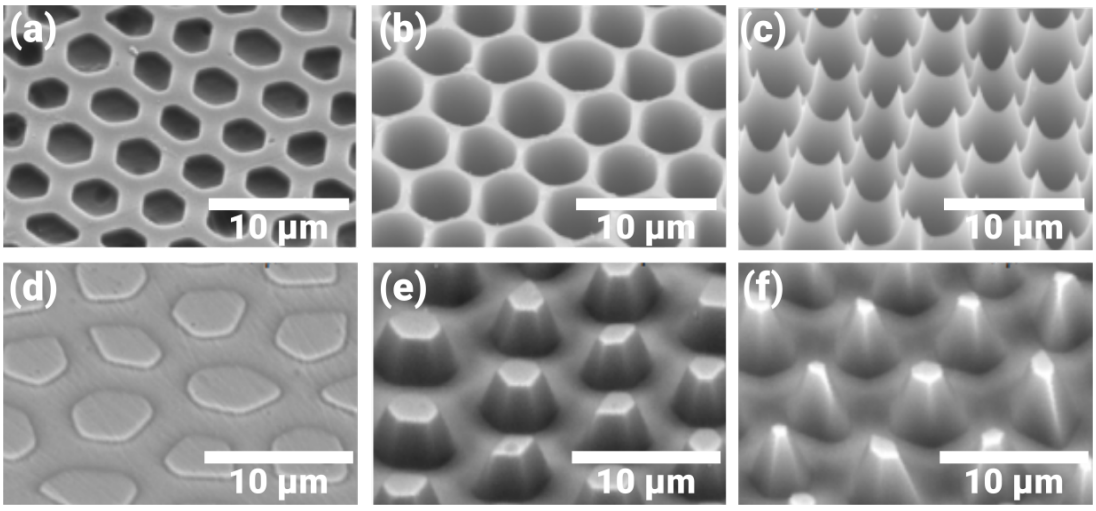

Figure 4.8 – SEM images of optical fibers presenting different core morphologies based on the etching parameters. (a-c) Etching solution in proportions 1:3:1 of NH_4F : HF : H_2O, fibers were exposed for: (a) 20 s, (b) 2 min and (c) 5 min. (d-f) Etching solution in proportions 5:1:1 of NH_4F : HF : H_2O, fibers were exposed for: (d) 2 min, (e) 14 min and (f) 25 min. Images adapted from Deiss[56].

Exploiting this process, Vindas[46] performed the evaluation of multiple tip morphologies for the development of SPR-based FOBS. From his work, it was concluded that truncated cone-like structures were the most suitable for the expected applications (Figure 4.8f).

4.2.3 Metallization of the nanostructures

As SPR was our amplification method of choice, we performed deposition of a thin layer of gold over the nanostructured fibers via Electron Beam Physical Vapor Deposition (EBPVD). This process was performed in the clean room facilities of the "*Plateforme Technologique Amont*" (PTA) at CEA Grenoble, using a MEB550 electron beam evaporator (Plassys, France) with a beam power of 10 kW. The conditions employed for the metallization have been previously optimized[46] and correspond to:

— Etching of the surface for 24 s using Ar^+ ions, removing any organic compounds from the surface that might affect the metal deposition process.

— Deposition of a thin titanium layer (3-4 nm) which served as an adhesion layer due to the poor attachment of gold directly on silica. This layer was performed at 10^{-5} mbar at a speed of 0.1 $nm.s^{-1}$.

— Deposition of a second layer of gold (∼50 nm at the lateral faces of the cones) performed at 10^{-5} mbar at a speed of 0.25 $nm.s^{-1}$.

The whole process was performed on a rotating holder which revolved at a speed of 5 rpm while the amount of deposited material was monitored in real-time by a quartz microbalance system. Due to the geometry of the nanostructures, the gold layer on the flat regions of the truncated cone presented a thickness of ∼150 nm. This region acts as a mirror ensuring the return of the light to the detecting system. Whereas, the layer formed at the sides of the cones (∼50 nm) allowed the generation of plasmonic phenomena (Figure 4.9).

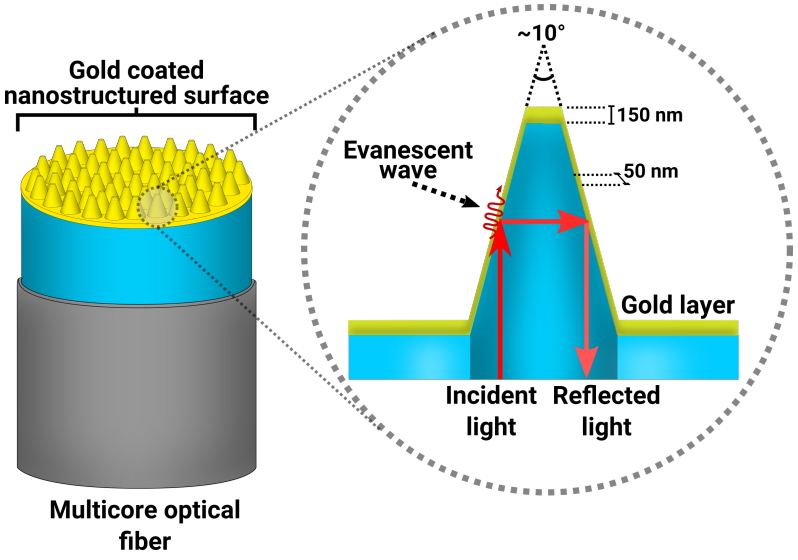

Figure 4.9 – Scheme of metallized nanostructures on the end-face of the fiber-bundle.

4.2.4 Optical setup and optical characterization

After obtaining the metallized fiber-bundles, we performed an optical characterization using the setup developed by Vindas[46] illustrated in Figure 4.10:

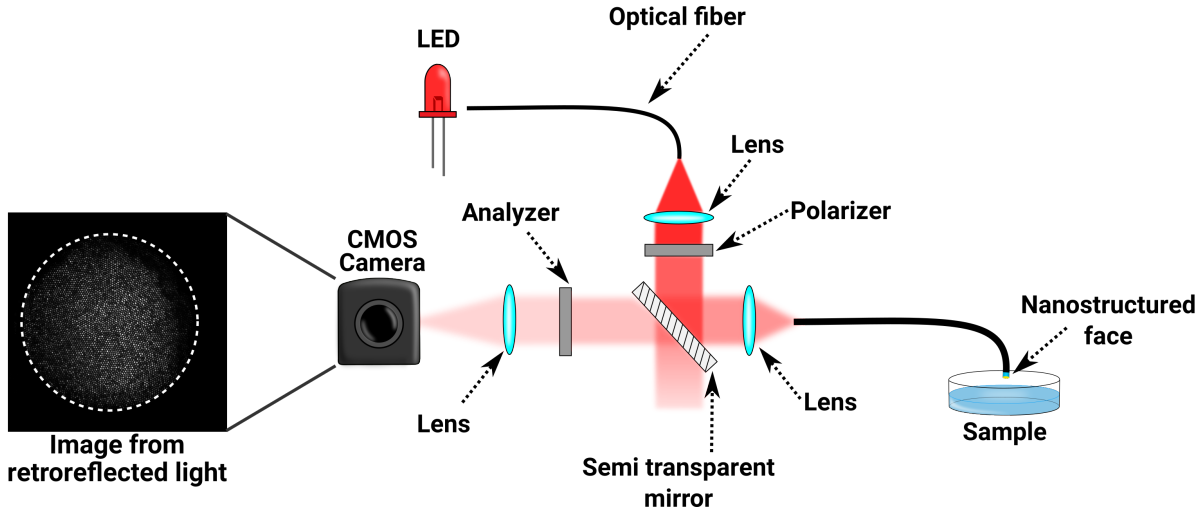

Figure 4.10 – Experimental setup used during characterization of the optical fiber bundles.

As depicted in the previous scheme, this setup consisted in:

- A system of exchangeable electroluminiscent diodes at 8 different wavelengths (455, 530, 590, 625, 660, 740, 780 and 850 nm) whose emission power is easily modulated.
- An optical fiber with a 1 mm ⌀ and numerical aperture (NA): 0.4, that delivers the light from the LED to the set-up.
- A holder for the FOBS which can be adjusted in x, y and z axis for aligning the sensor with the lens.
- A polarizer on a rotary holder .
- A semi-transparent mirror that sends 50% of the light to the imaging lens.
- A 20x Olympus microscope objective as imaging lens (NA: 0.4, long working distance), focused to the cleaved face of the fiber working simultaneously for light injection on the fiber as well as for recollecting the reflected light from the FOBS.
- To improve the signal to noise ratio, an analyzer is positioned in front of the camera to filter light that undergoes specular reflection on the input face of the fiber. This light is reflected back from the non-sensing part of the fiber and thus contributes to the noise.
- Lens with a focal point of 30 cm allowing to focus the image of the fiber on the CMOS device.
- A CMOS cooled camera for rapid image acquisition.

As our final goal consisted in performing SPR measurements in biological fluids, we needed our sensor to be sensitive in the range of refractive indexes at which most biological pro-

cesses occur, which is approximately between 1.34 to 1.37[57]. For the optical characterization of our sensor, we prepared aqueous solutions of varying refractive index (from 1.333 to 1.474) by increasing the concentration of glycerol (refractive index 1.474) in milliQ water (refractive index 1.333). The refractive index of the sample solutions was measured by a digital refractometer (Hanna HI96801).

Then, we measured the SPR response of our fiber-bundle sensor by immersion in the solutions. As the wavelength of the incident light affects the coupling conditions for the SPR phenomena, we performed the experiment using diodes of 590, 660, 740 and 780 nm (Figure 4.11).

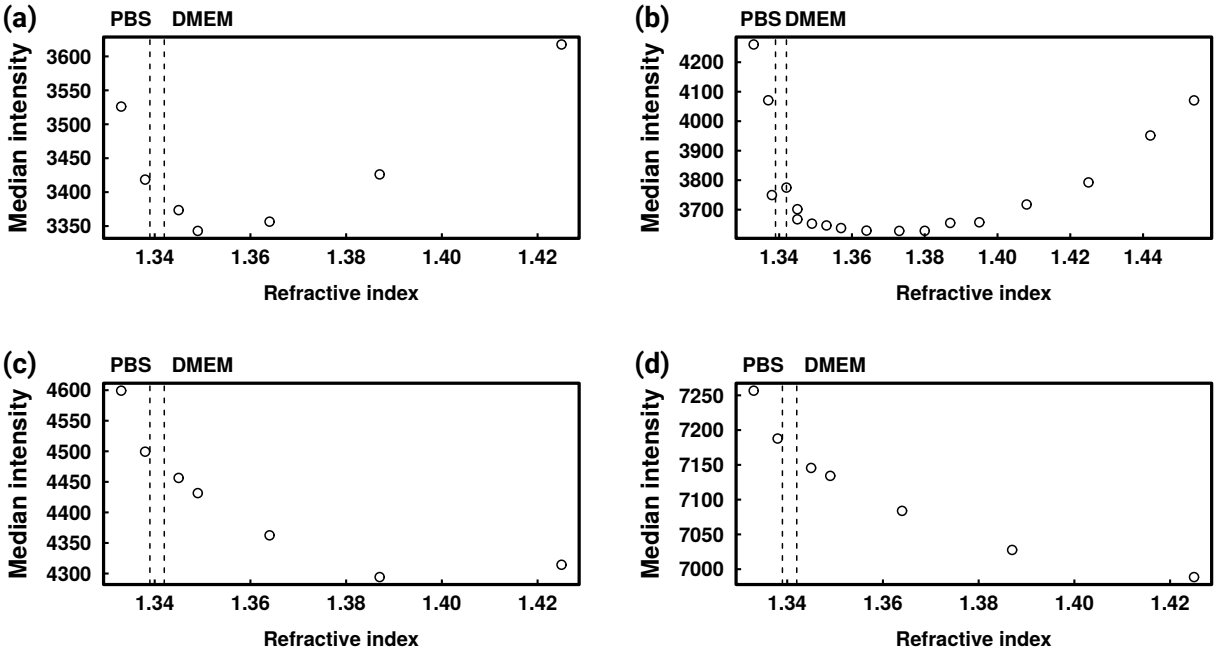

Figure 4.11 – Average SPR response of ∼6000 nanostructured cores exposed to solutions of varying refractive index at different wavelengths: (a) 590, (b) 660, (c) 740 and (d) 780 nm. The refractive index of two common buffers used during biological assays (PBS and the culture media Dulbecco's Modified Eagle's medium, DMEM) are marked in the graphs.

Optical characterization of the fibers showed an adequate response in all the used wavelengths. However, incident light at 660 nm showed the maximum sensitivity in the expected range for biological interactions and so, this wavelength was selected as a candidate for future biosensing assays.

4.2.5 From a sensor to a biochip - Challenges of multiplexed functionalization of optical fiber bundles

As it can be seen from the previous optical characterizations, these fiber-bundles can be effectively used as a SPR-based FOS. In his thesis, Vindas[46] showed the potential of

this system as a biosensor of biological interactions. This was done by using thiol-gold chemistry to immobilize short thiolated oligonucleotides. Then, SPR monitoring allowed the follow-up of the hybridization process with complementary strands of DNA.

Yet, our aim was to develop an optical fiber biochip and thus, multiplexed functionalization of the sensing area had to be performed. We focused on applying different strategies for the arraying of different biomolecules on the nanostructured surface. Nonetheless, some of the properties of the optical fiber-bundle made extremely challenging to perform localized and multiplexed functionalization. Among the main issues that we encountered, we can highlight:

— ***Mechanical fragility:*** Due to their small diameter (total diameter of ∼350 µm), the fibers can break during normal handling. Moreover, the nanostructured face is also sensitive to mechanical stress, limiting functionalization approaches based on contact printing.

— ***Small surface:*** The arraying had to be performed in a very small area (∼ 0.08 mm^2). This required micrometric precision for the alignment of the fiber, as well as the device used for functionalization, in all the axis, thus turning this into a laborious and delicate task. Furthermore, to avoid cross-contamination between the patterned features, either high resolution methods for surface modification or the use of picoliter volumes (incurring in evaporation issues) have been employed.

— ***Surface effects:*** Finally, micro/nanostructuring could create either super hydrophilic or hydrophobic surfaces[58]. This parameter is of utmost relevance specially when using contact-printing approaches. Highly hydrophilic surfaces would expand the deposited droplets of the spotting solution (which contains the biomolecules to be grafted) causing large features (reducing the level of multiplexing) and risking cross-contamination of the bioreceptors. On the other hand, hydrophobic surfaces would not allow the deposition of the spotting solution as the pin difference in wettability of the pin and the surface would inhibit liquid deposition.

To deal with these challenges, we evaluated multiple strategies based on two approaches: microcantilever- and photo-based functionalization techniques.

4.3 Functionalization based on microcontact printing (µCP)

4.3.1 µCP - immobilization via pyrrole electropolymerization

As described before in Chapter 1 section 1.4.2 and Chapter 3 Section 3.2.4.a, electropolymerization of pyrrole-coupled biomolecules over gold surfaces is a powerful and versatile tool to perform localized functionalization[59–63]. This allows the generation of a thin layer of polypyrrole (with a thickness of just a few nanometers[59,60]) keeping the arrayed probes inside the penetration depth of the evanescent field and thus, allowing SPR responses when a biological interactions occurs.

In contrast with the process used on flat gold surfaces, a microcantilever-based approach was implemented for functionalizing the optical fibers. These cantilevers were microfabricated by photolithography at LAAS in Toulouse, with a microfluidic channel and a gold electrode (Figure 4.12a).

Electrochemical functionalization could then be performed by filling the reservoir of the microcantilevers with a spotting solution (electrolytic buffer + free pyrrole + pyrrole-conjugated biomolecules). Then, via direct contact, deposition of picoliter droplets over the nanostructured face of the fiber was performed[46]. During the whole process, a constant difference of potential of 2 V was applied on the system, however, the circuit is closed only during 100 ms at the location of each feature at which the microcantilever (auxiliary electrode) comes in contact with the gold layer (anode) (Figure 4.12b).

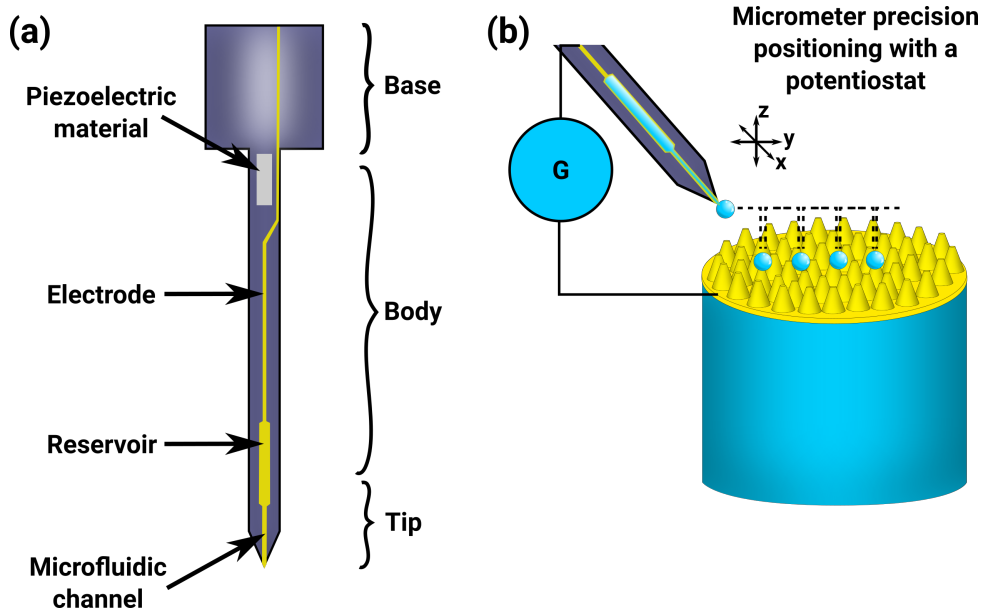

Figure 4.12 – Device used for electropolymerization over the nanostructured face of the fibers. (a) Scheme of a electrode-containing microcantilever, modified from Deiss[56] and (b) droplet deposition and grafting by electropolymerization on the optical fiber.

This approach has been evaluated on nanostructured optical fibers by Descamps et al.[64] as it can be observed in Figure 4.13. They successfully electrodeposited up to 400 microfeatures containing pyrrole-conjugated DNA over the nanostructured face of a similar fiber-bundle.

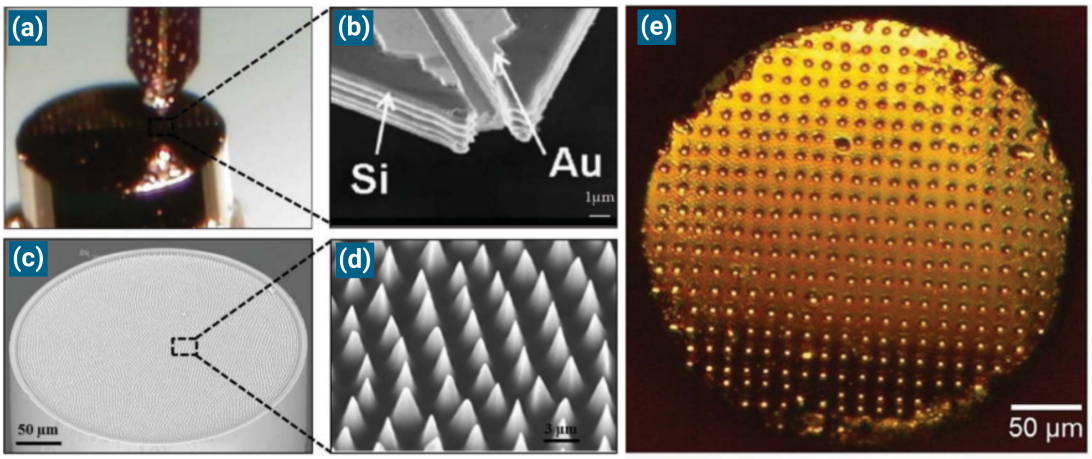

Figure 4.13 – Electrofunctionalization of a nanostructured optical fiber bundle. (a) Microcantilever electrochemically depositing spots over the gold-coated face of an optical fiber bundle; (b) SEM image of microcantilever; (c-d) SEM images of the nanostructured face of the fiber at different magnifications and (e) Nanostructured face with a matrix of 400 spots (pitch of 15 µm). Images taken from Descamps et al.[64].

However, the fibers used by Descamps et al.[64] presented a considerably thicker gold layer since (exact thickness is not specified in their article but), instead of a SPR-based biosensor, they developed an evanescent wave fluorescence-biosensor. This process was repeated and evaluated by Vindas Yassine[46]. Indeed, the method allows correct functionalization of the surface. Nonetheless, as the gold layer in our fibers was considerably thinner, we had to exert a higher pressure over the surface in order to ensure effective contact between the electrodes. By increasing the mechanical stress over the nanostructures, this functionalization procedure caused considerable structural damage on the contact sites, drastically reducing the sensing capabilities of the system (Figure 4.14).

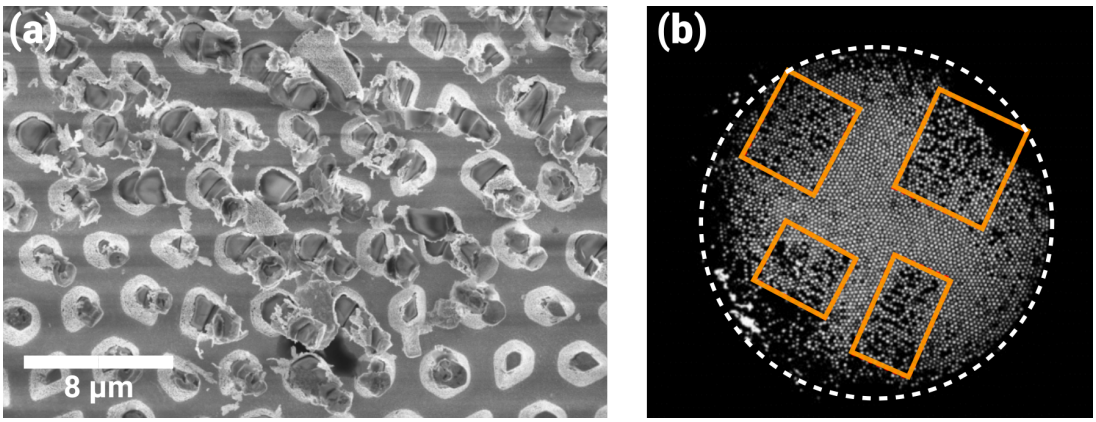

Figure 4.14 – Mechanical damage caused by the microcantilever to the nanostructures on the optical fiber. (a) SEM image showing broken cones in the contact areas and (b) Retroreflection image evidencing the reduction in reflective properties of 4 areas corresponding to the zones of mechanical contact with the microcantilever.

Moreover, the fact that this approach requires electrical contact with the gold layer is in itself a challenging issue. Considering that our metallization system performs a directional deposition of the gold, it results necessary to tilt the fiber in order to obtain a gold film on the side of the fiber. Such tilting produces heterogeneity in the thickness of the gold film at the sides of the truncated cones altering their SPR properties. As using electropolymerization for biomolecule immobilization led to extensive structural damage and modifications to the gold layer, we decided to evaluate a different approach. namely the formation of self-assembled monolayers via thiol-gold interaction.

4.3.2 µCP - immobilization via thiol adsorption

Silicon microcantilevers provided by the LAAS were used as well for this approach. However, contrary to the previous method no voltage was applied (Figure 4.15).

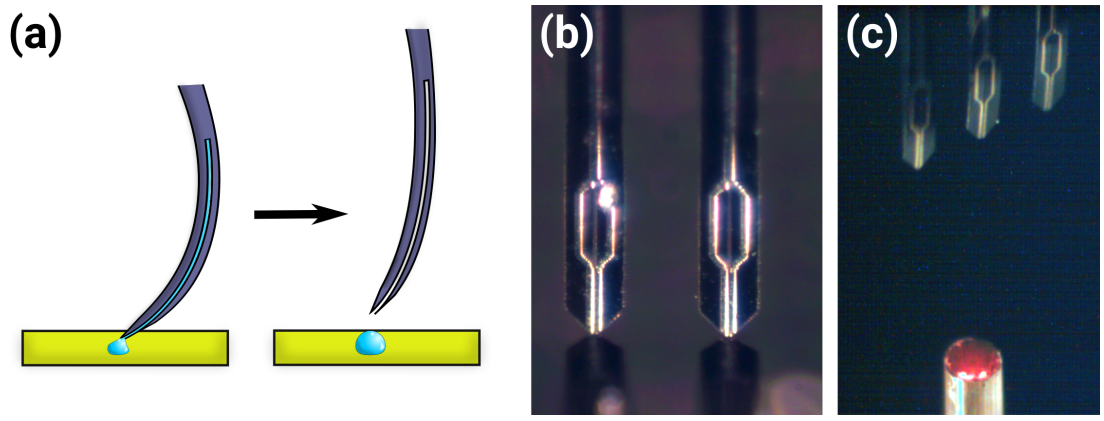

Figure 4.15 – Contact printing with flexible microcantilevers. (a) Scheme of microcantilevers flexing on its internal arc when it applies pressure to a surface, reducing the mechanical stress the cantilever exerts over it; (b) Droplet deposition on using the microcantilevers on flat surfaces and (c) Droplet deposition on using the microcantilevers on nanostructured optical fibers.

Droplet deposition occurred as described for the pin printing method (Chapter 2 Section 2.1.1.a). Briefly, direct contact of the microcantilever with the surface transfers a fraction of the spotting solution into the substrate forming a droplet. The volume of such droplets is determined by the wettability of both surfaces (the tip and the substrate), the viscosity of spotting solution as well as the angle and duration of contact between the tip and the substrate (usually being in the range of nanoliters).

In this case, the functionalization is mediated by interaction of thiol-containing biomolecules with the gold surface, forming Self-Assembled Monolayers (SAMs) as previously described in Chapter 1 Section 1.4. This interaction requires clean gold substrates and so, before each assay we immersed the fibers into piranha solution (H_2SO_4:H_2O_2 in a 3:1 ratio) for 5 min followed by dipping in milli-Q water to remove all potential organic contamination. Piranha solution was used instead of plasma treatment as the latter has been reported to cause significant damage to the gold layer on nanostructured fibers[46].

Characterization assays evaluated the feasibility of performing controlled-size droplets over the gold coated face of the fibers. We used the same optical setup as before but with the nanostructured face of the fibers fixed facing upwards Figure 4.16a. By aid of a set of lenses and a sub-millimetric precision manual controller (Figure 4.16b,c), we aligned the microcantilever with the optical fiber and made contact with the surface in two different regions with a standard buffer solution (PBS + 5% glycerol).

Since the viscosity of the solution affects the efficiency of hollow-pin printing (Chapter 2 Section 2.1.1.a), we added glycerol to simulate the usual spotting buffers; in which this compound slows down the evaporation rate by reducing the vapor pressure of the solution[65]. We monitored the whole process by using a 660 nm diode as light source while recording the retro-reflected light on a CMOS camera. Deposition of the glycerol-containing droplets was confirmed as we observed a strong increase in the intensity of the retro-reflected light on the spotted areas, due to a shift in the SPR angle (Figure 4.16d). However, after 45 min of incubation the droplets fused together which resulted in cross-contamination (Figure 4.16e).

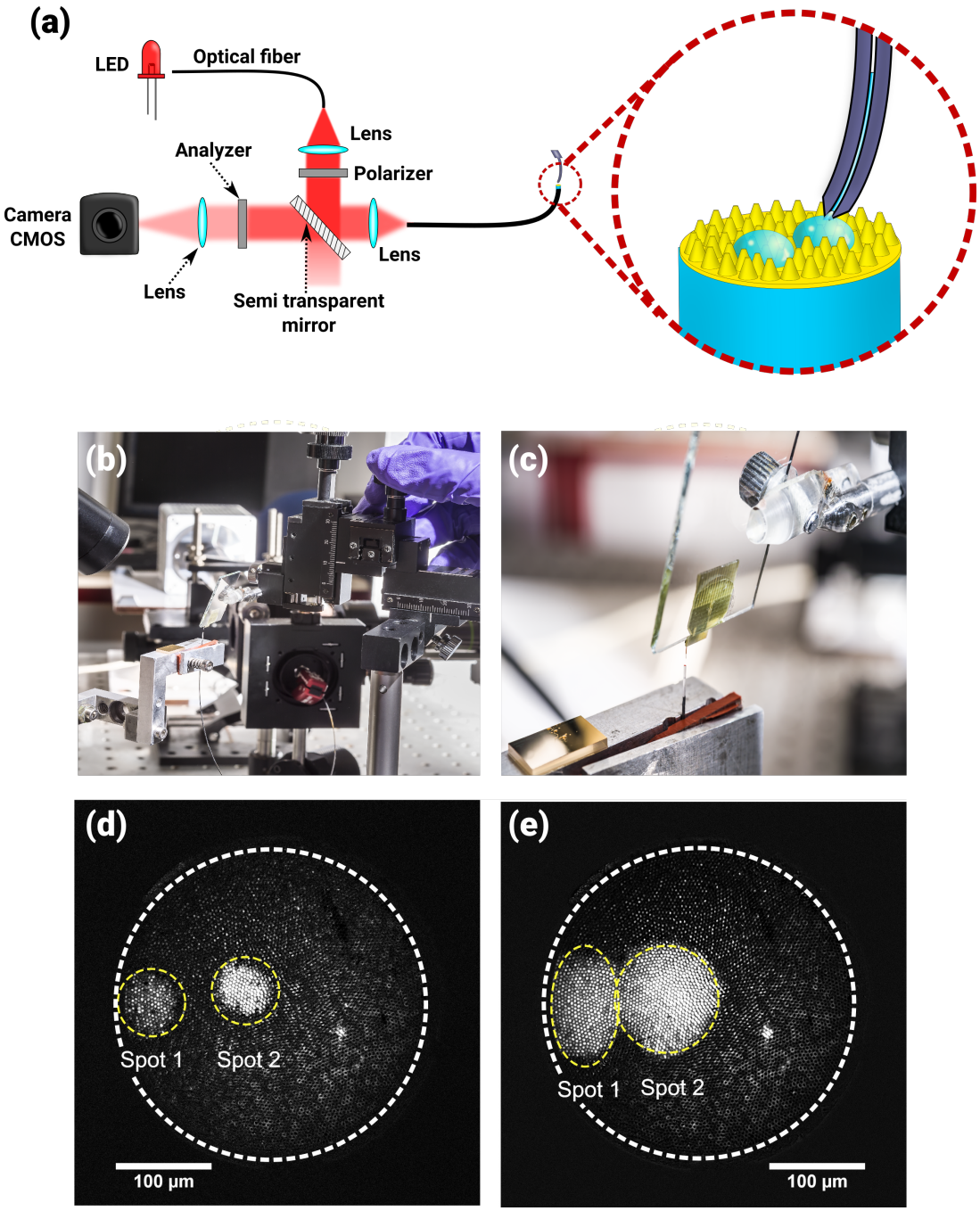

Figure 4.16 – Deposition of a spotting solution (PBS + 5% glycerol) on the nanostructured face of the optical fibers. (a) Experimental setup for SPR monitoring during the droplet deposition; (b,c) Photographies of the µcantilever and the mounting set-up during spotting over the fiber; (d-e) SPRi differential images obtained by the retro-reflected light at (d) 0 min and (e) 45 min after deposition.

Besides the fusion of the spots, we experienced other inconveniences with this approach such as: a big heterogeneity in the deposited volume, imprecision in the contact angle among experiments, clogging issues, great fragility of the microcantilevers and, in some

cases, even splitting of the tip during contact with the nanostructured surface as illustrated in Figure 4.17.

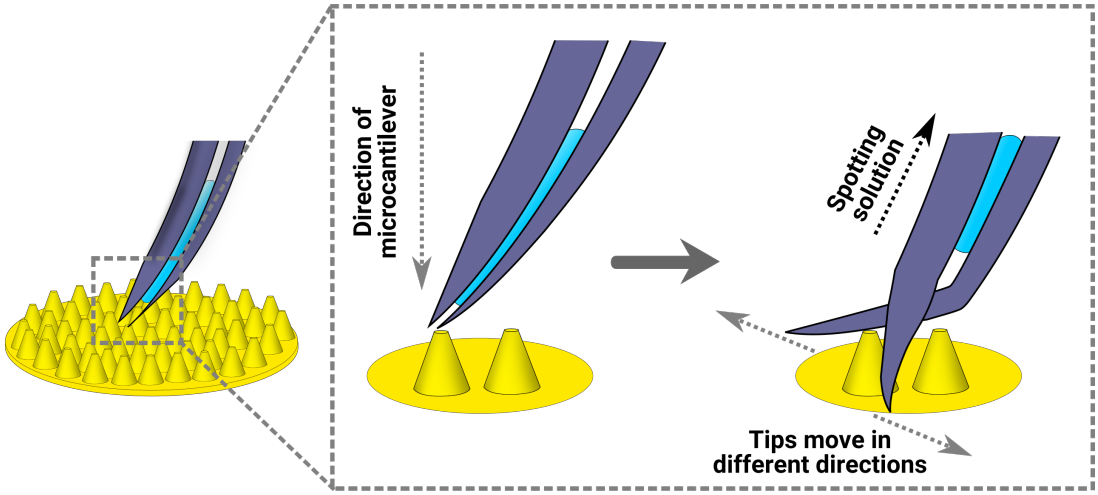

Figure 4.17 – Schematic representation of tip splitting on the cantilevers during contact with nanostructured surface.

Even though pin-based contact printing has been successfully used for functionalizing of flat surfaces, this technique does not seem to be a suited strategy for our system. The nanostructures present on the end-face of the fiber led to non-reproducible results when using this approach and so, we decided to evaluate an indirect contact printing method. In this case, droplets containing the biomolecules of interest can be arrayed on a flat substrate and used as a stamp for the patterning of the terminal face of the fibers (Figure 4.18).

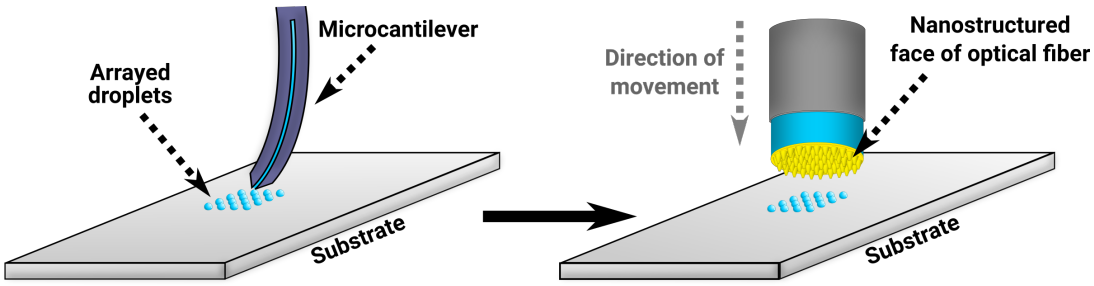

Figure 4.18 – Indirect contact printing on the optical fibers using flexible microcantilevers.

An assay was made as a proof of concept, in this case a gold coated glass slide was used as a flat substrate. In order to reduce the size of each spotted feature, the gold surface was turned hydrophobic by generating a dodecanethiol, $CH_3(CH_2)_{11}SH$, SAM. A solution of the fluorescent molecule fluorescein (1 mg.mL^{-1} in PBS with 5% glycerol) was manually arrayed on the surface and then, with the aid of a sub-millimeter precision manual controller, the nanostructured face of the optical fiber was put in contact with the array (Figure 4.19).

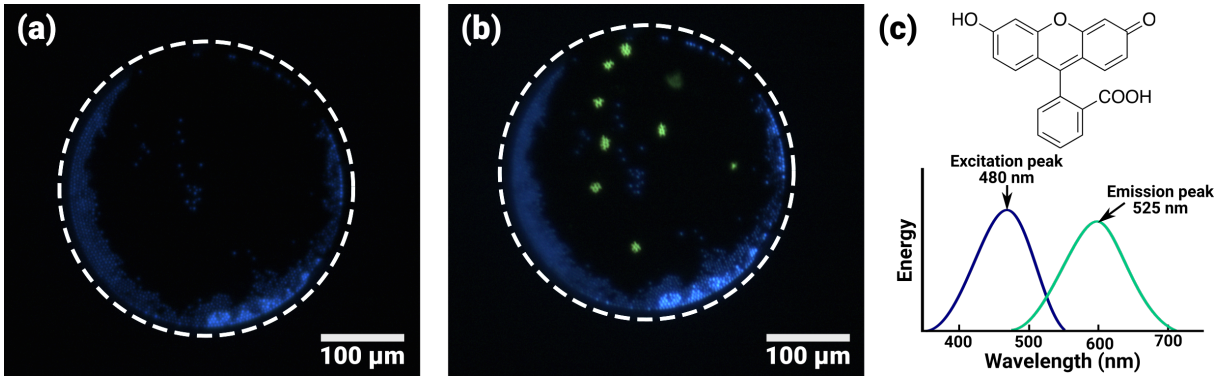

Figure 4.19 – Indirect transfer of a fluorescein-containing solution on the optical fibers. (a-b) Fluorescence imaging of the nanostructured face of the fiber (a) before and (b) after arraying with fluorescein droplets. Exposed germanium-doped cores, zones without a gold layer, emit blue light when irradiated with UV light (340-380 nm). Diameter of the fiber delimited by the white segmented line. (c) Chemical structure of fluorescein with its excitation and emission spectra.

The presence of individual fluorescent spots on the fiber indicates that this approach is feasible, yet highly impractical. This method required a precise parallel alignment of the substrate and the fiber. Under our experimental conditions, the fiber was slightly tilted (at micrometric level) which induced a distortion in the stamped pattern (Figure 4.19b). Such alignment mismatches can generate widespread mechanical damage on the nanostructures as illustrated by Figure 4.20, while limiting multiplexed functionalization as the printed pattern does not correspond to the original array.

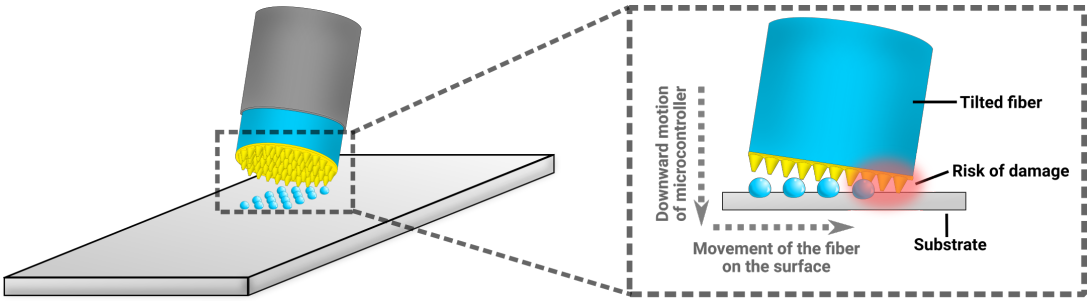

Figure 4.20 – Scheme representing mechanical damage to nanostructures due to improper alignment during stamp-based patterning.

All the contact printing strategies evaluated so far presented numerous drawbacks including as mechanical damage on the nanostructure surface, lack of reproducibility during spotting, as well as impractical operational conditions. Therefore, we decided to focus on non-contact functionalization strategies.

4.4 Laser-assisted thermal micropatterning

4.4.1 General principle

Laser-assisted thermal micropatterning was one of the non-contact functionalization methods that we evaluated. Similarly to the UV-mediated degradation process described in Chapter 2, this approach consisted in the desorption of a protective layer leaving bare regions that can be functionalized via thiol-gold chemistry. However, instead of using UV light, this method employed a focused laser beam inducing localized photo-thermal desorption of the SAM.

Successful photo-thermal micro/nanopatterning of SAMs have been described in numerous cases[66–70]. This method provides some benefits such as very fast kinetics (as the desorption time has been reported in the range of microseconds to seconds, depending power intensity of the laser)[69,71] and the fact that light transmission can be performed through the fiber which translates into a good control on the size and position of the irradiated areas.

Initially, photo-thermal induced desorption of alkanethiols on gold surfaces was thought to occur via oxidation[67,72]. However, it seems that the process starts with a direct cleavage of the S-Au bond followed to the formation of disulfides that are easily removed from the surface during the irradiation process[68,69,73–76] (Figure 4.21). Further thermal oxidation of the compounds can happen depending on the availability of oxygen and the local temperature.

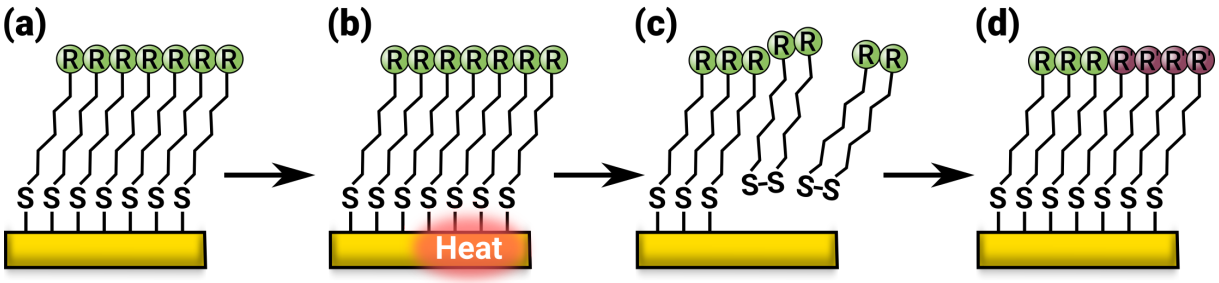

Figure 4.21 – Schematic representation of the thermal desorption of alkanethiols on gold. (a) Formation of a SAM; (b) Localized heating; (c) Formation of disulfide bonds and cleavage from surface and (d) Surface functionalization with different thiolated molecules. Scheme inspired from Shon and Lee[73].

4.4.2 Experimental setup

Transmission of the light through the fiber required the modification of the current optical setup. For such modifications, Vindas[46] proposed the system illustrated in Figure 4.22. In this setup, in front of the semi-transparent mirror, there is a dichroic mirror that allowed

simultaneous SPR monitoring of the system while also redirecting the laser to the optical fiber. A system with a 2-axis mirror galvanometer, controlled by a LabView program, regulated the angle of incidence and therefore, allowed the selection of which regions were exposed to the laser. After the desorption process, functionalization of deprotected zones can be performed as described for the UV-based method.

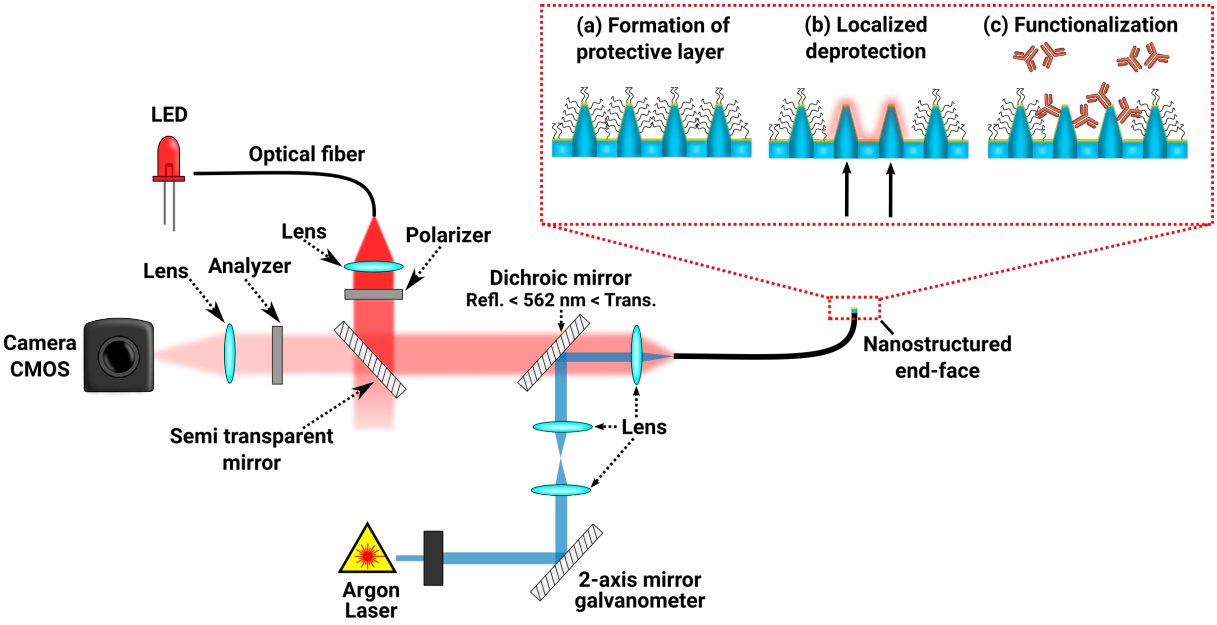

Figure 4.22 – Diagram of the experimental setup used for thermal desorption of SAMs on the optical fibers.

4.4.3 Validation of photo-thermal desorption on flat and nanostructured surfaces

A proof of concept was developed by Cloé Desmet and Loïc Leroy using laser-induced photo-thermal desorption over flat surfaces. For this, gold-coated glass slides were plasma treated (by the same procedure as described in Chapter 2) and immersed in a $PEG_{2000}SH$ 1 mM solution for 1 h. After rinsing with distilled water, the slides were positioned in the setup illustrated by Figure 4.22. A pattern was digitally designed and used as template for directing the irradiation. The SAM ablation process was performed using an argon ion laser (Omnichrome model 532-MA-A04) with a power of 50 mW at a writing speed of 2×10^{-5} s.pixel^{-1} (each pixel corresponds to ~1 µm).

Afterwards, the surface was incubated with a thiolated oligonucleotide (Zip6-SH, 20 µM) for 20 min and thoroughly rinsed with distilled water to remove unbounded molecules. Then, the surface was exposed to the biotinylated complementary strand of the oligo (1 µM for 20 min) and incubated with the a fluorescent protein conjugated with streptavidin (SAPE 10% v/v) for 20 min. After rinsing with PBS-Tween20 (0.05% v/v), a fluorescent pattern matching the digital design was observed (Figure 4.23).

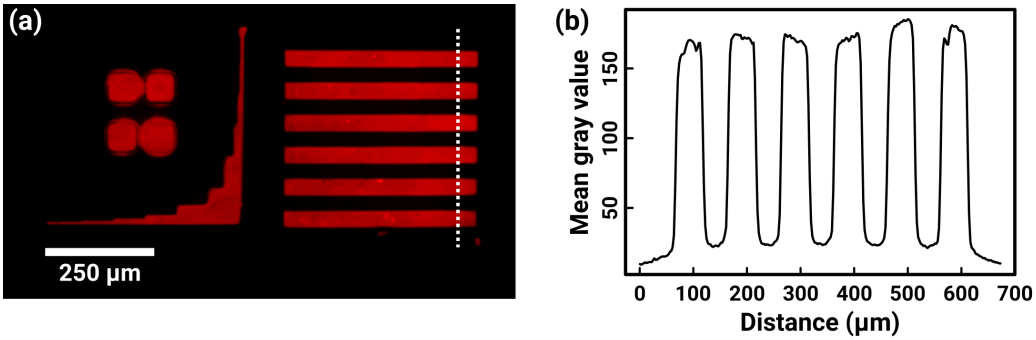

Figure 4.23 – Fluorescence validation of laser micropatterning on flat gold surfaces. (a) Fluorescence image after hybridization with a biotinylated complementary oligonucleotide and incubation in SAPE 10% (v/v) and (b) Image analysis performed on ImageJ[77,78] corresponding to the mean gray values on the segmented line shown in (a).

Analysis of Figure 4.23a resulted in the intensity curve shown in Figure 4.23b. By measuring the full width at half maximum of this curve, we estimated a resolution in the order of 10 µm. This limit might be related not only to the lenses used for focusing the laser beam but mainly to the high thermal conductivity of metals. As the temperature of the irradiated region increases, heat transfer to the surrounding area allows the latter to reach the temperature required for the desorption process. The level of heat diffusion might be regulated by optimizing the irradiation parameters (*e.g.* exposure time and power).

As this method seemed promising for fast and localized surface patterning, we conducted a similar test but on an optical fiber. Contrary to gold-coated glass slides, immersion in Piranha solution was used to clean the optical fibers (as described in page 141). Then, the terminal face was functionalized with a $PEG_{2000}SH$ protective layer by the same procedure used before. A new digital design was employed, this template consisted in squares of 100×100 pixels (50×50 µm) which were irradiated at 50%, 20% and 10% of the maximum power of the laser (50 mW). The writing speed was in the order of 1×10^{-5} s.pixel^{-1} with a total exposure time of 60 s.

During illumination of the fiber (back-illumination is traditionally performed using the SPR light source), the irradiated regions showed an important increase in the transmitted light suggesting defects in the gold layer. SEM imaging was used for analyzing the state of the nanostructures (Figure 4.24) which denoted extensive damage to the gold surface even in the zones irradiated at the lowest power.

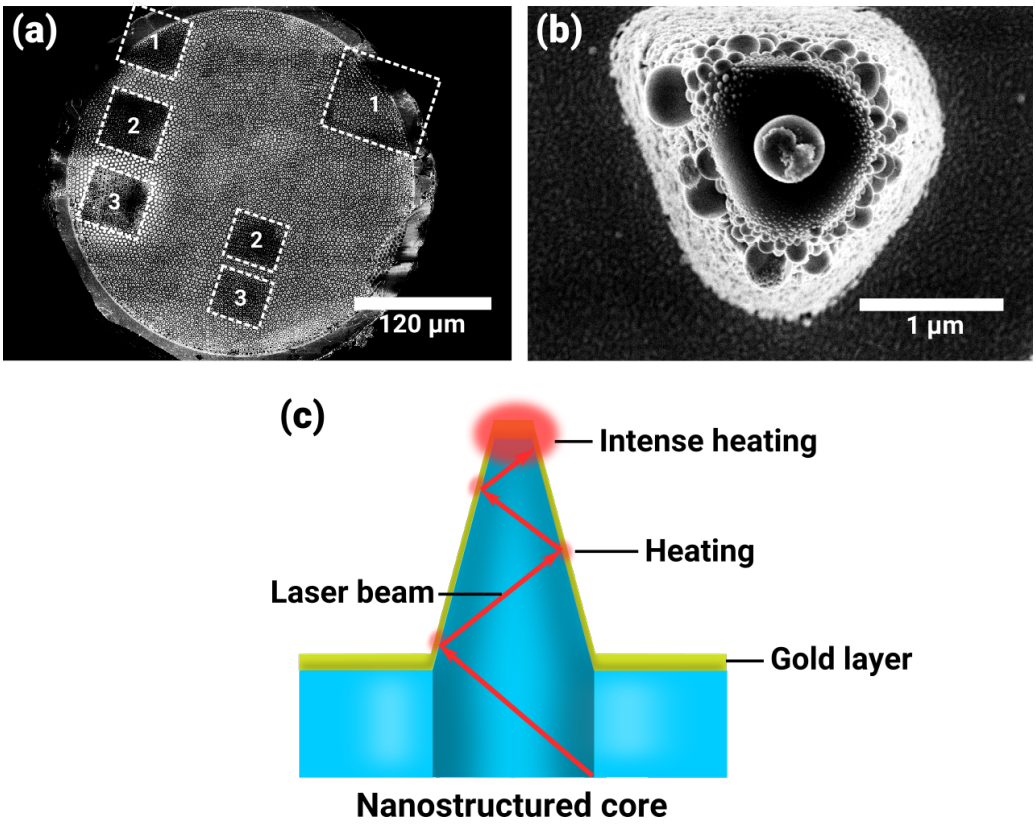

Figure 4.24 – Thermal damage to the gold layer of the nanostructured fibers. (a) SEM image showing the laser-irradiated zones which exposed to: *1.* 50%, *2.* 20% and *3.* 10% of the maximum power; (b) Zoom of a SEM image corresponding to a zone irradiated at 10% of the maximum power, small droplets of gold can be observed on the tip of the nanostructure; and (c) graphical representation of the localized heating phenomena.

Damage to the gold layer is a common drawback in laser-assisted SAM patterning[69]. The substrate temperature can rapidly reach a threshold at which there is gold ablation[69]. This ablation may be caused by metal evaporation and/or surface melting[76,79,80]. In our case, the main process seems to be macroscopic melting of the gold layer. Curiously, the gold ablation was not homogeneous over the gold surface and instead it focused on the tips of the nanostructures, forming micro- to nanometric droplets. Such phenomena might be caused by the effect illustrated in Figure 4.24c. Propagation of the laser through the fiber occurs via reflection until it reaches the cone-like structures. At this point, a portion of the light is absorbed by the gold layer generating localized heating while most of the light is reflected back. However, due to the geometry of the nanostructures, the light is guided until the tip where it cannot propagate and is mainly absorbed leading to an intense heating of the area melting the surrounding gold.

Such large modification of the gold layer would negatively affect its optical properties for the generation of SPR. After numerous efforts to optimize the ablation parameters, we could not overcome the heterogeneous heating and so, this approach was no further explored.

4.5 Indirect photo-assisted functionalization

4.5.1 General principle

Another non-contact printing method we evaluated consisted in the process extensively described in Chapter 2. As in the previous method, desorption of a protective layer is perform but in this case the process is mediated by UV-induced degradation of the SAM rather than by photo-thermal desorption. An advantage of this approach is the fact that UV-irradiation does not induce heating of the substrate. As the process does not depend on localized heating, there is no heat-transfer limited resolution of the system neither thermal ablation of the gold layer.

The precise chemical mechanism of this process is, currently, not completely understood. However it may be triggered either by ROS formation or direct photolysis of the PEG molecules as it is proposed in Figure 4.25.

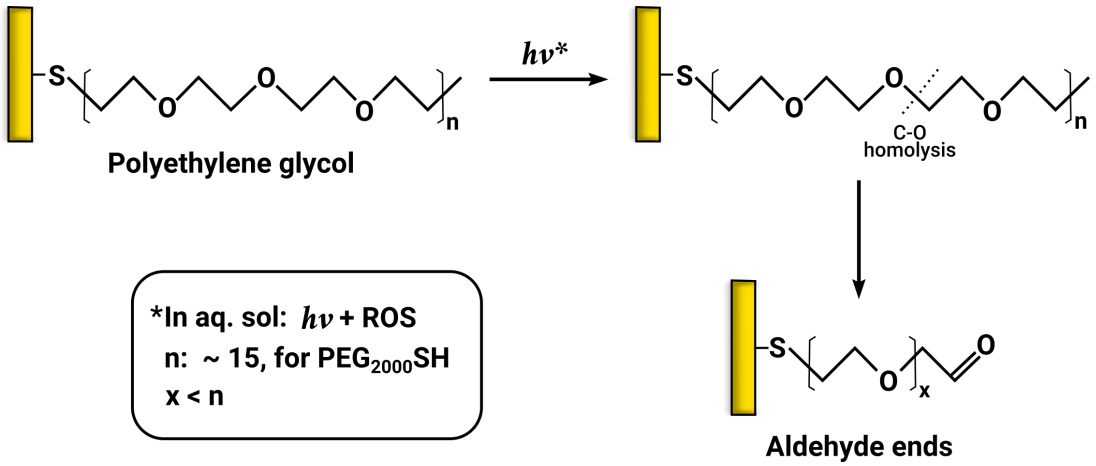

Figure 4.25 – Proposed mechanism for UV-mediated PEG degradation.

Such process would be triggered by generation of a carbon centered radical (caused by direct photolysis or hydrogen abstraction by a reactive oxygen species, which is expected to be the main process in aqueous solutions). Then, a carbon-oxygen homolysis may lead to the cleavage of the molecule leaving a surface with aldehyde ends as it was found by Weber et al.[81] and Ducker et al.[82]. In Chapter 2, this SAM degradation method allowed effective functionalization of flat gold surfaces. Therefore, we performed some adaptations in order to assess its feasibility for multiplexed functionalization of the nanostructured optical-fiber bundles.

4.5.2 Experimental setup

Since UV light cannot cross the gold layer[83] nor be transmitted through the cores of our fibers, we had to adapt the optical setup in order to perform the UV irradiation directly at the nanostructured face of the fiber. We fixed the end-face of the fibers in

an upward position similar to the procedure done for contact printing while UV-exposure was performed using the same illumination system used in Chapter 2 as can be seen in Figure 4.26.

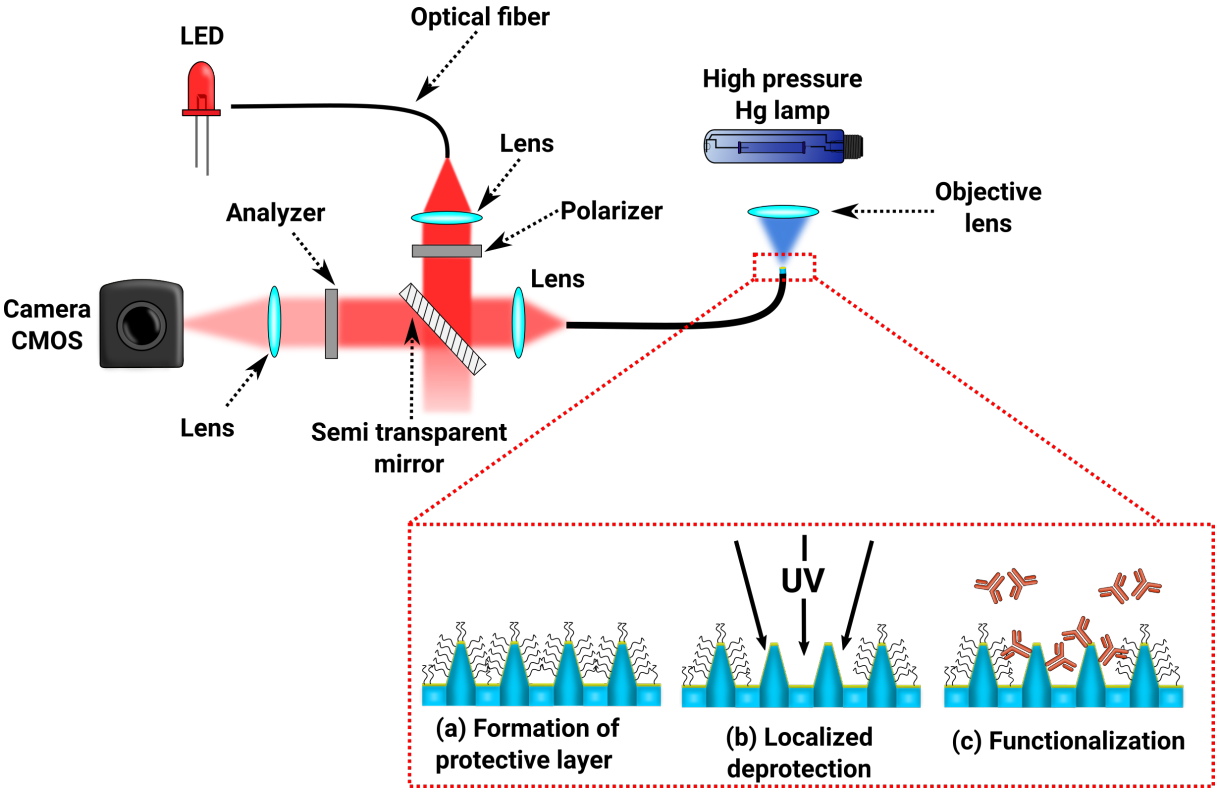

Figure 4.26 – Scheme representing the UV irradiation setup for functionalization of the optical fibers. (a) First stage consisting in the formation of a protective $PEG_{2000}SH$ SAM; (b) UV irradiation on the areas of interest allow localized deprotection of the gold substrate and (c) functionalization of unprotected zones with thiolated molecules.

As there was no microfluidic system adapted for the optical fibers, we performed the irradiation in air and manually immersed the fiber into the different solutions of interest. The extensive handling required for rinsing and functionalizing procedures was incompatible with continuous SPR monitoring and so, we carried out a proof of concept by detecting fluorescent markers rather than by using SPR.

4.5.3 Validation of UV-mediated desorption on optical fibers

For this experiment, the optical fiber was exposed to Piranha solution (5 min, r.t.), rinsed with milli-Q water and then immersed in a 1 mM $PEG_{2000}SH$ for 15 min at room temperature. After forming a protective layer, we exposed a specific area to UV irradiation for 30 min by adjusting the field diaphragm of the irradiating system. Then, the fiber was immersed multiple times in milli-Q water and exposed to a 100 µM solution of a thiolated oligonucleotide Zip6-SH (described in Chapter 3 Section 3.2.5.d) for 15 min.

After rinsing, the fiber was exposed to the biotinylated complementary oligo (Zip6c-Bio, 1 *micro*M) for 15 min. A new rinsing step in PBS allowed removal of non-hybridized strands while fluorescent revelation was performed after incubation of the fiber in SAPE 10% (v/v in PBS) for 20 min (Figure 4.27).

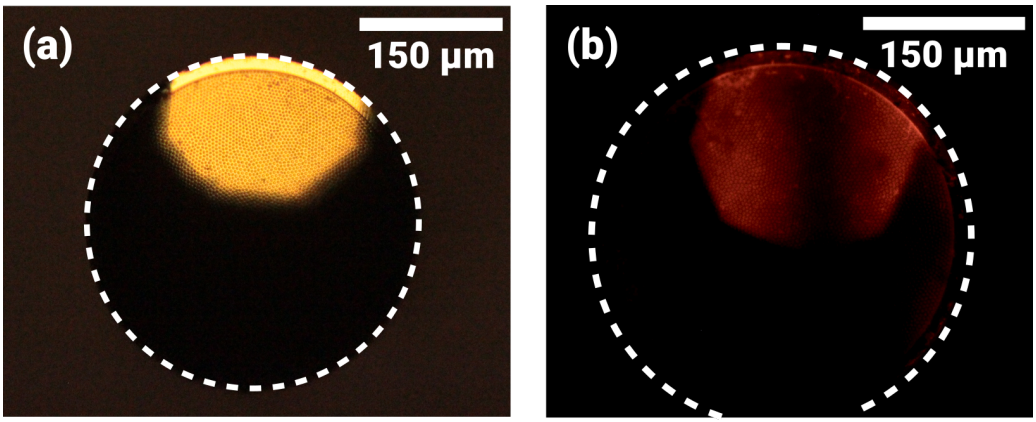

Figure 4.27 – Indirect photo-functionalization via UV-degradation of a protective SAM. All images correspond to the nanostructured face of the optical fiber. (a) Optical microscopy image showing the fiber before UV irradiation, observed with white light on a bright field filter; (b) Fluorescence revelation of the fiber after: UV-irradiation, functionalization with thiolated DNA, hybridization with the biotinylated complementary strand and exposure to SAPE 10% v/v.

The results obtained in Figure 4.27 are promising as functionalization on the fibers was observed. However, experiments performed by Cloé Desmet, a postdoctoral researcher in our team, showed that exposure times between 20-30 min (under our experimental conditions) were required for effectively deprotect the surface, which was considerably higher than for flat gold surfaces. Considering that the presence of cone-like nanostructures considerably increases the surface area of the tips (compared to a non-structure surface with the same perimeter), the energy delivered per surface area unit ($J.cm^{-1}$) was much lower on the fibers than on gold flat surfaces. As the energy per area unit decreases, a reduction in the degradation efficiency can be expected. Nevertheless, this can be easily addressed by employing a higher power light source.

Another fact to considerate is that the irradiation was performed in air instead of in aqueous media. Previously, we discussed that ROS formation (mainly hydroxyl radicals) in aqueous media can trigger the degradation of PEG when using a 365 nm light source. However, during the irradiation in air, ROS generation from water molecules becomes a secondary process (limited by the water molecules adsorbed at the surface) and PEG-degradation via direct photolysis may become predominant, resulting in a variation of the reaction kinetics.

From all these experiments, we can conclude that indirect photo-functionalization was effective for the grafting of biomolecules on the end-face of the optical fibers without damaging their structural integrity. A drawback of this technique was that the irradiation had to be performed in air which would lead to partial denaturation of proteins.

Yet, this issue can be approached by the development of a dedicated microfluidic system or the grafting of thiolated oligonucleotides allowing specific functionalization with complementary oligo-conjugated proteins. Even if this method is a promising approach for multiplexed functionalization on the fibers, the fact that it is based on thiol-gold chemistry limits its applicability as formation of even low-surface density SAMs requires several minutes and up to hours. Hence, a strategy with faster immobilization rates was needed.

4.6 Direct photo-assisted functionalization

4.6.1 Diazirine as a photoreactive moiety

In contrast with the previous method, direct photo-functionalization, as described in Chapter 2 Section 2.1.2, is a one-step process in which the grafting is performed at the same time as the irradiation. This is possible as the unstable species, formed during UV exposure, present very fast reaction kinetics leading to a significant reduction in the time required for multi-probe immobilization.

Among the possible direct photo-functionalization strategies, such as the use of photoinitiators[84] or catalysts[85,86], we decided to create a photo-activable SAM. From the available photoreactive moieties[87,88], we selected diazirine-derivatives since[89]:

— They present great stability (to nucleophiles such as thiols, to pH and temperature);

— Their activation wavelength range is compatible with biomolecules (330-370 nm, which causes relatively low damage to biomolecules during direct exposure);

— The formed carbenes are highly reactive;

— Diazirines are the smallest photoreactive functionalities

This latest aspect, the small size, is critical since coupling with bulky photoreactive moieties can dramatically alter the biological activity of the biomolecules of interest[88].

4.6.2 Action mechanism

Diazirines are molecules with a carbon atom bonded to a diazo moiety[90]. Upon exposure to UV light, diazirine enters a photogenerated excited state in which the two σ bonds connecting the sp^3 carbon atom to the azo moieties are cleaved causing a redistribution of the bonding electrons between the nitrogen molecule and a divalent carbon atom two non-bonding orbitals, namely a carbene[90–92].

Once formed, carbenes bind covalently to the nearest molecule via insertions of the type: C-C, C-H, O-H or X-H (with X being any atom except C or H in an organic compound)[88]. Nevertheless, the formation of carbenes is not the only viable pathway for this reaction. UV irradiation of diazirines can also generate diazo compounds as well as diazonium salts[90]. Diazo compounds can further react with UV light forming carbenes, yet, it is considered as an undesirable by-product since it can form diazonium ions and,

subsequently, carbocations[93]. These carbocations suffer from light-independent loss of molecular nitrogen leading to unwanted reactions[90,93] (Figure 4.28).

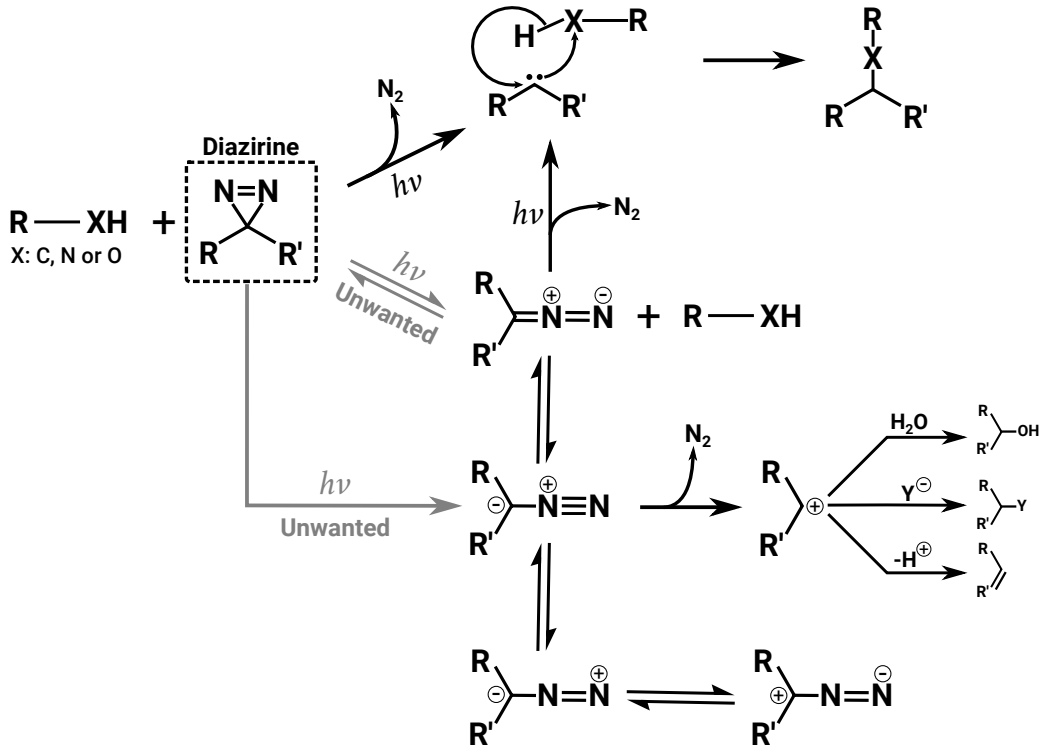

Figure 4.28 – Reaction of a diazirine with a R-XH compound, formation of a diazo compound and diazonium salts as unwanted by-products. Inspired from Preston and Wilson[90].

4.6.3 Diazirine-derivatives for surface functionalization

Diazirine-containing compounds have been widely exploited for photo-affinity labeling of biomolecules[88], yet, their use for surface grafting has not been extensively explored[94,95]. Before applying this method to nanostructured optical fibers, we evaluated the feasibility of using diazirine-based photoreactive surfaces for biomolecule arraying over flat surfaces. For this goal, we used plasma-treated (3 min, 75%:25% O_2:Ar, 0.6 mbar and at 80% of power) gold-coated glass slides which were then immersed for 1h in 1 mM solutions of either: (a) 11-Amino-undecane-1-thiol ($HS-C_{11}-NH_2$); (b) an alkyl oligoethylene glycol thiol ($HS-C_{11}-(H_4C_2O)_3-NH_2$, called HS-OEG-$NH_2$) and (c) thiolated polyethylene glycol ($CH_3O(CH_2CH_2O)_{44}CH_2CH_2SH$, called $PEG_{2000}SH$) as illustrated in Figure 4.29.

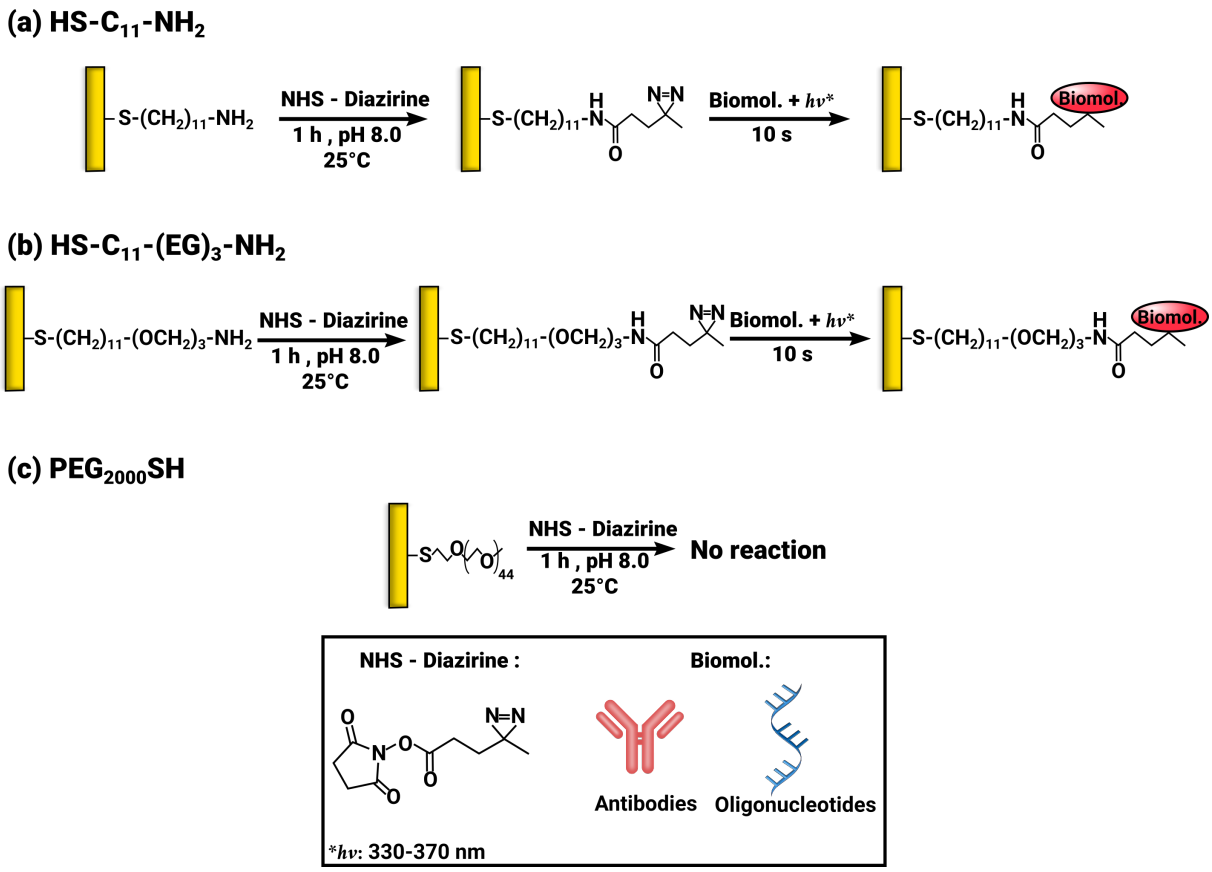

Figure 4.29 – Diazirine-based photoreactive surfaces for immobilization of biomolecules. Three different SAMs where used in the assays including: (a) an amino thiolated alkyl ($HS\text{-}C_{11}NH_2$), (b) an alkyl oligoethylene glycol thiol ($HS\text{-}OEG\text{-}NH_2$) and (c) $PEG_{2000}SH$ as negative control.

Afterwards, the slides were rinsed 3 times with 10 mL of ethanol 96% and then 3 times with distilled water (same volume). All the slides were covered with a NHS-Diazirine 3.3 mM solution in PBS pH 8.0 for 1 h at r.t. in a humid chamber (∼85% relative humidity) followed by the same rinsing cycle described before. Once the slides were dried, 100 µL of a 1 µM solution of a biotinylated oligo (IFN-γ aptamer, see subsubsection 3.2.5.d) were deposited on the surface and covered by a glass cover slip.

The irradiation area was arbitrary reduced by adjusting the field diaphragm and then pre-determined areas were exposed to UV light (∼365 nm) for 10 s. Immediately, the surface was rinsed 3 times with a PBS-T solution (PBS + Tween20 0.05% v/v) and then incubated with SAPE 10% v/v for 15 min at r.t. and, once more, washed with PBS-T. Fluorescence imaging showed fluorescence only on the irradiated zones of the diazirine slides and not on the negative control ($PEG_{2000}SH$) as observed in Figure 4.30.

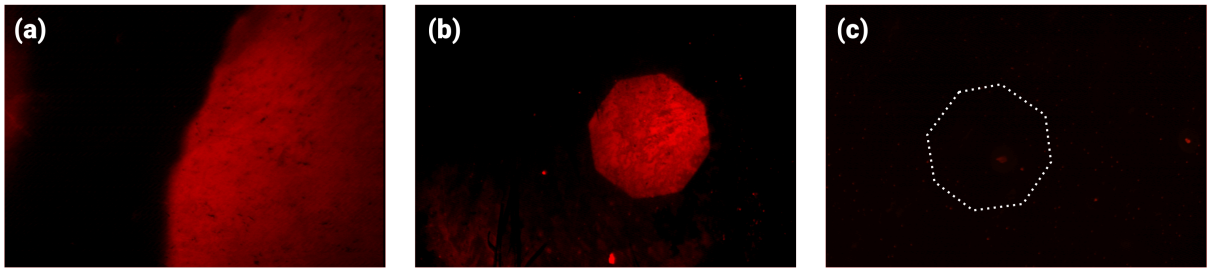

Figure 4.30 – Fluorescence validation of diazirine-based photoreactive surfaces. Images correspond to (a) $HS-C_{11}-NH_2$ SAM, (b) $HS-C_{11}-(EG)_3-NH_2$ SAM and (c) Negative control, ($PEG_{2000}SH$) SAM. On $HS-C_{11}-NH_2$ SAM (a), a much larger area was irradiated compared to that of the other SAMs (b and c).

This approach seemed very promising as the patterning could be performed in matter of seconds and without any modification of the probe (insertion of moieties such as thiol, biotin, pyrrole, etc). Cloé Desmet continued the evaluation of this approach by grafting oligonucleotides and proteins (biotinylated IgG antibodies) on similar surfaces. Although, the method was reproducible for oligonucleotides, it showed a poor grafting efficiency of proteins.

Photo-coupling of proteins in solution via diazirine has been reported to have low yields since the carbenes rapidly react with water molecules[88,96]. Since the coupling kinetics in solution are faster than for solid-liquid systems, we expected that the coupling of proteins to the surface would have a much lower yield than in solution. Such effect is attributed that, at relatively low target concentrations, mass transport plays a major role on the encounter rate[97] between the proteins and the carbenes at the surface. Therefore, the rate-limiting process is that of diffusion of the target biomolecules (vertical and lateral) to the active regions of the surfaces.

Yet, effective grafting of oligos on solid-liquid system was achieved when using similar concentrations (1 µM). We hypothesize that this might be caused by a faster diffusion of the oligonucleotides to the active surface, allowing reaction of the biomolecules with the carbenes before their interaction with water molecules. However, Lukacs et al.[98] reported a diffusion coefficient of 53 $\mu m^2.s^{-1}$ for oligonucleotides of similar length while Jossang et al.[99] reported a value of 39 $\mu m^2.s^{-1}$ for a human IgG. Such slight difference might not be able to explain the observed results.

4.7 Conclusions

We evaluated multiple contact and non-contact printing approaches for surface functionalization of gold coated nanostructured optical fiber-bundles. Based on our results, we can conclude that microcantilever-based functionalization is definitively not adapted for our fiber-bundle system. When performing pyrrole electropolymerization, we experienced numerous difficulties to establish a proper electrical contact, leading to extensive damage of

the nanostructures. While droplet deposition for thiol-based SAM formation suffered from lack of reproducibility, difficult manual alignment of the system and cross-contamination issues.

Among the photo-assisted functionalization methods, photo-thermal SAM desorption lead to heterogeneous heating of the nanostructures resulting in gold ablation of the tips. Such modification drastically altered the SPR capabilities of the system for which this approach was discarded. However, by modifying the setup to perform the irradiation on the nanostructured surface and not through the fiber, uniform heating of the surface could be achieved without damaging to the gold layer. This approach is yet to be tested but could be a feasible alternative.

In the case of UV-induced SAM desorption, this process allowed effective functionalization of the surface without damage to the gold layer. However, this method suffered from slow desorption times. This combined with the fact that thiol-gold SAMs require considerable amounts of time to form effectively, limited the applicability of this approach for multiplexed functionalization (as it could take hours to array more than 4 probes).

Finally, the use of photoreactive SAMs proved to be the most promising method. This method offered the simplest and fastest way to perform multiplexed functionalization on the optical fibers without any structural damage. However, it has been elusive to optimize and lacks reproducibility at the moment. These challenges could be overcome by using a pre-concentration strategy. Such strategy could be based either on drying effect (reducing or removing water from the droplet increasing the chances of interaction between the desired molecule and the carbenes) or by modifying the pH of the solution, as performed during ELISA, to favor protein adsorption on the surface (protein interaction with charged or slightly hydrophobic surfaces can be favored by adjusting the pH of the buffer based on the isoelectric point of the protein and the nature of the surface). Although it has yet to be optimized, this method will be continue to be explored for the creation of a fiber-optic biochips.

References

[1] Katzir, A. *Selected Papers on Optical Fibers in Medicine (SPIE Milestone Series Vol. MS11)*; SPIE Press, 1990.

[2] Méndez, A. In *Optics in Our Time*; Al-Amri, M. D., El-Gomati, M., and Zubairy, M. S., Eds.; Springer International Publishing: Cham, 2016; pp 299–333.

[3] Wen, H., Wiesler, D., Tveten, A., Danver, B., and Dandridge, A. (1998) High-Sensitivity Fiber-Optic Ultrasound Sensors for Medical Imaging Applications. *Ultrasonic Imaging 20*, 103–112.

[4] Epstein, M. (1982) Fiber optics in medicine. *Crit Rev Biomed Eng 7*, 79–120.

[5] Taffoni, F., Formica, D., Saccomandi, P., Pino, G., and Schena, E. (2013) Optical Fiber-Based MR-Compatible Sensors for Medical Applications: An Overview. *Sensors 13*, 14105–14120.

[6] An, S. S., Nguyen, T. T., Bae, S. O., Yoon, W. J., Kim, D. M., Park, J.-W., and Ju, H. (2015) A regenerative label-free fiber optic sensor using surface plasmon resonance for clinical diagnosis of fibrinogen. *International Journal of Nanomedicine* 155.

[7] Kishen, A., John, M., Lim, C., and Asundi, A. (2003) A fiber optic biosensor (FOBS) to monitor mutans streptococci in human saliva. *Biosensors and Bioelectronics 18*, 1371–1378.

[8] Ko, S., and Grant, S. A. (2006) A novel FRET-based optical fiber biosensor for rapid detection of Salmonella typhimurium. *Biosensors and Bioelectronics 21*, 1283–1290.

[9] Hayman, R. B. *Principles of Bacterial Detection: Biosensors, Recognition Receptors and Microsystems*; Springer New York, pp 125–137.

[10] Hu, D. J. J., Lim, J. L., Park, M. K., Kao, L. T.-H., Wang, Y., Wei, H., and Tong, W. (2012) Photonic Crystal Fiber-Based Interferometric Biosensor for Streptavidin and Biotin Detection. *IEEE Journal of Selected Topics in Quantum Electronics 18*, 1293–1297.

[11] Su, L.-C., Chang, Y.-F., Chou, C., an Annie Ho, J., Li, Y.-C., Chou, L.-D., and Lee, C.-C. (2011) Binding Kinetics of Biomolecule Interaction at Ultralow Concentrations Based on Gold Nanoparticle Enhancement. *Analytical Chemistry 83*, 3290–3296.

[12] Philip-Chandy, R., Scully, P., Eldridge, P., Kadim, H., Grapin, M., Jonca, M., D'Ambrosio, M., and Colin, F. (2000) An optical fiber sensor for biofilm measurement using intensity modulation and image analysis. *IEEE Journal of Selected Topics in Quantum Electronics 6*, 764–772.

[13] Wong, Y. M., Scully, P. J., Bartlett, R. J., Kuang, K. S. C., and Cantwell, W. J. (2003) Plastic Optical Fibre Sensors for Environmental Monitoring: Biofouling and Strain Applications. *Strain 39*, 115–119.

[14] Cennamo, N., Varriale, A., Pennacchio, A., Staiano, M., Massarotti, D., Zeni, L., and D'Auria, S. (2013) An innovative plastic optical fiber-based biosensor for new bio/applications. The case of celiac disease. *Sensors and Actuators B: Chemical 176*, 1008–1014.

[15] Wang, W., Mai, Z., Chen, Y., Wang, J., Li, L., Su, Q., Li, X., and Hong, X. (2017) A label-free fiber optic SPR biosensor for specific detection of C-reactive protein. *Scientific Reports 7*.

[16] Hasegawa, A. (2004) Theory of information transfer in optical fibers: A tutorial review. *Optical Fiber Technology 10*, 150–170.

[17] Senior, J. *Optical Fiber Communications: Principles and Practice (3rd Edition)*; Pearson, 2008.

[18] Leung, A., Shankar, P. M., and Mutharasan, R. (2007) A review of fiber-optic biosensors. *Sensors and Actuators B: Chemical 125*, 688–703.

[19] Knight, J. C. (2003) Photonic crystal fibres. *Nature 424*, 847–851.

[20] Haus, J. *Fundamentals and Applications of Nanophotonics*; Elsevier, 2016; pp 341–395.

[21] Joe, H.-E., Yun, H., Jo, S.-H., Jun, M. B., and Min, B.-K. (2018) A review on optical fiber sensors for environmental monitoring. *International Journal of Precision Engineering and Manufacturing-Green Technology 5*, 173–191.

[22] Matsuo, H., Kuniyoshi, S., Kudo, K., and Tanaka, K. (2000) Evanescent wave optical fiber sensor using adsorption LB films. *Synthetic Metals 115*, 37–39.

[23] Sutapun, B. (1999) Pd-coated elastooptic fiber optic Bragg grating sensors for multiplexed hydrogen sensing. *Sensors and Actuators B: Chemical 60*, 27–34.

[24] MacCraith, B. D., McDonagh, C. M., O'Keeffe, G., Keyes, E. T., Vos, J. G., O'Kelly, B., and McGilp, J. F. (1993) Fibre optic oxygen sensor based on fluorescence quenching of evanescent-wave excited ruthenium complexes in sol–gel derived porous coatings. *The Analyst 118*, 385–388.

[25] Xiong, Y., Xu, J., Wang, J.-W., and Guan, Y.-F. (2009) A fiber-optic evanescent wave sensor for dissolved oxygen detection based on novel hybrid fluorinated xerogels immobilized with [Ru(bpy)3]2^{+}. *Analytical and Bioanalytical Chemistry 394*, 919–923.

[26] Ghadiry, M., Gholami, M., Kong, L. C., Yi, C. W., Ahmad, H., and Alias, Y. (2015) Nano-Anatase TiO2 for High Performance Optical Humidity Sensing on Chip. *Sensors 16*, 39.

[27] Xie, W., Yang, M., Cheng, Y., Li, D., Zhang, Y., and Zhuang, Z. (2014) Optical fiber relative-humidity sensor with evaporated dielectric coatings on fiber end-face. *Optical Fiber Technology 20*, 314–319.

[28] Yang, M. Optical Fiber Sensors with Coatings as Sensitive Elements. Asia Communications and Photonics Conference 2014. 2014.

[29] Gupta, B. D., and Kant, R. (2018) Recent advances in surface plasmon resonance based fiber optic chemical and biosensors utilizing bulk and nanostructures. *Optics & Laser Technology 101*, 144–161.

[30] Caucheteur, C., Guo, T., and Albert, J. (2015) Review of plasmonic fiber optic biochemical sensors: improving the limit of detection. *Analytical and Bioanalytical Chemistry 407*, 3883–3897.

[31] Dwivedi, Y. S., Sharma, A. K., and Gupta, B. D. (2008) Influence of Design Parameters on the Performance of a Surface Plasmon Sensor Based Fiber Optic Sensor. *Plasmonics 3*, 79–86.

[32] Pollet, J., Delport, F., Thi, D. T., Wevers, M., and Lammertyn, J. Aptamer-based surface plasmon resonance probe. 2008 IEEE Sensors. 2008.

[33] Khijwania, S., and Gupta, B. (1999) *Optical and Quantum Electronics 31*, 625–636.

[34] Littlejohn, D., Lucas, D., and Han, L. (1999) Bent Silica Fiber Evanescent Absorption Sensors for Near-Infrared Spectroscopy. *Applied Spectroscopy 53*, 845–849.

[35] Guo, T., Liu, F., Guan, B.-O., and Albert, J. (2016) Tilted fiber grating mechanical and biochemical sensors. *Optics & Laser Technology 78*, 19–33.

[36] Erdene, N. (2011) Fabrication of fiber-optic localized surface plasmon resonance sensor and its application to detect antibody-antigen reaction of interferon-gamma. *Optical Engineering 50*, 124405.

[37] Lin, Y., Zou, Y., Mo, Y., Guo, J., and Lindquist, R. G. (2010) E-Beam Patterned Gold Nanodot Arrays on Optical Fiber Tips for Localized Surface Plasmon Resonance Biochemical Sensing. *Sensors 10*, 9397–9406.

[38] Nguyen, H., Sidiroglou, F., Collins, S. F., Davis, T. J., Roberts, A., and Baxter, G. W. (2013) A localized surface plasmon resonance-based optical fiber sensor with sub-wavelength apertures. *Applied Physics Letters 103*, 193116.

[39] Consales, M., Ricciardi, A., Crescitelli, A., Esposito, E., Cutolo, A., and Cusano, A. (2012) Lab-on-Fiber Technology: Toward Multifunctional Optical Nanoprobes. *ACS Nano 6*, 3163–3170.

[40] Piliarik, M., Homola, J., Manikova, Z., and Ctyroky, J. (2003) Surface plasmon resonance sensor based on a single-mode polarization-maintaining optical fiber. *Sensors and Actuators B: Chemical 90*, 236–242.

[41] Hassani, A., and Skorobogatiy, M. (2007) Design criteria for microstructured-optical-fiber-based surface-plasmon-resonance sensors. *Journal of the Optical Society of America B 24*, 1423.

[42] Lee, H. W., Schmidt, M. A., Tyagi, H. K., Sempere, L. P., and Russell, P. S. J. (2008) Polarization-dependent coupling to plasmon modes on submicron gold wire in photonic crystal fiber. *Applied Physics Letters 93*, 111102.

[43] Gao, D., Guan, C., Wen, Y., Zhong, X., and Yuan, L. (2014) Multi-hole fiber based surface plasmon resonance sensor operated at near-infrared wavelengths. *Optics Communications 313*, 94–98.

[44] Shi, S., Wang, L., Su, R., Liu, B., Huang, R., Qi, W., and He, Z. (2015) A polydopamine-modified optical fiber SPR biosensor using electroless-plated gold films for immunoassays. *Biosensors and Bioelectronics 74*, 454–460.

[45] Qu, H., Tian, F., Chen, S., Zhang, Y., Luo, J., Li, L., Yang, X., and Zhang, J. (2018) Two-core single-polarization optical fiber with a large hollow coated bimetallic layer. *Applied Optics 57*, 2446.

[46] Vindas Yassine, K. Development and optimization of new plasmon resonance based biochips and biosensors. Theses, Université Grenoble Alpes, 2017.

[47] Spierings, G. A. C. M. (1993) Wet chemical etching of silicate glasses in hydrofluoric acid based solutions. *Journal of Materials Science 28*, 6261–6273.

[48] Kikyuama, H., Miki, N., Saka, K., Takano, J., Kawanabe, I., Miyashita, M., and Ohmi, T. (1991) Principles of wet chemical processing in ULSI microfabrication. *IEEE Transactions on Semiconductor Manufacturing 4*, 26–35.

[49] Wong, L., Suratwala, T., Feit, M., Miller, P., and Steele, R. (2009) The effect of HF/NH4F etching on the morphology of surface fractures on fused silica. *Journal of Non-Crystalline Solids 355*, 797–810.

[50] Proksche, H. (1992) The Influence of NH[sub 4]F on the Etch Rates of Undoped SiO_2 in Buffered Oxide Etch. *Journal of The Electrochemical Society 139*, 521.

[51] Osseo-Asare, K. (1996) Etching Kinetics of Silicon Dioxide in Aqueous Fluoride Solutions: A Surface Complexation Model. *Journal of The Electrochemical Society 143*, 1339.

[52] Gorris, H. H., Blicharz, T. M., and Walt, D. R. (2007) Optical-fiber bundles. *FEBS Journal 274*, 5462–5470.

[53] Bierlich, J., Kobelke, J., Brand, D., Kirsch, K., Dellith, J., and Bartelt, H. (2012) Nanoscopic tip sensors fabricated by gas phase etching of optical glass fibers. *Photonic Sensors 2*, 331–339.

[54] Zuo, Z., Zhu, K., Ning, L., Cui, G., Qu, J., Huang, W., Shi, Y., and Liu, H. (2015) Composite silicon nanostructure arrays fabricated on optical fibre by chemical etching of multicrystal silicon film. *Nanotechnology 26*, 155601.

[55] Lin, J. (2000) Recent development and applications of optical and fiber-optic pH sensors. *TrAC Trends in Analytical Chemistry 19*, 541–552.

[56] Deiss, F. Développement de réseaux multiplexés de biocapteurs électrochimiques. Ph.D. thesis, 2009; Thèse de doctorat dirigée par Sojic, Neso Chimie - Physique Bordeaux 1 2009.

[57] Barrera, F. J., Yust, B., Mimun, L. C., Nash, K. L., Tsin, A. T., and Sardar, D. K. (2013) Optical and spectroscopic properties of human whole blood and plasma with and without Y_2O_3 and $Nd_3{}^+$:Y_2O_3 nanoparticles. *Lasers in Medical Science 28*, 1559–1566.

[58] Yu, D. I., Doh, S. W., Kwak, H. J., Kang, H. C., Ahn, H. S., Park, H. S., Kiyofumi, M., and Kim, M. H. (2015) Wetting state on hydrophilic and hydrophobic micro-textured surfaces: Thermodynamic analysis and X-ray visualization. *Applied Physics Letters 106*, 171602.

[59] Livache, T., Roget, A., Dejean, E., Barthet, C., Bidan, G., and Teoule, R. (1994) Preparation of a DNA matrix via an electrochemically directed copolymerization of pyrrole and oligonucleotides bearing a pyrrole group. *Nucleic Acids Research 22*, 2915–2921.

[60] Livache, T., Maillart, E., Lassalle, N., Mailley, P., Corso, B., Guedon, P., Roget, A., and Levy, Y. (2003) Polypyrrole based DNA hybridization assays: study of label free detection processes versus fluorescence on microchips. *Journal of Pharmaceutical and Biomedical Analysis 32*, 687–696.

[61] Bouguelia, S., Roupioz, Y., Slimani, S., Mondani, L., Casabona, M. G., Durmort, C., Vernet, T., Calemczuk, R., and Livache, T. (2013) On-chip microbial culture for the specific detection of very low levels of bacteria. *Lab on a Chip 13*, 4024.

[62] Suraniti, E., Sollier, E., Calemczuk, R., Livache, T., Marche, P. N., Villiers, M.-B., and Roupioz, Y. (2007) Real-time detection of lymphocytes binding on an antibody chip using SPR imaging. *Lab on a Chip 7*, 1206.

[63] Roupioz, Y., Berthet-Duroure, N., Leïchlé, T., Pourciel, J.-B., Mailley, P., Cortes, S., Villiers, M.-B., Marche, P. N., Livache, T., and Nicu, L. (2009) Electrochemical deposition: Small 13/2009. *Small 5*.

[64] Descamps, E., Duroure, N., Deiss, F., Leichlé, T., Adam, C., Mailley, P., Aït-Ikhlef, A., Livache, T., Nicu, L., and Sojic, N. (2013) Functionalization of optical nanotip arrays with an electrochemical microcantilever for multiplexed DNA detection. *Lab on a Chip 13*, 2956.

[65] Carr, A. R., Townsend, R. E., and Badger, W. L. (1925) Vapor Pressures of Glycerol-Water and Glycerol-Water-Sodium Chloride Systems. *Industrial & Engineering Chemistry 17*, 643–646.

[66] Ohayon, D., Pitsalidis, C., Pappa, A.-M., Hama, A., Zhang, Y., Gallais, L., and Owens, R. M. (2017) Laser Patterning of Self-Assembled Monolayers on PEDOT:PSS Films for Controlled Cell Adhesion. *Advanced Materials Interfaces 4*, 1700191.

[67] Kirkwood, S. E., Shadnam, M. R., Amirfazli, A., and Fedosejevs, R. (2007) Mechanism for femtosecond laser pulse patterning of self-assembled monolayers on gold-coated substrates. *Journal of Physics: Conference Series 59*, 428–431.

[68] Shadnam, M. R., Kirkwood, S. E., Fedosejevs, R., and Amirfazli, A. (2005) Thermo-Kinetics Study of Laser-Induced Desorption of Self-Assembled Monolayers from Gold: Case of Laser Micropatterning. *The Journal of Physical Chemistry B 109*, 11996–12002.

[69] Iversen, L., Younes-Metzler, O., Martinez, K. L., and Stamou, D. (2009) Chemically Specific Laser-Induced Patterning of Alkanethiol SAMs: Characterization by SEM and AFM. *Langmuir 25*, 12819–12824.

[70] Balgar, T., Franzka, S., and Hartmann, N. (2005) Laser-assisted decomposition of alkylsiloxane monolayers at ambient conditions: rapid patterning below the diffraction limit. *Applied Physics A 82*, 689–695.

[71] Mathieu, M., and Hartmann, N. (2010) Sub-wavelength patterning of organic monolayers via non-linear processing with continuous-wave lasers. *New Journal of Physics 12*, 125017.

[72] Tam-Chang, S.-W., Biebuyck, H. A., Whitesides, G. M., Jeon, N., and Nuzzo, R. G. (1995) Self-Assembled Monolayers on Gold Generated from Alkanethiols with the Structure RNHCOCH2SH. *Langmuir 11*, 4371–4382.

[73] Shon, Y.-S., and Lee, T. R. (2000) Desorption and Exchange of Self-Assembled Monolayers (SAMs) on Gold Generated from Chelating Alkanedithiols. *The Journal of Physical Chemistry B 104*, 8192–8200.

[74] Nishida, N., Hara, M., Sasabe, H., and Knoll, W. (1996) Thermal Desorption Spectroscopy of Alkanethiol Self-Assembled Monolayer on Au(111). *Japanese Journal of Applied Physics 35*, 5866.

[75] Nuzzo, R. G., Zegarski, B. R., and Dubois, L. H. (1987) Fundamental studies of the chemisorption of organosulfur compounds on gold(111). Implications for molecular self-assembly on gold surfaces. *Journal of the American Chemical Society 109*, 733–740.

[76] Shadnam, M. R., Kirkwood, S. E., Fedosejevs, R., and Amirfazli, A. (2004) Direct Patterning of Self-Assembled Monolayers on Gold Using a Laser Beam. *Langmuir 20*, 2667–2676.

[77] Schindelin, J. et al. (2012) Fiji: an open-source platform for biological-image analysis. *Nature Methods 9*, 676–682.

[78] Schneider, C. A., Rasband, W. S., and Eliceiri, K. W. (2012) NIH Image to ImageJ: 25 years of image analysis. *Nature Methods 9*, 671–675.

[79] Zhang, X., Chu, S., Ho, J., and Grigoropoulos, C. (1997) Excimer laser ablation of thin gold films on a quartz crystal microbalance at various argon background pressures. *Applied Physics A: Materials Science & Processing 64*, 545–552.

[80] Kirkwood, S., van Popta, A., Tsui, Y., and Fedosejevs, R. (2005) Single and multiple shot near-infrared femtosecond laser pulse ablation thresholds of copper. *Applied Physics A 81*, 729–735.

[81] Weber, T., Meyerbröker, N., Hira, N. K., Zharnikov, M., and Terfort, A. (2014) UV-mediated tuning of surface biorepulsivity in aqueous environment. *Chem. Commun. 50*, 4325–4327.

[82] Ducker, R. E., Janusz, S., Sun, S., and Leggett, G. J. (2007) One-Step Photochemical Introduction of Nanopatterned Protein-Binding Functionalities to Oligo(ethylene glycol)-Terminated Self-Assembled Monolayers. *Journal of the American Chemical Society 129*, 14842–14843.

[83] Loebich, O. (1972) The optical properties of gold. *Gold Bulletin 5*, 2–10.

[84] Fouassier, J. P., and Lalevée, J. *Photoinitiators for Polymer Synthesis*; Wiley-VCH Verlag GmbH & Co. KGaA, 2012.

[85] Tucker, J. W., and Stephenson, C. R. J. (2012) Shining Light on Photoredox Catalysis: Theory and Synthetic Applications. *The Journal of Organic Chemistry 77*, 1617–1622.

[86] Prier, C. K., Rankic, D. A., and MacMillan, D. W. C. (2013) Visible Light Photoredox Catalysis with Transition Metal Complexes: Applications in Organic Synthesis. *Chemical Reviews 113*, 5322–5363.

[87] MacKinnon, A. L., and Taunton, J. (2009) Target Identification by Diazirine Photo-Cross-linking and Click Chemistry. *Curr Protoc Chem Biol 1*, 55–73.

[88] Dubinsky, L., Krom, B. P., and Meijler, M. M. (2012) Diazirine based photoaffinity labeling. *Bioorganic & Medicinal Chemistry 20*, 554–570.

[89] Hatanaka, Y., and Sadakane, Y. (2002) Photoaffinity Labeling in Drug Discovery and Developments: Chemical Gateway for Entering Proteomic Frontier. *Current Topics in Medicinal Chemistry 2*, 271–288.

[90] Preston, G. W., and Wilson, A. J. (2013) Photo-induced covalent cross-linking for the analysis of biomolecular interactions. *Chemical Society Reviews 42*, 3289.

[91] Mueller-Remmers, P. L., and Jug, K. (1985) SINDO1 study of photochemical reaction mechanisms of diazirines. *Journal of the American Chemical Society 107*, 7275–7284.

[92] Gilchrist, T. L., and Rees, C. W. *Carbenes nitrenes and arynes*; Springer US, 1969.

[93] Preston, G. W., Radford, S. E., Ashcroft, A. E., and Wilson, A. J. (2012) Covalent Cross-Linking within Supramolecular Peptide Structures. *Analytical Chemistry 84*, 6790–6797.

[94] Blawas, A., and Reichert, W. (1998) Protein patterning. *Biomaterials 19*, 595–609.

[95] Wei, S., Wang, J., Guo, D.-J., Chen, Y.-Q., and Xiao, S.-J. (2006) Grafting Organic and Biomolecules on H-Terminated Porous Silicon from a Diazirine. *Chemistry Letters 35*, 1172–1173.

[96] Wang, J., Kubicki, J., Peng, H., and Platz, M. S. (2008) Influence of Solvent on Carbene Intersystem Crossing Rates. *Journal of the American Chemical Society 130*, 6604–6609.

[97] Bishop, J., Chagovetz, A., and Blair, S. (2008) Kinetics of Multiplex Hybridization: Mechanisms and Implications. *Biophysical Journal 94*, 1726–1734.

[98] Lukacs, G. L., Haggie, P., Seksek, O., Lechardeur, D., Freedman, N., and Verkman, A. S. (2000) Size-dependent DNA Mobility in Cytoplasm and Nucleus. *Journal of Biological Chemistry 275*, 1625–1629.

[99] Jossang, T., Feder, J., and Rosenqvist, E. (1988) Photon correlation spectroscopy of human IgG. *Journal of Protein Chemistry 7*, 165–171.

5 Conclusions and perspectives

During my PhD research project, I was involved in the development of novel SPR-based systems which showed promising *in vitro* and *in vivo* biosensing capabilities. One of the critical steps for the creation of such systems relies on effective multiplexed functionalization strategies which was the main focus of this doctoral thesis.

A common challenge for the efficient generation of biochips, specifically protein microarrays, is to preserve the biological activity of the proteins during their grafting. One of the main factors causing a decrease in protein functionality is the dehydration of the probes on the surface, which eventually affects the adequate folding of the protein. Therefore, our first approach addressed this issue by the development of a multiplexable arraying method that could be totally performed in aqueous media. This method, which was thoroughly described in Chapter 2, consisted in UV-assisted degradation of thiolated PEG SAMs over gold surfaces. PEG SAMs are used as protective layers avoiding further functionalization of the gold surface. Degradation of these SAMs in specific patterns allowed the grafting of the molecules of interest while maintaining a fully liquid environment in the whole process, ensuring the integrity of the proteins. We discovered some insights of the chemical mechanisms involved on this process and validated this approach by the creation of a protein microarray able to capture individual cells.

As this method relies on the degradation of the PEG chains, it should be possible to extend it for any PEG-derived SAM (either thiol or silane based). Furthermore, by varying the exposure time, gradient surface functionalization can be achieved. Such versatility makes this approach highly interesting for a wide range of substrates and applications that require biomolecule immobilization with micrometric resolution. However, this technique also presented several drawbacks.

While some minor issues, such as imperfections in the generated patterns, could be easily corrected by employing a microfabricated photomask, or a system of digitally regulated micro-mirrors, the major limitation of this procedure laid on the time required for multiplexed surface functionalization. Under our current procedure, each feature was generated by an UV irradiation step followed by incubation with a thiolated probe. While the degradation process could be accelerated by employing a high-power UV light source, the formation of an uniform SAM at functional surface densities required incubation times varying from minutes to hours. Such waiting times would made this method impractical for more than 4-5 multi-step functionalization processes on a single biochip.

Nonetheless, for some applications, the formation of thiol/silane-based SAMs might not

be required and so, the functionalization times can be greatly reduced. UV irradiation of PEG SAMs significantly decreased their anti-fouling properties allowing direct protein adsorption over the generated patterns. This adsorption may be based on the formation of reversible Schiff bases between the aldehydes on the surface and the amino moieties of the proteins in solution. For example, this technique could be applied as a fast and simple methodology for creating cell binding patterns. The functionalization of irradiated zones with extracellular matrix proteins (*e.g.* collagen, fibrinogen) would lead to preferential cell adhesion on such areas which can be used for the study of cell behavior (attachment, mobility, replication, etc.) on different substrates.

After developing a versatile surface functionalization technique that could be employed on a variety of substrates, we focused our efforts into the creation of novel SPR systems for biosensing. In this sense, as explained in Chapter 3, one of the main limitations for the dynamic SPR monitoring of cell cultures derived from the fact that the cells often induced a much larger signal than the target biomolecules. To address this problem, our laboratory has worked on multiple microstructurated platforms that could provide SPR monitoring of the target molecules while suppressing this cell-derived SPR signal. Among the evaluated microstructuration methods, the deposition of a monolayer of silica microbeads was the most promising alternative. However, we observed that the silica microspheres dissolved in the aqueous buffers used for the biological assays. We evaluated multiple stabilization methods and developed a thermal treatment that is able to provide long term stabilization of the microbeads in presence of several aqueous buffers. This thermal treatment is independent of the surface where the microbeads are deposited and so, can be useful for other applications, besides SPR sensing, that require a separating layer between cells and the substrate.

Interestingly, when we deposited a monolayer of the microbeads over SPR prisms we observed an additional optical phenomenon (possibly Whispering Gallery Mode, WGM) under a specific set of conditions. We performed some preliminary optical characterizations on this phenomenon and demonstrated its potential for sensing the microbead surface. The immediate application for WGM in our system consisted in the detection of cells over the microbead monolayer. Our results showed that this is feasible but further exploitation of WGM would require the development of a different optical setup. Such setup would employ two light sources for the excitation of both phenomena: WGM and SPR, to simultaneously monitor the microbead environment and the gold surface respectively.

SPR monitoring of this microstructured system in presence of different types of cells showed that we successfully achieved our initial goal: the microbead monolayer was able to suppress either totally or partially, depending of the type of cells evaluated, the cell-derived SPR signals. Even in the worst case evaluated, the microbeads achieved a 5-10 fold reduction of the SPR signal observed on bare gold surfaces which constituted a remarkable level of suppression. Future modification on the microbead size and an in-depth study of the cell behavior over the microstructured surface might allow total suppression of the cell-derived SPR signal.

As it was previously explained, multiplexed functionalization is a crucial step for the

development of novel SPR biochips. We implemented two orthogonal strategies which allowed the selective functionalization of either the microbeads or gold surfaces in predefined patterns. In the case of microbeads functionalization, we performed a two-step method consisting in a silanization with MPTS followed by protein grafting via thiol-maleimide reactions. We validated this approach by the arraying of antibodies that led us to selectively capture PBMCs. However, we observed that the microbead surface was not uniformly functionalized, possibly due to droplet evaporation behavior over the porous monolayer. A potential solution for this problem could be the use of higher protein and glycerol concentration in the spotting solution as well as longer incubation times. Regarding functionalization of the gold surface, grafting of biomolecules was performed by electropolymerization of pyrrole. We also faced some challenges during this step as some spots presented considerable variations in morphology and size. A potential solution would require to optimize the contact time between the tip and the surface (to avoid excess droplet expansion due to capillarity between the microbeads) and automatizing the electropolymerization process to ensure reproducible spotting. We performed dual functionalization of SPR biochips and evaluated them for the capture cells and the detection of biomolecules (IgG antibodies). Satisfyingly, our results showed that our biochips were able to capture cells while simultaneously performing biomolecule detection.

Nonetheless, the main limitation for the use of these biochips for the detection of cell secretions seems to be related to the sensitivity of our SPR system. After profiling the secretion kinetics of our cellular models as well as performing sensitivity assays on our SPR system, we concluded that the expected levels of cytokine secretion were below the limit of detection of our current system. Although, the sensitivity assays were performed using spots created by thiol-based SAMs and thus, cannot fully represent systems employing different grafting strategies. Evaluation using electropolymerization of pyrrole-conjugated aptamers, as well as employing the discussed extravidin method, could prove more effective for cytokine detection. Moreover, selection of aptamers with higher affinity by new cycles of SELEX could greatly enhance cytokine capture on the biochips.

It is important to highlight, that even though we focused our efforts on cytokine detection, the microstructured biochips we developed could be used for other targets which would also require suppression of cell-derived noise. Some potential applications involve the monitoring of viral infection in cell cultures, study of the quorum sensing process in bacteria as well as the different stages of biofilm formation.

While such microstructured systems offer a promising approach for cell, and biomolecule, dynamic monitoring *in vitro*, there is currently a strong drive for the development of point-of-care diagnostic tools. To address the need for innovative *in vivo* biosensing devices, our research team developed a nanostructured fiber-optic SPR sensor (which was described in Chapter 4). In order to transform this system into a biochip, we invested our efforts in the implementation of multiplexed functionalization methods.

Our initial approaches consisted in contact printing strategies, which showed either structural damage to the sensing surface or lack of reproducibility. Afterwards, we evaluated photo-thermal desorption which had the advantage, compared to contact printing strategies, of being faster, the irradiation can be directed through the fiber and the patterning

can be performed with high precision/resolution. Nonetheless, the photo-thermal approach led to heterogeneous surface heating and gold ablation even at the lowest laser intensities. We evaluated the indirect UV functionalization method described earlier which allowed effective grafting of the irradiated areas with thiolated oligonucleotides. Yet, difficulties related to the manual operation as well as the required functionalization time (involving UV irradiation and incubation with the probe) limited this method.

Finally, we evaluated the use of photo-reactive surfaces based on diazirine moieties which showed the most promising results. Preliminary results, using diazirine-containing SAMs, showed rapid functionalization (in the range of seconds) of flat surfaces using oligonucleotides. Before applying this method on the nanostructured system, the grafting protocol has to be optimized as it currently presents reproducibility issues. As the carbenes formed in this process are easily quenched by water molecules, a pre-concentration method (either by drying or pH dependent adsorption) could be evaluated.

Once multiplexed functionalization will be achieved, the sensitivity of this biochip to different targets in increasingly complex media has to be evaluated. Such media can vary from simple aqueous buffers to cell pellets, eventually paving the way for performing *in vivo* assays. Regarding the potential targets, cytokine detection is highly desirable but extremely challenging as these proteins are present at femto- to picomolar concentrations in the blood stream. A more plausible target could be the monitoring of antibodies as well as C-reactive protein (which is a biomarker of inflammation with high clinical significance) whose concentrations may vary drastically from nanomolar to micromolar range based on the clinical condition. Detection of whole cells (bacterial species or eukaryotic cell subtypes) is another possibility for this type of sensors. On the other hand, fiber-optic biochips are not limited only to biomedical applications. Their small size and flexibility are also attractive for food industry (specifically, for the monitoring of packed products) as well as *in situ* environmental monitoring.

The research developed through this doctoral thesis required a multidisciplinary approach ranging from physics and chemistry to biology. Hopefully, my work based on the characterization and functionalization of these SPR systems will contribute to the development of innovative biosensing tools for a multitude of *in vitro* and *in vivo* applications.

A

Annexes

Contents

A.1 Experimental procedures

A.1.1 SAM formation based on thiol-gold interaction

Initial cleaning is based on rinsing the surface 3 times with ethanol 96% followed by 3 rinses with distilled water. If the surface requires further cleaning, use the ultrasound bath for 10 min in absolute ethanol. After water, dry the surface with an air gun. Surface activation can be prepared by plasma treatment (3 min with an atmosphere 75% O_2:25% Ar, 0.6 mbar and at 80% of maximum power) or exposure to piranha solution (3 min immersion on a 1:3 v/v H_2O_2:H_2SO_4). Surface is highly reactive after activation, to ensure repeatability of results, the substrates are usually left at room temperature in clean containers overnight before their use.

PEG-based SAMs: After cleaning, the gold surface is immersed or covered (with an abundant volume) of a 1 mM solution of the PEG-SH derivative of interest in PBS for 10-60 min depending of the desired SAM surface density. The incubation time is performed in a humid chamber (in a sealed recipient with a KNO_3 saturated solution, at 25°C the relative humidity corresponds to ∼85%). The surface is then rinsed 3 times with distilled water, dried and stored at 4°C (preferably in an Ar atmosphere) until use.

Alkanethiol-based SAMs: Similar to PEG-based SAMs, the gold surface is immersed into a 1 mM solution of the alkanethiol of interest dissolved in DMSO or absolute ethanol for 10-60 min in a humid chamber. Afterwards, the surface is rinsed 3 times with absolute ethanol, 3 times with distilled water, dried and stored at 4°C (preferably in an Ar atmosphere) until use.

Oligonucleotide-based SAMs: After plasma treatment of the gold surface (and an overnight resting phase), functionalization with thiolated oligonucleotides was performed. For this, spotting solutions containing different ratios of the thiolated oligos with $PEG_{2000}SH$ were made (the ratios ranged from 20µM:10µM, 10µM:10µM and 10µM:20µM respectively) in a K_2HPO_4 1 M solution (pH 9.25). Spotting was performed with a robot followed by incubation in a humid chamber (85% relative humidity at 25°C) for 1h. Afterwards, the surfaces were rinsed 8x with distilled water (∼5 mL each time) and stored at 4°C until used. Before their use, the surfaces were exposed to $PEG_{2000}SH$ 100 µM for 10 min and rinsed 5x with distilled water.

A.1.2 UV photodeprotection of SAMs

A homemade optical device was used during the Surface Plasmon Resonance Imaging (SPRi) assays. This hybrid set-up combined a SPR device with a commercial optical microscope (Olympus BX-URA2) allowing exposure of the samples to UV light while monitoring the SPR signal over time. For the UV irradiation, a high pressure mercury

lamp was used as a light source, an Olympus filter (λ 330-380 nm, peak at 365 nm) and either a 10x or 20x lens (Olympus UPlanF) were used on the device. SPRi was performed using a λ 625 nm diode as light source.

A fluidic device with a temperature regulation module was made (315 µL inner volume, 2.5 mm internal height and covered by a 3 mm thick glass) using PDMS and PEEK tubes. A resistance and a sensor inside the device allow the monitoring and regulation of the temperature which was set to 25°C. A Cavro pump was used to regulate the flow rate of the liquid which passed through a degassing system before entering the fluidic device. However, the amount of dissolved oxygen could not be regulated as the PDMS and PEEK tubes are permeable to gasses.

For evaluating the UV-mediated desorption kinetics of the different SAMs, functionalization of the gold surface was done before setting the prism in the fluidic device. SAM formation was performed by direct exposure of the plasma treated prisms to 1 mM solutions of either PEG_{350}-SH, PEG_{2000}-SH or 6-mercapto-1-hexanol for 1 h followed by 5 rinses with distilled water. In the case of 1-dodecanethiol and 2-methyl-2-propanethiol, the prisms were exposed to 1 mM solutions of the respective compound for 2h at room temperature, then followed by three washes with 10 mL of 96% ethanol and other three washes with 10 mL of distilled water. Then, SPRi was performed using a λ 625 nm diode as light source. During UV irradiation, samples had a constant flow of PBS (0.5 $\mu L.s^{-1}$).

Regarding the multi-cycle adsorption/desorption of PEG derivatives, SAMs were formed via injection of 20 µM solutions of either PEG_{350}-SH or PEG_{2000}-SH at 0.1 $\mu L.s^{-1}$ with 1h of exposure followed by a 1.7 $\mu L.s^{-1}$ flow of PBS for 10 min. Similarly to previous tests, during UV irradiation the samples had a constant PBS flow of 0.5 $\mu L.s^{-1}$.

A.1.3 Determination of lower detection limit of EPR

A series of dilutions of the stable radical 4-Hydroxy-TEMPO (1) were prepared in PBS (2) at the followed concentrations: 10 mM, 1 mM, 100 µM, 10µM, 1µM, 100nM, 1nM.

Borosilicate glass capillars (VITREX Cat. no 1272, inner diameter ∼1mm) were used for storing the samples. 100 µL of each solution were taken into capillars which, afterwards, were sealed on one side. All the dilutions were kept in dark and stored at 4°C until used (<24h).

For the EPR experiment, the capillars were deposited into an RPE tube using the following parameters for its analysis:

— Modulation: 1 Gauss (measurements at 0.3 Gauss were performed for the highest and lowest dilution were a signal was observed)

— Accumulation time per point: 82 ms

— Gain: a gain of 10^5 was used for the concentrations ranging from 10 nM to 100µM,

(1). 4-Hydroxy-2,2,6,6-tetramethylpiperidine 1-oxyl, also know as TEMPOL

(2). Phosphate Buffered Saline. An aqueous buffer with 1M KH_2PO_4,1M K_2HPO_4 and 5M NaCl

a gain of 10^4 for 1 mM and 10^3 in the case of 10 mM

— Cavity working volume: 2/3 of cavity were used, equivalent to ∼30 µL

A.1.4 Functionalization of gold nanoparticles for EPR experiments

Citrate stabilized commercial gold nanoparticles were treated with a BSPP solution (to a final concentration of 3 mg.mL^{-1}) and incubated overnight at room temperature. Afterwards, samples were centrifuged at 16750 G for 15 min, the supernatant was discarded and suspended in 1 mL per sample of saline buffer (1 mg.mL^{-1} BSPP with 5 mg.mL^{-1} NaCl) was added prior to a new centrifugation. Each sample was suspended in 100 µL of PBS buffer containing 1 mg.mL^{-1} of BSPP and 10 µM of $PEG_{2000}SH$. Samples were incubated overnight at 4°C, and centrifuged and suspended in 200 µL of PBS. This step was repeated twice.

A.1.5 Amine NHS-mediated conjugation

For proteins, 200 µL of a 3.3 µM solution (previously purified from any sodium azide traces) were mixed with 34 µL of a 200 µM solution of the NHS-containing molecule of interest and 166 µL of PBS pH 8.3. After 2h incubation at room temperature the proteins were purified using Vivaspin columns (30 kDa).

For oligonucleotides, 20 µL of a 100 µM solution of oligos were mixed with 8 µL of a 40 mM NHS-containing molecule + 172 µL of PBS pH 8.3. After a 2 h incubation at room temperature, the oligos were purified with Sephadex NAP25 columns.

A.1.6 Functionalization of microbead-based biochips

Silane-based SAM on the gold surface: Plasma treated prisms (3 min, 75% O_2 25% Ar, 0.6 mbar and 80% of maximum power) are incubated overnight into a 30 mM solution of MPTS in toluene at room temperature. Afterwards, the prisms are rinsed with toluene, then ethanol absolute and finally distilled water (3 times per solvent, ∼10 mL of solvent each wash). Finally, the prisms are dried and stored in an Argon atmosphere at 4 ℃ until deposition of microbeads via the Boostream process.

Silane-based SAM on the microbead surface: After microbead deposition, the prisms are rinsed in absolute ethanol and dried. The prisms were stored in an glass container with an inert atmosphere (argon) and then incubated at 110 ℃ for 3 h. Then, the prisms were immersed into a 30 mM MPTS solution overnight at room temperature and rinsed as described before.

Grafting of antibodies on the gold surface via electropolymerization: Electopolymerization was performed by applying a 2V differential in the electric potential for 100 ms during the contact of the spotting solution and the gold surface. After spotting, the surface was rinsed 3 times with 10 mL of non-saline PBS (10 mM, NaH_2PO_4 is progressively added to a Na_2HPO_4 solution until reaching a pH: 7.4, does not contain NaCl nor KCl) and softly dried.

Grafting of antibodies on the microbead surface via thiol-maleimide interactions: Maleimide conjugated antibodies (1 µM) are deposited on the surface for 30 min in a humid chamber. Afterwards, the prism is deposited into a container with 15 mL of a 5 mM solution of maleimido-hexanoic acid in order to block the free thiol moieties on the microbead surface. Finally, the prism is rinsed via immersion for 15 min in a non-saline PBS + Tween20 0.02% solution, rinsed 3 times with 10 mL of non-saline PBS and stored in non-saline PBS at 4 ℃ until use.

A.1.7 Chemical composition of solutions used during microbead-based assays

A.1.7.a Phosphate Buffered Saline (PBS):

Composition of the culture media described by Sigma-Aldrich, pH 7.4 at 25 °C.:

Compound	Concentration (mM)	Concentration ($g.L^{-1}$)
NaCl	137	8.0
KCl	2.7	0.2
Na_2HPO_4	10	1.44
KH_2PO_4	2	0.24

A.1.7.b Roswell Park Memorial Institute (RPMI 1640):

Composition of the culture media described by Sigma-Aldrich:

Inorganic salts ($g.L^{-1}$): $Ca(NO_3)_2 \cdot 4\,H_2O$ 0.1; $MgSO_4$ (anhyd) 0.04884; KCl 0.4; $NaHCO_3$ 2.0; NaCl 6.0; Na_2HPO_4 (Anhyd) 0.8.

Amino acids ($g.L^{-1}$): L-Arginine (free base) 0.2; L-Asparagine (anhyd) 0.05; L-Aspartic Acid 0.02; L-Cystine·2HCl 0.0652; L-Glutamic Acid 0.02; L-Glutamine 0.3; Glycine 0.01; L-Histidine (free base) 0.015; Hydroxy-L-Proline 0.02; L-Isoleucine 0.05; L-Leucine 0.05; L-Lysine·HCl 0.04; L-Methionine 0.015; L-Phenylalanine 0.015; L-Proline 0.02; L-Serine 0.03; L-Threonine 0.02; L-Tryptophan 0.005; L-Tyrosine·2Na·2 H_2O 0.02883; L-Valine 0.02.

Vitamins ($g.L^{-1}$): D-Biotin 0.0002; Choline Chloride 0.003; Folic Acid 0.001; myo-Inositol 0.035; Niacinamide 0.001; p-Amino Benzoic Acid 0.001; D-Pantothenic Acid·$\frac{1}{2}$Ca 0.00025; Pyridoxine·HCl 0.001; Riboflavin 0.0002; Thiamine·HCl 0.001; Vitamin B-12 0.000005;

Other ($g.L^{-1}$): D-Glucose 2.0; Glutathione (reduced) 0.001; Phenol Red·Na 0.0053

The above medium was supplemented with Fetal Bovine Serum (FBS) to a final concentration of 10% (v/v) and Penicillin-Streptomycin (100 U penicillin and 100 µg streptomycin).

A.1.8 Quantification of insulin secretion

Insulin secretion test based on glucose concentration was designed for RIN-m cells based on the information provided by G.Müller (DOI: 10.1007/978-3-319-05392-9_158).

Table A.1 – Preparation of 300 mL of KRBH buffer

Compound	MW ($g.mol^{-1}$)	Concentration (mM)	Mass required for 300 mL (mg)
NaCl	58.44	118.5	2077.5
$CaCl_2 \cdot 2H_2O$	147.02	2.54	102
KH_2PO_4	136.09	1.14	48.6
KCl	74.55	4.74	106.0
$NaHCO_3$	84.01	5	126.0
$MgSO_4$	120.37	1.19	43.0
HEPES	238.3	10	714.9
BSA	—	0.5% (m/v)	1500

Add water type 1 to reach 300 mL, mix and sterilize it (using 0.22 µm filters).

Insulin secretion assay: RIN-m cells are seeded into 12 well multiwell plates at $1.0x10^6$ $cells.well^{-1}$. After 24h of being incubated in standard conditions, medium is removed and substitute with KRBH pre-warmed buffer. The cells are incubated in the buffer for 30 min at 37°C to reset their metabolic activity. Buffer is removed and the respective media is added to each well high glucose (25 mm) or no glucose (buffer) media.

After predetermined intervals, media is collected from the respective wells and stored at -20°C (secreted material). Cells are washed with 0.5 mL of DPBS and then exposed to NaOH 100 mM (0.5 mL) to induce their lysis. After overnight incubation at 37°C, the intracellular contents are collected and stored at -20°C.

A.1.9 Activation of PBMC

PBMC cells are thawed and cultured for 18h in a T-25 flask with AIM V Serum Free Medium at 5% CO_2 and 37 ℃ for 18h (2.5×10^6 cells.mL−1). Afterwards, cells were concentrated and resuspended in the respective culture media (Activation media: AIM-V + Ionomycin (500 ng.mL^{-1}) + PMA (100 ng.mL^{-1}); Normal media: AIM-V) to a concentration of 2.4×10^6 cells per mL.

Cells were seeded in a 96 multiwell plate with (200 µL per well of the respective culture equivalent to 4.8×10^5 cells). Samples were cultured in duplicated for each treatment (Activated or Non-activated) and sampling hour (0h, 2h, 4h, 6h, 24h, 30h and 48h of incubation). To avoid border effect, only the wells in the middle were seeded with cells while the bordering empty wells were filled with PBS to diminish dehydration. Samples were taken at the previously described times and frozen at -20°C until use. For the ELISA test, samples were diluted 1:100 using ELISA diluent (2% w/v BSA in PBS + 0.05%Tween20).

A.1.10 THP-1 differenciation and activation

These protocols are derived from Nanobiose with small modifications. The media used were prepared as follow:

- Culture media (RPMIc): RPMI 1640 with 2mM of L-glutamine, 10% fetal bovine serum (FBS), PeniStrepto, 4.5 g/L glucose, 1 mM sodium pyruvate.

- Thawing media: The same as RPMIc but with 20% FBS

- Cryopreservation media: 90% FBS + 10% DMSO

- Differentiation media: RPMIc + PMA (10 ng.mL^{-1} final concentration)

- Activation media: AIM-V + LPS (0.1 µg.mL^{-1}) + R848 (0.2 µg.mL^{-1}) + 10 mM HEPES

Differentiation: After removing the supernatant via centrifugation for 5 min (1500 rpm), cells are resuspended into differentiation media at a concentration of 2x10^5 cells.mL^{-1}. Then, 500 µL of the cell solution are seeded on each well of a 24-multiwell plate. The plate is incubated at 37 ℃ (5% CO_2 atmosphere and 85% relative humidity) for 72 h. Then, new media is added the plate is incubated for additional 24h. After this step, the cells are ready for activation.

Activation: Culture media is removed from each well while traces of Fetal Bovine Serum are removed by washing each well with 0.5-1 mL of DPBS. Then, 0.5 mL of trypsin 0.05% + 0.001% EDTA is added to each well. After incubation at 37 ℃ for 5-7 min, 0.5 mL of $RPMI_c$ are added to inactivate the trypsin. All the wells were merged and centrifuged 5 min at 1500 rpm. Afterwards, the cells are resuspended into AIM-V media to a 2.0×10^5 cells.mL^{-1}. In a 96 multi-well plate, 150 µL of the cell suspension are deposited per well. After 2-4 h incubation at 37 ℃, the culture media is removed and substituted either by

150 µL of activation media (1.996 mL AIM-V, 2 µL LPS (0.1 mg.mL^{-1}) + 2 µL R848 (0.2 mg.mL^{-1})) or control media ((1.996 mL AIM-V, 2 µL DMSO and 2 µL PBS).

A.2 Additional experiments

A.2.1 Effect of ROS inducers in UV-assisted desorption of PEG-SAMs

A PEG-based SAM was prepared over a SPR prism by exposing the surface for 30 min before copious rinsing with distilled water. Using a microfluidic device, a constant flow of 2.5 µL.s^{-1} either PBS or H_2O_2 was performed while simultaneously irradiate the surface with UV-light.

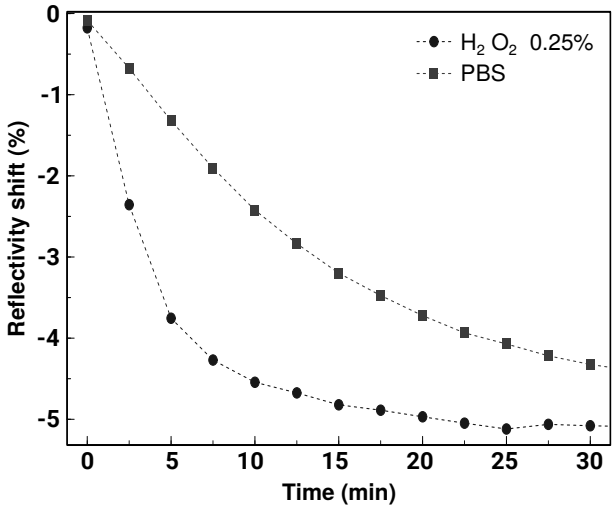

Figure A.1 – Desorption kinetics of $PEG_{2000}SH$ when exposed to 0.25% of H_2O_2 during UV irradiation.

B

Version française

Introduction

L'évolution a doté les organismes vivants d'une multitude de stratégies de détection qui leur permettent de percevoir, d'interagir et de s'adapter à leur environnement. Parmi ces organismes, les humains ont utilisé avec succès leurs capacités cognitives pour augmenter leurs sens naturels. En utilisant des outils artificiels pour surmonter nos limites, nous avons pu observer des phénomènes jusqu'alors inconnus, ce qui nous a permis de mieux comprendre la structure et le fonctionnement de nous-mêmes et également de notre univers.

Plus précisément, lorsqu'elles sont utilisées pour explorer les interactions biomoléculaires (biodétection), ces technologies de détection sont devenues d'une importance capitale dans le domaine médical (découverte de médicaments, diagnostic et surveillance des maladies), en sécurité alimentaire et en surveillance environnementale, pour ne citer que quelques exemples. D'autre part, le besoin de comprendre toujours plus finement les systèmes étudiés requiert le constant développement d'outils de biodétection innovants. L'objectif de cette thèse de doctorat est de participer à cet élan d'innovations en élaborant de nouveaux systèmes de biodétection et les stratégies pour les mettre en œuvre. En particulier, j'ai exploré de multiples techniques de fonctionnalisation et leurs mises en place sur trois systèmes de détection sans marquage basés sur la plasmonique (SPR).

Chacun de ces systèmes de détection présente un ensemble unique de défis, puisque le substrat présente soit une morphologie plane, microstructurée ou nanostructurée composée d'un ou deux matériaux différents. La fonctionnalisation de surfaces aussi variées a nécessité l'adaptation de différentes approches chimiques telles que les monocouches auto-assemblées (SAMs pour Self-Assembled Monolayers) à base de thiol et de silane, l'électropolymérisation du pyrrole, la fonctionnalisation photo-assistée, etc.

Dans cette thèse, les principaux chapitres sont consacrés à la présentation des stratégies mises en places sur les différents systèmes SPR et les défis relevés pour leur fonctionnalisation.

Chapitre 1

Dans ce chapitre, un aperçu des principales stratégies de biodétection sans marquage est présenté, avec notamment un accent sur la résonance des plasmons de surface (SPR pour *Surface Plasmon Resonance*). Une brève introduction du principe physique du SPR ainsi que les configurations existantes sont ensuite décrites. Enfin, un état de l'art est dressé et une liste non exhaustive des méthodes de fonctionnalisation les plus courantes pour les systèmes de biodétection SPR est présentée.

Chapitre 2

Le greffage des protéines est utilisée dans un large éventail d'applications, allant de l'analyse des microarrays de protéines à l'organisation des cellules en 2D. Toutefois, des limites se présentent en raison de la nature très sensible des protéines, qui nécessitent une manipulation soigneuse pour assurer leur intégrité structurelle et fonctionnelle pendant le processus de greffe.

Dans ce chapitre, nous décrivons un protocole de fonctionnalisation qui maintient les protéines dans un environnement aqueux pendant leur immobilisation, évitant ainsi la perte de leur activité biologique. Le procédé est basé sur l'élimination par UV des monocouches auto-assemblées de polyéthylène glycol (PEG) dans une chambre microfluidique transparente, donnant accès à des motifs micrométriques de géométries prédéfinies. Ensuite, des protéines modifiées peuvent être greffées sur les motifs définis par la précédente exposition UV. Nous avons également étudié l'influence des espèces réactives de l'oxygène pour mieux comprendre les mécanismes chimiques impliqués dans ce processus. Enfin, comme preuve de concept, un microréseau de protéines a été créé en greffant des anticorps capturant des cellules sanguines humaines. Confirmant ainsi la fiabilité de notre procédé pour assurer la production de dépôts structurés à l'echelle de quelques micrometres de protéines ayant conservé leur fonctionnalité.

Chapitre 3

Beaucoup d'efforts ont été consacrés à la détection des cytokines et des chimiokines. Ce sont des protéines solubles qui sont sécrétées par une grande variété de cellules pour moduler dynamiquement la réponse de l'organisme aux blessures et aux infections. Cependant, la nature éphémère des cytokines ainsi que leur présence en très faibles concentrations (du femto au picomolaire) rendent leur détection en temps réel très difficile. En ce sens, la SPR peut être un outil puissant pour la détection des cytokines. Cependant, elle présente plusieurs points critiques: la limite de détection sans marquage est proche de la concentration des cytokines à détecter et il présente des problèmes d'adsorption non-spécifique avec des échantillons "complexes", en particulier ceux causés par les cellules. Dans ce chapitre, nous décrivons la conception d'une nouvelle biopuce SPR incorporant une couche micro-

structurée qui sépare les cellules de la région de détection, supprimant ainsi efficacement leur signal SPR faisant office d'espaceur.

Pour le développement de ces biopuces SPR, nous avons réalisé différents traitements de surface pour la stabilisation mécanique et chimique des microstructures, des caractérisations optiques et la mise en œuvre de stratégies de fonctionnalisation orthogonale. La stabilisation chimique des microbilles a été réalisée par un traitement thermique. Leur immobilisation chimique sur les surfaces en or a été basée sur la formation de SAM hétérobifonctionnelles. La caractérisation optique de ces biopuces microstructurées a montré la présence d'un autre phénomène de résonance, en plus de la SPR, que nous avons attribué aux *Whispering Gallery Modes* (WGM). Comme indiqué précédemment, notre objectif était de supprimer les signaux SPR provoqués par les cellules car ils masqueraient la détection de leurs sécrétions. En éliminant la signature SPR des cellules, il était à craindre que l'ajout d'un système d'observation microscopique soit réquis pour corréler les signaux de sécretions aux positions des cellules. Cependant, la présence de ce nouveau mode optique nous permettrait de visualiser les cellules via WGM tout en effectuant simultanément la détection SPR de leurs sécrétions. Nos résultats ont montré que le WGM peut être utilisé efficacement pour la détection cellulaire tandis que la détection SPR à l'aide de ce système microstructuré en présence de différents types de cellules a montré une suppression efficace des signaux SPR produit par les cellules.

De plus, nous avons appliqué deux stratégies de fonctionnalisation qui ont permis l'immobilisation sélective sur des surfaces de microbilles ou sur des surfaces d'or selon des modèles prédéfinis. Les résultats expérimentaux ont validé ces approches puisque nos biopuces ont permis de capturer des cellules sanguines humaines tout en effectuant simultanément la détection des protéines. Cependant, l'optimisation de ces processus reste nécessaire pour converger vers l'application détection de sécrétion de cytokines.

Chapitre 4

Bien que de tels systèmes microstructurés offrent une approche prometteuse pour la surveillance dynamique des cellules et des biomolécules *in vitro*, il existe actuellement une forte demande pour le développement d'outils de diagnostic au chevet du patient. Pour répondre au besoin d'appareils de biodétection innovants *in vivo*, notre équipe de recherche a mis au point un capteur SPR à fibre optique nanostructurée. Afin d'exploiter ce système comme une biopuce, nous avons dû effectuer un processus de fonctionnalisation multiplexé. Or, les dimensions très reduites (300 µm de diamètre) et le caractère microstructuré/nanostructuré du dispositif en font un veritable défi pour le greffage de biomolécules. Nous avons mis en œuvre et comparé différentes stratégies de fonctionnalisation des surfaces.

Nos approches initiales ont consisté en des stratégies d'impression par contact, qui on montré soit des dommages structurels à la surface de détection de la fibre, soit un manque de reproductibilité. Ensuite, nous avons évalué la désorption photo-thermique qui avait l'avantage, par rapport aux stratégies d'impression par contact, d'être plus rapide. L'irra-

diation peut être réalisée à travers la fibre et le motif peut être reproduit avec une haute résolution. Néanmoins, l'approche photo-thermique a conduit à un chauffage hétérogène de la surface et à une ablation de l'or même aux intensités laser les plus faibles. Nous avons alors évalué la méthode de fonctionnalisation UV indirecte décrite au chapitre 2, ce qui a permis de greffer efficacement les zones illuminées avec des oligonucléotides thiolés. Cependant, les difficultés liées à l'opération manuelle ainsi que le temps de fonctionnalisation requis (impliquant l'irradiation UV et l'incubation avec la sonde) ont limité la portée de cette méthode.

Enfin, nous avons évalué l'utilisation de surfaces photoréactives à base de fragments de diazirine qui ont donné les résultats les plus prometteurs. Les résultats préliminaires, utilisant des SAMs contenant de la diazirine, ont montré une fonctionnalisation rapide (de l'ordre de quelques secondes) des surfaces planes à l'aide d'oligonucléotides. Avant d'appliquer cette méthode au système nanostructuré, le protocole de greffage doit être optimisé car il présente actuellement des problèmes de reproductibilité.

Conclusions

Au cours de mon projet de recherche de doctorat, j'ai participé au développement de nouveaux biocapteurs basés sur une transduction optique par SPR. Ces travaux ont démontré des capacités prometteuses de biodétection *in vitro* et *in vivo* par ces approches. L'une des étapes critiques pour la création de tels systèmes repose sur des stratégies de fonctionnalisation multiplexées efficaces, ce qui était l'objectif principal de ce travail.

Tout d'abord, nous avons développé une technique polyvalente de fonctionnalisation de surface qui peut être utilisée sur une grande variété de substrats. Comme cette méthode repose sur la dégradation de PEG, il devrait être possible de l'étendre à toute SAM contenant des motifs du PEG (à base de thiol ou de silane). De plus, en variant le temps d'exposition, il est possible d'obtenir un gradient de fonctionnalisation de la surface. Cette polyvalence rend cette approche très intéressante pour une large gamme de substrats et d'applications qui nécessitent l'immobilisation de biomolécules avec une résolution micrométrique. Toutefois, cette technique présente aussi plusieurs inconvénients, dont le plus important est lié au temps nécessaire à la formation d'une SAM uniforme à des densités de surface fonctionnelles. Néanmoins, pour certaines applications, la formation de SAM à base de thiol/silane peut ne pas être nécessaire et ainsi, les temps de fonctionnalisation peuvent être considérablement réduits.

Ensuite, nous avons concentré nos efforts sur la création d'une biopuce SPR microstructurée pour la surveillance simultanée des cellules et de leurs sécrétions. Nous avons réussi à créer une biopuce qui supprime de façon significative les signaux SPR dérivés des cellules tout en effectuant une détection biomoléculaire des protéines par SPR. Cependant, la sensibilité de notre système ne nous a pas permis de mesurer directement la sécrétion de cytokines. Les technologies employées pour la conception de ce système ainsi que la biopuce pourraient être néanmoins adaptées à de nombreuses applications qui nécessitent la séparation de cellules d'un substrat particulier. Par exemple, l'analyse du processus de

quorum sensing ou la formation des biofilms.

Par la suite, nous avons évalué de différentes stratégies de fonctionnalisation multiplexée d'une biopuce nanostructurée prometteuse de SPR composée de faisceau de fibres optiques. Parmi toutes les approches évaluées, l'utilisation de surfaces photoréactives (SAM contenant de la diazirine) a donné les meilleurs résultats. Cependant, le protocole de greffage nécessite une phase d'optimisation supplémentaire avant son utilisation comme stratégie de fonctionnalisation universelle.

La recherche développée dans le cadre de cette thèse de doctorat a nécessité une approche multidisciplinaire allant de la Physique à la Biologie en passant par la Chimie. J'espère que mon travail basé sur la caractérisation et la fonctionnalisation de ces systèmes SPR contribuera au développement d'outils de biodétection innovants pour une multitude d'applications *in vitro* et *in vivo*.